DETERMINISTIC AND PROBABILISTIC TSUNAMI STUDIES IN CALIFORNIA

FROM NEAR AND FARFIELD SOURCES

by

Burak Uslu

A Dissertation Presented to the
FACULTY OF THE GRADUATE SCHOOL
UNIVERSITY OF SOUTHERN CALIFORNIA
In Partial Fulfillment of the
Requirements for the Degree
DOCTOR OF PHILOSOPHY
(CIVIL ENGINEERING)

December 2008

Table of Contents

List of Figures

List of Tables

Abstract

California is vulnerable to tsunamis from both local and distant sources. While there is an overall awareness of the threat, tsunamis are infrequent events and few communities have a good understanding of vulnerability. To quantitatively evaluate the tsunami hazard in the State, deterministic and probabilistic methods are used to compute inundation and runup heights in selected population centers along the coast.

For the numerical modeling of tsunamis, a two dimensional finite difference propagation and runup model is used. All known near and farfield sources of relevance to California are considered. For the farfield hazard analysis, the Pacific Rim is subdivided into small segments where unit ruptures are assumed, then the transpacific propagations are calculated. The historical records from the 1952 Kamchatka, 1960 Great Chile, 1964 Great Alaska, and 1994 and 2006 Kuril Islands earthquakes are compared to modeled results. A sensitivity analysis is performed on each subduction zone segment to determine the relative effect of the source location on wave heights off the California Coast.

Here, both time–dependent and time–independent methods are used to assess the tsunami risk. In the latter, slip rates are obtained from GPS measurements of the tectonic motions and then used as a basis to estimate the return period of possible earthquakes. The return periods of tsunamis resulting from these events are combined with computed waveheight estimates to provide a total probability of exceedance of given

waveheights for ports and harbors in California. The time independent method follows the practice of past studies that have used Gutenberg and Richter type relationships to assign probabilities to specific tsunami sources.

The Cascadia Subduction Zone is the biggest near–field earthquake source and is capable of producing mega–thrust earthquake ruptures between the Gorda and North American plates and may cause extensive damage north of Cape Mendocino, to Seattle. The present analysis suggests that San Francisco Bay and Central California are most sensitive to tsunamis originating from the Alaska and Aleutians Subduction Zone (AASZ). An earthquake with a magnitude comparable to the 1964 Great Alaska Earthquake on central AASZ could result in twice the wave height as experienced in San Francisco Bay in 1964.

The probabilistic approach shows that Central California and San Francisco Bay have more frequent tsunamis from the AASZ, while Southern California can be impacted from tsunamis generated on Chile and Central American Subduction Zone as well as the AASZ.

Chapter 1

Introduction

Rapid development in California in the past thirty years and the size of economy so dependent on ports and harbor for trade, necessitates quantitative studies of tsunami hazard in California.

In the past 110 years, California has experienced seven substantial tsunamis; i.e., the 1896 Sanriku Japan, 1946 East Aleutians (Unimak), 1952 Kamchatka, 1957 Aleutians, 1960 Chile, 1964 Alaska and 1975 Hawaii tsunamis. The 1896 Great Meiji earthquake along the Sanriku trench triggered a wave locally running up $38m$ killing 26,000 people (Lander et al., 1993). The tsunami reached $1.5m$ and caused damage at Santa Cruz, California (Soloviev and Go, 1974). The 1946 Aleutian earthquake ($M_w \approx 8.6$; Lopez and Okal, 2006) not only destroyed the lighthouse at Scotch Cap on Unimak Island, but also generated a devastating tsunami that killed 173 in Hawaii with $17m$ runup (Okal et al., 2003). The Pacific Tsunami Warning Center was established in response to this event. The 1952 Kamchatka and 1957 Aleutian tsunamis were also noticed, the latter damaging San Diego Harbor (Soloviev and Go, 1974). The 1960 $M_w \approx$ 9.5 Great Chilean event, featuring the largest seismic moment ever recorded instrumentally, was caused by the rupture of $1,000km$ long $150km$ wide segment with an average displacement around $20m$ (Plafker, 1972). These earthquakes and the subduction zones in Japan, Kuril Islands (KSZ), Alaska-Aleutians (AASZ), Cascadia (CSZ) and South America–Chile (SASZ) are shown in figure 1.1.

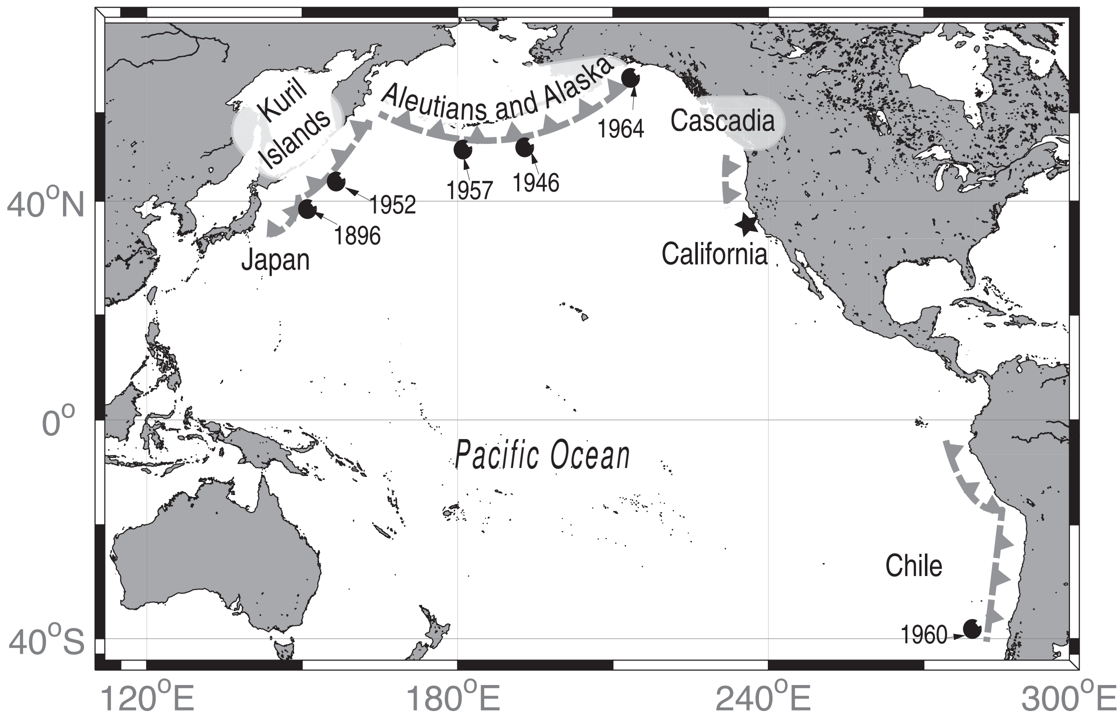

Figure 1.1: Major Subduction zones that can trigger tsunamis that will be effective in California.

The largest tsunami waves are generated along subduction zones, where oceanic floor subducts under the adjacent continental plate. Earthquakes along subduction zones are responsible for about 90% of the total seismic moment released from 1900 through 1989 (Yeats, 1997).

California population, commerce and industry are concentrated in coastal regions. Therefore, even a small tsunami can substantially damage California's economy. Due to its importance, analysis of tsunami hazards in California have been studied most qualitatively, and it is briefly described in the following section.

Location	R_{100} (m)	R_{500} (m)
La Jolla	1.9	3.9
San Onofre	1.7	3.4
Newport Beach	1.9	3.3
Long Beach	2.1	3.0
Dockweiler Beach	2.9	4.7
Topanga	3.2	5.1
Ventura	3.2	6.6

Table 1.1: Houston and Garcia (1974) tsunami height predictions close to shore.

Location	Predicted (m)	Observed (m)
Alamitos Bay	0.7	0.5
Santa Monica	0.9	0.8
Avila Beach	1.1	1.3
Crescent City	2.2	2.4

Table 1.2: Houston and Garcia (1974) tsunami height predictions for 1964 Alaska tsunami.

1.1 Review of Earlier Work

The first detailed study of farfield tsunami hazards in California was undertaken by Houston and Garcia (1974) and Houston (1980). This work was followed by McCulloch (1985), who concentrate farfield and nearfield tsunami hazards in the Los Angeles area.McCarthy et al. (1993) then qualitatively assessed the tsunami hazard for the entire state, while Synolakis et al. (1997) attempted to infer inundation estimates from the McCarthy et al.'s work. Borrero (2002) did a comprehensive study of local tsunamis in southern California.

1.1.1 Houston and Garcia 1974 and 1980

Houston and Garcia (1974) calculated 100–year and 500–year tsunami runup heights for different locations along California's coastline state by using a combination of numerical and analytical methods. They considered tsunamis emanating from both AASZ and SASZ, based on the 1964 Alaska and 1960 Chilean earthquakes.

In their methodology, they discretized AASZ into twelve segments, and then they recreated "worst case scenarios" by assuming initial ground deformations by a hypothetical uplifting mass of ellipsoidal shape, about $1000km$ long, with an aspect ratio of $1:5$ and maximum vertical uplift of 8–$10m$. Using a one–dimensional linearized shallow water equation in spherical coordinates, they propagated their initial waves from the Alaskan and Chilean sources to California. At the continental shelf, an analytical expression was derived to match the inner and outer wave amplitudes. Then, they obtained a simple amplification factor for a sinusoidal wave to generate the final wave amplitude offshore of the target. Their 100–year (R_{100}) and 500–year (R_{500}) results are summarized in Table 1.1, with a comparison of Houston and Garcia's (1974) results with the 1964 Alaska tsunami tide gauge record shown on Table 1.2.

Houston and Garcia's (1974) results showed greater accuracy than even what would had been optimistically anticipated when compared to the 1964 tidal gauge records (Synolakis et al., 1997). Yet, their solution had three areas that warranted improvement. First, a one dimensional model was applied for the solution of nearfield events, and this solution is not a priori appropriate for complex nearshore bathymetry, such as in narrow bays. Second, they used a sinusoidal wave in the analytical solution close to shore, and this can lead to substantial errors in the solutions of the runup. Third, small scale nearshore features affect local inundation and runup to first order, and were neglected in the coarse gridded computation of Houston and Garcia (1974).

A few years later, Houston (1980) performed a further comprehensive study, utilizing finite elements solutions of nonlinear shallow–water wave equations including friction terms. His work was an improvement over Houston and Garcia (1974), but was limited to farfield sources in Alaska and South America. The Pacific Ocean was modeled as a $500m$ constant depth basin with a $2miles$ square grid. Nearshore bathymetry was also modeled with a $2miles$ square grid. His solution did not include inundation computations and coastal boundaries were modeled as vertical walls. It was later shown that inundation calculations change the runup predictions substantially (Titov and Synolakis, 1997, 1998) compared to threshold models that stop the computation at some offshore location, as Houston (1980) did. Threshold models remained the only choice until the development of inundation models in the 1990s (Synolakis and Bernard, 2006).

1.1.2 The McCulloch 1985 USGS Professional Paper

McCulloch (1985) studied the tsunami hazard in the Los Angeles area using nearfield and farfield sources. For farfield sources, he relied on results from Houston and Garcia (1974) and Houston (1980).

McCulloch (1985) did not use any hydrodynamic model for predictions, but used an empirical formula that related earthquake magnitude to tsunami wave height. Synolakis et al. (1997) explained that such empirical formula were developed for use in specific locales Japan, and generally under–predicted the runup in other earthquake regions.

McCulloch (1985) inferred that the hazard from local tsunamis in California was low and argued that a local earthquake with magnitude of 7.5 could produce a tsunami accompanied by $4-6m$ runup. The tsunami wave height at Crescent City during the 1964 Alaska event was about $7m$. Furthermore, worldwide field surveys since 1992 have showed that a $4m$ tsunami can be very damaging to flat coastlines and can kill people. In general, as (Ambraseys and Synolakis, 2009) argue, general relationships between earthquake intensity and tsunami runup are not credible, because even during the same event runup varies substantially locally.

McCulloch (1985) also considered landslide waves whose initial heights were calculated using Murty's empirical formulae (Murty, 1979). For the Palos Verdes debris avalanche, Borrero et al. (2001); Borrero (2002) discovered that McCulloch calculations contained an arithmetic error, that underestimated the size of the resulting wave by a factor of 100. Until the 1998 Papua New Guinea tsunami (Kawata et al., 1999; Synolakis et al., 2002), McCulloch's assertion that the initial wave was $0.14m$ was never critically examined, and landslide waves had been believed to be a lesser hazard than tectonic tsunamis, even locally.

Despite this last shortcoming, McCulloch's (1985) report was a huge leap forward in tsunami hazard assessment in southern California.

1.1.3 McCarthy et al.'s (1993) Analysis

McCarthy et al. (1993) performed a systematic analysis of all historical and possible future tsunami hazards in California, following the 1992 Cape Mendocino event. The earthquake generated a small tsunami wave that reached northern California within 20 minutes after the earthquake. McCarthy et al. (1993) named this event a "wakeup" tsunami.

Synolakis et al. (1997) reanalyzed McCarthy's work and commented on its contributions and shortcomings. Borrero (2002) discussed McCarthy et al. (1993) in more detail, as summarized here. The 1992 Cape Mendocino was important not only because the wave reached the coastline within minutes of the earthquake, giving no time to coastal communities for evacuation, but also it had a very long duration. In addition, the tsunami occurred during low tide, and its impact would have been greater at high tide.

McCarthy et al. (1993) split California into four coastal sections and qualitatively evaluated each section according to tsunami risk. They calculated the tsunami hazard in California as *high* along the line from Crescent City to Cape Mendocino, *moderate* from south of Cape Mendocino to north of Monterey, *high* from Monterey to Palos Verdes, and *moderate* from south of Palos Verdes to San Diego.

1.1.4 Borrero's (2002) Analysis of Nearfield Hazards

Borrero (2002) remains to this day (2008) the most detailed study of local tsunamis in southern California. He discussed nearfield tsunamis in detail and introduced a new and comprehensive analysis of waves from landslide sources. The hydrodynamic model he used to assign initial conditions for landslides, while empirical, had been partially validated, see Synolakis (2003).

The motivation for Borrero's (2002) work was that the development in state–of–the art numerical modeling had showed that McCarthy et al.'s (1993) results had to be revised Synolakis (1987). In the meantime, the 1998 Papua New Guinea event showed that even a moderate earthquake could produce a highly localized catastrophic impact through the triggering of a submarine landslide (Synolakis et al., 2002), a fact that remained controversial for many years (Geist, 2000, 2001; Okal and Synolakis, 2001) .

Borrero (2002) investigated fossil submarine landslides documented in the Santa Barbara Channel, Santa Monica and Redondo Canyons and off the Palos Verdes Peninsula, as well as potential future ones. The waves generated by catastrophic failures during these events caused high, but localized inundation and runup.

As an extension of the inundation studies Borrero et al. (2005) used a distributed impact model to assess economic damages which they calculated in the range of 5–35 billion of 2002 US $, for $4m$ tsunami runup in the Ports of Los Angeles and Long Beach following a hypothetical landslide tsunami off Palos Verdes.

1.1.5 Earlier Northern California Tsunami Studies

Prior to the recognition of the CSZ as a potential local tsunami source, Wiegel (PG&E, 1966) analyzed a $7.5m$ runup from a locally generated magnitude 8 earthquake, with a return period of 800 years, and postulated only a small likelihood for the generation of a large tsunami near Humboldt Bay.

Fourteen years later, Houston (1980) estimated the 100–year tsunami runup at the entrance of the Humboldt Bay as $3.2m$ and the 500–year "runup" as $6.3m$, above mean lower low water.

Whitmore (1993) numerically computed tsunami amplitudes without inundation calculations from CSZ sources along the coast of Washington, Oregon, northern California, and adjacent areas to the north and south, using relatively moderate magnitude earthquake sources. His largest event was $M_w \approx 8.8$, with relatively small slip ($3.7m$), along a $640km$ rupture dipping 13^o, and extending from central Washington to a point between Eureka and Crescent City. He computed the maximum tsunami amplitudes as $6m$ over the entire domain, with values of $2.7m$ at the ocean side of the Humboldt Bay at the North Spit, $50cm$ at Eureka, $20cm$ at Fields Landing and Bucksport, and $85cm$ between Eureka and Fields Landing.

Bernard et al. (1994) developed seismic source models for the CSZ to predict the generation of significant tsunami waves impinging on Humboldt Bay and Crescent City, and then performed numerical modeling of inundation in these two areas. The initial results of the seismic source modeling produced estimates of tsunami wave amplitudes from the CSZ, which they judged as unreasonably small. As a result, they used a brazenly empirical approach based on local tsunami observations during the 1964 Alaska and 1993 Hokaido to derive a figure of $10m$ for the incident wave at a $50m$ water depth to be used as an initial condition in inundation models.

Lamberson et al. (1998) developed a calibrated numerical tidal model for Humboldt Bay. They performed a pilot study to assess the feasibility of using their finite-difference tidal model to simulate tsunami wave amplitudes and water velocities inside Humboldt Bay. They tested their model at low tide using an arbitrary input set of three large ($4 - 6m$ amplitude) sinusoid waves at the mouth of Humboldt Bay with a period of $15min$. The third wave resulted in maximum wave height of $8m$ at the entrance to Humboldt Bay. They did not include any effects from the wave overtopping the spits in their model, possibly they didn't simulate it, although the input wave clearly would have washed over the South Spit and the southern portion of the North Spit at Samoa County, where they computed water elevations exceeding $5m$ above mean lower low water, with maximum current velocities of $2m/s$.

Myers et al. (1999) developed a finite element model for propagation of Cascadia Subduction Zone (CSZ) tsunami waves, from their source near the plate interface offshore in the Pacific northwest to the coastlines. To generate the tsunamis, they used various rupture models for the CSZ, as presented in Priest et al. (2000). These models assumed a geometry of the plate interface and varied the rupture dimensions by adjusting the locations and amounts of slip on the seaward and landward transition zones around a central locked zone. They estimated regions and amounts of seafloor uplift corresponding with each of these rupture scenarios, and assumed that the uplift was directly transferred to the sea surface, thus creating initial conditions for their model. They then propagated the tsunami wave trains through their finite–element grid toward the coast, and reported estimates of wave heights and run-up velocities, for a number of locations along the coast from Cape Mendocino to the northern Olympic Peninsula.

Because they are derived from a relatively coarse finite–element grid, these results are useful in estimating the tsunami-focusing mechanisms offshore, but must be considered only approximate estimates of runup at the coast (Baptista, 2002). The finite element grid was much denser than the regional grid at Seaside and Newport, Oregon, to permit detailed estimation of runup routes, flow velocities, and runup heights. The authors reported that the predicted wave heights and runup velocities are very sensitive to grid density, reinforcing the notion that estimates of runup outside of Seaside and Newport should be considered approximate. Furthermore, Baptista (2002) reported that runup velocities predicted by these models are much less accurate than wave heights. His estimates of wave heights at the coast were 4–$9m$ at Humboldt Bay, and 5–$14m$ at Klamath near Lagoon Creek, California.

The PG&E (2003) study investigated the tsunami hazard in Humboldt County for future residential developments. Thus summarized tsunami wave heights from a large rupture on the CSZ as of 9–$12m$ at Humboldt Bay from literature reviews. A tsunami of this height would overtop the southern spit of the Bay, but not the northern. There is geological evidence of extremely high runup values ($20-21m$) at Orick, $60km$ to north of Humboldt Bay, however its specific cause remains not known. A large coseismically induced landslide and bathymetric focusing could be possible reasons for the excessive runup.

The PG&E (2003) report did note that recent detailed bathymetric mapping of the Cascadia continental margin has revealed several enormous landslide masses off Oregon that have features interpreted as indicative of large and sudden movements involving thousands of cubic kms of the lower continental slope. The presence of these large offshore submarine landslides suggests a mechanism for generating anomalously large tsunamis at infrequent intervals.

The PG&E (2003) report provides an overview of tsunami modeling efforts performed for this region. Based on empirical data alone, it suggested that a tsunamigenic earthquake of magnitude 8.8 on the Cascadia subduction zone would generate runup heights along the northern California coast of $9.5m$. The runup range empirically inferred for M_w 8.5 to 9.2 events is $8 - 11m$, in general agreement with estimates of $9 - 12m$ for waveheights offshore Humboldt Bay, estimated based on paleotsunami studies in northern California.

1.1.6 Earlier work on Tsunami Hazards in San Francisco Bay

Several previous studies have looked at inundation, tsunami heights, and estimated recurrence for San Francisco Bay. Ritter and Dupre (1972) mapped areas of potential tsunami inundation within the bay (Figure 1.2). They assumed only teletsunami sources and used a waveheight of $6.1m$ at the Golden Gate. This value was chosen because it was the approximate value of peak inundation at Crescent City in 1964. They used Magoon's (1966) attenuation relation to estimate heights of possible flooding throughout the bay. For example, the peak amplitude at Oakland was found as $3m$, and at Mare Island as $0.6m$. They extrapolated Wiegel's (1970) frequency of occurrence graph for San Francisco Bay to estimate that the mapped inundation (Figure 1.2) represented a 200–year event. Wiegels frequency graph was based primarily on five events (1946,

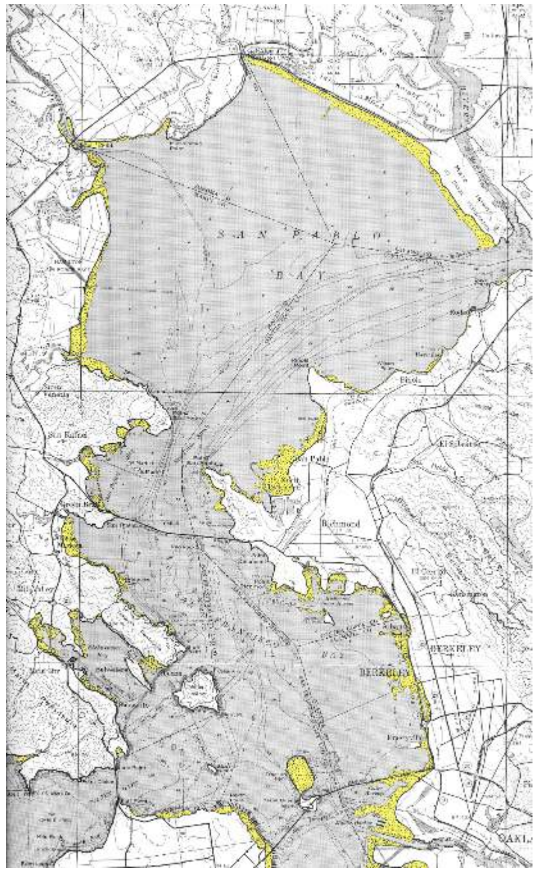

Figure 1.2: Areas of potential tsunami inundation (yellow) by a $20 feet$ ($6.1m$)tsunami at the Golden Gate (after Ritter and Dupre, 1972).

1952, 1957, 1960, 1964), and the slope extrapolated by Ritter and Dupre was chosen to parallel the Crescent City recurrence data, with no other justification.

Garcia and Houston (1975) made 100 and 500-year tsunami predictions for San Francisco Bay for the Federal Insurance Administration, for a flood insurance study. They considered the probabilities of teletsunami sources only from Alaska and the Aleutian trenches assuming that the 100–year and 500–year events are not strongly affected by tsunamis from other regions of the Pacific. They did not address the possibility of locally generated tsunamis. Using a numerical model, they predicted the height of these tsunami waves along the Pacific Coast of North America, and inside San Francisco Bay.

Garcia and Houston's (1975) 100–year and 500–year values do not mimic the attenuation relation suggested by Magoon (1966). Their recurrence estimate for Alaska and Aleutian events was based only on historic events. The mid-20th century might had been anomalous for large Alaska tsunamigenic events, hence these recurrence relationships need to be re-evaluated using paleoseismic data, as now available. The restriction of tsunami sources affecting California from Alaska and the Aleutians also needs to be re-examined, particularly in light of the CSZ megathrust events that are believed to have an approximate 500–year return period, and are capable of producing tsunami amplitudes in the source area comparable to the 1964 Alaska or 2004 Sumatra events.

The Houston and Garcia's studies, while ground–breaking at the time undertaken, are computationally crude, when compared to the level of sophistication in modern numerical tools or the resolution of bathymetric data now available.

Houston and Garcia computed tsunami wave amplitudes outside of San Francisco Bay, then performed their calculations inside the bay using a forced wave input for a monochromatic wave with the precomputed amplitude and a set period of $38min$, a value based on observations during the 1964 Alaskan event. The present study differs in that it considers a wider variety of input sources from subduction zones around the Pacific, and directly computes the tsunami wave from the source to the study area, using a single model, when necessary inundation is computed directly at high resolution.

Parsons et al. (2003) performed hydrodynamic modeling to examine the tsunamigenic potential of the Hayward – Rodgers Creek "stepover", i.e., the lateral offset between two strike–slip segments. Subsidence in the stepover region was modeled as a slip of $0.35m$ on a high–angle $18km$ wide normal fault. The maximum wave height in the Bay predicted by this model was $0.1m$, well below the $\approx 0.6m$ reported for the 1898 $M_w \approx 6.7$ Rodgers Creek event by the *Union Record* newspaper. It is possible these

1898 reported water heights are inaccurate, as the event occurred at night, and storm activity obscured any recording on the Presidio marigram (Lander et al., 1993). Furthermore, it is not clear how and where the estimates were made. Parsons et al. (2003) used a uniform slip distribution and suggested that heterogeneous slip might locally amplify the peak water heights. Finally, in terms of California tsunamis Geist and Zoback (1999) modeled the tsunami triggered by 1906 earthquake as a right–lateral step–over tectonic mechanism offshore the Golden Gate.

1.2 The Tsunami History of California

Table 1.3 lists significant historical tsunamis which have affected California since 1868. In relatively recent history, two very large earthquakes along the Pacific Rim have generated tsunamis which damaged port and harbor facilities in the State. In 1960, a large earthquake in Chile generated a tsunami which caused over $1 million in damage in Los Angeles Harbor, broke the moorings of a dozen boats in Santa Barbara, causing minor damage, and destroyed a $50m$ dock in San Diego (Lander et al., 1993).

The 1964 Alaska Earthquake and tsunami caused eleven fatalities. Damage estimated exceeded $17 million in California (Lander et al., 1993). In Crescent City, the tsunami drowned ten people. The waterfront and 29 city blocks were damaged or destroyed and total damage was estimated at $15 million. Figure 1.3 shows the inundation in a diagram (Griffin, 1964). The tsunami was recorded on tidal gauges statewide and caused approximately $1 million damage at various marinas inside San Francisco Bay, including Sausalito, San Rafael and Berkeley. The tsunami also caused strong surges that tore 75 small vessels from their moorings and sank three boats in Los Angeles Harbor. Unconfirmed reports from Ventura Harbor suggest that the tsunami damaged

Date	Source	M_w	Damage/Effect
1868	Peru	9.3	Minor flooding in San Pedro and Wilmington
1877	Chile	8.3	No details
1896	Japan	8.0–8.6	Damage in Santa Cruz
1906	Ecuador	8.3	Ships caught in eddies in San Francisco
1922	Chile	8.3	Strong currents
1923	Kamchatka	8.4	Shipping affected in Los Angeles
1946	Aleutian Islands	8.6	$90cm$ tsunami in Crescent City, broken moorings in northern California and one fatality.
1952	Kamchatka	9.0	4 boats sunk in Crescent City
1957	Aleutian Islands	8.3–8.6	Damage to ships and docks in San Diego
1960	Chile	9.5	$1 million damage in LA Harbor
1964	Alaska	9.2	$17 million damage+12 fatalities
1965	Aleutian Islands	8.7	$60cm$ sea level rise in Santa Cruz
1975	Hawaii	7.2	Minor damage to a dock on Catalina Island.
2006	Kuril Islands	8.3	$9.7 million in damage in Crescent City

Table 1.3: List of the significant teletsunamis that have affected California (Lander et al., 1993), Seismic moments updated (Okal, 1992, 2007).

several vessels (Synolakis, 2008). There were also reports of strong surges and a water level rise of $2m$ in San Diego (Lander et al., 1993).

Other notable events in order of decreasing importance include the 1946 Aleutian Islands earthquake, whose tsunami carried boats a quarter mile inland in Half Moon Bay, washed away a pier on Catalina Island, broke ship moorings in Los Angeles and caused minor damage in Santa Cruz. The 1952 Kamchatka tsunami capsized five small boats and moved a 60-ton mooring buoy in Crescent City, and also caused damage in Santa Cruz. The 1896 Sanriku earthquake in Japan generated a teletsunami which destroyed a dike and caused damage to a ship in Santa Cruz (Lander et al., 1993).

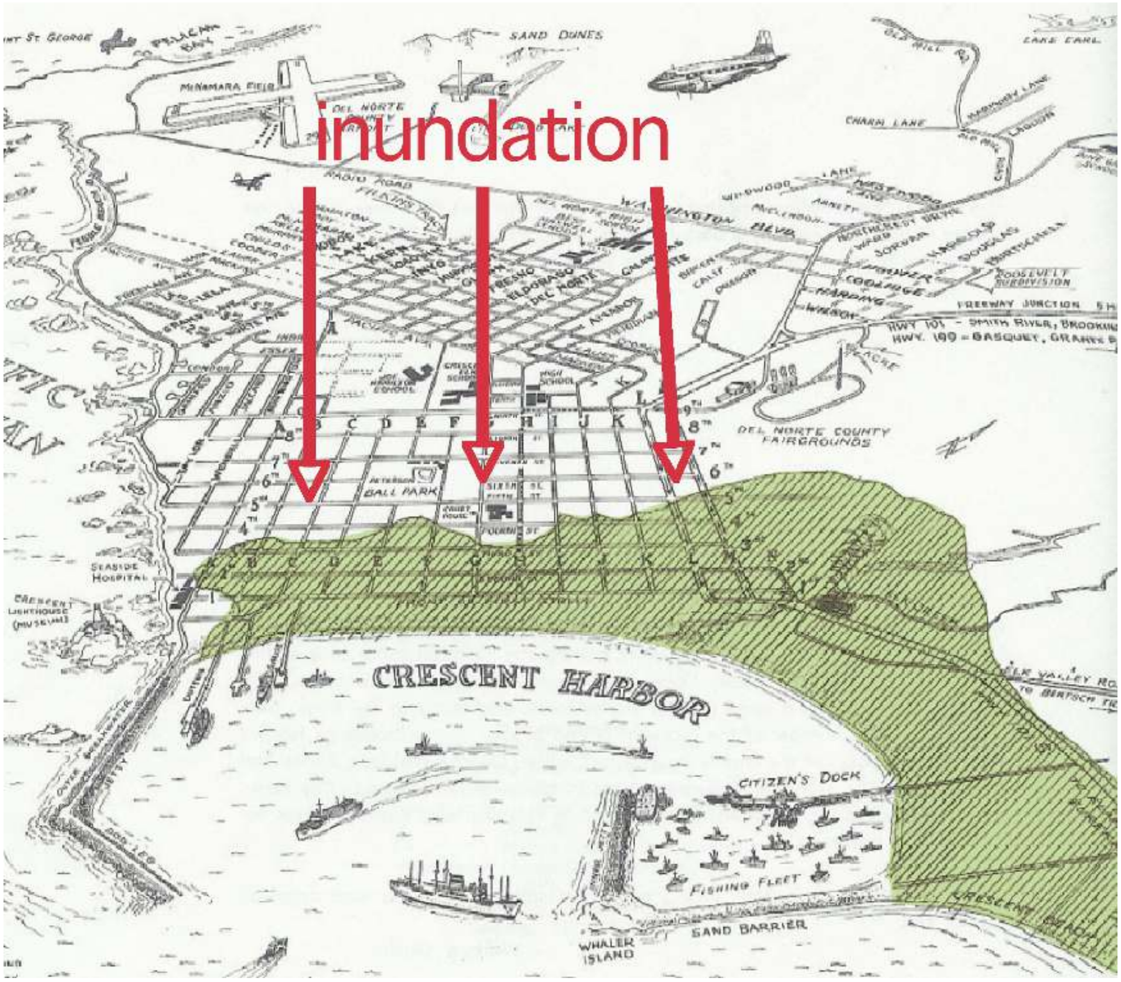

Figure 1.3: Tsunami inundation in Crescent City from 1964 Alaska tsunami by Griffin (1964).

1.2.1 The Teletsunamis from Kuril Islands in California

On 15 November, 2006 a $M_w = 8.3$ earthquake occurred in the Kuril Islands trench causing significant damage in Crescent City. This was followed on 13 January 2007 by a slightly smaller ($M_w = 8.1$) earthquake, 70 km to the SE. In addition, a large earthquake had happened on 4 October 1994 $650km$ to the SW. Interestingly, these earthquakes all have different mechanisms, even though adjacent along the same subduction zone. While the 2006 event is a classical inter-plate thrust, the 2007 one involved normal faulting in the outer rise, probably triggered by stress transfer from the 2006 one. The 1994 earthquake featured slip on a relatively deep ($68km$) vertical tear in the slab near the Hokkaido corner (Tanioka et al., 1995).

All three events generated tsunamis with diverse characteristics. The 1994 Shikotan tsunami ran up locally to 5 to 9 m and inflicted significant damage on the southern Kuril Islands (Yeh et al., 1995). It was recorded with an amplitude of 30 cm on the tide gauge at Crescent City. The 2007 tsunami was moderate with an amplitude of only 25 cm in Crescent City.

The $M_w \approx 8.3$ 15 November 2006 earthquake occurred at approximately 11:14 (UTC) offshore of the central Kuril Islands of Simushir, Rasshua and Matua, which are uninhabited and inaccessible during the winter. Therefore, the local impact of its local tsunami remained unkown until recent field work during the 2007 summer season revealed runup of up to 21 m on Matua (Bourgeois, 2007; Levin et al., 2008).

The tsunami reached Hanasaki, in Hokkaido Japan in $64min$ and was measured on tide gauges in Japan at only half a meter. As a result, a large tsunami was not anticipated in Alaska or the U.S. Pacific coast. Yet, in the afternoon of 15 November 2006, Crescent City was hit by a series of strong surges, completely damaging 3 of the 8 docks in the harbor.

This recent damage to Crescent City harbor provided an opportunity to use the state–of–the–art hydrodynamic inundation code MOST (Titov and Synolakis, 1998) code for a transpacific simulation and compare its results at Crescent City with the measurements. Modeling the tsunami surges within a harbor is a challenging task due to the shallow depth of the basin, the resolution and the high frequencies often involved in harbor seiching, which may violate some of the basic assumptions of the shallow water

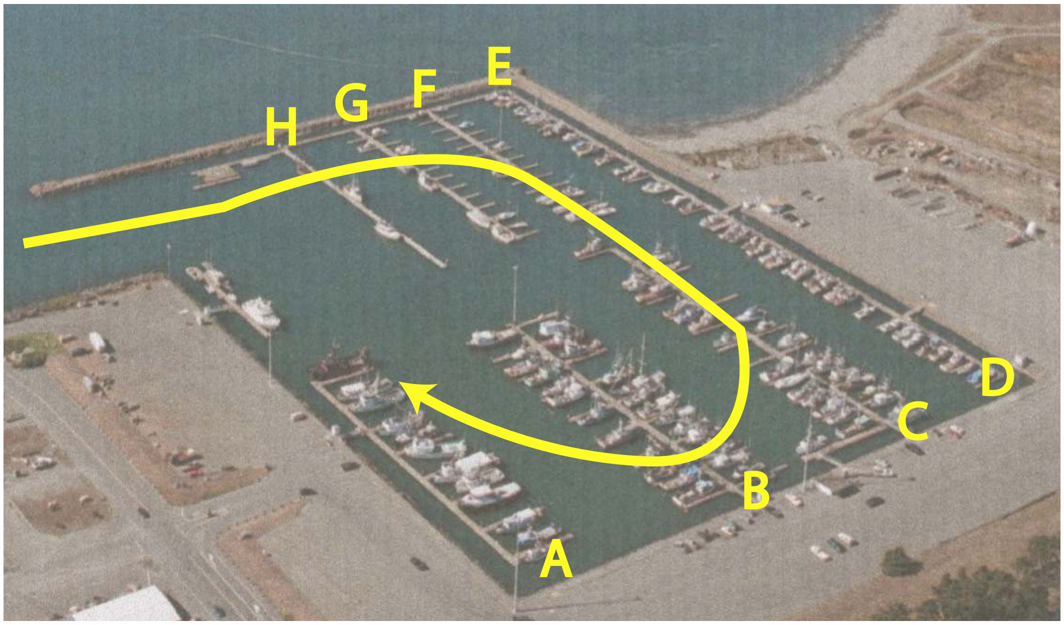

Figure 1.4: Dock locations and aerial view of the Crescent City harbor prior to 2006 Event. Arrow indicates the direction of the in the port triggered by the tsunami.

theory. Most numerical codes used for tsunami inundation solve depth–averaged equations, which may not always be applicable for "intermediate" free surface waves, i.e. when the waveheight to wave length is less 0.05. Given the importance of this events both for validation of hydrodynamic codes and for assessing the impact of even small tsunamis, it will be described in greater details.

1.2.2 Summary of Eyewitness Accounts from 15 November 2006 Event for the Crescent City Harbor

Around 11 a.m. PST, on 15 November 2006, the Crescent City, California Harbor Control and Emergency offices received a warning for possible strong tsunami surges which were expected to arrive around 11:30 a.m. (19:30 UTC). Because the tsunami had been expected to be relatively minor, a full evacuation was not ordered, but rather targeted verbal warnings were issued for people in the harbor. Mr. Erik Macee, a fisherman, from the fishing vessel *Resolution* confirmed that he was warned by the harbormaster at around 11:10 a.m.

The first wave arrived at the expected time, but was not noticed by the harbormaster. Mr. Macee said he was in his boat when he first noticed the withdrawal, a manifestation of leading depression N–wave of Tadepalli and Synolakis (1994, 1996). He was able to watch the tsunami from his boat looking at the water elevation change at the piling and on the restraining wall.

The tsunami surges did not cause any damage until after 2 p.m. Mr. Macee said the largest waves arrived possibly between 2:00 and 2:30 p.m. The second in the series of larger waves did the most damage when mooring lines from vessels berthed at Dock H (Figure 1.4) were severed. Dock H had three boats, including the biggest boat in the harbor, *Delana*, moored directly to the piling, while the other two vessels were tied to the exposed deck of the dock. As it turned out, the dock could not resist the strong current and the pull coming from the boats, and failed.

The current was so strong that harbor facilities manager Paul McAndrews reported that a white buoy at the entrance of the harbor was buried under water as the current flowed out of the harbor. He also noted that harbor seals and sea lions were not able to swim against the current.

Many witnesses described the tsunami in the harbor as "flowing like a river". It caused a clockwise rotating vortex, as shown in Figure 1.4 Dock H was closest to the entrance of the protected harbor in the flow direction and failed first, then Dock G (Figure 1.4). The loose boats and pieces of Dock H crashed into Dock G, and later, into Dock F. A large portion of Dock F was damaged, but it did not wander erratically around, as did Docks G and H.

Docks E, F and G had been used for small craft and sail boats. “Windrose” and “Allarion” are two of the sail boats that used Dock G. Robert Nunneley and Jim Herriott, owners of the vessels, learned about the tsunami and arrived at the harbor around 3:40 p.m. They noticed that the currents were still very strong. “Windrose” and “Allarion” had been pushed on to the other boats at Dock C. The Coast Guard helped to move the two boats from Dock C to F.

Sam and Kathleen Burke work at a local RV camp and returned to the campground around 2:30 p.m. They noticed that the tide level was different from what had been expected for that time. They also observed several water level changes. Mrs. Burke reported the time between successive wave crests as $\approx 12min$. She repeated her estimate for three more waves to confirm her observation.

Public works technician Kevin Tupman came to north harbor around 2:40 p.m. He also observed the changes in water level due to the tsunami. Mr. Tupman estimated the distance from the low water mark to the high water mark as approximately 260 m. He was at the north harbor from 3 until 4 p.m, and saw three full wave cycles, thus confirming Mrs. Burke’s observation.

Fortunately, it was low tide when the tsunami surges first arrived around 11:38 a.m ($8.4hr$ after the earthquake, Figure 1.5). Total damage to the harbor, initially estimated at $\approx$ \$ 1 million, had exceeded \$ 9.2 million by the summer of 2007 (Young, 2006). Had the tide been high at the time of tsunami arrival, the damage could have been more extensive and costly.

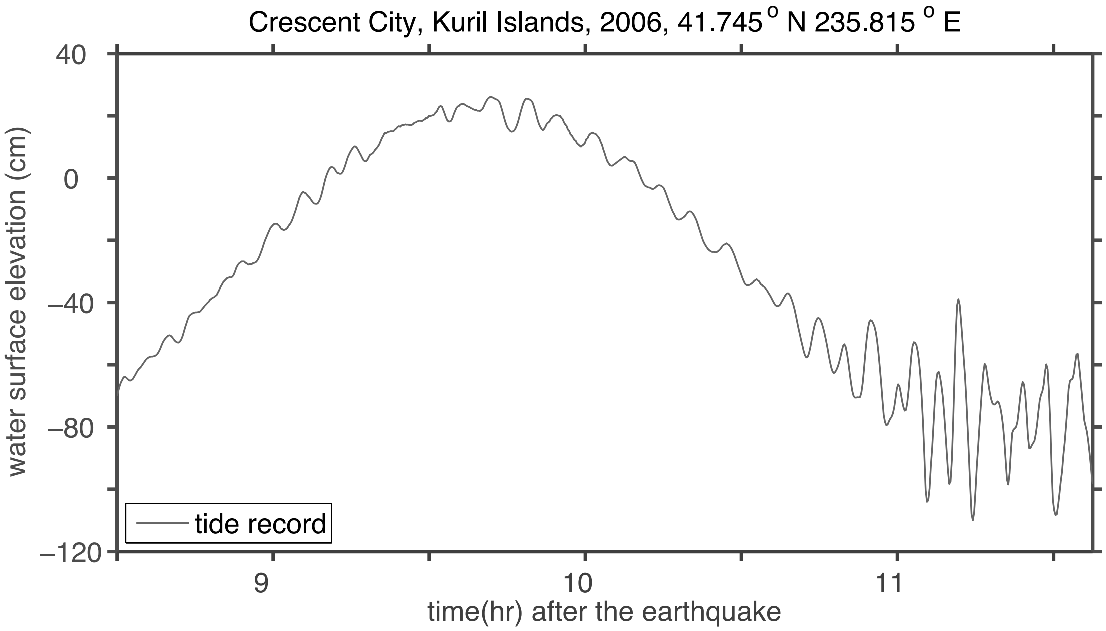

Figure 1.5: The water surface elevation at Crescent City tide gauge following the 2006 Kurils Islands earthquake.

1.3 Historical Farfield Events in San Francisco Bay

During historic times, "51" credible tsunamis have been recorded or observed in the San Francisco Bay area. Six of these tsunamis likely originated from within San Francisco Bay, two from rest of the California, nine from Japan, seven from the Kurils and Kamchatka, nine from Alaska and the Aleutians, two from Hawaii, ten from South America, three from the SW Pacific, one the from Central America and the remaining two teletsunami from unknown sources (Lander et al., 1993).

Only five historic tsunamis have produced runup that likely exceeded $0.5m$ inside the San Francisco Bay. The best–documented events are the 1946, 1960 and 1964 teletsunamis, generated by earthquakes in the Aleutian Islands, Southern Chile and Prince William Sound, Alaska, respectively. In addition, three local tsunamis in the nineteenth century may also have generated waves in excess of $0.5m$; none were recorded on tide gages and the height has been estimated from eyewitness accounts only (Lander et al., 1993; Toppozada et al., 1992; Borrero et al., 2006a) .

Since 1854, there has been a tide gauge in operation in San Francisco Bay. It had been originally installed at Fort Point, was moved to Sausalito in 1877, and then to its present location at the Presidio in 1897 (Bromirski et al., 2002). Other stations inside the bay have operated on an interim basis including Hunters Point, Alameda, Oakland and Mare Island (see Figure 2.7). While the original tide gauge in Presidio has been in operation since 1854, some of the records have been lost or events not recorded due to instrument problems or severe weather conditions.

Forty-three of the 51 historic tsunamis recorded or observed in San Francisco Bay originated from distant sources involving at least four hours travel time from the source to the Bay. The most frequent source area appears to have been the northwestern Pacific (Japan and the Kamchatka-Kuril Trenches), followed by South America and the Alaska–Aleutian Islands. Two of the 51 tsunamis, the 1960 $M_w = 9.5$ Chile earthquake and 1964 $M_w = 9.2$ Alaska earthquake, did cause tsunami damage in San Francisco Bay.

The tsunami waves from the 1960 Chile earthquake arrived in the Bay at 10:12 UTC (2:12 a.m. PST), fifteen hours after the earthquake. The tsunami was recorded on the tide gauges at the Presidio and Alameda, as well as on a 33–gauge array of water level recorders fortuitously present in San Francisco Bay during the tsunami (Magoon, 1962). The waves were observed on six of the thirty three gauges, and the maximum recorded wave heights are shown in Table 1.4.

The top two frames of Figure 1.6 show the 1960 Presidio and Alameda tide gauge recordings. The plots illustrate a feature of many recorded tsunamis within the Bay.

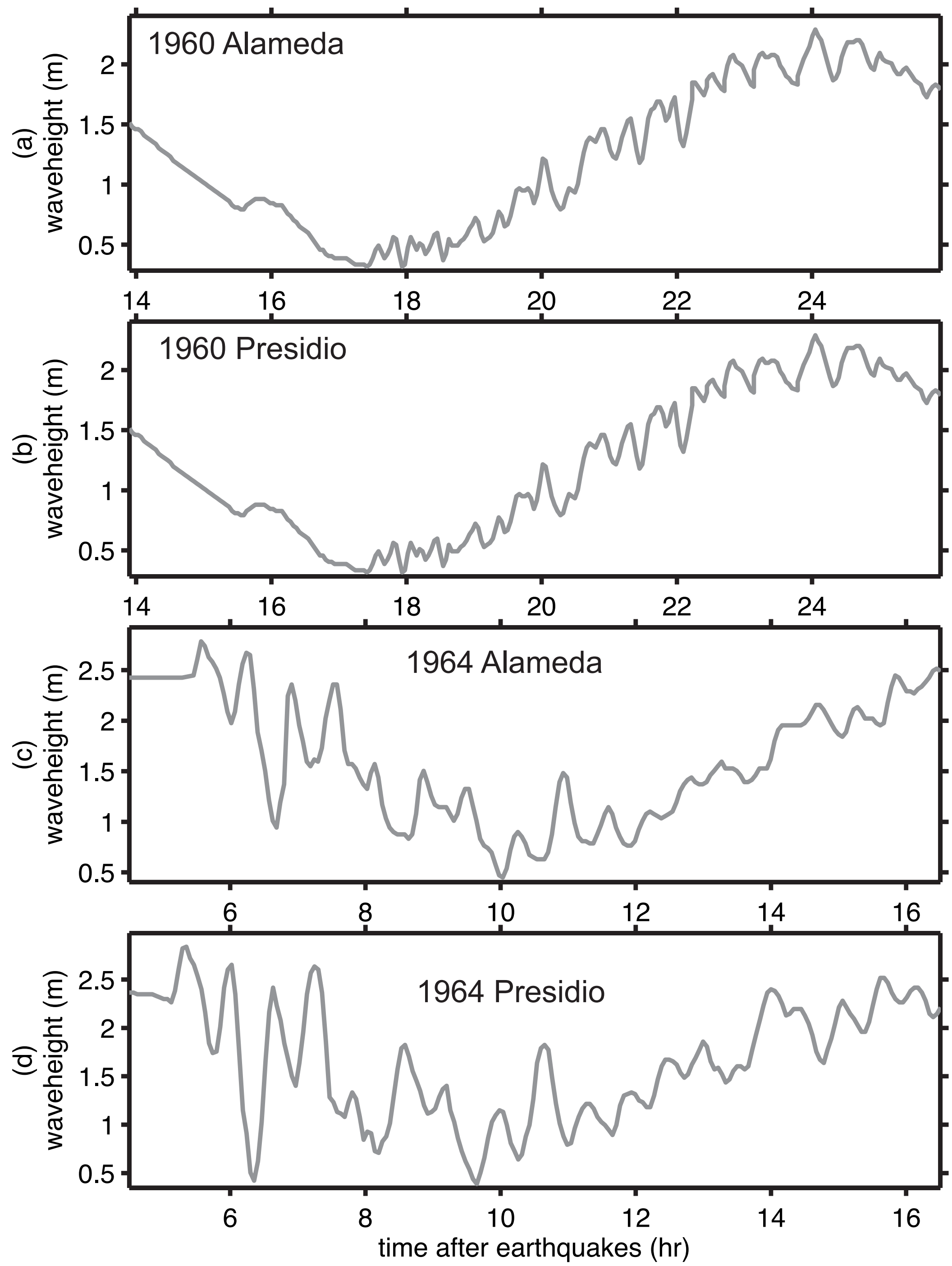

Figure 1.6: Twelve hours long tide gauge records at San Francisco Bay. (a) The record of tsunami from the 1960 Chile earthquake at the Alameda and (b), Presidio tide gauge. Similarly (c), the tsunami record at Alameda and (d), record at Presidio from 1964 Alaska earthquake. The water level time histories are not detided

Location	Max. wave height (m)
Presidio	0.88
Hunters Point	0.12
Alameda	0.58
Oakland	0.37
Carquinez Strait	0.03
Benicia	0.06

Table 1.4: Recorded wave heights in SF Bay from Magoon (1962), for the 1960 Chilean event.

The initial cycle is relatively long period ($72min$), followed by shorter period oscillations (about $30min$) that last more than $10hours$. According to Wilson and Torum (1967), the fundamental free period for oscillations in the Bay is $114min$, the second harmonic is about $57min$ and the third is $38min$. They speculated that the long–duration short–period oscillations are the result of near–resonance, with the third harmonic developing as a result of the entrance constriction at the Golden Gate. The marigrams also illustrate the attenuation of wave energy as the waves transit the bay. The amplitude of the Alameda signal is about half that of the Presidio. It should be emphasized that the largest waves recorded on the time series occurred four to eight hours after the first wave arrival. In 1960, the only reported damage in the Bay was a catamaran yacht torn from its moorings in a lagoon north of the Golden Gate (Magoon, 1962). The San Francisco Ferry Service was disrupted by a current that has been described as "running like the Mississippi River" (Lander et al., 1993).

The 1964 Great Alaskan tsunami also caused flooding in the Bay, reported up to $2.1m$, and affected many areas inside it (Lander et al., 1993). The strongest effects were observed in the northeastern parts of the Bay, particularly in Sausalito and other Marin County locations. Strong surges and high water were also observed in Berkeley, Richmond and Oakland. Damage included boats being torn from moorings, docks, piers and floating docks; the latter came loose and were carried away from their original locations.

The tsunami was noted at 27 locations within the bay (Magoon, 1966). There were numerous reports of strong currents within the bay. The largest amplitude waves were again at the Presidio; there the second oscillation had a $2.3m$ peak–to–trough amplitude. Tide gauge records from the 1964 event at the Presidio and Alameda are shown in the two bottom frames of Figure 1.6. Spectral analysis by Wilson and Torum (1967) of the 1964 Presidio marigram identified two dominant periods, in addition to the tidal forcing, at $100min$ and a $38.5min$. They attributed the shorter period to resonance with the third harmonic of the bay oscillation, and concluded that the geometry of the bay entrance will excite at this period for any large tsunami entering through the Golden Gate.

Had the largest waves coincided with high tide, the absolute water level could have reached $3.8m$ above sea level at the Presidio during the 1964 tsunami. Magoon (1966) compiled runup data from both the 1960 and 1964 tsunamis within the bay and produced empirical attenuation estimates. According to his data, the tsunami wave height was reduced by 50% between the Presidio, just inside the Golden Gate, and at Hunters Point on the San Francisco Peninsula and Richmond or Oakland on the eastern shore of the Bay. The wave height was further reduced to 10% of its original height by the time it reached the northwestern shore of San Pablo Bay and the southern end of San Francisco Bay (Figure 2.7).

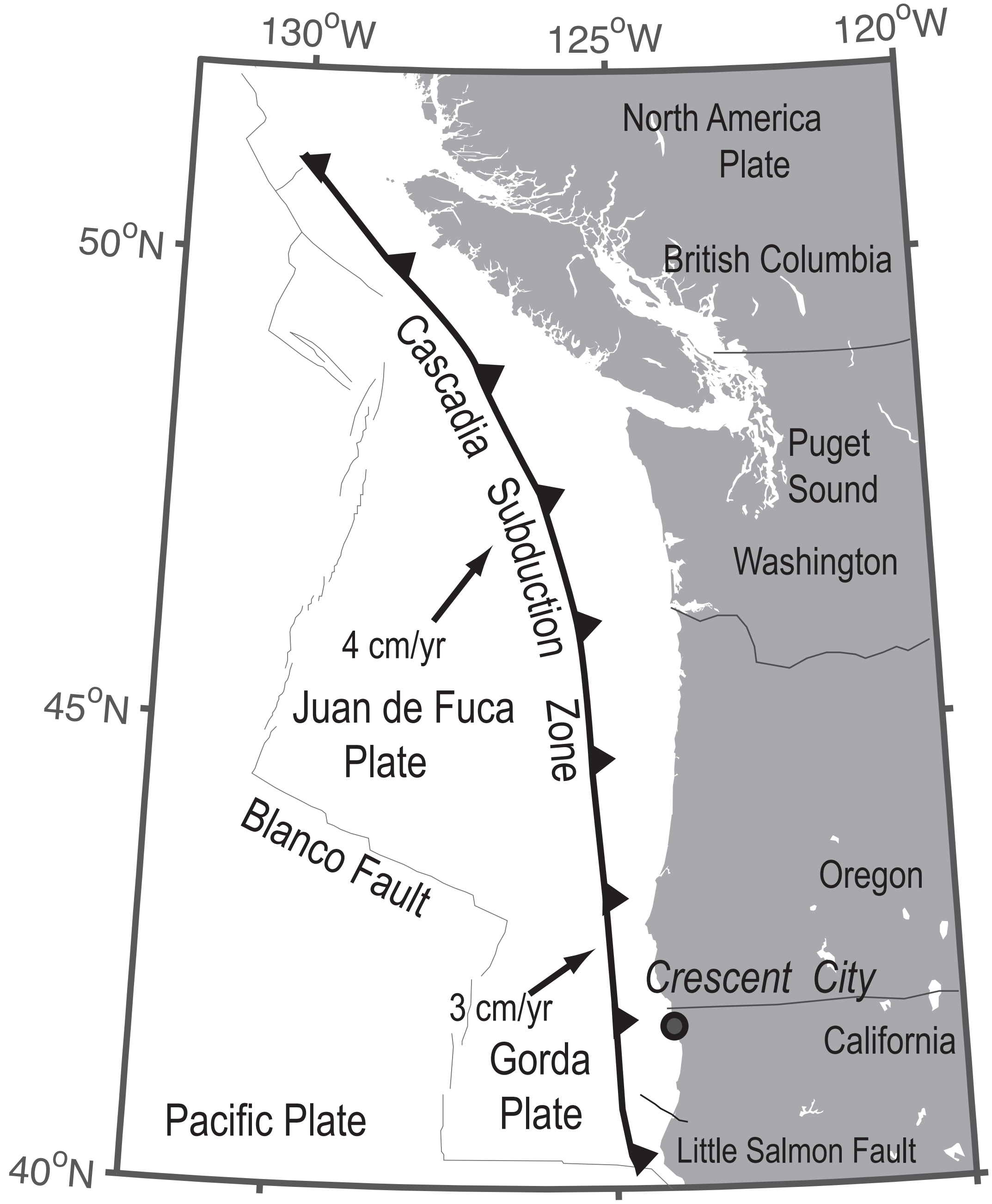

Figure 1.7: Map of the Cascadia subduction zone, modified from Satake et al. (2003).

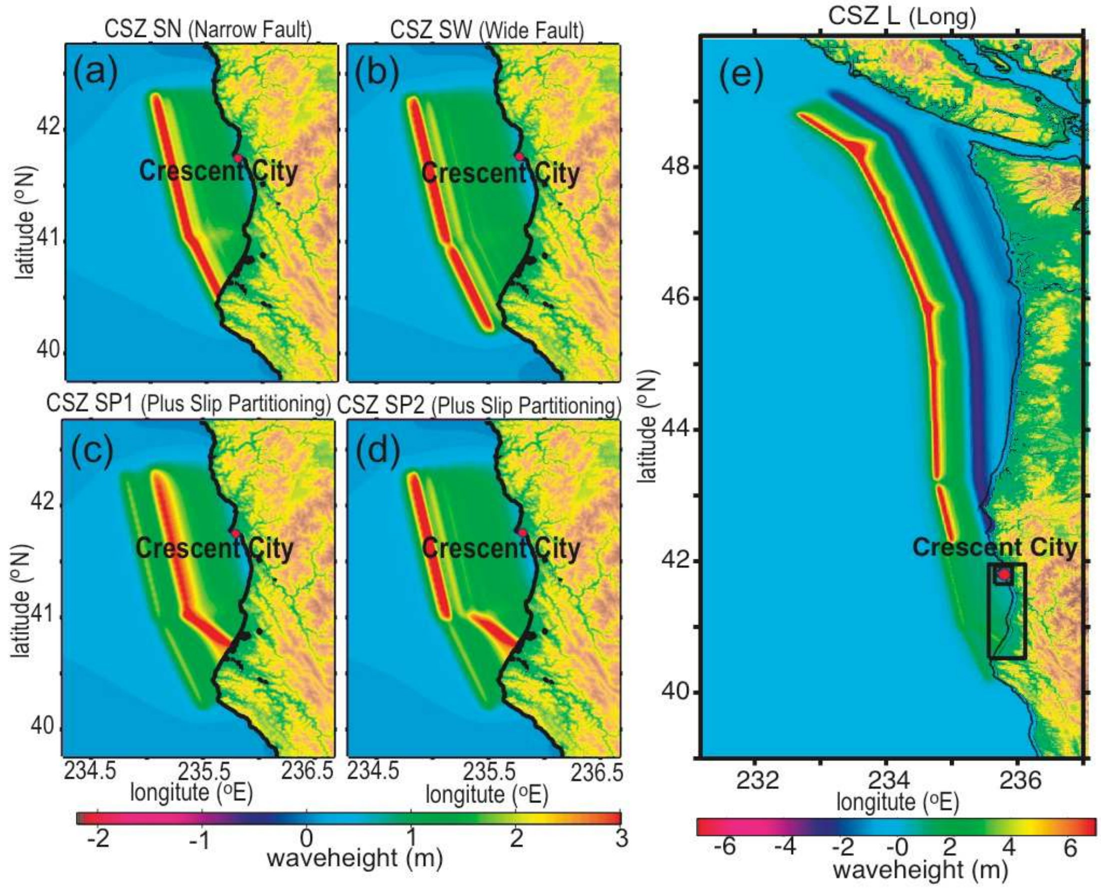

Figure 1.8: Initial free surface elevations for scenario earthquakes CSZ SN, SW, SP1, SP2 and L. Note that (e) CSZ L uses a different color scale a, b, c and d. A sixth scenario CSZ N is similar to (e), but the rupture does not extend into California.

1.4 Local Tsunamis and Sources for California

1.4.1 The Cascadia Subduction Zone

Figure 1.7 shows the location of the Cascadia Subduztion Zone CSZ, which runs from Cape Mendocino, California in the south and extends to beyond Vancouver Island in the north for a total length of $1000km$. The CSZ has a variable subduction rate, approaching $4cm/yr$ where the Juan de Fuca plate subducts beneath the North American plate in the vicinity of Washington State (Satake et al., 2003). Then, it slows to $3cm/yr$ at the northern end of the Gorda plate beneath southern Oregon (Wang et al., 2001) and reaches almost zero at the southern end of the Gorda plate near the Mendocino triple junction in northern California (Clarke and Carver, 1992).

In a study of crustal strain, Savage et al. (1981) suggested a potential mega–thrust earthquake from the CSZ. Then, Heaton and Kanamori (1984) compared the CSZ to other more analyzed subduction zones, and Atwater (1987) found indications of seismic subsidence in western Washington associated with great local earthquakes. Jacoby et al. (1995) and Yamaguchi et al. (1997) calculated the timing of the earthquake to within one year of 1700 AD using tree ring dating. Satake et al. (1996, 2003) showed that the year 1700 corresponds to a historically reported tsunami in Honshu, Japan and then used coastal subsidence data and numerical simulation to infer that the tsunami was originated around 5:00 (UTC) on 27 January 1700 from a $M_w \geq 9.0$ earthquake (Uslu et al., 2008).

Since there are no direct seismic or geodetic observations to identify the physical behavior of the rupture zone, Wang et al. (2003) combined information about the 1700 A.D. earthquake with relevant data from other subduction zones and calculated windows for the potential extent of rupture, and for strains, rupture velocities and uplift rates. Their approach for the CSZ assumes a full coseismic rupture over the entire subduction zone with an average recurrence of 500 years, a scenario believed to be conservative.

Although paleoseismic data support the possibility of a long rupture and there is consensus that the 1700 A.D. event involved the entire zone (Satake et al., 2003), this may not happen in every CSZ event. The stress field and rates of strain accumulation vary from north to south and it is possible that some events are segment ruptures. For example, Clarke and Carver (1992) define a southern (Gorda) segment with dimensions of about $240km \times 80km$ with a fault dip of 10–20°. Paleotsunami studies from southern Oregon show several events not present in records from elsewhere on the subduction zone (Nelson et al., 2006), thus they are possibly related to segment rutpures. This apparently random alternation between segment ruptures and mega–events involving the whole length of the fault was first described in Japan by Ando (1975) and more recently documented in other provinces (Cisternas et al., 2005; Nanayama et al., 2005; Okal and Synolakis, 2008). In addition to the main rupture zone, a number of subsidiary faults in the CSZ acretionary fold and thrust belt pose an additional tsunami hazard (Clarke and Carver, 1992). Finally, Toppozada et al. (1995) proposed a scenario involving a simultaneous or triggered rupture of the Little Salmon fault (seen at the bottom of the right of Figure 1.7), located along the northern edge of the Eel River basin and extending offshore for at least $150km$.

1.4.2 Local Tsunamis in San Francisco Bay

San Francisco Bay experienced six credible and several other possible tsunamis from local sources and two additional credible tsunamis from other source regions in northern California (Table 1.5). Of the six credible local source events, four were probably caused by earthquakes and two by earthquake-triggered landslides. One event in 1887 was associated with no known earthquakes and, if real, may represent slumping within the bay. Perhaps the most notable aspect of historic local-source tsunamis is that they all occurred in the 19th and early 20th century. Toppozada (2006) suggests that the high frequency of local events in the late 1800s reflects the overall activity of the San Andreas system prior to the 1906 San Francisco earthquake.

Lander et al. (1993) lies reported a $6m$ water surge after the 1868 Hayward Fault earthquake, oddly outside the harbor on the west side of the Golden gate at the Cliff House. The wave was recorded near Alameda at Government Island, but that record is now believed to be lost, hence the lower validity in Table 1.5. Only a few vessels reported "some" wave activity after the earthquake. This wave at the Cliff House has been attributed to an earthquake–triggered landslide by Lander et al. (1993).

The largest credible tsunami wave heights within San Francisco Bay from a local tsunami were triggered in 1898, by the Mare Island earthquake. This earthquake is believed to have been centered on the southern end of the Rodgers Creek fault system (Toppozada et al., 1992). The Rodgers Creek fault is probably the right-stepping continuation of the Hayward fault (Parsons et al., 2003). In a right-lateral strike-slip environment, a right step produces an area of localized pull–apart extension. Under this model, it is not purely coincidence that the deepest part of San Pablo Bay would be centered over the stepover, since repeated movement on the two faults would cause subsidence in that area.

The tsunami from the 1898 Mare Island earthquake at an unspecified location in the bay was estimated at $0.6m$ and Lander et al. (1993) reported the accounts for this event, *"...the waters of San Francisco Bay rose in a tidal wave two feet high, but almost immediately subsided"* from the *Record Union* and *"the water off the Oakland mole (breakwater) was churned into big seas, and the yachts were severely tossed about for several minutes. Large waves beat against the rocking ferry houses but did no damage"* from the *San Francisco Call*.

Parsons et al. (2003) did a detailed study of the stepover zone between the Rodgers Creek and Hayward faults and included a numerical modeling of a stepover-induced tsunami that is used as a local source in the next chapter. They reported that historic hydrographic surveys before and after the earthquake suggest that subsidence occurred in the stepover region, presumably related to the earthquake.

A small tsunami was recorded at the Fort Point tide gauge after the April 18, 1906 Great San Francisco earthquake, as a $10cm$ fall in sea level that began 8 to $9min$ after the earthquake and lasted approximately $15min$. Following this water motion, there was no significant elevation wave, but rather a series of 2 or 3 more depression waves with a period of approximately $45min$ and an amplitude of $5cm$ (Lander et al., 1993). Numerical modeling of the 1906 tsunami by Geist and Zoback (1999) suggests that the tsunami was generated by coseismic subsidence just offshore, where the San Andreas fault undergoes a short right step.

Date	Source Area	Val.	Cause	Location of Effects	Runup (m)	Comments
1851	San Francisco	1	E	San Francisco	Observed	Unusual water movement felt on ships.
1852	San Francisco	1	E	San Francisco	Observed	Lake Merced drained.
1854	San Francisco	2-3	E	San Francisco	Observed	Water rose $1m$ with high waves in calm weather on Angel Is.
1856	San Francisco	3	L	San Francisco	0.6	Water rose and stayed high for $5mins$. Followed by a $M_w \approx 5.9$ earthquake.
1868	$M_w \approx 7$	1	L	Government Is.	Observed	Recorded an unusual. rise in water.
	Hayward	1		Sacramento	Observed	$0.6m$ wave observed.
		3		San Francisco	4.5	4–$6m$ above the usual mark at Cliff House.
1869	San Francisco	1	M	San Francisco	Observed	Earthquake recorded on tide gage.
1869	N. California	3	E?	San Francisco	Observed	Recorded
1887	N. California	2	L?	Sausalito	Observed	Distinct waves. No source known.
1898	$M_w \approx 6.7$ Mare Island	3	E	SF Bay	0.6	Earthquake tossed boats in the bay.
1906	N. California	3	E	San Francisco	0.1	Slight drop in water level.
1927	Pt. Arguello	4	E	San Francisco	<0.1	Recorded
1992	Cape Mendocino	4	E	Alameda	<0.1	Recorded
				San Francisco	<0.1	Recorded

Validity (Soloviev and Go, 1974; Cox and Morgan, 1977))	Cause:(Toppozada et al., 1992)
1= probably not a valid report	L= landslide
2= possibly a valid report	M= Meteorological
3= probably a valid report	E= Earthquake
4= certainly a valid report	

Table 1.5: Local and regional San Francisco tsunamis (Borrero et al., 2006a)

1.5 Mathematical Modeling of Tsunamis

Tsunamis are triggered from seafloor deformations or other impulsive geophysical events that displace large water volumes. The initial displacement of the water surface is of profound significance in calculating the evolution of the resulting waves. In some cases, such as landslide generated waves, it is sometimes speculated that the precise history of the landslide motion is also important. Liu et al. (2005) suggest that even landslide–triggered water waves are formed almost immediately post the initiation of failure and the tsunami striking the adjacent coastline is not, to first–order, dependent on the exact history of the motion of the sea floor. If it is assumed that the seafloor displacement is instantaneous, then the net seafloor displacement is the initial condition for the free surface. Even for the 26 December 2004 event with a rupture that may have lasted up to ten minutes over more than $1000km$, evolution models with initial conditions for the free water surface based on the assumption of instantaneity have been shown to represent the megatsunami satisfactorily, at least as compared to satellite measurements (Titov et al., 2005b,a; Geist et al., 2005).

The most general equations of motion for incompressible fluids are the Navier–Stokes equations. They are representations of the conservation of momentum, and they equate the mass per unit volume of a fluid particle times its material acceleration to the gradients of tangential surface forces arising from viscosity, of normal stresses such as pressure, and of body forces such as gravity. Coupled with the conservation of mass equation, sometimes referred to as continuity, they form a set of four nonlinear and coupled partial differential equations for the four unknowns, namely the three velocity components and pressure. They are generally insolvable, even numerically, in all but the simplest cases, when geometry allows for simplifications.

Free–surface motions are described using an additional variable, namely the wave height at the free surface, introduced through the so–called free surface kinematic boundary condition. The latter requires that the vertical velocity of the fluid at the free surface equal the material derivative of the wave height. Sometimes this is described as a condition that ensures that the particles on the free surface stay there, i.e., do not to mix with the rest of the fluid. When the waves climb on dry land, additional conditions are required to describe the runup and rundown.

As Liu et al. (1991) wrote, a certain approximation of the Navier–Stokes equations known as the Shallow–Water Wave equation (SWE) models the hydrodynamic evolution and runup of tsunamis unexpectedly well. The SWE are derived from the N–S equations, if the latter are depth–averaged and the pressure is assumed hydrostatic. Another depth–averaged formulation results into the Boussinesq equations, where the pressure is not assumed hydrostatic. The latter equations are referred to as dispersive, in the sense that they appropriately model shorter waves, than the SWE affected by frequency–dependent propagation. Both the SWE and Boussinesq approximations are valid for long waves, where depth averaging is a reasonable assumption. There is no further limitation on the wave height. Wind waves produce disturbances that affect a small fraction of the water column, and depth–averaging is not appropriate. Long waves are defined as waves with wavelengths much longer than the local depth, typically more than twenty times. Wind waves are generally dispersive, their phase and group velocities differ; hence, the wave packet evolves rapidly, even across oceans of constant depth. A long wave will maintain its overall shape over constant depth far longer than wind waves. For a complete discussion, refer to Synolakis (2003).

MOST is a numerical model that solves the SWE equations, developed by Titov and Synolakis (1997) and further described by Titov and Synolakis (1998) and Titov and

González (1997). When a seafloor deformation is specified, it is transferred to the free water surface as an initial condition and the computation begins. MOST computes the evolution of the tsunami using SWE and finally calculates the runup on the shoreline by introducing moving grids to model the evolution on initially dry land. Defining the total depth $h = \eta(x,y,t) + d(x,y,t)$, where $\eta(x,y,t)$ is the wave amplitude at the surface and $d(x,y,t)$ is the undisturbed water depth. $u(x,y,t)$ and $v(x,y,t)$ are depth–averaged velocities in the onshore x and long-shore y directions, respectively, and g as the acceleration of gravity, the SWE equations are

$$h_t + (uh)_x + (vh)_y = 0, \tag{1.1}$$

$$u_t + uu_x + vu_y + gh_x = gd_x \tag{1.2}$$

and

$$v_t + uv_x + vv_y + gh_y = gd_y \tag{1.3}$$

This is a 2+1 problem with two–directional propagation and one time dimesnion. In MOST, these equations are solved by the splitting method and reduced into two 1+1 problems :

$$\begin{aligned} h_t + (uh)_x &= 0 \\ u_t + uu_x + gh_x &= gd_x \\ v_t + uv_x &= 0 \end{aligned} \qquad \text{and} \qquad \begin{aligned} h_t + (vh)_y &= 0 \\ v_t + vv_y + gh_y &= gd_y \\ u_t + vu_y &= 0 \end{aligned} \tag{1.4}$$

The splitting technique is also known as the method of fractional steps (Yanenko, 1971). In MOST, it was found advantageous to use the splitting method in combination with an explicit finite difference technique. Titov and Synolakis (1997, 1998); Titov and

González (1997) solve the SWE in spherical coordinates with Coriolis terms in the more common form of the SWE, Equation 1.3.

$$
\begin{aligned}
h_t + \frac{(uh)_\lambda + (vh\cos\phi)_\phi}{R\cos\phi} &= 0 \\
u_t + \frac{uu_\lambda}{R\cos\phi} + \frac{vu_\phi}{R} + \frac{gh_\lambda}{R\cos\phi} &= \frac{gd_\lambda}{R\cos\phi} + fv \\
v_t + \frac{uv_\lambda}{R\cos\phi} + \frac{vv_\phi}{R} + \frac{gh_\phi}{R} &= \frac{gd_\phi}{R} - fu
\end{aligned}
\tag{1.5}
$$

Here, λ is the longitude, ϕ the latitude, f is the Coriolis parameter ($f = 2\omega\sin\phi$) and where ω is the earth's angular rotation and R is the earth's radius.

Applying the SWE (Equation 1.5), for wave evolution through deep ocean can be calculated over very long distances. For more efficient computation, the version of MOST used here works with three nested grids for wave propagation. As shown in Figure 1.9, large, medium and small grids are used. Wave propagation through deep ocean uses coarse grid –typically 4 minutes of arc ($\approx 7km$) which saves computer time and storage. Inundation computations require a much finer grid.

FACTS (Facility for the Analysis and Comparison of Tsunami Simulations) is a web–based database developed by NOAA–PMEL (Pacific Marine Environmental Laboratory) that stores earthquake information for subduction zones around the Pacific Ocean. The FACTS server is utilized to provide boundary conditions for modeling cases in Alaska-Aleutian, South America–Chile, Cascadia, Kuril Islands amd Japan Trench subduction zones. The specific inundation studies are developed with site–specific three–deep nested grids.

1.5.1 The FACTS Database

In the FACTS database server, the Pacific Rim subduction zones have been discretized into 177 fault segments, each $100 - km$ long and with unit $(1m)$ slip. The database has precomputed the complete propagation results of tsunami waveforms across the Pacific Basin over all grid points, emanating from each segment. Then sources can be later linearly combined to create larger seismic sources, capable of producing damaging trans–pacific tsunamis. Sources can also be scaled to reflect the actual slip. The underlying assumption is that the deep–sea evolution is linear, even though the equations used for propagation are nonlinear. Given the typical size of tsunamis in the deep ocean, this is not an unreasonable assumption, as in deep water the contributions of the nonlinear terms in the wave evolution are negligible. Once in shallow water, the superposition probably is not applicable, hence a site–specific inundation model is created to study the terminal effects.

While there is no a priori justification for the FACTS ad hoc assumption that unit sources can be combined to produce large sources is adequate, both the succesful forecast of the 2003 Adreanof event that resulted in the cancellation of a warning in Hawaii (Titov et al., 2005a), the forecast of 15 August 2007 Peru tsunami.(Wei et al., 2007)), and the comparison to be presented here of the tide gauges in SF Bay from the 1964 event, all suggest that the method works satisfactorily, certainly in the very least, for screening tsunami zones and identifying sources of exceptional risk at any given location from any of the 177 segments that have been indentified this far as tsunamigenic around the Pacific Ocean.

1.5.2 Numerical Grids

As shown in Figure 1.9, the model used in this study was prepared with a system of nested grids derived from a $3arcsecond$ combined topography and bathymetry grid. The outermost grid was sampled to $30arcsec$ ($\approx 750m \times 900m$) , the intermediate grid to $15arcsec$ ($\approx 450m$) while the full resolution ($3arcsec$, $\approx 75m \times 90m$) data was used in the innermost grids for several locations along the California coast, Crescent City, Orick, Humboldt Bay, Shelter Cove, Cape Mendocino, San Francisco Bay, Morro Bay, Los Angeles/Long Beach and San Diego.

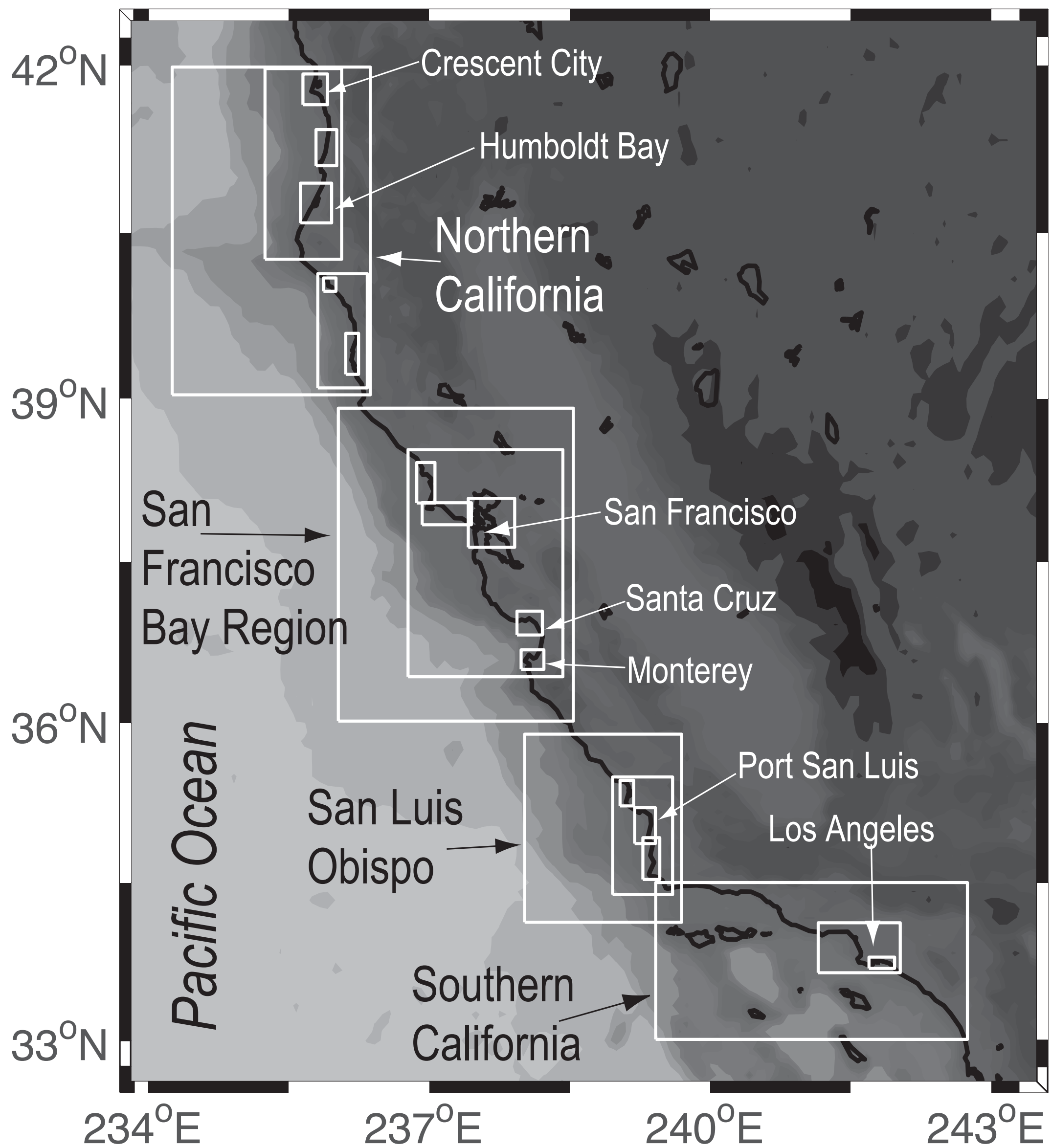

Figure 1.9: Nested numerical grids for the tsunami numerical computations presented in this thesis for California.

Chapter 2

Modeling Tsunamis for California Ports and Harbors

2.1 Introduction

California has been affected by tsunamis originating both nearfield and farfield. The last century, teletsunamis such as the 1964 Alaskan and 1960 Chilean events caused damage to ports in San Francisco and Los Angeles. Nearfield events such as the 1927 Point Arguello tsunami affected Morro Bay in the central coast. Limited experience with the impact of any size tsunamis in modern port operations, combined with the dense coastal land use and the importance of California's maritime facilities on the regional and global economies make the assessment of tsunami impacts along the coast and in ports a vexing.

West Coast ports play a major role in the US economy. According to Pacific Merchant Shipping Association (PMSA, 2003), they account for nearly 95% of all the goods imported into the US from Asia. California has 11 cargo seaports and 27 small craft harbors. California port activities support more than 500,000 jobs and contribute statewide $30.5 billion in income.

As a result, tsunami scenarios have become part of emergency response plans in many coastal cities. The aim of this thesis is to assist in the quantification of the hazard from nearfield and farfield events. To quantify the effects on California ports, first historical tsunamis and numerical simulations of these events are examined to identify the relative tsunami hazard. Then, a deterministic approach is used to model a various cases based on historical events which represent "worst-case" scenarios for transoceanic tsunami generation from subduction zones around the Pacific rim. The results from these investigations are compared and a database of model outputs for archived scenarios is produced.

2.2 Tsunami Sources

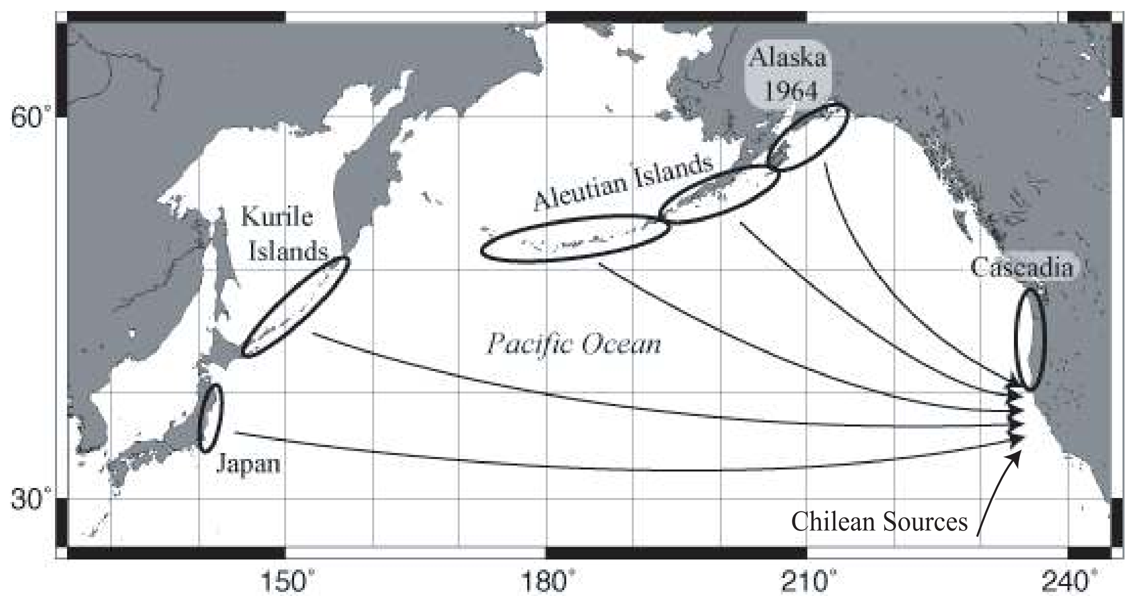

Figure 2.1: Source regions around the Pacific for farfield tsunami affecting California.

In this study, farfield and nearfield sources are considered separately. A farfield source is one whose source region is located a great distance away from the region where the tsunami coastal effects are studied. Typically, farfield sources are located at distance greater than $1800km$ and the tsunami travels over water $> 1000m$ deep from

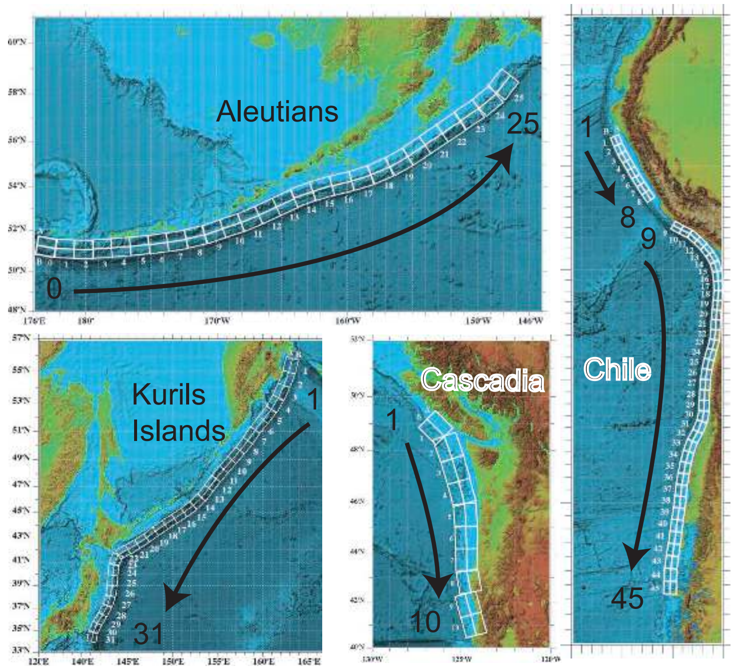

Figure 2.2: Subduction zones of the Pacific Rim discretized into 2 parallel rows of $100km$ long by $50km$ wide fault segments. Clockwise from upper left; Alaska-Aleutian Islands (AASZ), South America-Chile (SASZ), Cascadia (CSZ) and Kamchatka-Kuril-Japan (KSZ).

Tsunami Source Name	L (km)	W (km)	disp (m)	Mw
Alaska 1964	–	–	–	9.2
Segment 1	400	290	10	
Segment 2	400	175	10	
Aleutian I	600	100	10	8.8
Aleutian II	600	100	10	8.8
Aleutian III	700	100	25	9.2
Kuril I	1000	100	9	9.0
Kuril II	400	100	10	8.7
Kuril III	400	100	10	8.7
Kuril IV	400	100	10	8.7
Japan I	900	100	5	8.8
Japan II	400	100	10	8.7
Chile 1960	1000	100	20	9.3
Chile North–Peru	1400	100	25	9.4

Table 2.1: Source parameters for farfield tsunami scenario simulations.

source to target. Potential farfield sources for California include large earthquakes on the various subduction zones around the Pacific Rim. Thus, the Cascadia Subduction Zone (CSZ), the Alaska-Aleutian Subduction Zone (AASZ), the Kamchatka - Kuril Island - Japan Subduction Zone (KSZ) and the South American Subduction Zone (SASZ) are considered (Figure 2.1) in this analysis.

Nearfield sources are the local offshore fault lines in the study region. The San Gregorio and Rodgers Creek faults are nearfield sources for the San Francisco Bay area. The Santa Catalina Island thrust fault is an example of a nearfield source for southern California. The southern end of the CSZ is located close to the Oregon–California border, which makes the CSZ a nearfield source for northern California.

2.2.1 Farfield Tsunami Sources for California

In order to model the farfield events, NOAAs FACTS (Facility for the Analysis and Comparison of Tsunami Simulations) database was employed. This database contains the full trans-oceanic simulations for tsunamis generated from “unit” segments of the major subduction zones along the Pacific Rim. The database is the foundation of the new tsunami forecast system under development for the NOAA Tsunami Warning Centers, i.e., the PTWC (Pacific Tsunami Warning Center) and the WCATWC (West Coast and Alaska Tsunami Warning Center). This research work illustrates another application of this general-purpose archive for tsunami hazard assessment.

NOAA’s database was created by subdividing each subduction zone along the Pacific Rim into two parallel rows of $100km$ long by $50km$ wide fault segments (Figure 2.2). A pure thrust earthquake mechanism with unit slip $(1m)$ is then imposed on each segment and the resultant trans-oceanic wave propagation is computed up to a certain threshold depth in the vicinity of the coastline, then stored. Larger earthquakes (and thus tsunamis) are created from this database by combining segments and scaling the slip by an appropriate factor to reach the desired earthquake magnitude.

To calculate the moment magnitude M_w, the formula: $M_w = \frac{2}{3}(\log_{10} M_o) - 6.0$ (Kanamori, 1977b) is used, where M_o is the seismic moment in Nm. The seismic moment is computed using $M_o = \mu u A$, where u is the slip on the fault, A is the area of the fault plane and μ shear modulus of elasticity of the crust, and usually taken as $3 \times 10^{10} N/m^2$ (Yeats, 1997). Non–uniform slip sources can be constructed by adding $100km$ long and $50km$ wide segments to produce earthquakes of "any" size. For example, a $M_w = 8.9$ earthquake with a fault length of $800km$ and a fault width of $100km$, requires an average slip of $9.3m$ on each fault segment. The computed tsunami heights from the eight adjacent pairs of $100km$ segments is multiplied by 9.3, and the results linearly combined into one resultant wave field. The underlying assumption is that the propagation in deep water is linear, thus unit solutions are superposed; at a waveheight of tens of cm in thousand kilometer depth of water and wavelengths of 100 of km, the assumption is appropriate. Times series of waveheight and velocity estimates at grid points over the entire Pacific are then interpolated at the boundary of the outermost local grid (see Figure 1.9) and used as an initial condition to the local tsunami inundation model (Borrero et al., 2004a). A summary of the subduction zones fault scenarios used in here is given in Table 2.1.

The Cascadia Subduction Zone (CSZ) lies just offshore along the North American continent, spanning the coastline from northern California to British Columbia, a distance of about $1000km$. It is now widely believe to produce infrequent, but very large earthquakes (Heaton and Kanamori, 1984; Atwater, 1987; Goldfinger et al., 2003). See the northern California section of this chapter.

Using Satake et al. (2003), three earthquakes were used in this analysis from the CSZ unit sources for farfield with M_w ranging from 8.8 to 9.1 as possible farfield scenarios for southern California, and an additional five for northern California. The first scenario is $800km$ long and $100km$ wide with $11.1m$ slip corresponding to a $M_w = 8.9$ earthquake. The second is $600km$ long and $100km$ wide with $10m$ slip, corresponding to a $M_w = 8.8$ event. The third case is the full rupture of $1000km$ long and $100km$ wide with $20m$ slip corresponding to a $M_w = 9.1$ event, as shown in Figure 2.2.

The 1964 Great Alaskan $M_w = 9.2$ Earthquake triggered the largest tsunami to hit the California coastline in the past century. It resulted in observable crustal deformation of unprecedented extend (Plafker, 1965), and the resulting observations were instrumental in proving the theory now known as plate tectonics. Hence, the Alaska–Aleutian Subduction Zone (AASZ) is studied in detail, for tsunamigenesis, and another three additional scenarios are considered, as discussed below.

The $M_w = 9.2$ earthquake struck the Prince William Sound area of Alaska on March 28, 1964, at UTC=03:36:14. Its epicenter was located at $61.04°$ N. and $147.73°$ W (Plafker, 1965; Johnson et al., 1996), about $120km$ SE of Anchorage and $90km$ E of Valdez, with a hypocentral depth of about $25km$. Before the 26 December 2004 Great Sumatran earthquake, it was believed to be the second largest earthquake ever recorded, in instrumental history (Stein and Okal, 2005). Recently, the size of the 1964 earthquake has been recalculated and some have argued that it may have been reached $1.2 \times 10^{23} Nm$, making it slightly larger than the 2004 Boxing Day earthquake (Nettles et al., 2005; Synolakis and Kong, 2006).

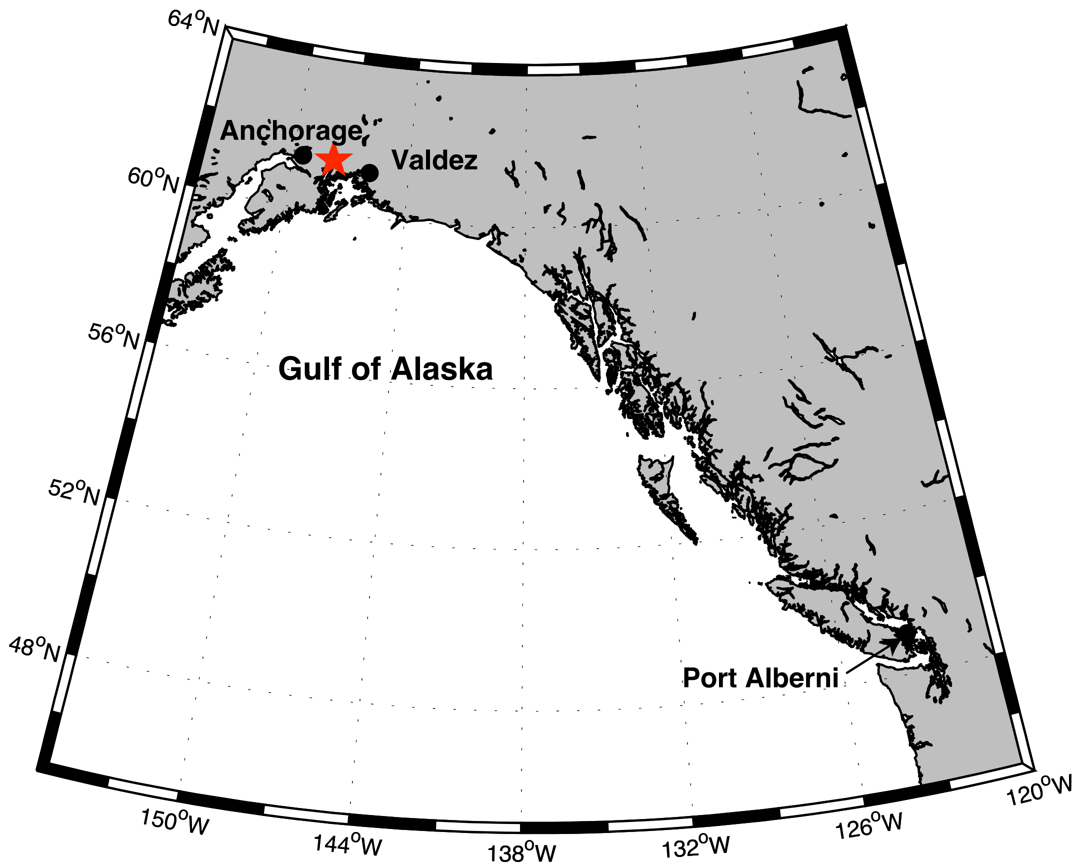

Figure 2.3: Locations of Valdez and Port Alberni in Gulf of Alaska.

The shock generated a massive tsunami that devastated many towns along the Gulf of Alaska and caused substantial damage at Alberni and Port Alberni, Canada, $1900km$ from the epicenter. The maximum runup was reported as $67m$ (Plafker, 1969) in Valdez inlet (Figure 2.3). The tsunami also travelled to Hawaii causing minor damage, with typical runup heights of about $2m$. The tsunami waves strongly affected the California coast and caused significant damage to Crescent City, as well as damage and flooding in San Francisco Bay. The average height along the west coast was about $2m$, with its maximum of $5m$ at Crescent City (Lander et al., 1993). California sustained more damage than any other state, except Alaska (Plafker, 1972). Eleven people lost their lives and thirty–five were seriously injured at Crescent City, where the wave was observed larger than in surrounding areas, possibly because of local topographic amplification.

Plafker (1972) reported that the earthquake deformation caused regional displacement over an area of $140,000$km^2, which is about the size of Greece. The zone of major uplift was inferred was 950km long and 200km wide with a maximum uplift around $11m$ and $2m$ subsidence. Plafker (1969) determined the vertical displacements using a comparison of pre and post tide gage records and survey level lines based on vegetation patterns. He also compared before and after depth soundings and measured the runup of the tsunami along the coast, in what appears to be the first ever comprehensive quantitative tsunami post-event field survey (Synolakis and Okal, 2005).

The Alaska–Aleutian Subduction Zone (AASZ) is the result of Pacific Plate subducting under the North American Plate. The AASZ is one of the longest subduction zones known, starting from longitude $165°$E to almost $140°$W. The AASZ also has a history of rupturing in large and great earthquakes(Johnson et al., 1996). Five great earthquakes in the last century were the 1938, 1946 Unimak, 1957 Andreanof Islands, 1964 Prince William Sound (or Alaskan) and 1965 Rat Island events. All five of them happened in sequence, one of the longest in the 20$^{\text{th}}$ century, although not spatially distributed temporarily. In this study, four scenarios have been modeled with the objective to identify physically realistic extreme future events, but not necessarily to model any particular historic events earthquakes, except for the 1964 event which was done for validation.

The fault mechanism suggested by (Plafker, 1969, 1972) for the 1964 earthquake uses a fault length of $890km$, different from his inferred zone of uplift ($950km$). The northern segment was estimated as $600km$, then the rupture continued E-W for another $200km$. The down–dip width was proposed $290km$ at the north, and $175km$ on the south. The dip angle was estimated at approximately $9°$ with a slip of more than $20m$. This entire ground motion was a predominantly reverse fault, triggering a megathrust with $M_w = 9.2$.

In the first AASZ scenario, the 1964 Alaskan tsunami is modeled with a double fault mechanism. The first fault is $400km \times 290km$ with $10m$ slip, and the second $290km \times 175km$ with $20m$ slip. In the second scenario, an $800km$ long, $100km$ wide rupture is considered in the central Aleutians. The third scenario is identical to the second, but located in the eastern Aleutians; both are $M_w = 8.8$ events. The fourth scenario considers a $700km$ long, $100km$ wide fault, with $25m$ slip, centered in the eastern Aleutians, with $M_w = 9.2$ rupture.

The Kuril Islands Subduction Zone (KSZ) is quite active and has triggered the 1923 Kamchatka, the 1952 Kamchatka, the 1963, the 1994 Shitokan, the 2006 Kuril Islands and the 2007 Kuril Islands tsunamis (Lander et al., 1993; Dengler et al., 2008). The $M_W \approx 8.4$ 1923 Kamchatka earthquake triggered a transoceanic tsunami that was recorded in Santa Cruz and Los Angeles. The tsunami from the $M_W \approx 9.0$ 1952 Kamchatka earthquake caused extensive devastation locally including the reported landing of several Russian submarines. It also, allegedly caused boats to sink at Crescent City. The $M_W = 8.5$ 1963 Kuril Island event was also observed at Crescent City.

The KSZ is studied here also with four different tsunami scenarios. In the first, most of the zone ruptures at once, in a $1000km \times 100km$ event with $9m$ slip, producing a $M_w = 9.0$ earthquake. The other three scenarios divide the KSZ into three segments. Their size is identical, $400km \times 100km$ with $10m$ slip, thus representing $M_w = 8.8$ earthquakes at the northern, middle and southern part of the KSZ.

Japan is one of the most seismically active regions on earth, with a long history of reported tsunamis. Even the word tsunami is Japanese. Pacific wide tsunamis in

Japan are triggered along the Japan Subduction Zone (JSZ) located along the NE of Honshu Island. The JSZ is possibly an extension of the KSZ. This JSZ has produced very large earthquakes, notably the 1896 $M_w = 8.0$–8.5 Sanriku event. The latter not only triggered a catastrophic tsunami locally, but in California also caused damage at Santa Cruz, was observed at Mendocino and was reportedly recorded at Sausalito. The 1933 normal faulting event ($M_w \approx 8.3 - 8.7$) also happened off the coast of Sanriku was recorded in six locations California (Lander et al., 1993; Dengler et al., 2008).

The JSZ is modeled with two different $M_w = 8.8$ scenarios, one with $900km \times 100km$ rupture and $5m$ slip, and the other with $400km \times 100km$ with $10m$ slip.

On 22 May 1960, the South American Subduction Zone (SASZ) triggered the largest earthquake ($M_w = 9.5$) that has ever been instrumentally recorded Berkman and Symons (1964) with runup in the immediate area reaching $25m$ (Plafker, 1972; Instituto Hidrografico de la Armada, 1982) and causing at least 1200 deaths. The tsunami crossed the Pacific and caused damage throughout the Pacific basin, with 61 casualties in Hawaii (Cox and Mink, 1963) and 180 in Japan (Duke, 1960). The wave caused over $1 million in damage in Los Angeles and Long Beach harbors, as well as a $2.5m$ peak to trough wave recorded in Crescent City tide gauge (Berkman and Symons, 1964).

In modeling the SASZ two scenarios were used in this analysis. First, the 1960 Great Chilean Earthquake was modeled with a $1000km \times 100km$ rupture with $20m$ slip to represent a M_W 9.3 earthquake, as per Plafker (1972). The other scenario was a $M_w = 9.4$ event in the northern part of the subduction zone, involving a rupture extending into Peru along a $1400km \times 100km$ fault area and a $25m$ slip.

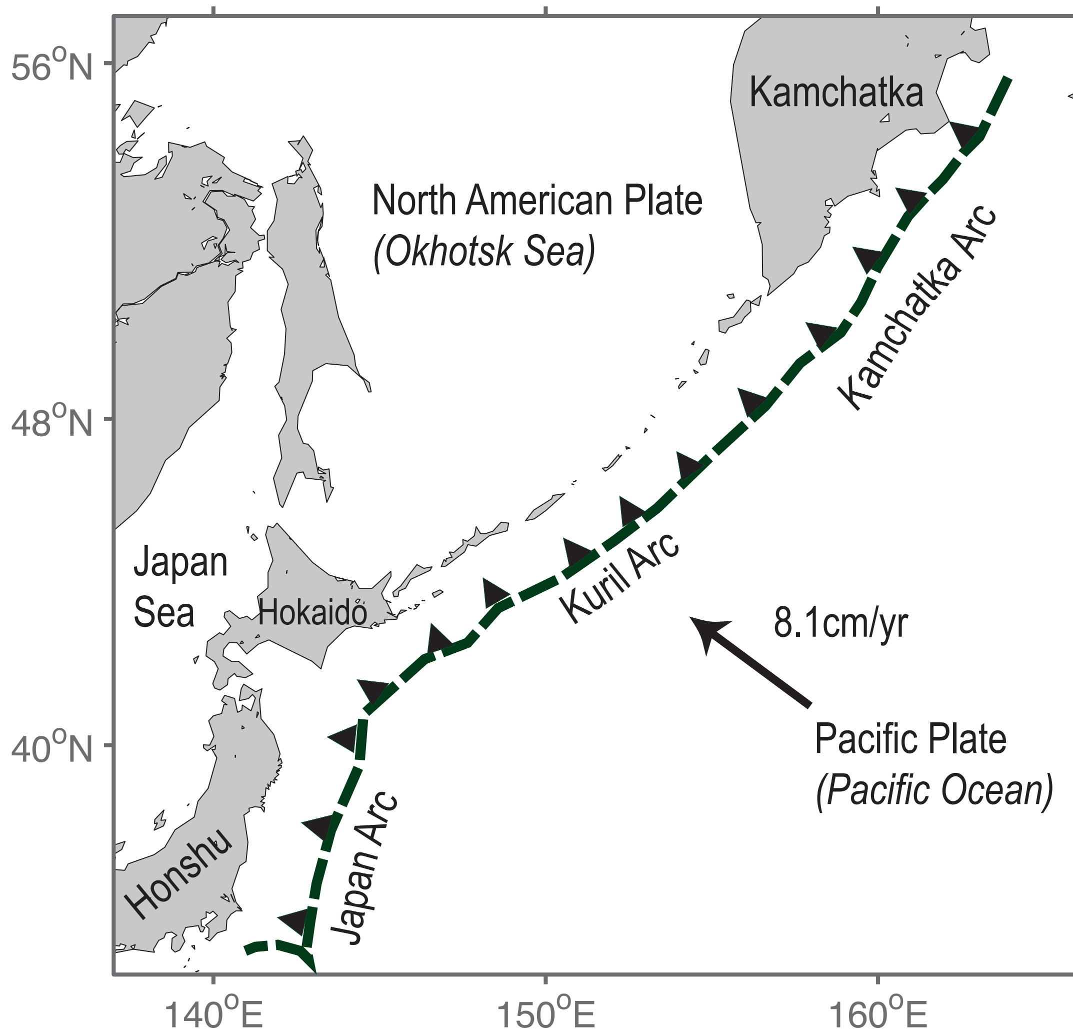

Figure 2.4: Kuril Islands Subduction Zone, starting from Kamchatka in the north and going down to Honshu Japan in the south with $8.1cm/yr$ Stein and Okal (2007).

The Recent Kuril Islands Events

The Kuril Islands Subduction Zone (KSZ) is located on the Pacific Rim (Figure 2.4) and it is one of the active fault zones that is responsible from some of the mega earthquakes of the last century. It starts in the north at Kamchatka and runs south following the Kuril Islands, and ending at the Honshu–Hokkaido boudnary in Japan. The Kuril Islands slip

(a) Historical events on the KSZ

Date	Source	M_w	Damage/ Tsunami effects
1896	Japan	8.0-8.6	Damage in Santa Cruz
1923	Kamchatka	8.4	Strong currents that affected shipping in Los Angeles
1933	Japan	8.3-8.7	recorded in San Francisco
1952	Kamchatka	9	4 boats sunk in Crescent City

(b) Recent events from KSZ

Date	Source	M_w	Damage/Tsunami effects
4/10/94	South KSZ	8.3	Recorded in Crescent City.
15/11/2006	Central KSZ	8.3	Up to a million dollar damage in Crescent City harbor.
13/1/2007	Central KSZ	8.1	nothing significant, but noted.

Table 2.2: Events from KSZ are listed above in the table. (a) lists the significant events that affected California. (b) lists the recent events and their impact. Pre–1994 observations from Lander et al. (1993).

rate has been estimated around $94mm/yr$ by Minster and Jordan (1978), corrected to $81mm/yr$ by DeMets et al. (1994) and kept as $81mm/yr$ by Stein and Okal (2007).

Table 2.2 is a list of historical events from Japan and the KSZ that have affected the California coastline. The table starts with the 1896 Great Sanriku event that caused damage in Santa Cruz, followed by the 1923 Kamchatka earthquake which affected the shipping in Los Angeles Harbor (Lander et al., 1993), the 1933 Japan event that was instrumentally recorded in San Francisco Bay, and finally the 1952 Kamchata event which sank four boats in Crescent City. Starting in 1994, this trench has produced three large earthquakes, as shown in Figure 2.5; the $M_w = 8.3$ 1994 South KSZ, the $M_w = 8.3$ 2006 Central KSZ and the $M_w = 8.1$ 2007 Central KSZ earthquakes. All three generated tsunamis; however, the only one that caused damage in Crescent City harbor was the 2006 earthquake.

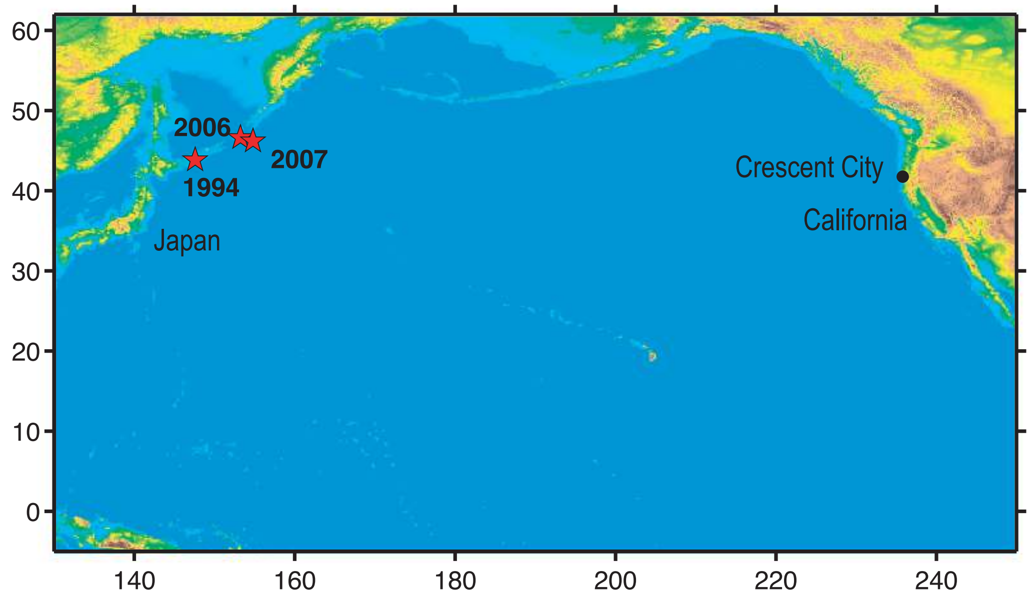

Figure 2.5: Epicenter of 1994, 2006 and 2007 events.

2.2.2 Nearfield Tsunami Sources for California

Here a "variety" of tectonic sources was used depending on the study region. Four Cascadia cases are considered for northern California (N.C.); in addition to the three long farfield ruptures a scenario rupturing the Little Salmon Fault is also considered (Bernard et al., 1994). Two local ruptures, on the Hayward-Rodgers Creek and San Gregorio faults, are studied in the San Francisco Bay region (S.F. Bay) (Borrero et al., 2006a). Seven different fault ruptures are used in the detailed modeling of southern California (S.C.), which are discussed in Borrero et al. (2001) and Borrero et al. (2004b). Local earthquakes in southern California are generated at the Channel Islands, Anacapa-Dume, Santa Monica Bay, Lausen Knoll, San Clemente and San Mateo (Table 2.3).

In the study of local sources, aside dislocations, landslide–generated tsunamis are also considered for San Francisco Bay and southern California. A dipole source with a $10m$ waveheight is used in the Farallon Islands to simulate a landslide–triggered tsunami

Local Tectonics	L (km)	W (km)	slip (m)	Dip (deg)	Rake (deg)	dep. (km)	seg's	M_w	region
Cascadia SN	240	80	8	10	90	5	2	8.44	N.C.
Cascadia SW	240	100	8	10	90	5	2	8.51	N.C.
Cascadia SP1	240	100	7	10	90	5	4	8.48	N.C.
Cascadia SP2	240	100	8	10	90	5	4	8.5	N.C.
CSZ N	800	100	11	n/a	90	n/a	16	8.95	N.C.
CSZ L	1040	100	11	n/a	90	n/a	22	9.02	N.C.
C. Mendo. 1992	21.5	16	2.7	12	107	6.3	1	6.96	N.C.
Hayward-Rodgers	10	18	1.5	70	-90	5	1	6.6	S.F. Bay
San Gregorio	50	15	2	60	90	5	1	7.1	S.F. Bay
Channel Islands	56	34	3.6	20	90	17	1	7.54	S. C.
Anacapa-Dume	40	18	2.5	55	90	15	1	7.15	S. C.
Santa Monica Bay	40	18	2.4	55	90	15	1	7.14	S. C.
Catalina Fault	164.3	14	4.46	n/a	n/a	n/a	7	7.66	S. C.
Lausen Knoll	16.7	12.5	2.2	n/a	n/a	0.5	2	6.76	S. C.
San Clemente Is.	30	8	8	70	162	7.6	1	7.3	S. C.
San Mateo	31.9	12	4	45	120	0.5	3	7.11	S. C.
Local Slump/Slide			positive wave			negative wave			
Farallon Islands			3			-7			S.F. Bay
Goleta			6			-18			S. C.
Palos Verdes			3			-7			S. C.

Table 2.3: Source parameters for nearfield tsunami scenarios.

and a similar source is also used around Palos Verdes. A bigger landslide source has been used to model tsunamis around Goleta in Santa Barbara County by Borrero et al. (2001).

Tsunamis from the Cascadia Subduction Zone

Six scenarios were modeled to assess the local tsunami hazard from a CSZ rupture. The scenarios ranged in M_w from 8.4 to 9.0 and varied in slip, width and length of rupture (Table 2.4). Scenarios SN and SW involve rupture of the southern or Gorda segment of the subduction zone only, and differ only in the width of the rupture zone. Scenarios SP1 and SP2 not only rupture the Gorda segment, but also partition the "available" slip between the Little Salmon fault and the CSZ (the Little Salmon is shown in Figure 1.7

Table 2.4: Source parameters used in modeling from Bernard et al. (1994) and Satake et al. (2003) and 1964 Alaska event.

Sources		L (km)	W (km)	Disp (m)	M_w
CSZ SN	Gorda Segment Narrow	240	80	8	8.44
CSZ SW	Gorda Segment Wide	240	100	8	8.51
CSZ SP1	Gorda–Little Salmon 1	240	100	7	8.48
CSZ SP2	Gorda Segment Narrow 2	240	100	8	8.50
CSZ N	Juan de Fuca Segments	800	100	11	8.95
CSZ L	Full Rupture	1040	100	11	9.02
C. Mendo. 1992		21.5	16	2.7	6.96

located in northern California near the south end of the CSZ and is capable of producing infrequent earthquakes with $M_w > 7.6$, per Clarke and Carver 1992). Scenario CSZ N considers only slip on the northern or Juan de Fuca segment of the CSZ, with $11m$ of slip along a $800km \times 100km$ rupture, stopping just north of the California border. Scenario CSZ L, the largest magnitude event modeled, simulates rupture of the entire subduction zone with characteristics believed similar to the 1700 rupture (Atwater and Hemphill-Haley, 1997). CSZ-L combines the average slip and the dimensions of Satake et al. (2003) with partitioned slip on the Gorda segment similar to SP1. The northern $800km$ is characterized by a slip distribution with an average of $12m$. The southern part includes slip on both the CSZ and the Little Salmon fault and is identical to SP2. The initial conditions for these scenarios are shown in Figure 1.8.

The 1992 Cape Mendocino earthquake was also used as an example source for a local event in northern California with a $M_w \approx 7.0$.

Tsunami Sources inside San Francisco Bay

For farfield scenarios, the “standard” sources of FACTS from subduction zones in the Pacific were used, as discussed in see Chapter 1. In addition, sources within the Bay

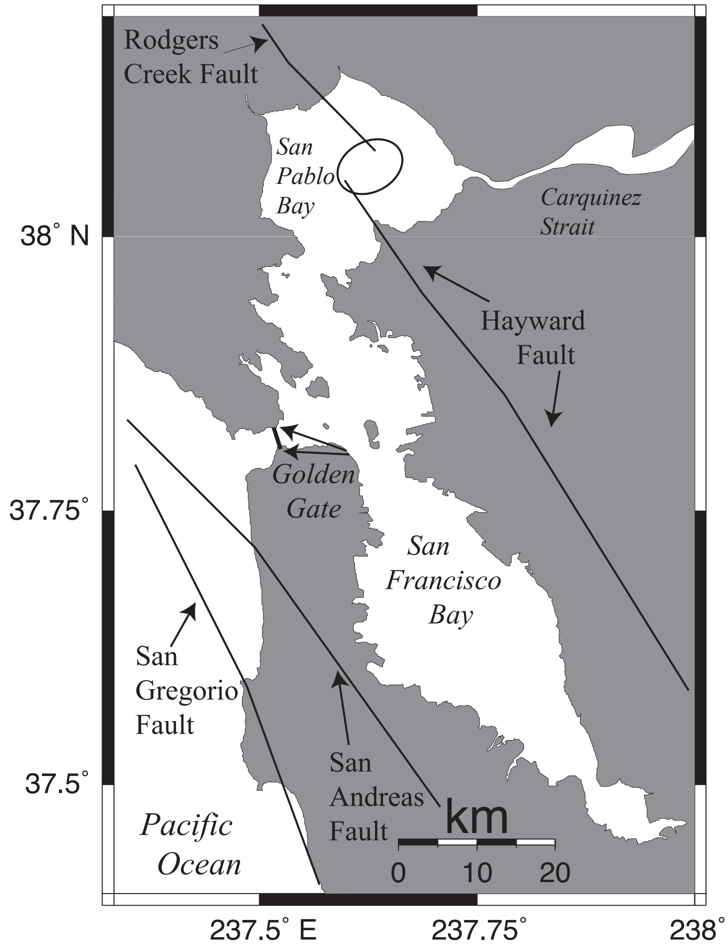

Figure 2.6: Major faults of the San Francisco Bay Region. Arrows show the mostly strike-slip sense of tectonic plate motion accomodated by earthquakes and aseismic creep on faults(Working Group on California Earthquake Probabilities, 2003 and Borrero et al., 2006a).

area itself were modeled. The farfield sources include events on the Cascadia subduction zone, the Alaska-Aleutian subduction zone, the Kuril Island and Japan subduction zones and the South America-Chile subduction zones (Table 2.1). Nearfield sources are underwater faults that might produce vertical deformation within the Bay or immediately adjacent to the Golden Gate, or sites with the potential to produce large submarine or subaerial landslides.

Several local sources were considered in order to assess the tsunami hazard in San Francisco Bay, as listed in Table 2.3 along with other nearfield scenarios for California. A Working Group on California Earthquake Probabilities (2003) study placed a 10 to 30% probability of a magnitude 6.7 earthquake or greater in 30 years, on any of three potentially tsunamigenic faults near San Francisco Bay. The probability was listed as 10% for the offshore segment of the San Gregorio Fault, 21% for the offshore strand of the San Andreas Fault and 32% for the Rodgers Creek Fault running through San Pablo Bay (Figure 2.6).

The San Gregorio fault is part of a system of offshore faults that parallel the coast from Point Arguello in the south to Bolinas Bay in the north. Just west of San Francisco, the San Gregorio fault converges with the San Andreas Fault in a region of complex faulting which includes several other parallel fault strands including the Golden Gate fault and the Potato Patch fault (Bruns et al., 2002; Borrero et al., 2006a). These fault strands trend northwest and merge onshore as the northern segment of the San Andreas fault. Though it is believed to be predominantly strike-slip in nature, the San Andreas does exhibit reverse faulting characteristics (Bruns et al., 2002) in an area west of the northern segment of the San Gregorio Fault known as the San Gregorio Structural Zone. In order to place an upper bound on the tsunamigenic potential of this fault, a large ($Mw = 7.1$) thrust mechanism earthquake is modeled with a fault length of $50km$ that traverses the bight west of the entrance of San Francisco Bay.

The northeast of San Francisco Bay is known as San Pablo Bay. Underneath San Pablo Bay, there is a stepover between the right lateral Hayward and Rodgers Creek faults (Figure 2.6). The details of this stepover were studied by Parsons et al. (2003). They contend that the Hayward–Rodgers Creek fault stepover was the source for the

1898 Mare Island earthquake and tsunami. They modeled the tsunami using a slip mechanism on a normal fault which steps over from the Hayward to the Rodgers Creek fault. Their simulations were for an earthquake with an approximate magnitude of 6.0, corresponding to $0.35m$ of slip on a fault plane $6km$ long by $18km$ wide. Parsons et al. (2003) suggest $0.1m$ as the maximum waveheight in the Bay, in contrast to the $0.6m$ reported in historical accounts. A similar fault geometry is used here with higher slip, to again place an upper bound on the tsunami waves and currents that could be generated by such a mechanism. The simulation uses a slip of $1.5m$, resulting in an earthquake of $M_w = 6.6$.

In addition to regional faults, the potential tsunami hazard caused by submarine or subaerial landslides is also examined. These are potential areas of large slope instabilities within the Bay and adjacent to the Golden Gate. The Farallon Islands are a rocky archipelago 45 to $65km$ offshore the entrance of the Bay. The Farallons sit on the continental slope; the easternmost island lies in about $150m$ water depth which increases to over $3000m$ only $5km$ to the southwest. According to Borrero et al. (2006a), the sea floor around the diorite islands is littered with the debris of submarine slides and with debris flows ranging in scale from a few square meters to hundreds of square meters (Karl and Schwab, 2001). The largest credible landslide on the east slope of the easternmost island is modeled using the same parameters as for the Palos Verdes slide (Borrero, 2002).

The potential slumps and landslides inside the bay itself was also examined to assess the potential of exciting seiches by earthquake surface waves. The topography on the Bay margins is generally gentle (no steep slopes and canyons, see Figure 2.7), and there is no history of large volume failures into the Bay. Most of the Bay is very shallow,

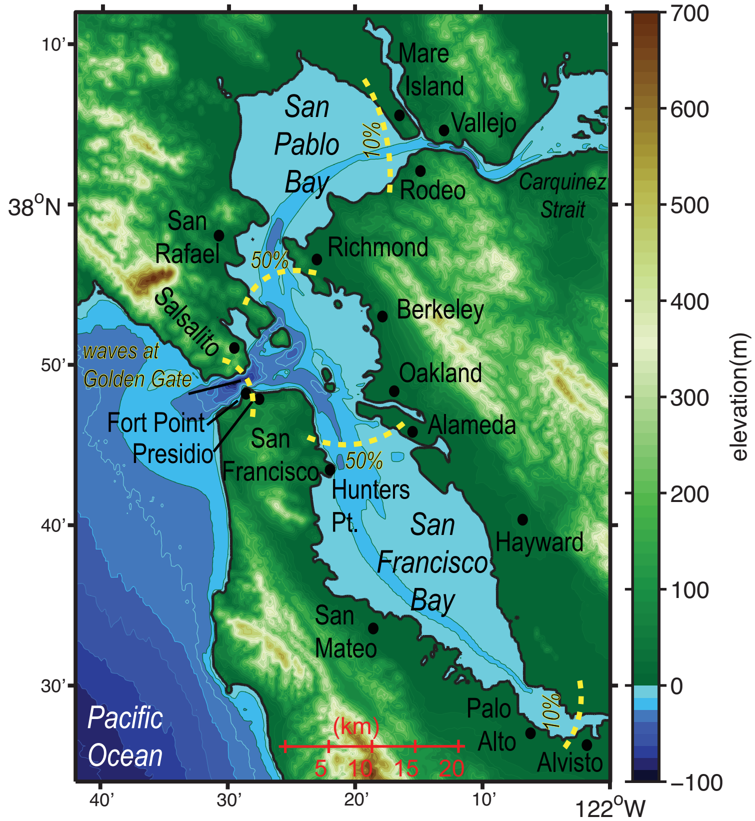

Figure 2.7: Topographic map of San Francisco Bay area with Magoon's (1966) waveheight attenuation estimates for a wave at Golden Gate, based on observations from the 1960 (Chile) and 1964 (Alaska) tsunamis.

and even if a large slide were to enter the Bay, the volume of water displaced would be small, presumably limiting the size of the resulting wave.

The Golden Gate is a steep gorge that separates San Francisco from Marin County. The Bay reaches its maximum depth of $109m$ at the Golden Gate. Only the headlines on the north side are steep enough to pose any slide hazard into the Bay and historically slides in this area have been small and few (Wentworth et al., 1997). There is no credible basis to support a large slide in this area.

The Carquinez Strait connects San Pablo Bay to Suisan Bay (Figure 2.7). Only the western end is steep enough to pose slide hazards. The Strait is less than a kilometer wide and no where deeper than $30m$. Wentworth et al. (1997) mapped the landslide hazard and found the bathymetry unable to pose a tsunami hazard compared to other sources examined in this study.

Earthquake surface waves are known to produce seiches in closed bodies of water and bays (Raichlen, 1966; Ruscher, 1999; Rueda and Schladow, 2002; Barberopoulou et al., 2004; Synolakis, 2003). The large amplitude surface waves are believed amplified by basin geometry, exciting water oscillations or seiches. To produce significant seiching in a body of water, the forcing periods must be close to the natural period of bay or of an overtone. The typical characteristic periods for San Francisco Bay range from 30–45 minutes and are much longer than surface wave periods; thus, non-tsunami induced seiches in San Francisco Bay are not considered to pose a hazard comparable to the other sources modeled in this study.

2.3 Using MOST to Simulate Historical Events

To check the validity of our model and method, we compare results of the simulation of historical events to its available instrumental records from tide gauges at various locations along the California coast.

2.3.1 Comparison to Historical Measurements from the 1960 Chilean tsunami

Figure 2.8 shows a comparison between modeled and recorded waveheights for the 1960 Chilean tsunami at several locations in California. The modeled results agree well with the observed data in terms of amplitude and period. There is a discrepancy in the modeled arrival time, which is only about 7 minutes and thus negligible when compared to the more than 14 hours, to travel from South America. The model used assumes an instantaneous rupture and displacement at the earthquake source, when in fact earthquakes of this size may take five minutes or longer to rupture the complete fault zone, explaining at least a part of the time discrepancy. Tsunami travel times are also affected by the shallow water bathymetry in the earthquake source region and the deep ocean bathymetry along the tsunami travel path, neither of which are modeled perfectly given the coarse grid resolution in the source region.

2.3.2 Comparison to Historical Measurements from the 1964 Alaska tsunami

A comparison of recorded and modeled waveheights for the 1964 event is shown in Figures 2.9 and 2.10. While the model overpredicts the initial wave crest and first large trough, especially on the Presidio tide gauge, the amplitudes and periods of the subsequent peaks match quite well. There is a slightly larger discrepancy in arrival times, approximately 15 minutes, than for the 1960 case. It can be argued that this difference is negligible in terms of hazard assessment for these distant events. The good fit of the model data to the tide gauge recordings gives confidence in the computational formalism and provides a strong foundation for investigating the relative influence of different farfield sources.

For the Alameda gauge in Figure 2.8, the calculation captures the initial wave form approximately the first several hours of the 1960 tsunami better, but does not reproduce the large amplitude oscillations which begin some five hours after the first wave arrival and persist for over three hours, see Figures 1.6. The exact cause for these late arriving waves has not been explained before; they have been noticed in recent tsunamis, e.g., in the 2006 Kuril Islands tsunami at Crescent City, and they appear to be the result of a resonance effect (Synolakis, 2003), as proposed by Wiegel (1970). These waves can probably be modeled better using higher resolution grids (Okal et al., 2006a,b,c) Note that the same observation can be made from Figure 2.10 for the 1964 Alaskan tsunami of Alameda.

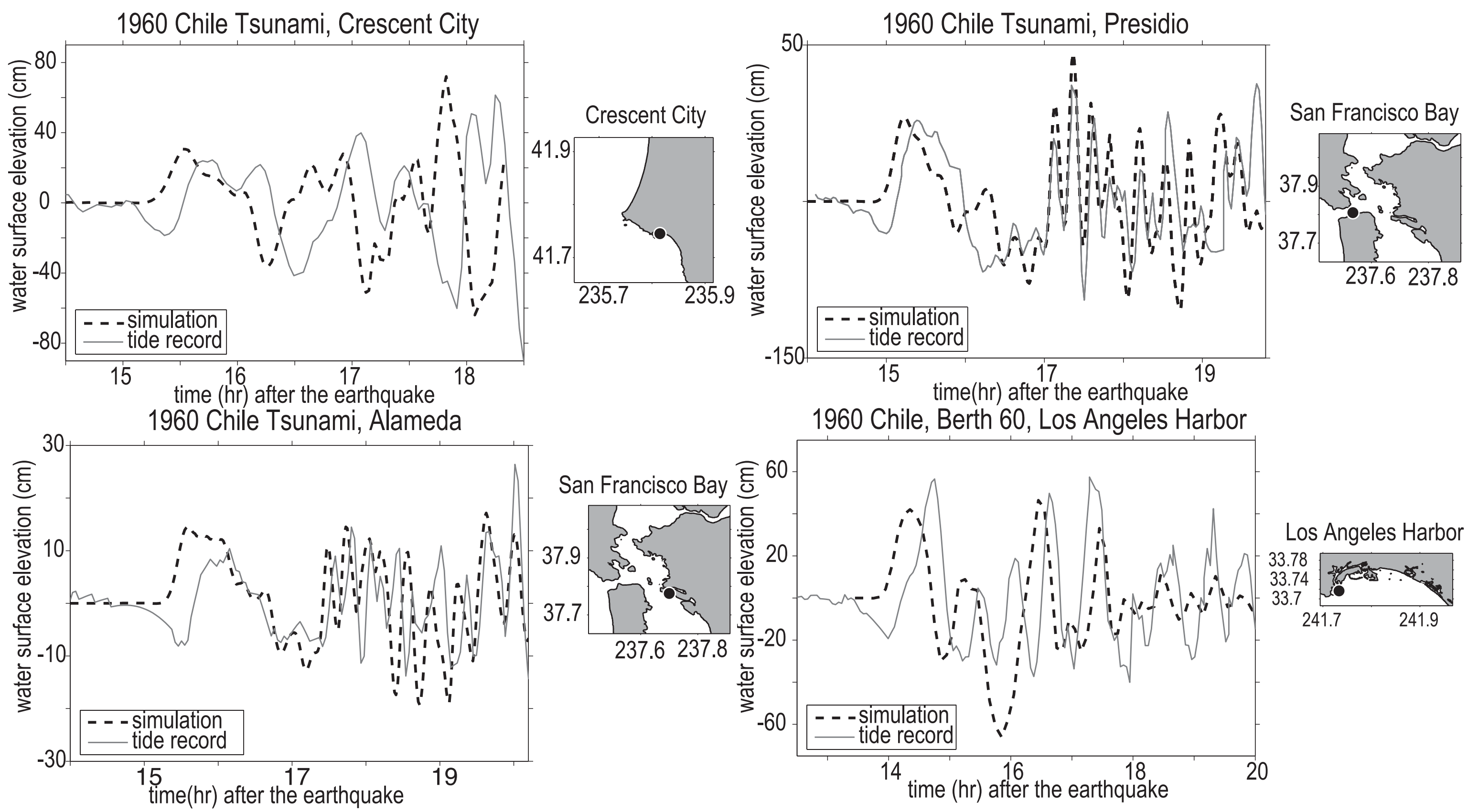

Figure 2.8: Modeled compared to recorded time series of water surface elevations at various locations along the California coast for the 1960 Chilean tsunami.

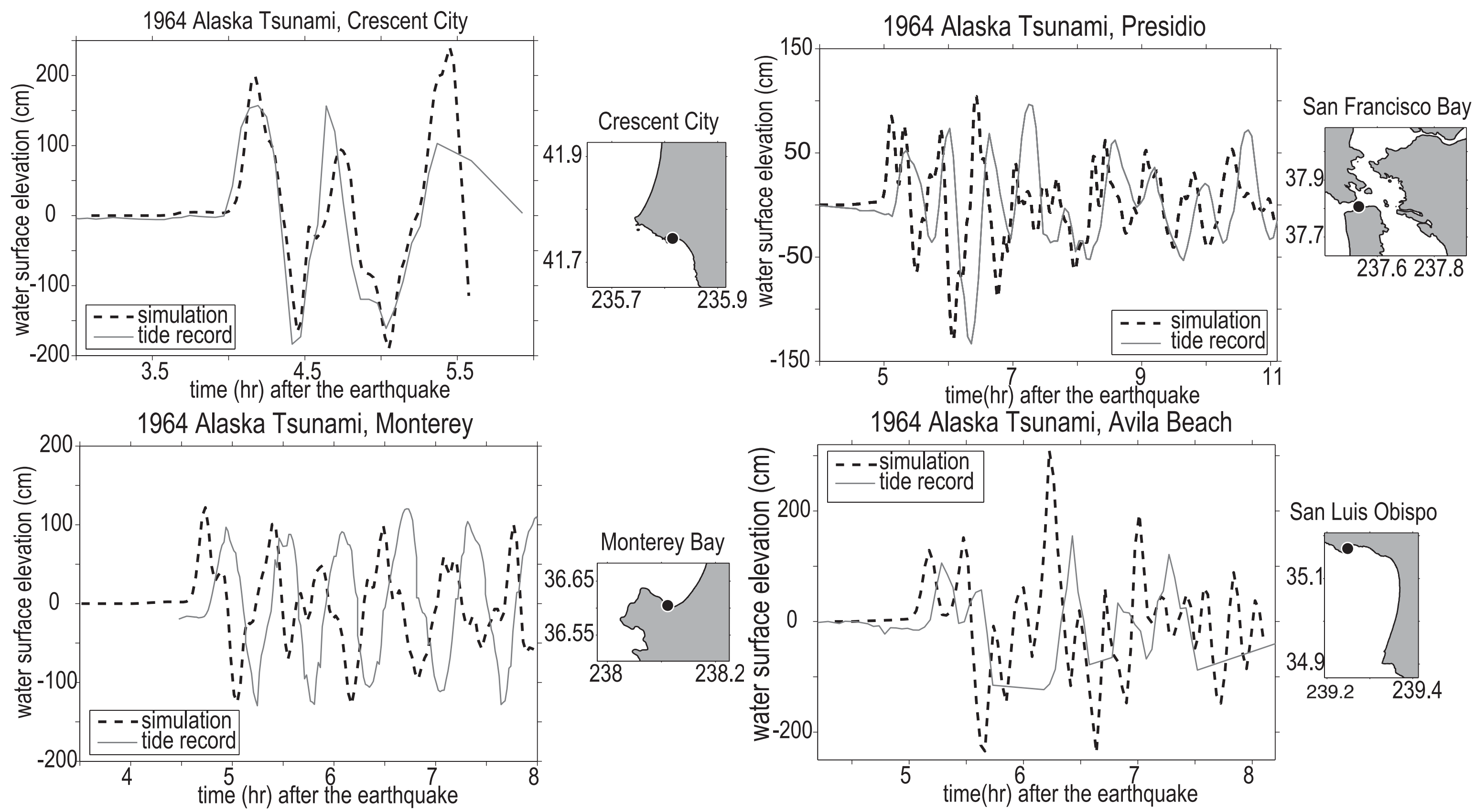

Figure 2.9: Modeled compared to recorded time series of water surface elevation at various locations along the California coast for the 1964 Alskan tsunami.

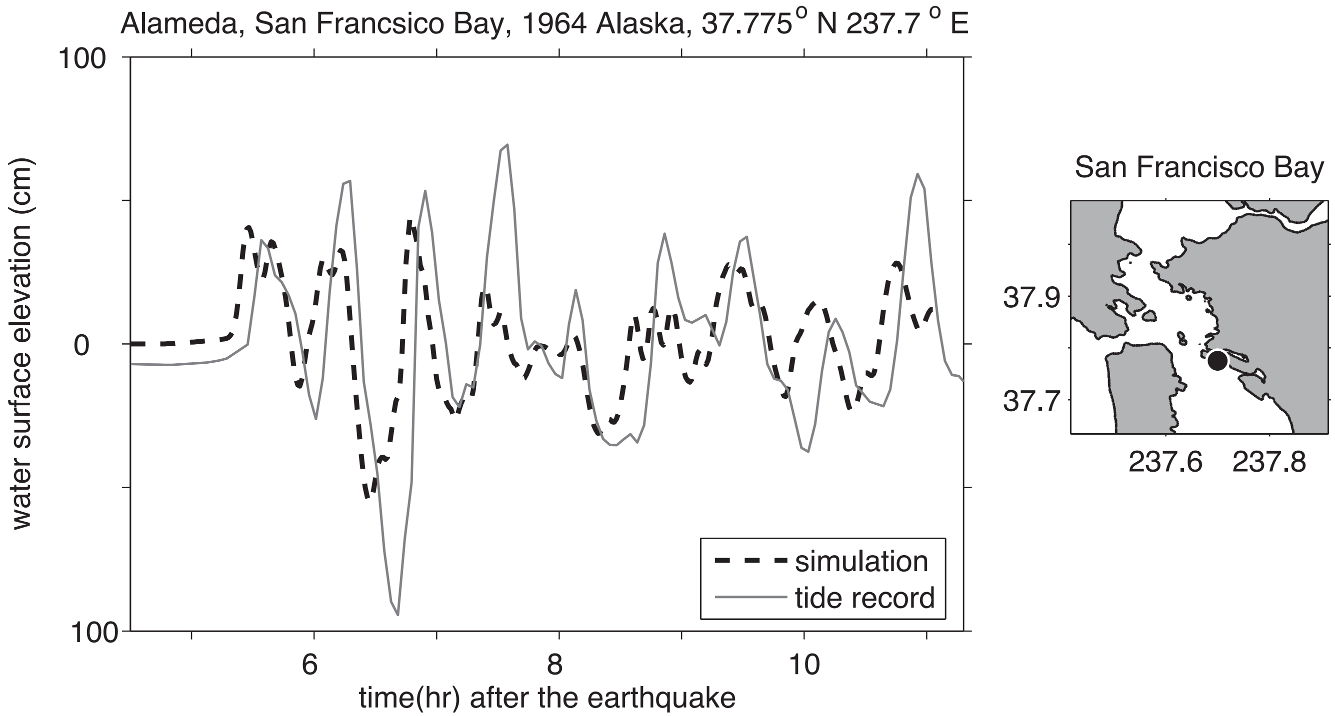

Figure 2.10: Modeled compared to recorded time series of water surface elevations at Alameda for the 1964 Alaskan tsunami.

Figure 2.11 shows the response in San Francisco Bay to tsunamis triggered from different segments of the subduction zones around the Pacific Rim that may produce damaging teletsunamis. In the figure, the maximum waveheight is shown for each location and origin segment, Figure 2.11b shows the maximum drawdown . Note that during oil transfer operations, the drawdown is as important as the local maximum waveheight. Tankers and cargo ships have a large buoyancy and are moored very tightly to limit oscillations from wind waves and passing ships during transfer operations. Even tsunamis with a $1m$ main phase amplitude have caused large vessels to break their moorings and drift dramatically within harbors, upon arrival of shorter–periods waves delayed by, but capable of setting the harbor basin in resonance.

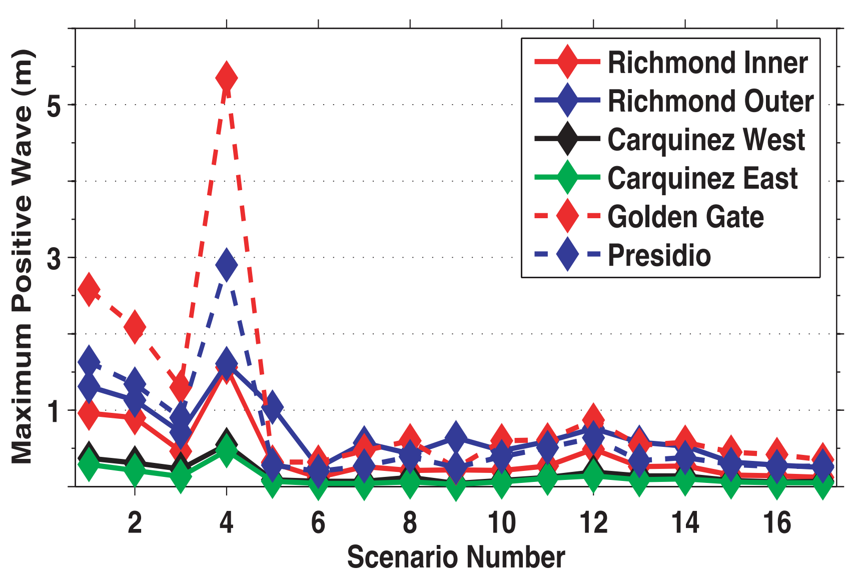

Scenario	No
Alaska 1964	1
Aleutians I	2
Aleutians II	3
Aleutians III	4
Kuril Islands I	5
Kuril Islands II	6
Kuril Islands III	7
Kuril Islands IV	8
Japan I	9
Japan II	10
Chile 1960	11
Chile North	12
Cascadia I	13
Cascadia II	14
Cascadia SN	15
Cascadia SW	16
Cascadia SP2	17

(a)

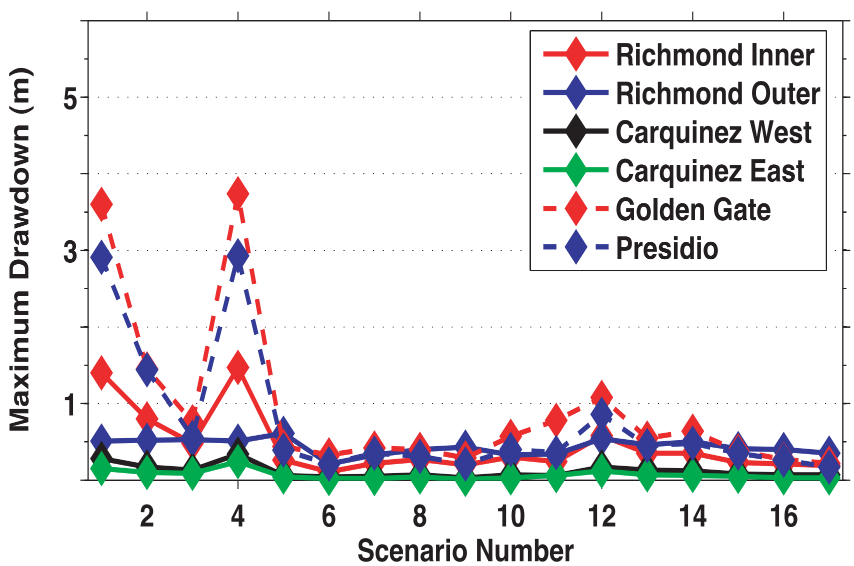

Scenario	No
Alaska 1964	1
Aleutians I	2
Aleutians II	3
Aleutians III	4
Kuril Islands I	5
Kuril Islands II	6
Kuril Islands III	7
Kuril Islands IV	8
Japan I	9
Japan II	10
Chile 1960	11
Chile North	12
Cascadia I	13
Cascadia II	14
Cascadia SN	15
Cascadia SW	16
Cascadia SP2	17

(b)

Figure 2.11: Maximum positive (upper panel) and negative (lower panel) waveheight for each scenario at specific locations within San Francisco Bay from 17 farfield scenarios numbered on the table on side and explained on Tables 2.1 and 2.3 for detailed information on source parameters. Note that the only sources from the AASZ appear to produce positive or negative waveheights in excess of $1m$ at inner Richmond.

2.4 Sensitivity of Local Tsunami Amplitudes to the Source Regions Around The Pacific

Using the FACTS database (see Chapter 1), the effect of the location of the tsunami source region on the waveheight was investigated for several locations along the California coast. This was done by comparing the maximum computed waveheight at locations of interest along the coast arising from tsunamis from each of the unit sources in the FACTS database. Recall that each unit source depicted in Figure 2.2 has a dimension of $100 \times 50km$. Two parallel segments are used to make a unit source of $100 \times 100km$ with a coseismic slip of $1.0m$ on each segment. This corresponds to an initial seafloor displacement of approximately $35cm$, at the source.

Figure 2.12 compares the relative effects of tsunamis originating from the Alaska Aleutian Subduction Zone (AASZ) to events originating from the South American Subduction Zone (SASZ) for four locations. At Crescent City and San Francisco, the response from the AASZ sources is greatest for the part of the subduction zone west of segment 14 (see Figure 2.2 for segment numbering along each subduction zone). San Francisco, in particular, shows an elevated response for segments 15 through 22. At Crescent City, the response steadily increases as the earthquake source region "moves." There is a noted increase in the response for segments 19–22, for Crescent City. The maximum response for Crescent City from ASSZ is triggered of tsunami originating at the segments 23–29, as shown in Figure 2.14

Inspection of the response curves for SASZ sources shows that southern California features an elevated response relative to northern and central California. Los Angeles and San Diego see the largest response from segments 25 to 35 of the SASZ. In fact, at

Los Angeles, the largest response of all scenarios examined was from sources in central Chile. San Diego has a roughly equal response for sources in the AASZ or the SASZ.

Figure 2.13 shows the resulting maximum waveheight at locations offshore California ports. By comparing the response curves, one infers that north Pacific subduction zone sources have a stronger effect than southern sources, for locations north of Pt. Conception. However, south of Pt. Conception South Pacific sources can be equally responsive depending on the port.

2.4.1 A Worst Case Scenario for Ports and Harbors in California

Based on the response curve shown in Figures 2.12 and 2.13, one observes that one version of a worst case, farfield scenario for locations north of Point Conception could be a rupture along the central and western segments of the AASZ (roughly from segments 15 to 22 for San Francisco and segments 23 to 29 for Crescent City, Figure 2.2). Scenario "AASZ III" (Table 2.1) was constructed as another worst case scenario. Figure 2.15 shows the waveheight distribution from this scenario across the Gulf of Alaska and the north east Pacific. Source directivity is apparent by the long tongue of elevated waveheights projecting to the south east from the Aleutians. This tongue is sometimes referred to as "a finger of god," since it is pointing to the location of maximum impact. Figure 2.16 compares computed results from the Aleutian III scenario to both tide gauge recordings and model results from the 1964 Alaskan tsunami at Crescent City and the Presidio tide gauge, at the entrance to San Francisco Bay.

Figure 2.16 shows that waveheights from such an event would be larger at both Crescent City and San Francisco than the effects observed during the 1964 Alaska tsunami.

Modeled waveheights are two to five times greater than observed in 1964. Such an event would have devastating consequences statewide.

Detailed Modeling Inside Ports and Harbors

Detailed inundation modeling for each region specified in Figure 1.9 was carried out for each of the scenarios listed in Tables 2.1 and 2.3. Figures 2.17 and 2.18 compare the modeling results for the 1960 and 1964 tsunamis in Los Angeles Harbor and San Francisco Bay. Differences can be seen both in waveheights and in areas prone to amplification or focusing.

The modeling clearly shows the qualitative difference between north Pacific source and south Pacific sources as far as impact for locations in California is that the terminal effects concentrate above or below Point Conception. Figure 2.17 illustrates how a South American source produces larger sea level fluctuations in Los Angeles than does a tsunami generated in Alaska. The opposite is evident for San Francisco, where the 1964 Alaska tsunami was more severe in its effects than the 1960 Chilean event.

Results from farfield scenarios have been compiled for each of the port areas into a database accessible through a common web browser (FACTS). Information such as waveheight, current speed and inundation areas can be extracted for further analysis. This easily expandable data framework can be the basis for deterministic or probabilistic tsunami hazard studies or used to produce inundation maps for emergency and evacuation planning. Scenario specific results can be used in real time by emergency operators in the event of an real tsunami warning.

The numerical results generated in this and other modeling exercises have been archived and are available for comparison and use in other studies. Data from the USC-FACTS system were used to initialize the numerical modeling for the Ports of

POINT ID	Description	Longitude	Latitude
1	BP WEST Coast Products, Richmond	237.6342	37.9133
3	Chevron USA, Inc., Richmond	237.5892	37.9225
5 and 12	Kinder Morgan and Conocophilips, Richmond	237.6350	37.9167
6 and 11	IMTT and Shore Terminals, LLC , Richmond	237.6317	37.9208
7	Shell Oil Products, US, Martinez	237.8758	38.0325
9	Pacific Atlantic Terminals, Martinez	237.8983	38.0467
13	Conocophillips, Rodeo Refinery	237.7417	38.0542
14	Tesoro, Inc. - Avon Warf	237.9092	38.0492
15	Tesoro, Inc. - Amorco Warf	237.8775	38.0350
16	Valero Refining, Berth 1, Benica,	237.8817	38.0367
17	Valero Refining, Berth 2, Benica	237.8600	38.0417
18	Mirant Potrero LLC, San Francisco, CA	237.6317	37.7517
19	Golden Gate, entrance to San Francisco Bay	237.5200	37.8067
20	Presidio	237.4167	37.8067

Table 2.5: Locations in geophysical coordinates of existing oil terminals in San Francisco Bay

Los Angeles and Long Beach as described by Dykstra and Jin (2006). This approach was also the basis for a comprehensive study on tsunami effects at marine oil transfer terminals (MOTs) in San Francisco Bay (Borrero et al., 2006a).

2.4.2 Inside San Francisco Bay

The San Francisco Bay area, shown on Figure 2.7, has approximately 6.8 million inhabitants, most of whom live on coastal lands (Working Group on California Earthquake Probabilities, 2003). It is a mostly enclosed body of water with a narrow opening, the Golden Gate, to the North Pacific Ocean. San Francisco Bay is shallow and covers $1000km^2$ of area with an average depth of only $4.2m$ (The Bay Institute, 2006). In the central section of the Bay and near the Golden Gate, there is more bathymetric relief, andthe deepest part of the Bay lies beneath the Golden Gate, reaching up to $113m$. The shallow bathymetry is a factor in wave dynamics within the Bay, as it attenuates tsunami waves that may reach inside the Bay.

The Bay is fed mainly by the Sacramento and Napa rivers, as well as many other minor streams. San Francisco Bay and its northern arm San Pablo Bay cover some 4100 square kilometers. The Bay is located within the Greater San Andreas transform fault system, part of the boundary between the Pacific and North American tectonic plates. The majority of the slip on this plate boundary is accommodated by the San Andreas Fault, however, part of the relative plate motions are taken up by several other smaller faults. Three earthquakes of likely magnitude 7 or larger and numerous smaller events have occurred in the Bay region in historic times. In 1989, the $M_w = 6.9$ Loma Prieta earthquake caused 63 fatalities and substantial damage in the Bay area including failure of a segment of the Bay Bridge between San Francisco and Oakland (USGS Earthquake Database, 2007).

Oakland and San Francisco have major port facilities and marine oil terminals, described in greater details in Borrero et al. (2006a). There, petroleum products are transferred from ships to refineries on shore. The marine oil terminals are generally located on the north eastern shore of the Bay, near the cities of Oakland, Richmond and Vallejo. The locations of known oil terminals inside San Francisco Bay are listed in table 2.5 and also shown in Figure 2.19. The figure shows the Presidio tide gage and selected points of interest in the subsequent text. For better visualization the geography of the Carquinez Straight and Richmond Bay are extracted to a larger size map, and oil terminals in these regions are shown inside this larger map. Note that eighteen existing oil terminals inside SF Bay did not exist in 1964, when the last tsunami hit the Bay. It is thus of interest to study the possible impact of future tsunamis in those locations inside the Bay.

scenario	M_w	Golden Gate (m)	Presidio (m)	Outer Richmond (m)	Inner Richmond (m)	Carquinez Straight (m)
Alaska 1964	9.26	2.58	1.63	0.96	1.31	0.4
Aleutian I	8.78	2.09	1.34	0.9	1.13	0.3
Aleutian II	8.78	1.3	0.9	0.46	0.68	0.2
Aleutian III	9.15	5.35	2.9	1.56	1.59	0.5
Kuril I	8.95	0.32	0.28	0.31	0.62	0.1
Kuril II	8.72	0.2	0.32	0.12	0.24	0.1
Kuril III	8.72	0.47	0.27	0.26	0.56	0.1
Kuril IV	8.72	0.6	0.39	0.21	0.36	0.1
Japan I	8.75	0.24	0.25	0.22	0.49	$< .1$
Japan II	8.72	0.6	0.39	0.21	0.43	0.1
Chile 1960	9.26	0.61	0.39	0.21	0.43	0.1
Chile 1960W	9.43	1.34	0.78	0.42	0.83	0.2
Chile North	9.35	0.87	0.64	0.49	0.73	0.2
Cascadia I	8.84	0.54	0.34	0.26	0.55	0.1
Cascadia II	8.95	0.58	0.38	0.27	0.49	0.1
Cascadia III	9.17	1.39	1.39	0.67	0.87	0.2
Cascadia SN	8.4	0.45	0.29	0.15	0.28	0.1
Cascadia SW	8.5	0.42	0.26	0.14	0.24	0.1
Cascadia SP2	8.5	0.35	0.27	0.12	0.23	0.1
Hayward-Rodgers Creek	6.61	0	0.01	0	0.02	$< .1$
San Gregorio	7.1	0.6	0.4	0.26	0.42	0.1
Farallons	landslide	0.74	0.15	0.08	0.21	$< .1$

Table 2.6: Results of tsunami wave heights at five different locations, triggered from the scenario events on the left column. Locations are shown in Figure 2.19 and geophysical coordinates of are listed in Table 2.5

Results for San Francisco Bay and Discussion

A summary of peak water heights from twenty tsunami scenarios at five locations inside the Bay are given on Table 2.6. The largest amplitude waves are generated by the Aleutian III scenario followed by Alaska 1964. Cascadia III produces a 1.4 m peak wave at the Presidio, larger than any historic event except the 1964 tsunami. Cascadia III could cause some damage to boats and floating structures inside the Bay, especially if coincident with high tide, but the impacts should be less than in 1964. A Cascadia tsunami will cause major damage along the northern California, Oregon and Washington coasts but, the San Francisco Bay area is favorably oriented parallel to the strike of the fault zone, and therefore outside of the lobe of directivity of Cascadia originating tsunamis. These conclusions are supported by field observations from the Indian Ocean tsunami that show wave amplitudes decaying quickly south of Meulaboh (Jaffe et al., 2006), i.e., in coastal areas with a similar orientation as San Francisco relative to Cascadia (see also Okal et al., 2006b).

The modeling suggests that the three local sources produce very small waves inside the Bay. The Hayward–Rodgers Creek stepover produces a peak height of $0.2m$ in the Carquinez Strait and in the Inner Richmond Waterway, values larger than the $0.1m$ estimates of Parsons et al. (2003), but still significantly less than $0.6m$ estimated from eye–witness accounts during the 1898 Mare Island Earthquake. The $M_w = 7.1$ San Gregorio earthquake produces tsunamis with slightly larger waves at Inner Richmond ($0.4m$), but still much less than the larger teletsunami events. The Farallon landslide produces a negligible wave. Note that at the entrance to the Bay, the San Gregorio and Farallon landslide scenarios produce localized water heights comparable to tsunamis from the South American and northeastern Pacific subduction zones, but that's the volume of water displaced by these local scenarios is much smaller and translates into very small tsunami heights in the inside the Bay.

Figure 2.20 plots the variation of the peak water height value at the Golden Gate, Outer and Inner Richmond, and Carquinez locations in Table 2.6 versus the amplitude at the Presidio tide gauge site. The amplitudes for each site shows a rough linear relationship to the Presidio values. Presidio water heights average 60% of the water heights at the entrance to the Bay (Golden Gate). The Outer Richmond values are about 56% of the Presidio water heights, very close to the 50% attenuation Magoon (1966) estimated from 1960 and 1964 marigrams between these two locations. At the Carquinez location, water heights are only about 20% of the Presidio values. The Inner Richmond site shows the most scatter in tsunami height estimates, but always larger than Outer Richmond and averaging 70% of the Presidio values. The regression is not as good as at the other sites, suggesting complex amplification within the narrow Richmond Channel.

Effects of Source Region and The Worst–Case Tsunami Scenario for San Francisco Bay

We utilized the discretized fault segment database from FACTS and investigated the effect of the location of the tsunami source region on the wave height at the entrance to San Francisco Bay. This was done by comparing the maximum computed wave height from each of the unit sources in the FACTS database (Figure 2.2).

The computed wave heights are shown in Figure 2.21 plotted as vertical bars above the geographic location of the unit sources in the FACT database. It can be seen that the strongest response in San Francisco Bay arises from the AASZ and CSZ. Segments 14 through 19 (See Figure 2.2) produced a higher result compared to KSZ, CASZ and SASZ. This is an important factor to consider when assessing the relative hazards posed to San Francisco Bay by the different subduction zone sources in the Pacific .

To investigate the sensitivity of the response at terminal locations inside the Bay, the maximum wave height and wave drawdown for each terminal location and each of the tsunami sources (Figure 2.11) were plotted. The corresponding source numbers are on the table in Figure 2.11. It is evident that the strongest response occurring in the Richmond area is from sources in AASZ. The next largest response is caused by the rupture of the entire Cascadia Subduction Zone, producing peak heights and drawdowns close to $1m$. While larger than for South America and the northwestern Pacific sources, this

Region	Farfield		Local	
	wave height (+)	wave height (-)	wave height (+)	wave height (-)
Richmond, outer (3)	0.96	-1.40	0.26	-0.18
Richmond, inner (1,5,6,11,12)	1.74	-1.56	0.49	-0.57
Carquinez, West (13,10)	0.37	-0.31	0.13	-0.21
Carquinez, East (13,10)	0.29	-0.17	0.10	-0.14
Golden Gate (19)	2.59	-3.61	0.60	-0.71
Presidio (20)	1.62	-2.93	0.40	-0.32

Region	Farfield	Local
	current speed (m/s)	current speed (m/s)
Richmond, outer (3)	0.92	0.21
Richmond, inner (1,5,6,11,12)	5.02	2.24
Carquinez, West (13,10)	0.45	0.20
Carquinez, East (13,10)	0.30	0.16
Golden Gate (19)	2.01	0.53
Presidio (20)	2.92	0.48

Table 2.7: The upper table shows the maximum wave height and drawdown at different locales inside SF Bay, for farfield and local earthquake scenarios. The lower table shows the tsunami induced current speeds at the same regions. The numbers in parentheses identify the marine oil terminals in each location listed in Table 2.5.

response suggests that the CSZ probably is not the "dominant player" for tsunami hazards along the central California and southern California coast. While great earthquakes on the CSZ will produce significant and damaging runup in the immediate source area, the modeling shows that most of this energy is radiated offshore towards Hawaii and Japan, while relatively little wave energy is propagated south along the coast. This is also shown in the maximum transpacific wave height plots for the Cascadia subduction zone cases presented in Section 2.5. The smaller ruptures of the CSZ pose very little hazard for San Francisco Bay. The largest South American sources pose less hazard than Cascadia III (which produced the highest response among Cascadia events). A much smaller response appears to be excited by sources in the Kuril Islands and Japan.

The available historical information and modeled historical scenarios for tsunami affecting San Francisco Bay are combined with analysis of the tsunami response from displacements along the various subduction zone segments on the Pacific Rim, to determine the worst case scenario. All of the results suggest that the largest wave will hit San Francisco Bay from a tsunami triggered along the AASZ, when the hypothetical $M_w = 9.2$ earthquake occurs along $700km$ of the fault, in the area of the most sensitive response for San Francisco Bay. The magnitude and the size of the displacement for this case was designed to be similar to that of 1964 Alaskan earthquake and 2004 Sumatra earthquakes.

Figure 2.22 shows the comparison between the "designed" $M_w = 9.2$ AASZ III event and the 1964 tide gauge records at the Presidio and Alameda tide gauge stations. The worst case scenario produces two to three times larger wave heights than does the 1964 event. This AASZ III scenario produces larger waveheights at the station compared with all modeled scenarios. It also features the highest tsunami current speeds at Outer Richmond, East of Carquinez, Golden Gate and Presidio.

Table 2.7 lists the maximum modeled values for positive and negative water surface level at 6 regions inside San Francisco Bay. The computed maximum values are in the range of values that Magoon's (1966) amplitude attenuation suggests. The maximum wave heights at the Carquinez Strait are on the order of 25% of the values at Richmond and 10% of those modeled for the Golden Gate. Similarly, the attenuation of the outer Richmond area is of the order of 53% of the Presidio value, whereas in the inner Richmond area, it is only 30%.

Discussion and Conclusions for Tsunami Impact in San Francisco Bay

Among all scenarios for tsunamis affecting the SF Bay, AASZ produces the highest impact. Inspection of computed wave height distributions over time for the scenario AASZ III shows that higher wave heights enter San Francisco Bay through the Golden Gate compared to what was observed in 1964 and propagate directly across the Bay into the Richmond, Berkeley and Oakland areas. All of the synthetic marigrams exhibit the long–duration of wave activity that also characterizes the historic records from past teletsunami events. The long duration compared to the event time may be indication of resonant oscillation in the waterway.

The study also suggests that nearfield tsunami sources may present a lesser tsunami hazard for marine facilities inside San Francisco Bay than would be otherwise anticipated on the basis of earlier work. The modeled wave heights and velocities for the largest nearfield event (e.g. San Gregorio) are 25% or less of the largest farfield event (e.g. AASZ III), see Tables 2.7. It must be stressed that only one submarine landslide source has been included in the tsunami scenarios for the Bay, located in the Farallon Islands $50km$ offshore and the mouth of the Bay. The bathymetry of San Francisco Bay is generally shallow with very gentle slopes, with no known history of massive slides into the Bay. Submarine landslides within the Bay thus do not appear a primary source for tsunami wave generation.

The most significant historic event was the March 28, 1964 tsunami generated by the $M_w 9.2 =$ Alaska earthquake. Of the twenty one modeled scenarios, the event with the largest water heights and greatest water velocities within the Bay was a $M_w = 9.2$ earthquake on the Alaska Peninsula segment of the Alaska-Aleutian subduction zone referred to here as scenario AASZ III. This event as simulated generated peak water heights at the entrance to the Bay of over $5m$.

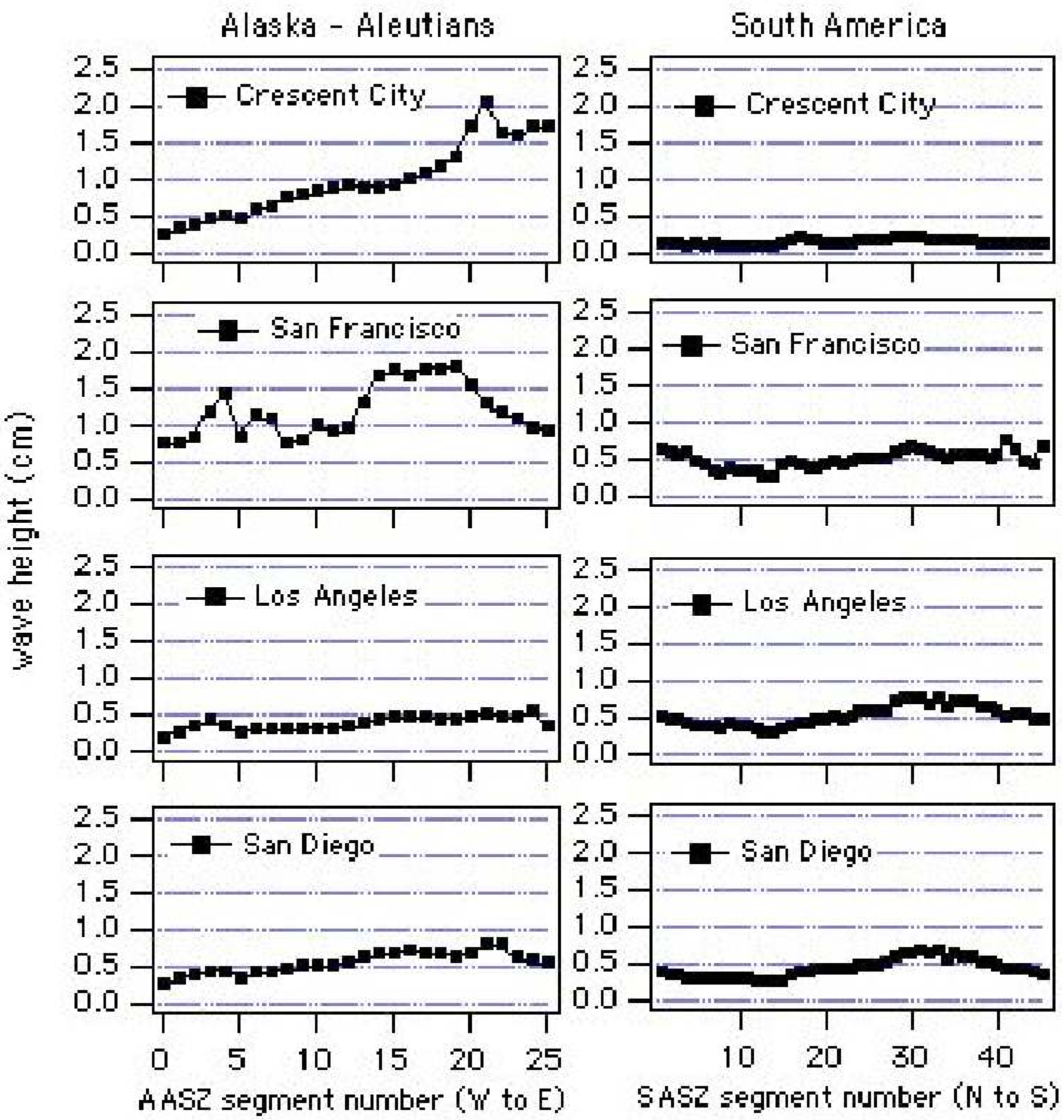

Figure 2.12: Comparing waveheight response at four locations offshore California ports for unit sources along the AASZ and SASZ.

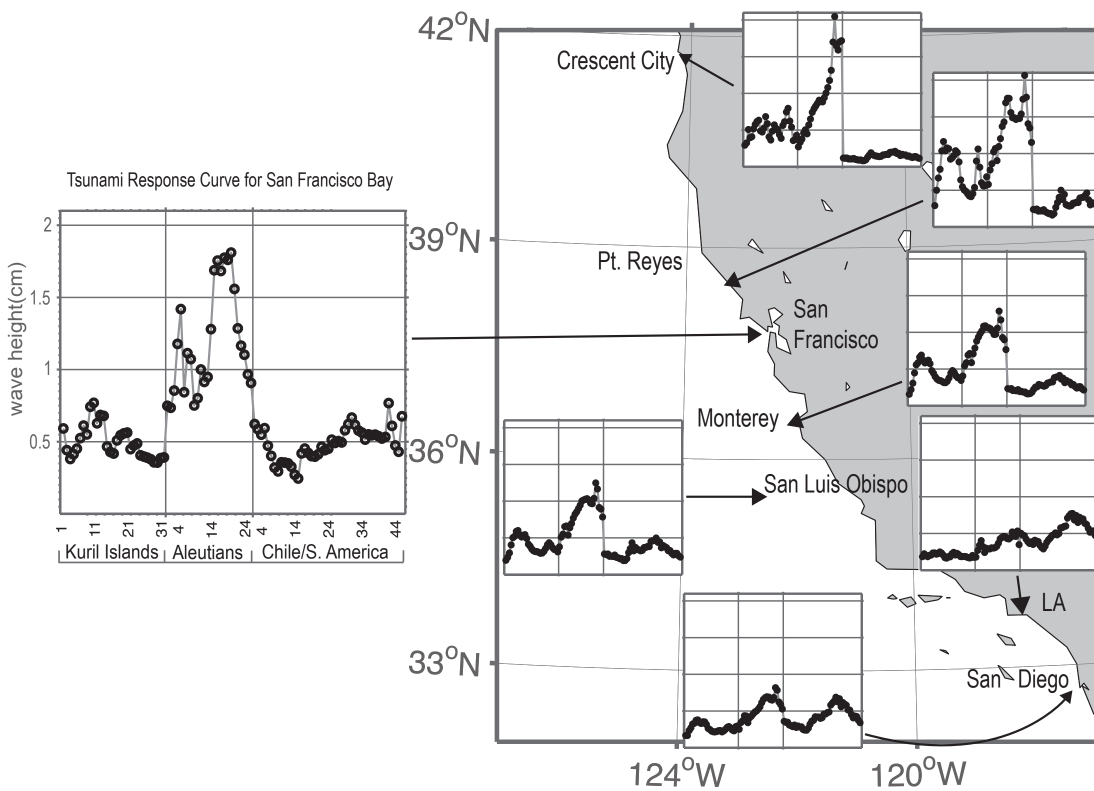

Figure 2.13: Offshore response at various locations along the California coast for tsunamis generated by individual fault segments depicted in Figure 2.2. All responses are plotted with the same scale as in San Francisco.

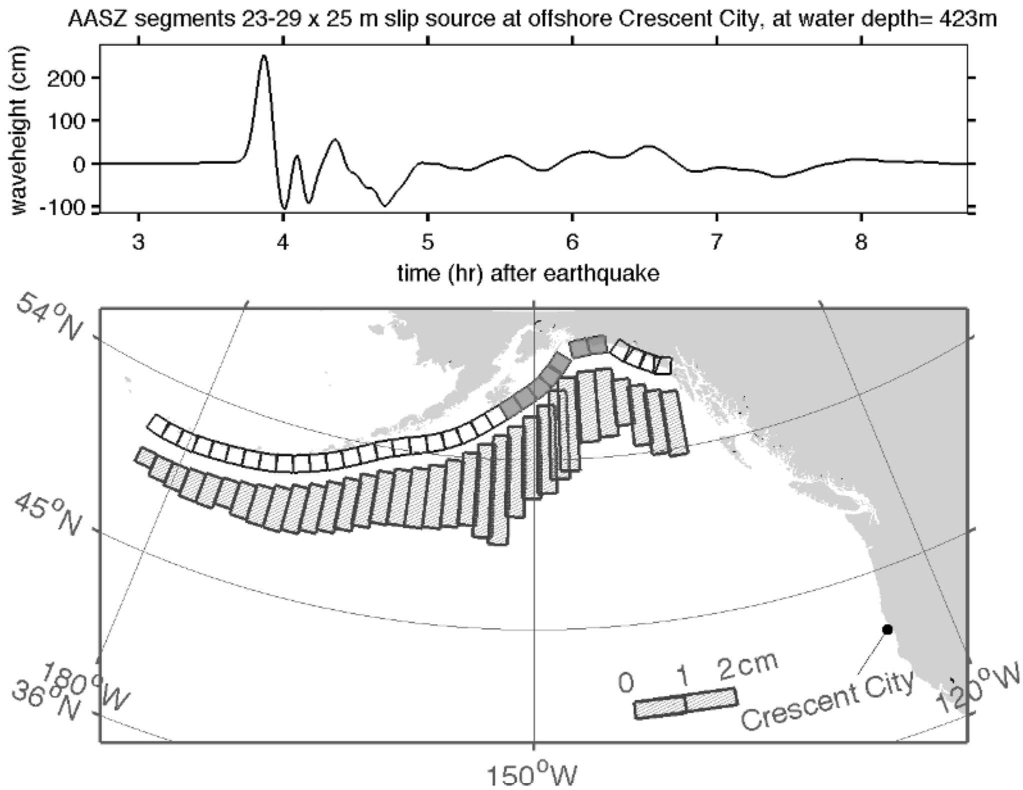

(a)

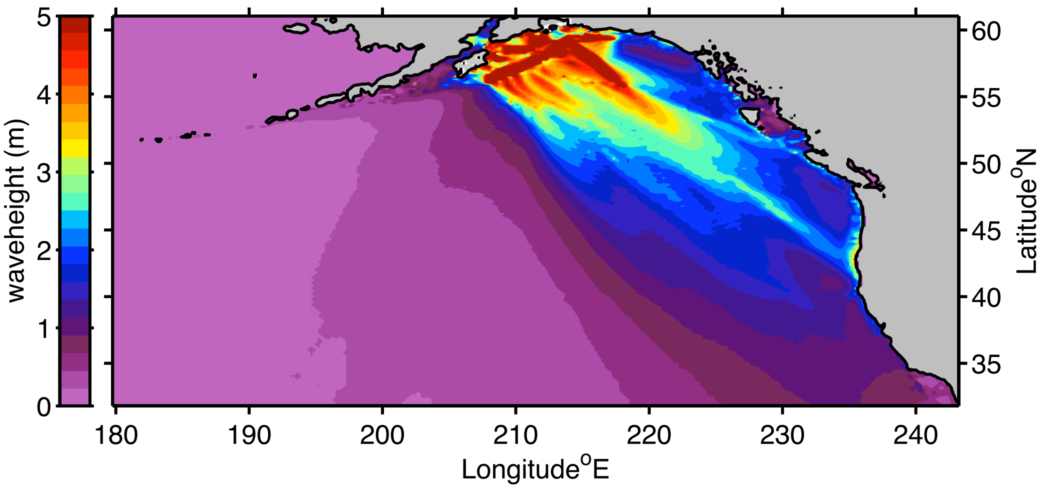

(b)

Figure 2.14: (a) $700km \times 100km$ scenario with 25 m slip on AASZ on segments 23–29 results in the highest tide gauge reading offshore Crescent city. (b) Maximum wave-height distribution from this scenario is shown.

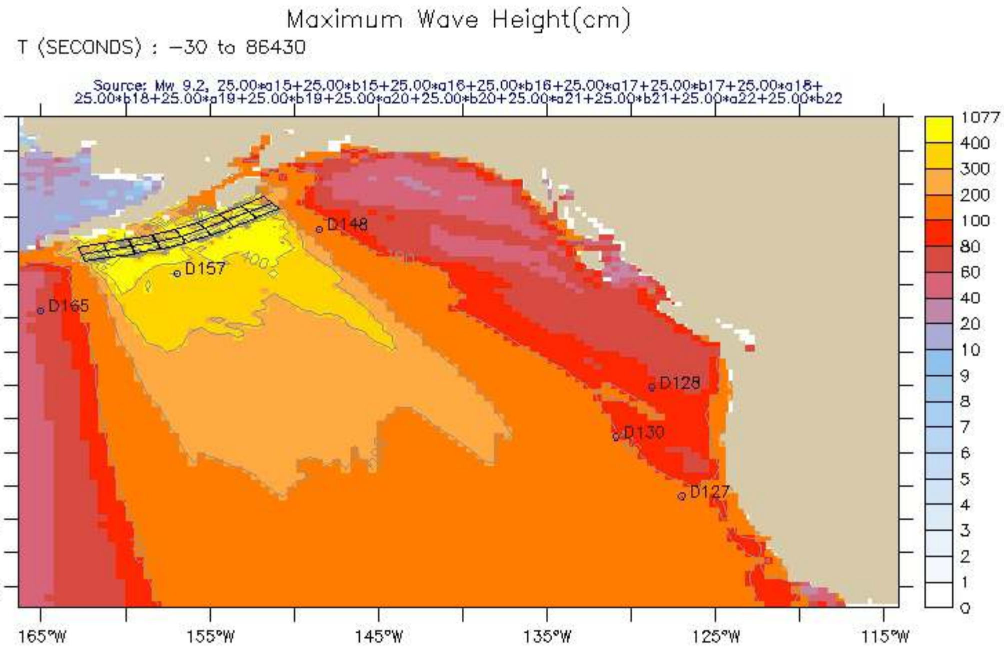

Figure 2.15: Distribution of waveheights across the Gulf of Alaska to California for a hypothetical Mw = 9.2 earthquake in the Aleutians Islands.

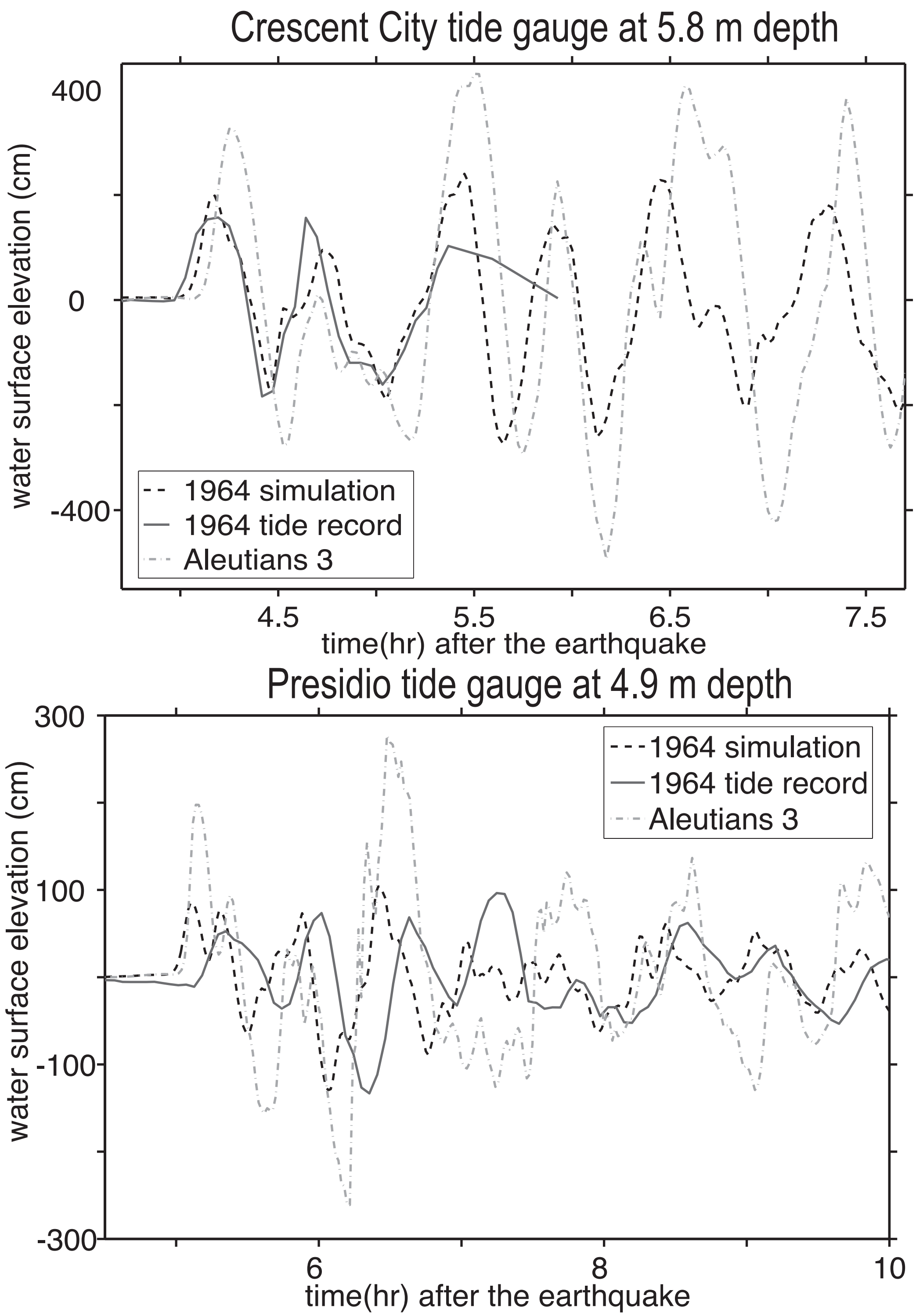

Figure 2.16: Comparison of modeled results from a hypothetical Mw = 9.2 AASZ III earthquake compared to tide gauge recordings and model results for the 1964 Alaskan tsunami at Crescent City and at Presidio San Francisco Bay .

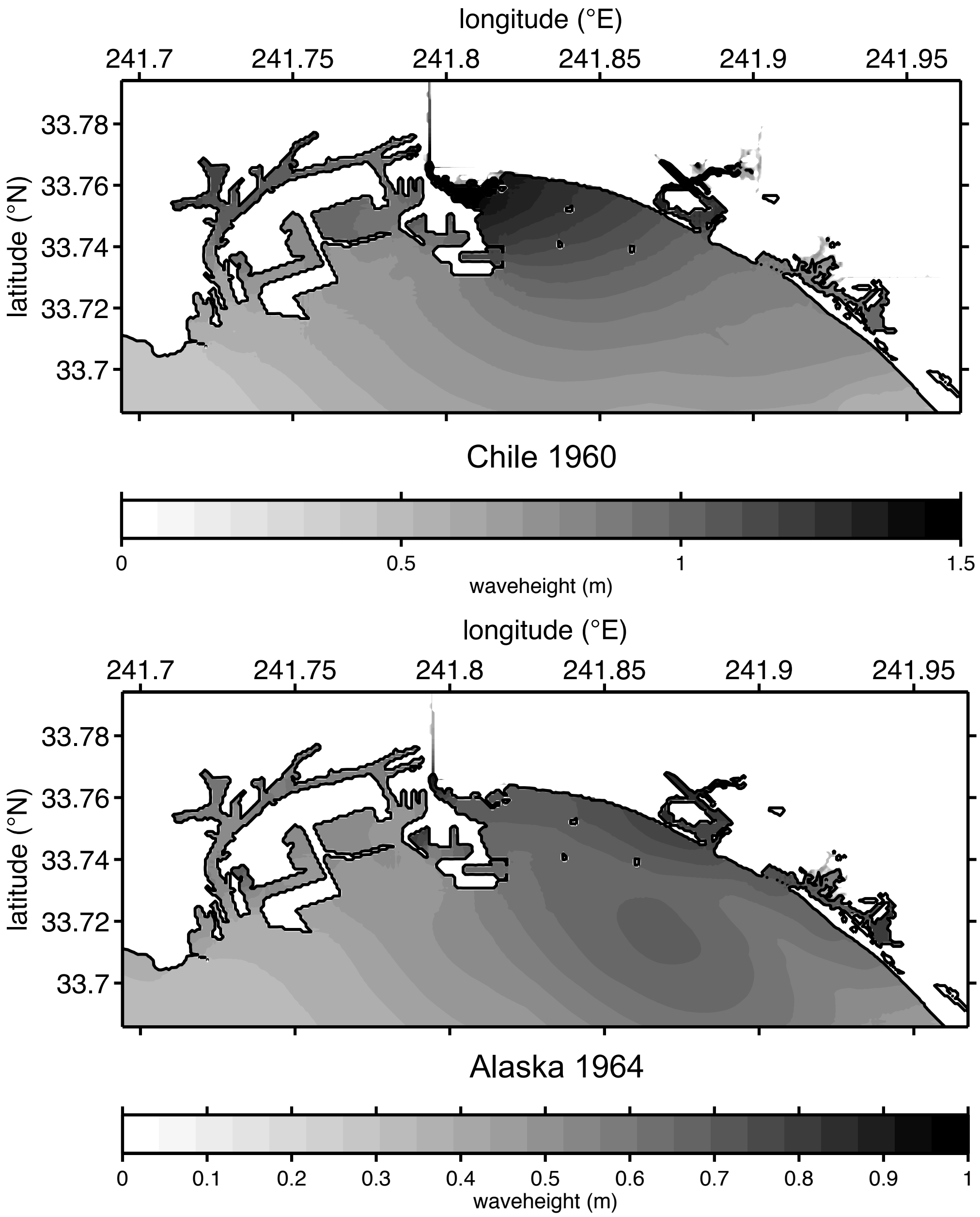

Figure 2.17: Comparison of modeled maximum waveheight for the 1960 Chilean (upper panel) and 1964 Alaskan (lower panel) tsunamis in the ports of Los Angeles and Long Beach. Note the differences in waveheight and locations of wave focusing for each scenario.

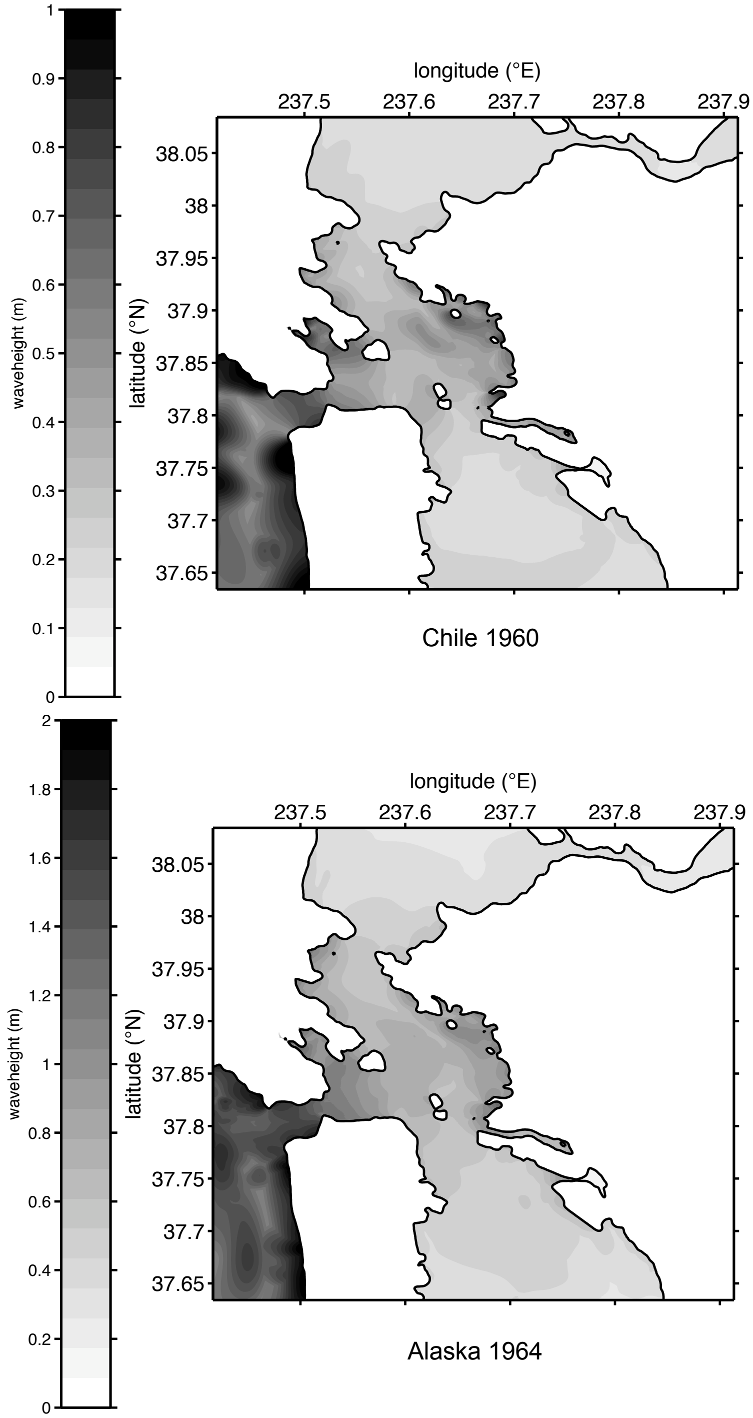

Figure 2.18: Comparison of modeled maximum waveheight for the 1960 (upper panel) and 1964 (lower panel) tsunamis in San Francisco Bay. Note the difference in the waveheight from the Scale bars on the left.

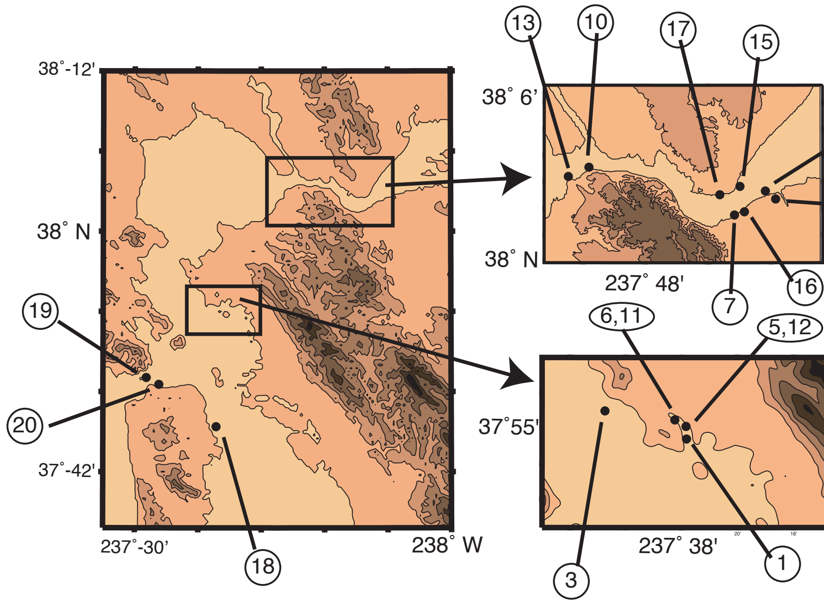

Figure 2.19: Marine oil terminals location shown inside the San Francisco Bay.

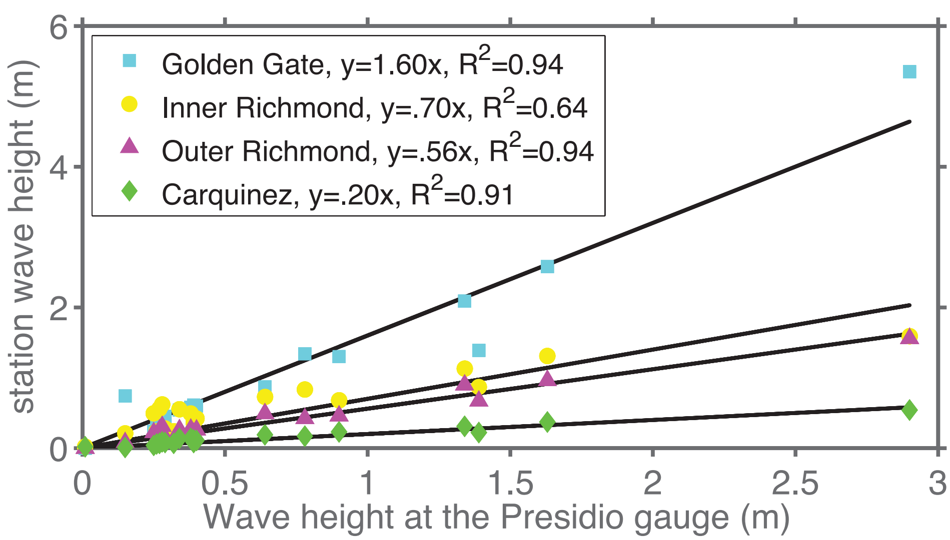

Figure 2.20: Comparison of peak water heights to Presidio tide gauge site for the locations listed in Table 2.6. Linear trends for each data set given with coefficient of determination (R^2).

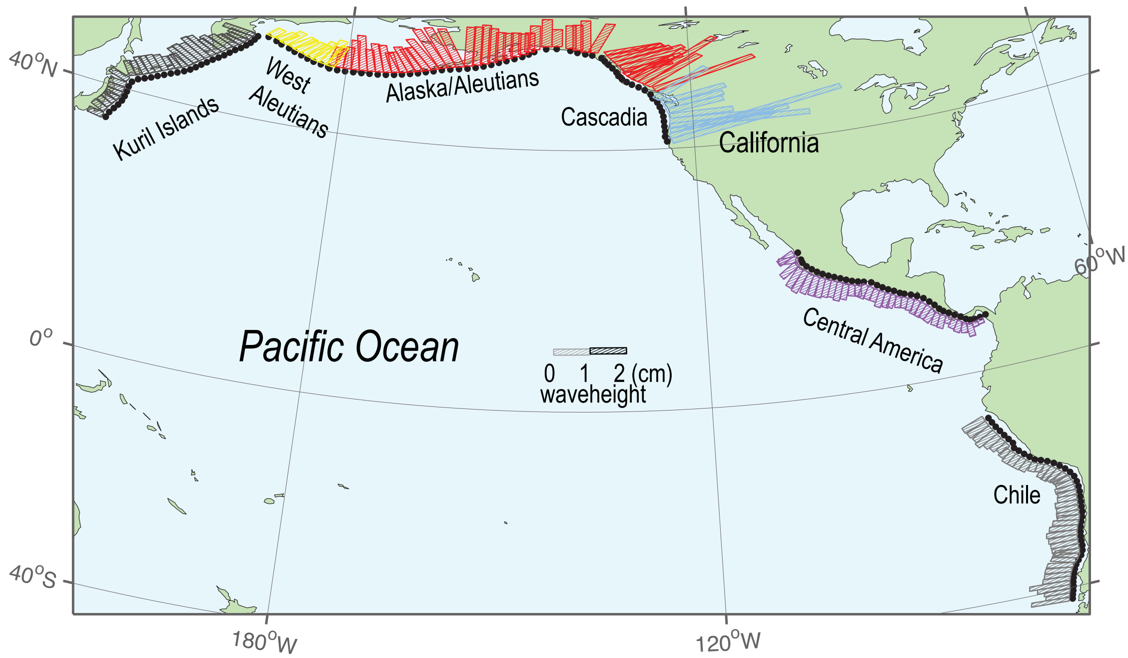

Figure 2.21: Computed tsunami wave height at $37.7° N$, $122.67° W$ (offshore of the entrance to San Francisco Bay) from individual unit ($1m$) slip sources along three different subduction zones.

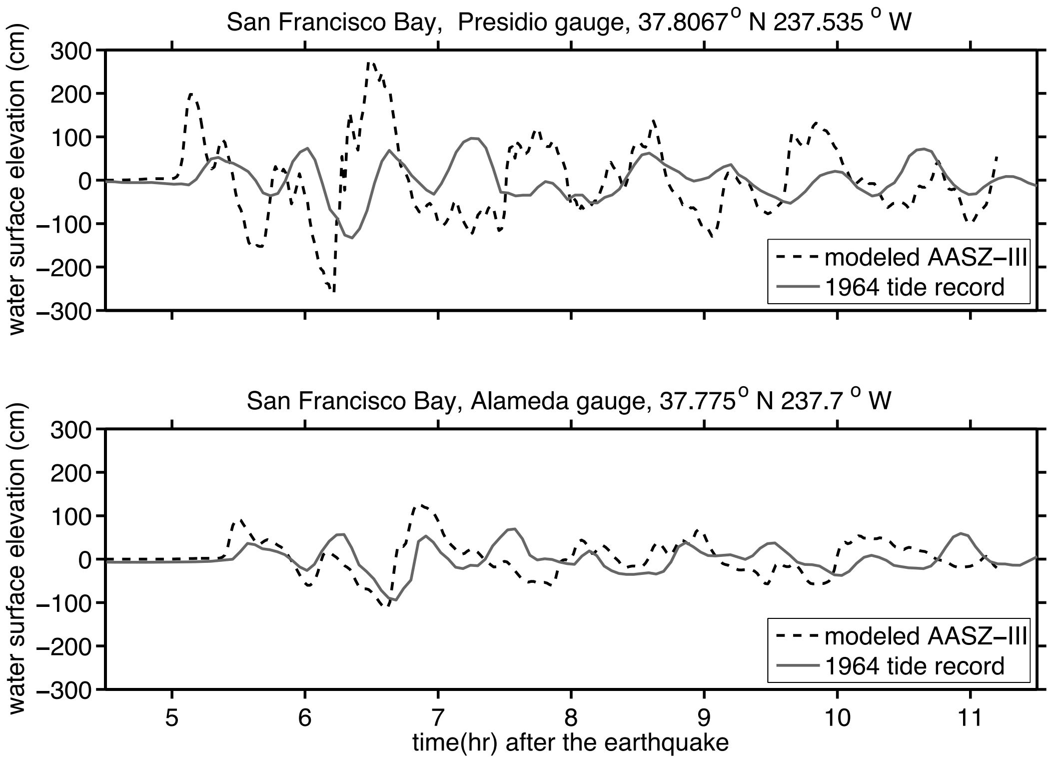

Figure 2.22: Comparison between the tide gauge record from 1964 Alaskan tsunami and a simulated $M_w = 9.2$ earthquake tsunami at Presidio and Alameda.

2.5 Modeling the Kuril Islands Events of 2006 and 2007

The KSZ has been discretized by thirty one double fault segments as shown in Figure 2.23. Every segment pair corresponds to a $100km \times 50km \times 2$, earthquake with unit seismic slip of $1m$. The initial waves from these equal sized events are propagated through the Pacific and the resulting response at the Crescent City Harbor is computed for each segment. The 2006 event corresponds to rupture of segments 12 and 13, the 2007 event, being an outer–rise normal–faulting source, lies east of the segments shown, and thus was modeled separately (In the figure only its approximate location is shown). As for the 1994 event, it represents a more complex case, since it involves a tear in the down–going slab, and consequently is not part of the FACTS database. Nevertheless, it was modeled as a combination of ruptures of segments 18 and 19; this may be an appropriate model for large scale interplate earthquakes similar to the large 1963 event to the NE and recently documented in the paleo–seismic record by Nanayama et al. (2005). This scenario is referred to here as the pseudo–1994 event.

The computed results shown in Figure 2.23 suggest that the maximum response at Crescent City emanates from earthquakes in segments 25 and 26, off the Sanriku coast of Japan in the vicinity of Miyako, with a secondary maximum for segments 13 and 14 in the immediate vicinity of the 2006 source. Thus the 2006 event may not have been the worst case scenario among for Crescent City among $M_w = 8.3$ events along the Japan–Kuril trench. On the other hand, sources from central Kamchatka (segments 1 and 2) are seen to be the least affective. The damage during the 1952 earthquake (boats sunk in Crescent City, Lander et al., 1993) probably resulted from its extreme size with the rupture extending all the way south to segment 8.

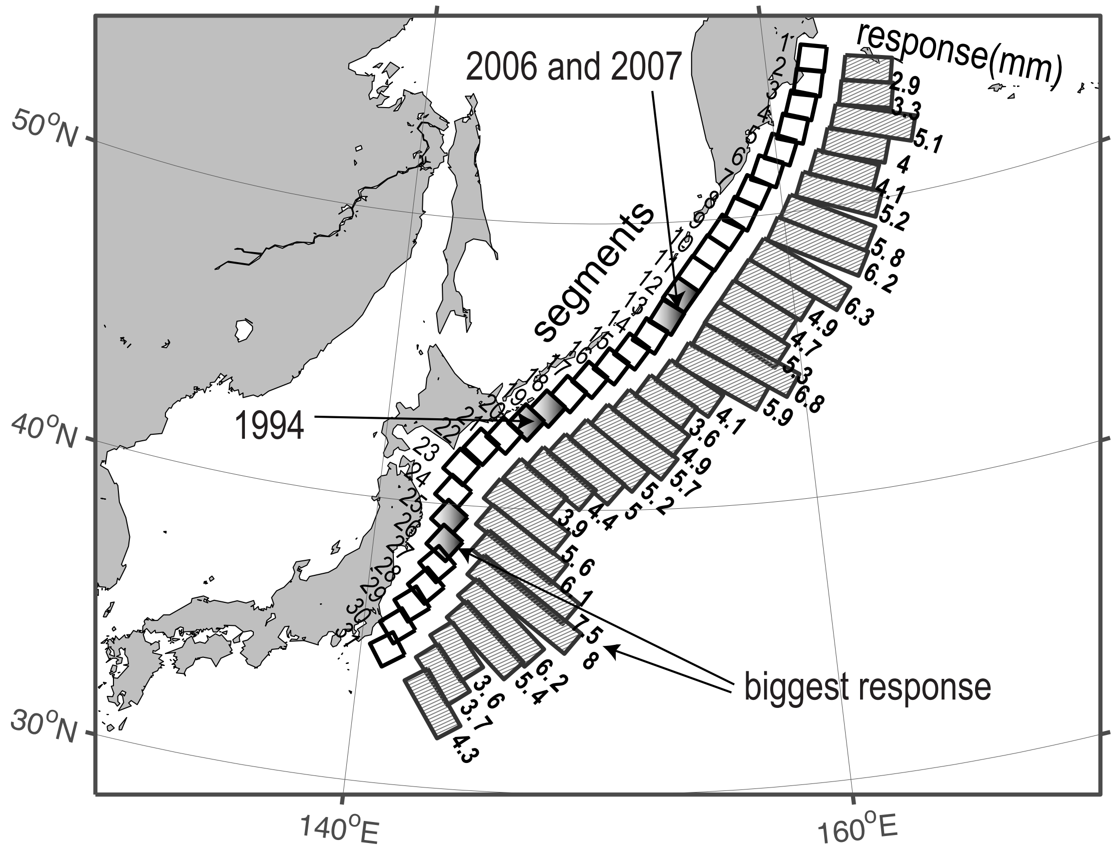

Figure 2.23: Response tsunami amplitudes offshore Crescent City from unit size thrust fault earthquakes from Kuril–Kamchatka–Japan Subduction Zone.

Simulations were propagated through the Pacific Ocean to understand the difference in response at Crescent City and in particular the effect of directivity. For this purpose four scnearios were used, namely the 2006, 2007, pseudo–1994 events with an additional source centered at segments 25 and 26 off the coast of Japan. Figure 2.24 shows the maximum waveheight distribution for all cases. For the 2006 source (subfigure b), waves are seen to be oriented southeastwards with a finger directed towards northern California, suggesting a particularly large amplitude at Crescent City. By contrast, the

2007 (subfigure c) event has the most southward directed waves. The pattern for pseudo-1994 (subfigure a) event is oriented at an intermediate azimuth towards Micronesia, but is probably not representative of the true event. The worst case "Japanese" scenario (subfigure d) creates an eastward lobe of amplitudes and produces the largest waveheight off California.

The 2006 Kuril Islands earthquake triggered tsunami alert bulletins. However, the California coast was never placed in a Warning or Watch, before the alerts were cancelled 3 1/2 hours after the earthquake. Concern over the event anyway, prompted local officials in Crescent City to verbally warn people on adjacent beaches and the harbor, and only two people were in the harbor area when the strongest surges, with peak to trough heights of $1.76m$, arrived more than two hours after the first wave (Kelley et al., 2006). The model used here captures the initial wave arrival, the wave periods and the maximum waveheight, but not the precise time history. Higher resolution is needed to model the complex harbor resonance effects at the shorter periods generated by this smaller event (see also Section 1.2.1).

2.5.1 Discussion and Conclusion of Kuril Island Tsunamis

To examine the hazard in Crescent City from earthquakes in the KSZ, computations were presented with tsunamis from KSZ sources initially propagated in a $4 - arcmin$ resolution bathymetry over the Pacific and then passed through nested grids to increase resolution, until Crescent City harbor. Figure 2.25 compares the modeled tsunami records at $1arc$–sec and $3arc$–sec resolution to tide records at Crescent City, and also compares the 1994, 2006 and hypothetical Japan tsunamis to each other. Figure 2.25, shows a fairly good agreement with the tide records from 1994 and 2006. Initially, the harbor was modeled with $3arc$–sec bathymetry, and good phase and initial waveheight agreement was achieved, yet Figure 2.25a and b show that the model underestimated the size of the wave in the later stages, in this resolution. Note the good agreement for the 1994 event despite the inappropriate geometry used for the source, which expresses the robustness of farfield tsunami generation with respect to fault parameters as discussed; see for example, Okal (1988); Okal and Synolakis (2008).

Higher resolution of $1arc$–sec was then used to help improve the accuracy of the computation for longer time evolution. As expected, the results show better agreement in Figure 2.25a after 10 hours and in Figure 2.25b after 11 hours. This suggests that the use of a higher resolution bathymetry is necessary to model special harbor effects and resonance.

Figure 2.26a shows a comparison of spectra between the tide gauge record of the 2006 Kuril Islands event and its numerical simulation. The tide record appears to have three dominant periods, and these also appear in the numerical simulation, but with different spectral amplitudes. Similarly, Figure 2.26b shows spectra of simulations for the 2006, pseudo 1994 and worst–case Japan events, and the dominant periods are seen in agreement for all three scenarios, but with deviations in spectral magnitudes.

Using the waveheight distribution in Figure 2.24 and the wave response from Figure 2.23, one can conclude that tsunami from off northern Honshu, Japan will have a much higher impact in northern California than from the other portions of the KSZ. Figure 2.25c compares the simulation for Japan with 2006 and pseudo–1994; the wave–height from the Japanese scenario is higher than for 2006, as expected. All three events have similar time histories and wave periods, but different arrival times, the 2006 being the earliest arriving in Crescent City.

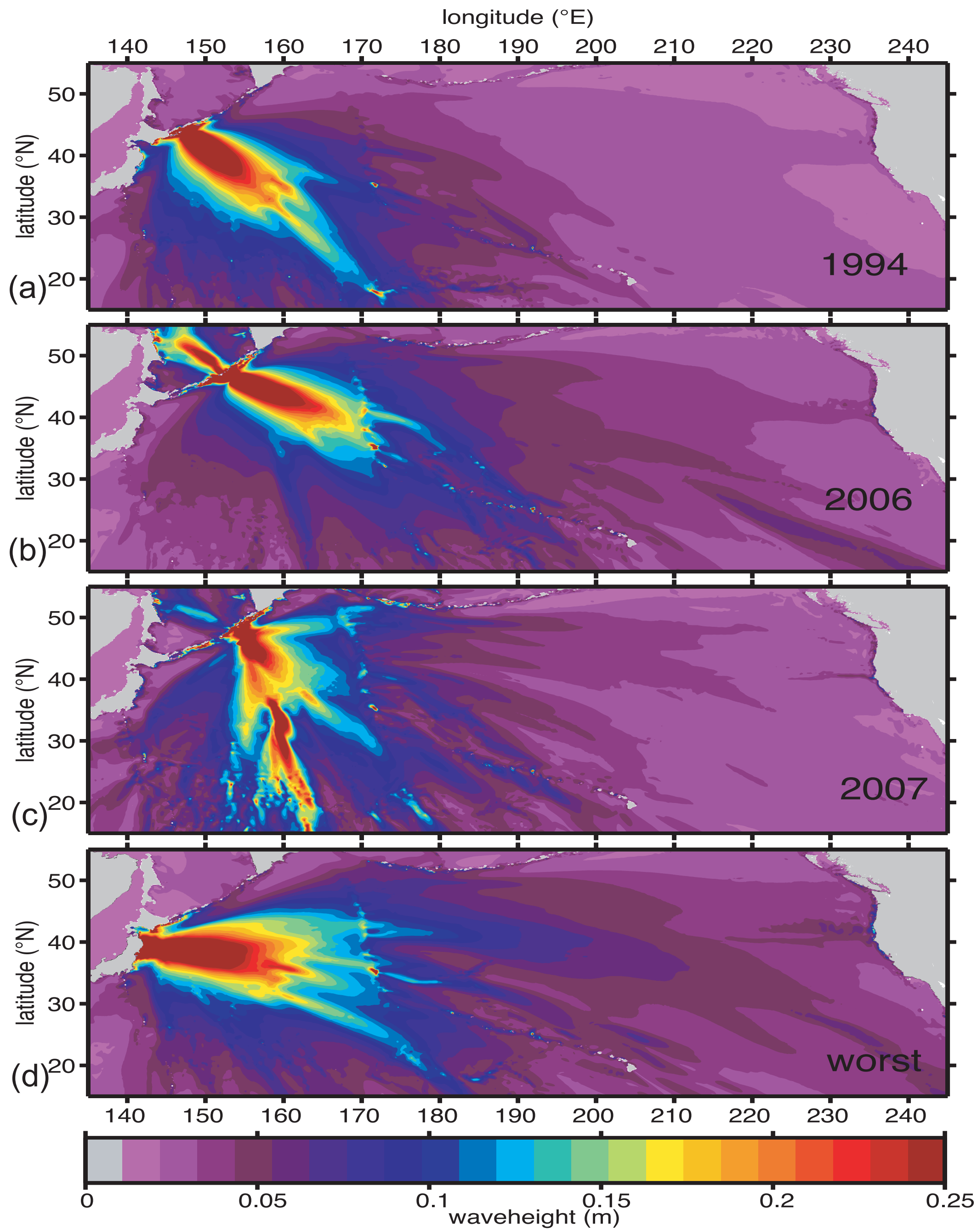

Figure 2.24: Maximum waveheight on Pacific Ocean basin is shown for each recent KSZ events. They all show different directivity.

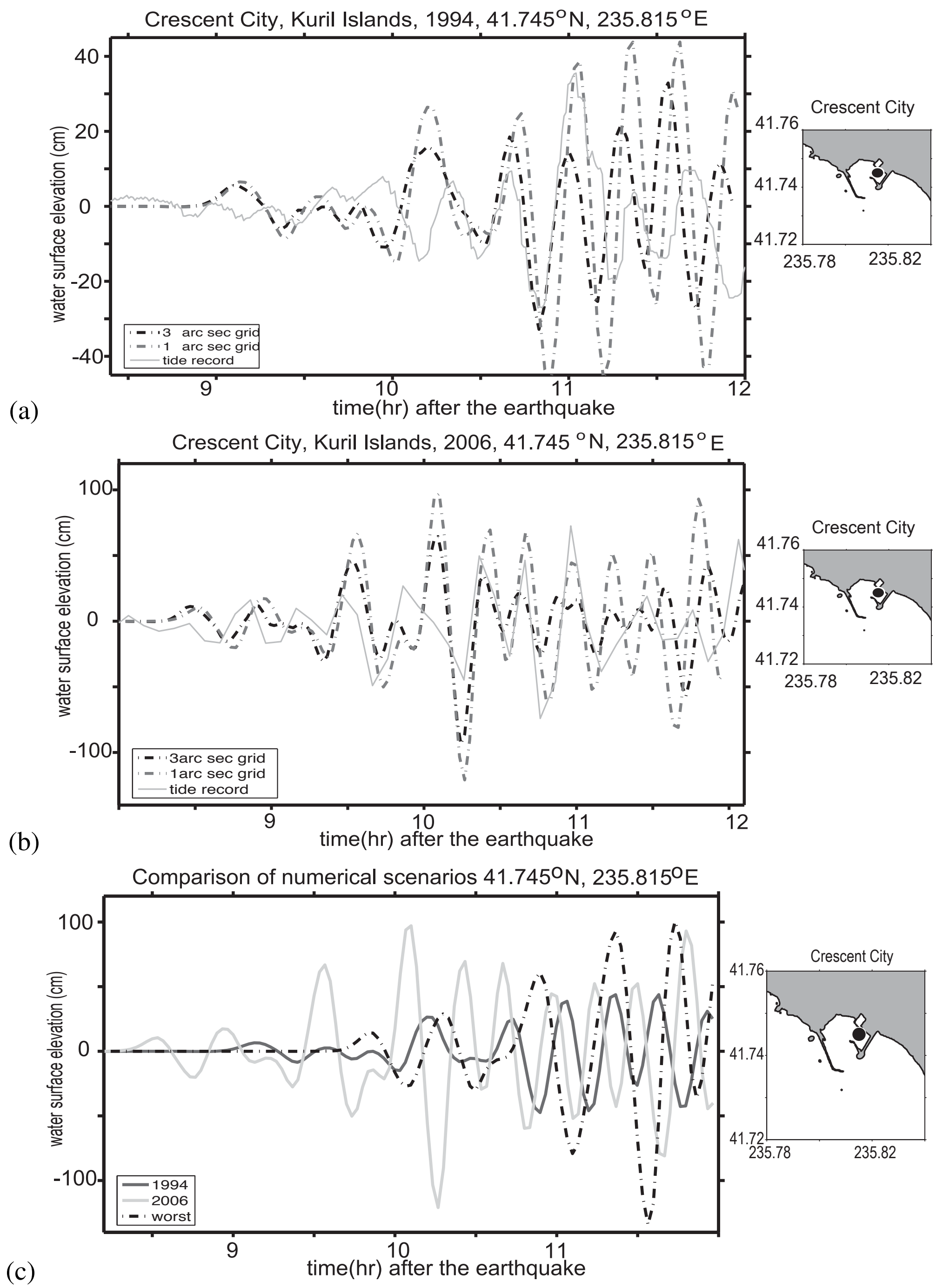

Figure 2.25: (a) Tide gauge comparison of the 1994 event with simulation. (b) Tide gauge comparison of 2006 event with simulation. (c) Synthetic Tide gauge results of the three large scenarios. The worst case was selected as the largest scenario to affect Crescent City.

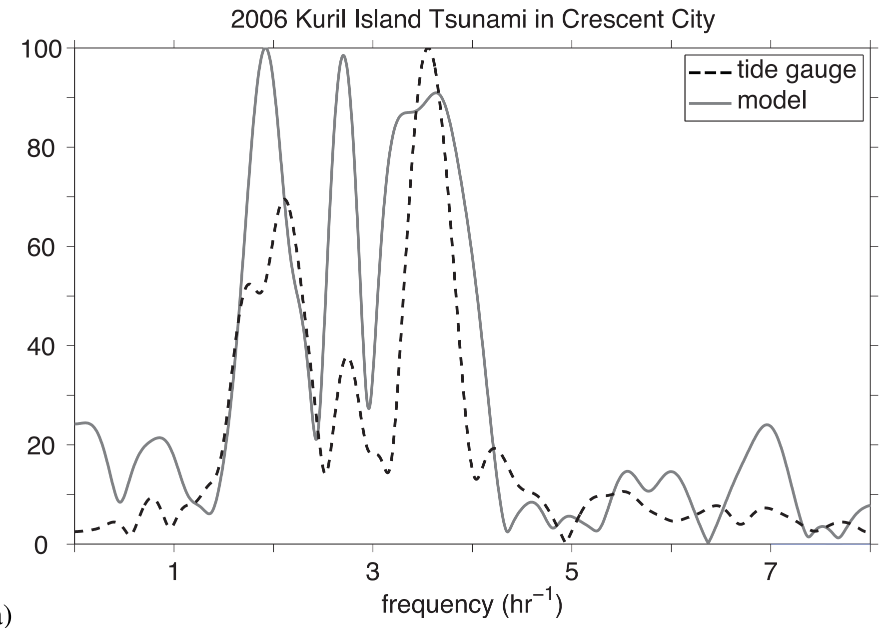

(a)

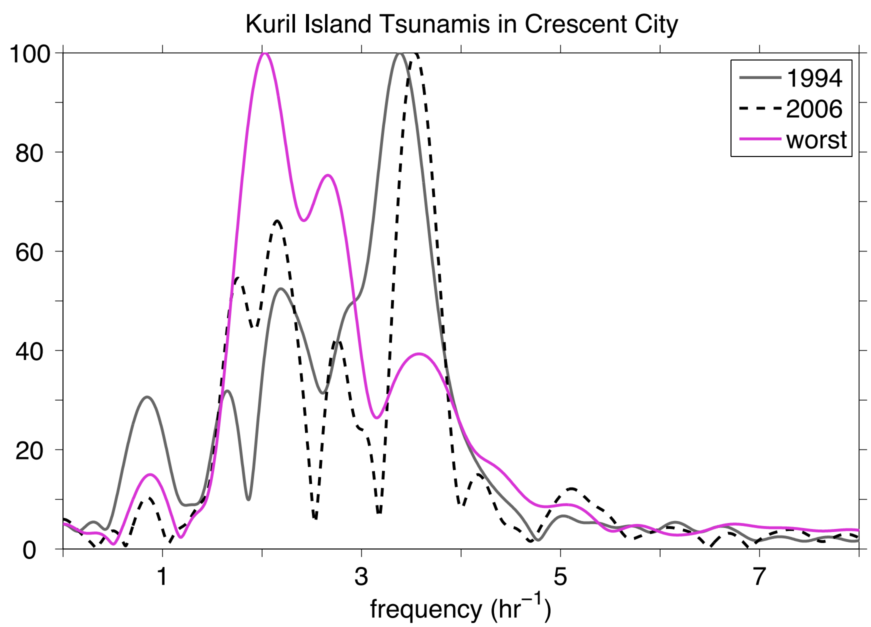

(b)

Figure 2.26: (a) Comparison of the 2006 tide record spectrum to the computed spectrum at Crescent City. (b) comparison of numerical simulation spectra from the 1994, 2006 and Japan cases.

2.6 Local Tsunamis generated at the Cascadia Subduction Zone

The Cascadia Subduction Zone (CSZ) runs along the Pacific Northwest coast of North America and has been compared to the Sunda–Andaman subduction zone based on probable earthquake magnitudes and paleotsunami records (Dengler, 2006). Abundant paleoseismic data from northern California, Oregon, Washington and Vancouver Island, Canada (Atwater et al., 1995), and modeling results based on Japanese historic records (Satake et al., 2003) suggest that past tsunamis were of comparable size to the 2004 Indian Ocean event.

Crescent City, located on the California coast about 460 kilometers north of San Francisco, is near the southern end of the CSZ and is particularly vulnerable to tsunami damage from distant, events as discussed in earlier sections. Twenty-four tsunamis have been recorded since 1938, nine with amplitudes of 0.5 meters or larger (Dengler and Magoon, 2006). The tsunami triggered by the March 28, 1964 ($M_w = 9.2$) great Alaskan earthquake killed 11 and caused $15 million in losses (Lander et al., 1993). On November 15, 2006 a tsunami generated by an earthquake in the Kuril Islands caused $5.9 million in damages to the small boat basin in Crescent Harbor (Kelley et al., 2006 ; Young, 2006).

Several studies have looked for geologic evidence of past tsunamis in the Crescent City (CC) area (Abramson, 1998; PG&E, 2003); deposits interpreted as tsunami sands have been found in a number of locations suggestive of inundation significantly greater than observed in 1964. Numerical modeling for an earthquake on the southern Cascadia subduction zone by the California Division of Mines and Geology (CDMG) showed flooding about twice as far inland as in 1964 (Bernard et al., 1994; Toppozada et al., 1995). Bernard et al. (1994) used an early generation hydrodynamic model to estimate inundation in Crescent City. That model was never validated through benchmark testing (Yeh et al., 1996; Liu et al., 2007) and the results were incompatible with some paleotsunami data, particularly in the Humboldt Bay region (PG&E, 2003; Synolakis et al., 2007).

Here, the tsunami hazard in CC from Cascadia earthquakes is re-examined, using the numerical model MOST (Titov and Synolakis, 1998; González et al., 2007; Synolakis et al., 2007), the relative tsunami hazard posed by segmentary and full ruptures of the CSZ and the sensitivity of the results to slip partitioning are investigated. [1]

2.6.1 Tsunami Modeling

Three levels of nested grids were used, as shown in Figure 1.8e. The highest resolution grid was itself sampled twice with uniform $3arc$–sec (93 by 69 m at $41.7°$ N) and $1arc$–sec ($31m \times 23m$ at $41.7°$ N) resolution. The outermost grid was resampled to $30arc$–sec, and the intermediate grid to $15arc$–sec. Similar multi grid computations for southern California are discussed in Borrero et al. (2006a).

2.6.2 Tsunami Hazard Assessment in Crescent City

Using the scenarios discussed in Section 2.2, as *Tsunami Sources*, modeled water level histories at the site of the CC tide gauge are presented in Figure 2.27c. The four Gorda scenarios (SN, SW, SP1 and SP2) show very similar results. The differences are well within the error margins of the simulations. The full Cascadia rupture CSZ L is only

[1] This section follows Uslu et al. (2007)

marginally larger than the Gorda segment events. The only scenario that is significantly smaller is the northern segment rupture CSZ N.

Figure 2.28 shows the expected inundation from the CSZ scenarios compared to the observed flooding measured by Magoon (1966) for the 1964 tsunami. Again, the full rupture CSZ L produces nearly identical inundation to the partitioned slip model, CSZ SP1, and the other three Gorda segment ruptures (not shown). The maximum extent of flooding is $3.8km$ from the coastline in the vicinity of Elk Creek, more than twice as far inland as observed in 1964. Note that the flooding in the City of Banda Aceh during the big tsunami reached $4km$, Borrero (2005); Fritz et al. (2006). Only the northern segment rupture CSZ N produces less extensive flooding than the 1964 event.

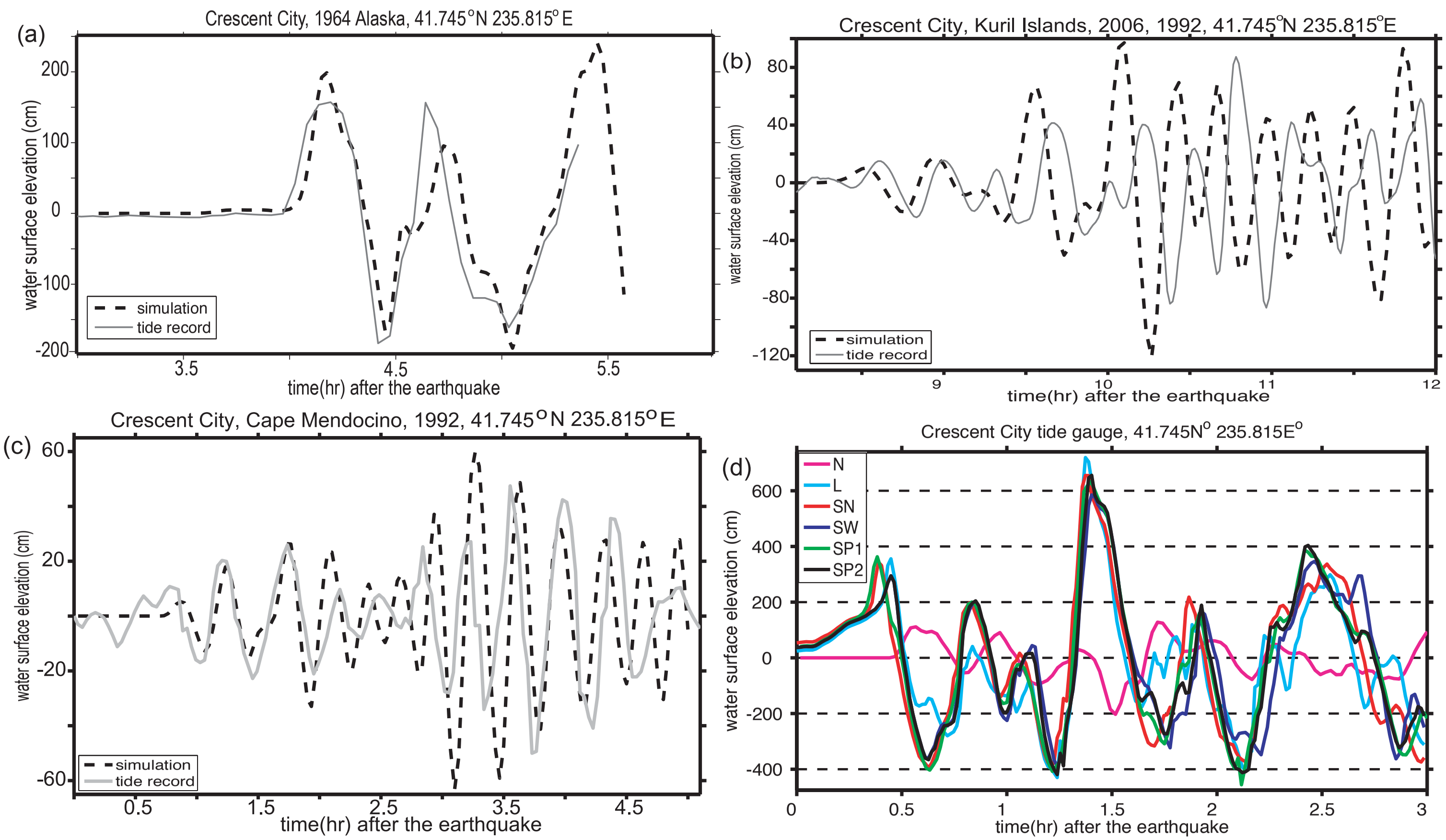

Figure 2.27: Comparison of tide gauge records of computed results of the 1964 and 2006 events and computations from CSZ-SN, SW, SP1 and SP2 at the Crescent City tide gauge station. Zero represents mean sea level. Note differences in scale.

2.6.3 Discussion and Conclusion for the Tsunami Hazard in Crescent City

Detailed inundation modeling was presented for tsunamis affecting CC using both near and farfield sources. The computations simulated fairly accurately the water level history produced by the March 28, 1964 Alaska earthquake and the November 15, 2006, Kuril Islands earthquake. The main result is that a tsunami caused by ruptures on the Cascadia Subduction Zone would impact Crescent City worse than in 1964. Such an event would inundate $3.8km$ inland, twice as far as the 1964 event. Inundation distances of this order were observed in Aceh during the 2004 mega–tsunami (Synolakis and Kong, 2006; Borrero, 2005). Note that the maximum seismic slip in any of the scenarios for the Gorda rupture is $8m$; substantially larger slips, would result in greater wave heights and inundation extents.

Rupture of the Gorda segment of the Cascadia subduction zone controls the tsunami hazard at Crescent City. The full rupture (scenario CSZ L) produces marginally larger inundation than the four other scenarios that only involve a Gorda rupture. The width of the rupture and the amount of slip partitioning between the CSZ megathrust and the Little Salmon fault has little effect into the wave field. In contrast, the northern rupture (CSZ N), an event nearly as large in magnitude as the full rupture and significantly larger than any of the Gorda segment events, produces less inundation than the 1964 tsunami, possibly due to directivity effects.

The onset of the tsunami for all Gorda ruptures is only minutes after the triggering earthquake is initiated. The crest of the first tsunami wave arrives at the tide gauge in CC in 25 min (Figure 2.27c). Because the north coast of California is so close to the leading edge of the subduction zone, the adjacent offshore area is predominantly

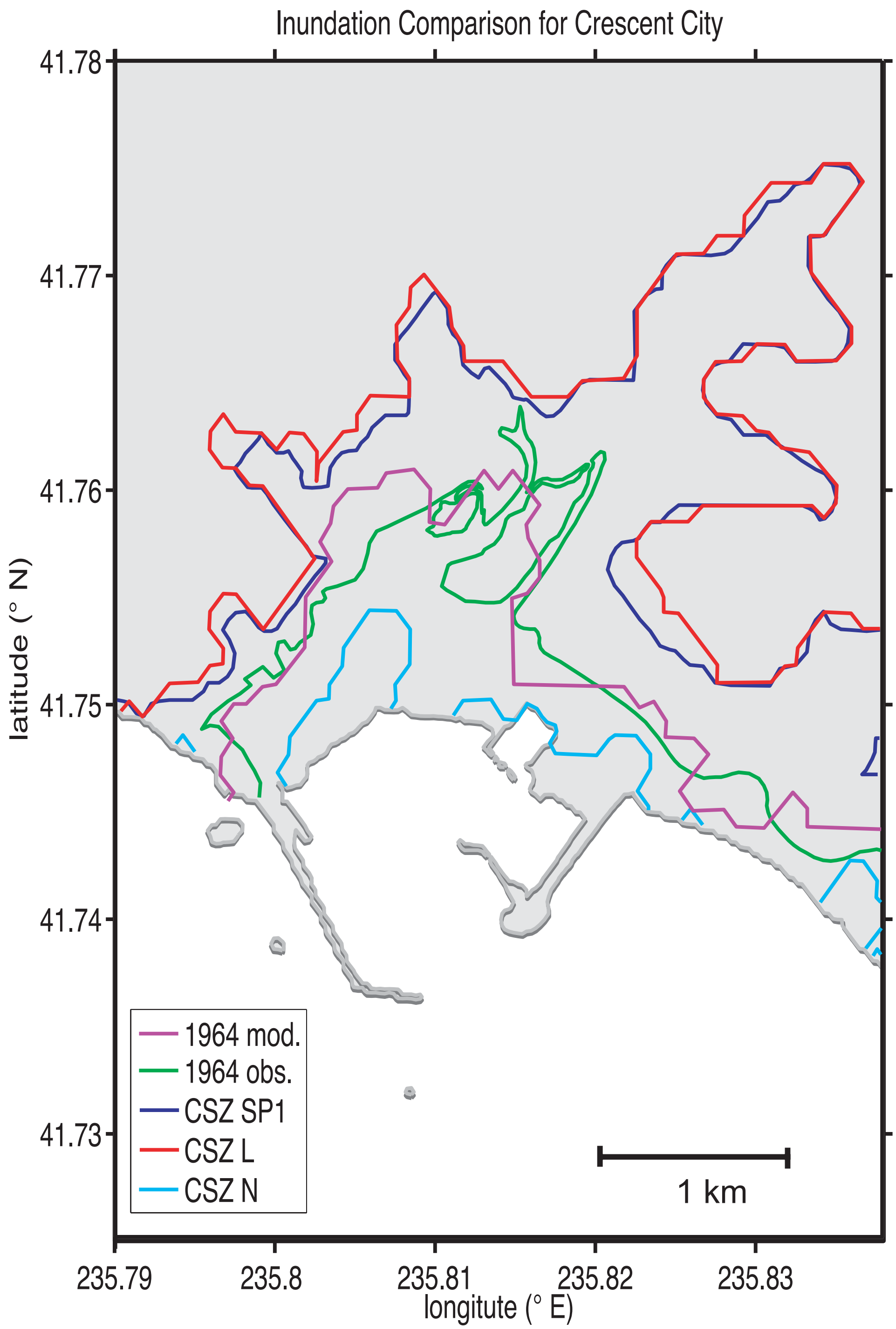

Figure 2.28: Observed tsunami inundation distances from the 1964 event (Magoon, 1966) compared to selected CSZ scenario events.

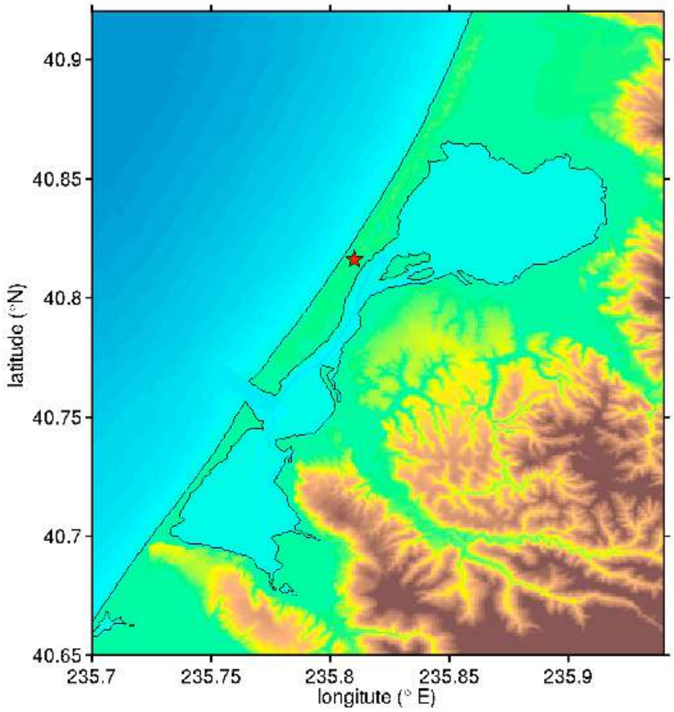

Figure 2.29: Location of Humboldt Bay and Samoa County.

uplifted in a Cascadia event producing a leading–elevation wave (Tadepalli and Synolakis, 1994, 1996). For subduction zones that are further offshore, subsidence produces a leading–depression wave on the adjacent coastline, thus providing a recognizable natural warning signal and additional time to evacuate. For Crescent City, the water level will begin rising almost immediately after the earthquake. Residents must be prepared to self evacuate, after any violent shaking that lasts more than $30sec$.

2.6.4 Tsunami Hazard in Humboldt Bay

Humboldt County, is located in northern California $130km$ south of Oregon border and $220km$ north of San Francisco. Humboldt County accommodates about 120,000 people, as of 1998. The Samoa region, marked with red star in Figure 2.29, located on the north

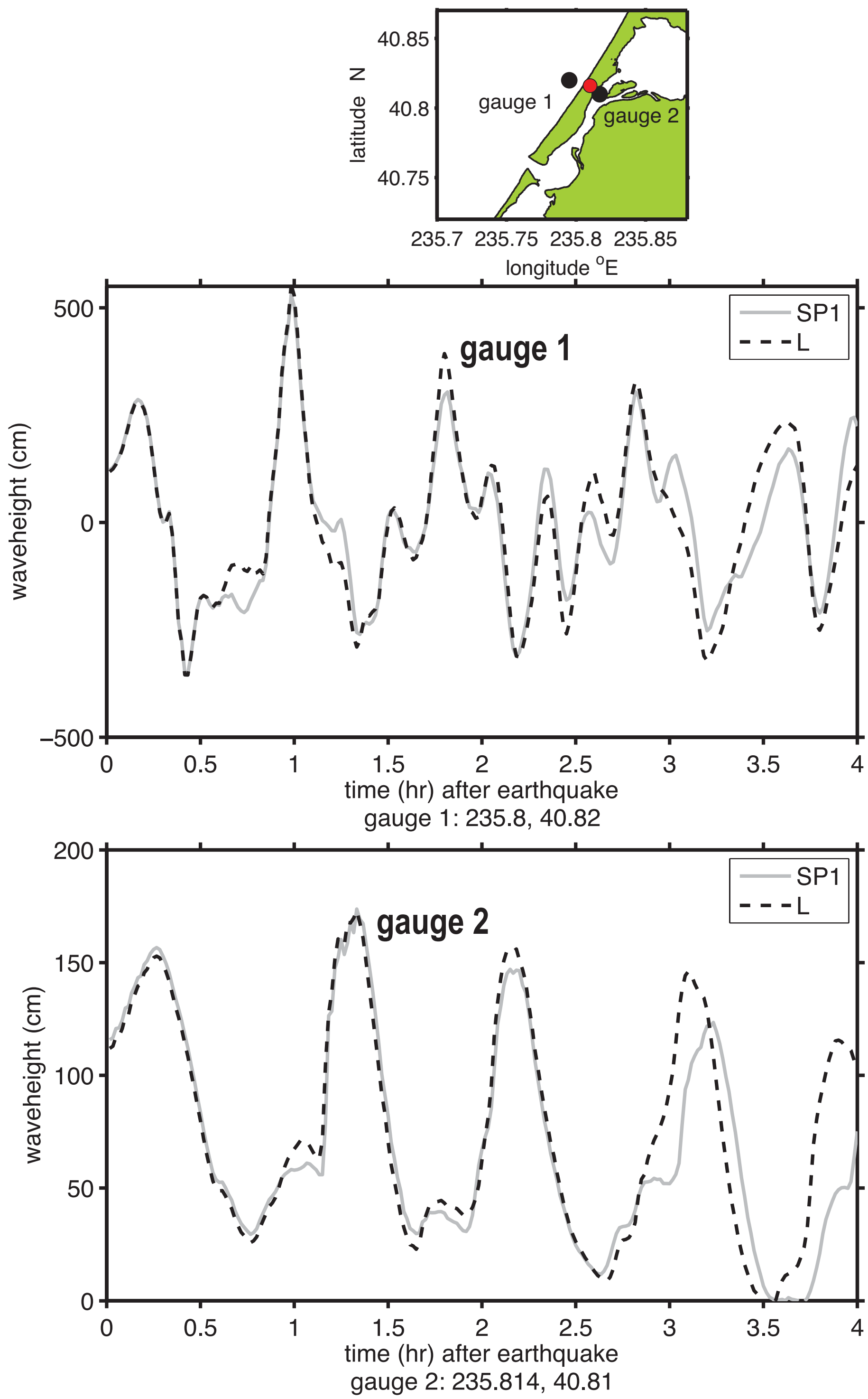

Figure 2.30: Comparison of the CSZ SP1 and L scenarios at the two gauges from numerical simulations inside and outside of the bay.

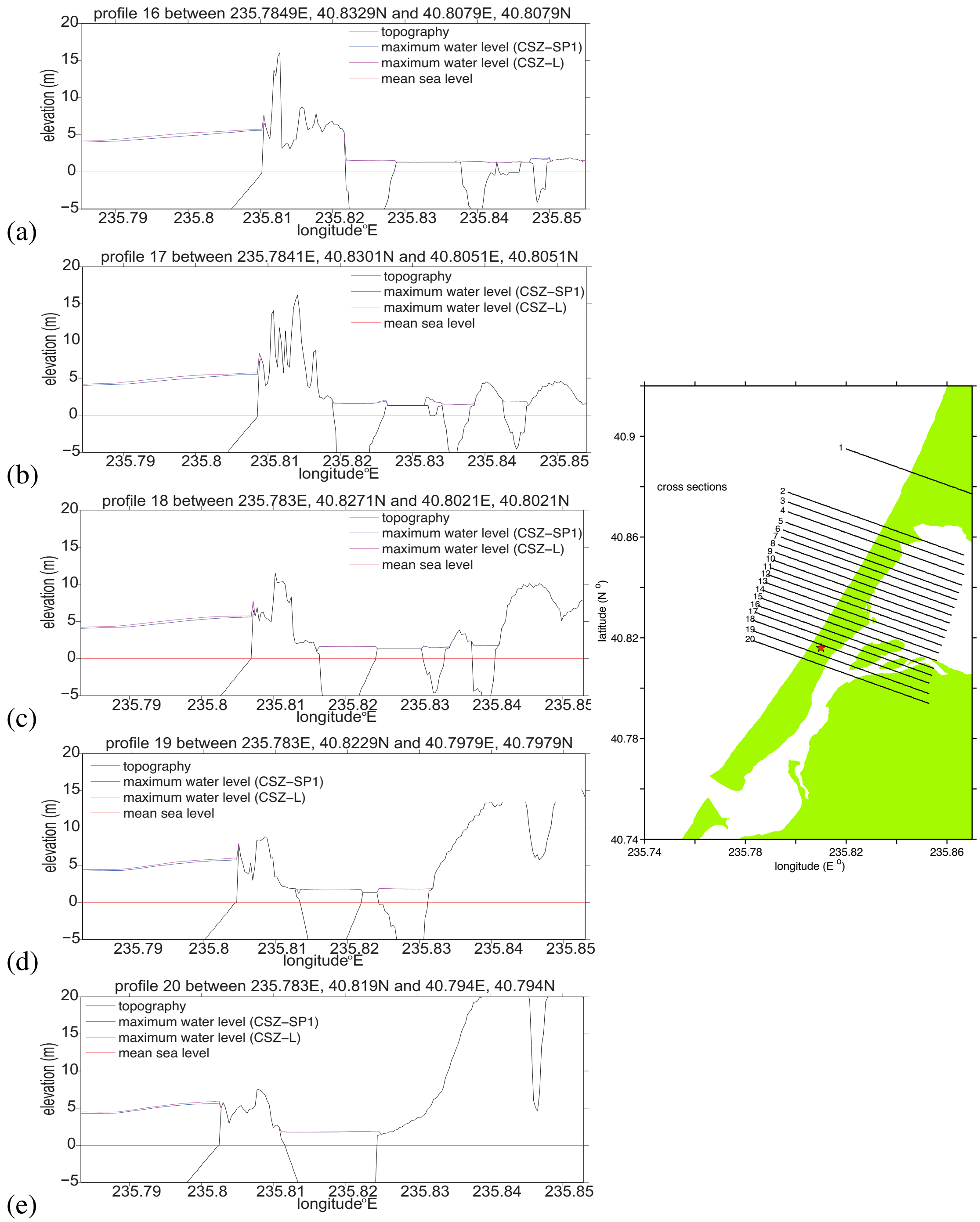

Figure 2.31: Five selected profiles are shown on the left from Samoa township, Humboldt County shown on the right.

spit in the Humboldt Bay will be having new residential developments, and thus has been studied as a special interest locale in this section. Humboldt Bay area is a tsunami high risk area, composed of north and south spit, where the south part of the spit of is low terrain, extremely susceptible to any flooding. The northern part has sand dunes that appeared to have protected Humboldt County during historical events (Dengler, 2007).

Computed Inundation Heights in Humboldt Bay and Discussion

Figures 2.30 and 2.31 compare computed results from the CSZ SP1 scenario earthquake. The inundation from the CSZ SP1 and CSZ L cases was calculated at $30m$ resolution as shown in Figure 2.31. Luckily, for each of the cases modeled, it appeared that the Samoa area was being not inundated. The model suggests that for these events the dunes on the northern sand spit might be high enough to prevent inundation directly from the sea. This is shown in Figure 2.31, where cross sections of maximum tsunami wave height are plotted over the local topography.

It is also interesting to note that the region is not inundated from the lagoon side, either. Animations of the time histories of water levels from the simulations do not show this area being flooded. This may be attributed to the degree of local co-seismic uplift which is incorporated into the simulation. Because the ground level was raised during the seismic event, the end result is that waves which would have otherwise inundated the area are unable to flood over the new land level. This effect was observed in recent tsunami events such as the March 28, 2005 Nias-Simeulue tsunami where local ground uplift was on the order of 2–$4m$ (Borrero et al., 2006b).

Figure 2.30 show time series histories of water levels on either side of the north spit. The time histories are shown relative to ground levels before the earthquake event. The time series are taken from gauges located in deep enough water to see the full cycle of the wave, i.e. gauge 1 was located at $7.6m$ depth and gauge 2 was located at $4.55m$ depth. Both sites are uplifted about $1.2m$ during the earthquake from scenarios CSZ SP1 and CSZ L.

Humboldt Bay area is undeniably a high risk for tsunamis and earthquakes. Any future developments in this area should carefully weigh the tsunami hazard before allowing an increase in population density. Ten $meter$ elevations for habitable building floors for Samoa appear conservative under the assumptions in this study and might serve as a guideline for construction.

The modeling presented here supports the field–geology evidence that the north spit has not been overtopped by direct tsunami attack (Dengler, 2007). However this does not mean, that overtopping may never happen, especially in light of the extreme runup heights inferred from paleo–tsunami studies at nearby, e.g. Orick ($\approx$ $23m$; PG&E, 2003) and documented in Aceh, during the horrendous 2004 Boxing Day tsunami (up to $32m$), Synolakis and Kong (2006); Borrero (2005); Borrero et al. (2006c). Furthermore, the particular source models used for this study were based on those of Bernard et al. (1994), which the authors themselves remark may be too small to accurately represent the hazard. Larger events can be arbitrarily constructed that will result in larger runup and possibly overtopping of the north spit dunes, especially towards the southern end of the north spit where maximum dune elevations are lower.

Finally note that, Bernard et al. (1994) argued that due to averaging in the determination of fault plane solutions, tsunami wave amplitudes may be higher than an individual fault plane generating mechanism might indicate. The PG&E (2003) study stated: *"Potential tsunamis from the Cascadia Subduction Zone could generate wave runup along the open coast at Humboldt Bay. The height would probably be greater, if the earthquake also triggered one or more large submarine landslides off the adjacent* *coast; however, no evidence of large, landslide-generated tsunamis in the past 2000, and probably the past 3600 years has yet been found in Humboldt Bay".*

2.6.5 Discussion and Results for Cascadia Subduction Zone Scenarios

The tsunami hazard in northern California was assessed at five different locations, Crescent City, Orick, Humboldt Bay, Shelter Cove and Cape Mendocino (Figure 2.34f). The three of the former have been described in detail in earlier sections. There are two different patterns of inufndation. First, the northern group of locales, (Crescent City, Orick and Humboldt Bay) are aligned along the Gorda Plate, and their tsunami hazard is primarily controlled by ruptures the Gorda plate. On the contrary, the second group (Shelter Cove and Cape Mendocino) are located south and have their hazard governed primarily by the ASSZ.

Figure 2.32 shows the local response at Orick, Shelter Cove and Cape Mendocino for tsunamis triggered by distant sources. The local response from the earthquakes in the KSZ, WASZ, AASZ, CASZ and SASZ are shown. All three beaches appeared to be at risk from tsunamis emanating from AASZ and the detailed responses are shown in Figure 2.33 with design earthquakes highlighted, each using seven segments and capable of triggering the worst case scenarios.

In Figure 2.34, the runup heights and maximum wave heights for five beaches in northern California are shown. Figure 2.34a shows the maximum runup in Crescent City, $\approx 7m$ with inundation distances reaching up to $3km$ and maximum wave height offshore exceeding $5m$. Inundation in Orick is shown in Figure 2.34b, ranging from 5 to $10m$ with two peaks. Figure 2.34c shows the Humboldt Bay results. Maximum wave

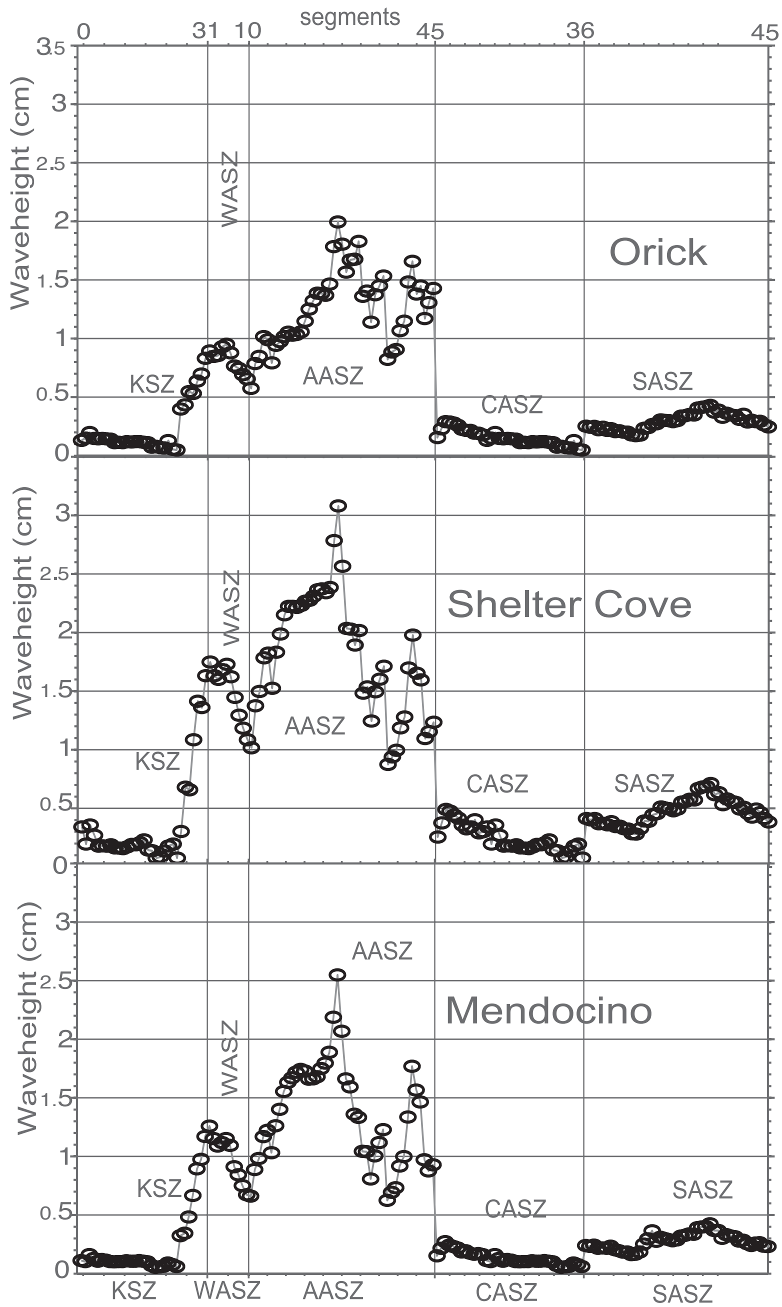

Figure 2.32: Farfield earthquake tsunami responses at Orick, Shelter Cove and Mendocino.

heights are concentrated along the north spit, where the topography does not permit the water to overtop. The south spit shows the most extensive inundation.

Shelter Cove shows a smooth wave height distribution outside the harbor, up to $6m$. The peninsula causes the waves to scatter around, resulting in a maximum runup in the bay of $\approx 7m$ (Figure 2.34d). Cape Mendocino has very rough and complex bathymetry, with an offshore reef that may work as a barrier. Tsunamis coming from Cascadia sources show low runup heights; however, the tsunamis from ASSZ come directly to the beach and they can penetrate through, causing around 5–$10m$ runup, with a maximum shown in Figure 2.34e at the Albion cove, through the river bed. Otherwise, Cape Mendocino has renowned steep cliffs that may protect the township.

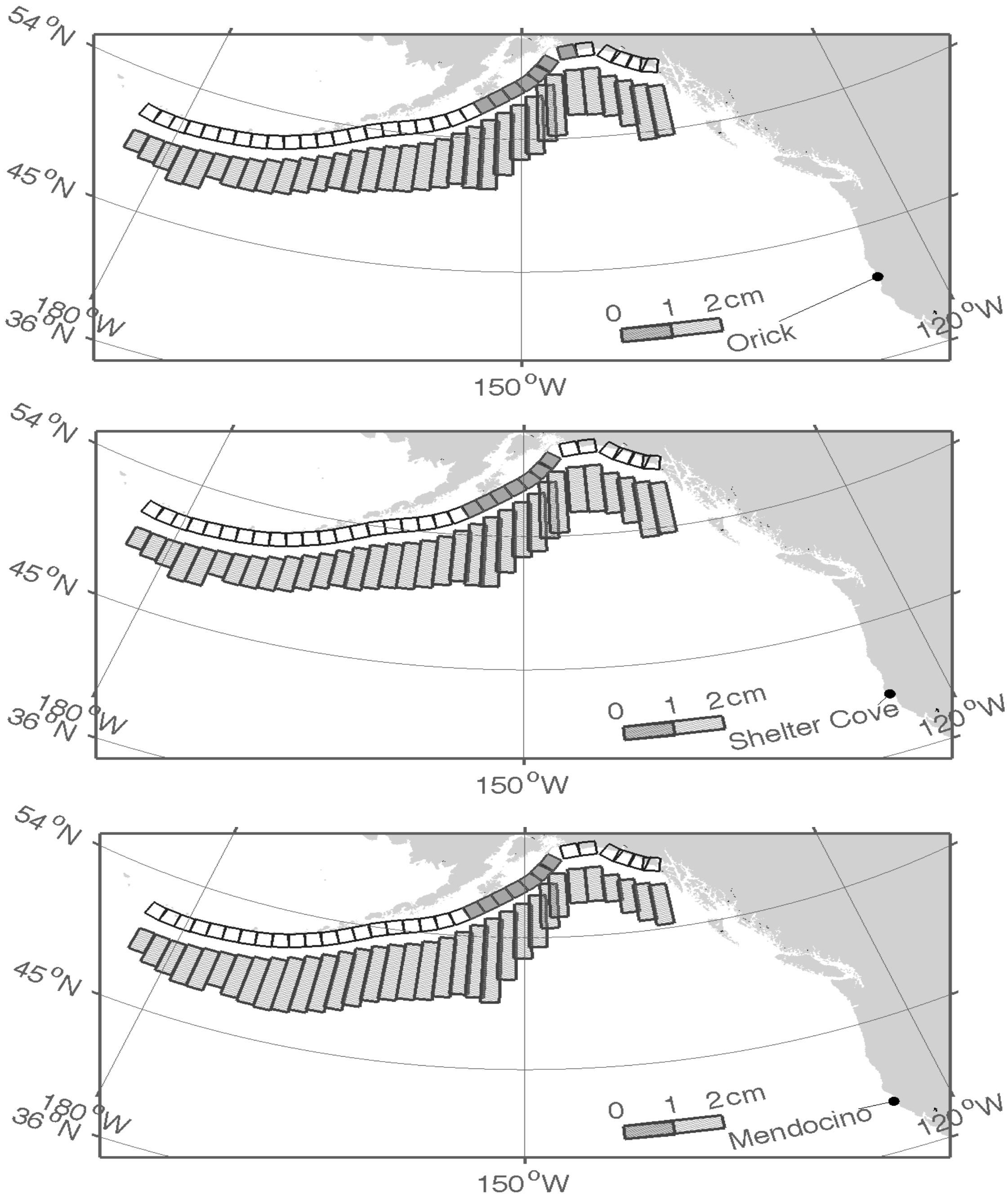

Figure 2.33: Farfield earthquake tsunami responses at Orick, Shelter Cove and Mendocino.

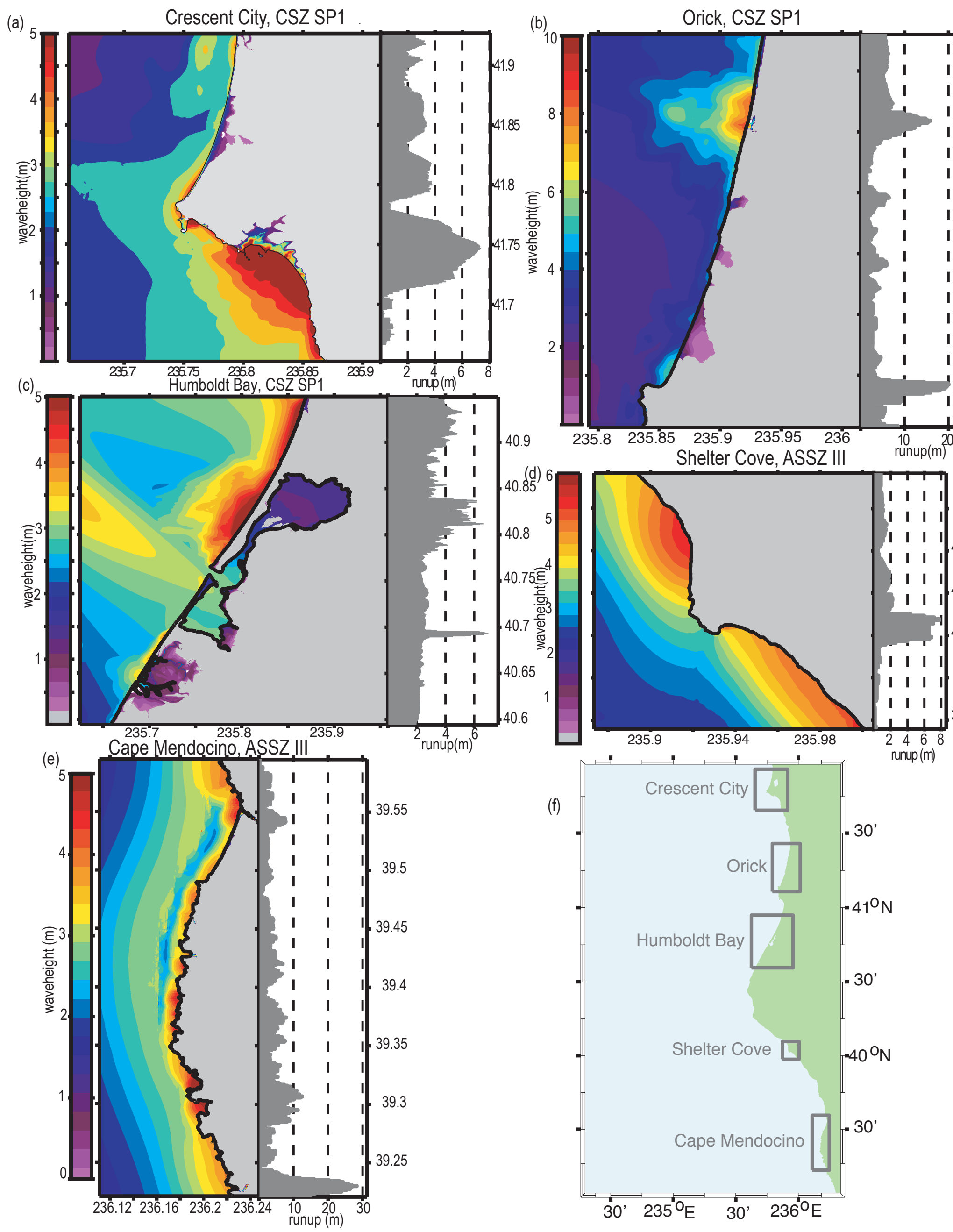

Figure 2.34: Northern California, tsunami runup plots at the study sites: Crescent City Harbor, Orick, Humboldt Bay and Samoa County, Shelter Cove and Mendocino.

Chapter 3

Probabilistic Tsunami Hazard Assessment

3.1 Introduction

Probabilistic hazard analysis in tsunami studies involves determining the probability of exceedance of specific runup values in specific time windows through the superposition of runup predictions from specific sources and their probabilities of occurrence during the same time windows. An extreme event may have small probability but high impact, as opposed to a more frequent event with lower impact. The sum of individual probabilities of exceedance of a set of particular runup heights in a given analysis over all possible scenarios for a specific return period will provide the total probability of exceedance of the smallest runup height in the set.

Consider the probability of $2m$ runup in a given location 10% in a five year interval from a given source A, while the probability of $10m$ runup from another source B is 1% in the same interval. Then one could conclude that the expected runup value for five years for this location from sources A and B is $0.21m$. This prediction is less useful than the probability of exceedance of a given runup value in the same time interval from different sources, because the two sources A and B are unlikely to rupture simultaneously in the same time interval. For example, one expects that, if the probability of exceeding $10m$ in any given year is 1% from source A, and 0.01% from source B, the combined probability for the two sources is 1.01%. In general, there has been comparatively much less research in tsunami hydrodynamics on calculating probabilities of exceedance or determining return periods for specific runup values than in estimating inundation distances. A brief summary of existing work will be provided here.

Clearly, tsunami probabilistic hazard analysis is an assessment of the tsunamigenic potential of different fault zones overtime to obtain a comprehensive probability analysis for runup values for a target region. However, given the large range of subduction phenomena which may trigger waves that strike a given locale, it is not possible to obtain probabilities for all possible scenarios with the same level of confidence. Also, because of the directivity of tsunamis, it is rather unlikely that all source scenarios will contribute to first order to the probability of exceedance in any given locale.

In order to identify coastal areas in California that are particularly vulnerable to farfield tsunamis, the subduction zones around the Pacific Ocean have been divided into 177 pieces of equal–size $100km$ long segments. This division spans Japan, the Kuril Islands, the West Aleutians, the Alaska-Aleutians, Cascadia, Central America and South America–Chile. Each of the 177 segments is $100km$ long and $50km$ wide. A second $100km \times 50km$ segment is located adjacent along the length axis, but deeper along the slab. Each double segment, $100km \times 100km$, corresponds to a $M_w = 7.6$ earthquake with unit seismic slip of $1m$, or a moment of $3 \times 10^{27} dyne–cm$ and maximum surface displacement of 30–40cm depending on the specific parameters of the subduction zone. The segments are described in greater detail in Chapter 2, Section 2.2.

Tsunami wave amplitudes for each of the 177 sources have been computed along the coastline of California. For example, in Figure 2.13, the response curves for Crescent City, Pt. Reyes, San Francisco Bay, Monterey, Avila Beach, Los Angeles and San Diego have been presented as a function of the unit source location. For instance, the resulting waveheight offshore from a unit seismic displacement on segments 14 to 18 in the Aleutians is $1.5 cm$. These response curves help identify the vulnerability of any specific locale to tsunamis from a given source region. For example, San Francisco Bay has a far greater response (i.e., is more vulnerable) to tsunamis from the Aleutians than from South America or Japan. Here, probabilities for those scenarios will be determined through either literature review or standard seismic hazard assessment methods or both.

3.2 Probabilistic Seismic Hazard Assessment

Earthquake statistics are used for forecasting the likelihood of future large damaging earthquakes, and form the basis of earthquake probabilistic hazard assessment. The major problem facing the use of statistics in seismology is the relative rarity of earthquakes, which results in severe undersampling of the dataset. Seismology is a young science and there is only access to a consistent homogeneous database since the 1900s, and perhaps a few centuries of paleoseismic records, but without clear understanding if all events large and small are equally represented in historic pre–1900 time series (Ambraseys and Synolakis, 2009). By contrast, recurrence times at major plate boundaries are thought to be of the order of centuries. As a result, at the very best, existing databases cover a handful of seismic cycles (Stein and Wysession, 2002), which are themselves non periodic (Ando, 1975). For example, in predicting extreme events in hydrology, engineers here access to continuous rainfall or flood records for many decades, all measured at the same location. Then the prediction of 100–year event is far less onerous than it is in seismology.

Nevertheless, a number of statistical approaches (Papoulis, 1965) have been used traditionally to estimate earthquake risk. The most commonly used distribution for rare

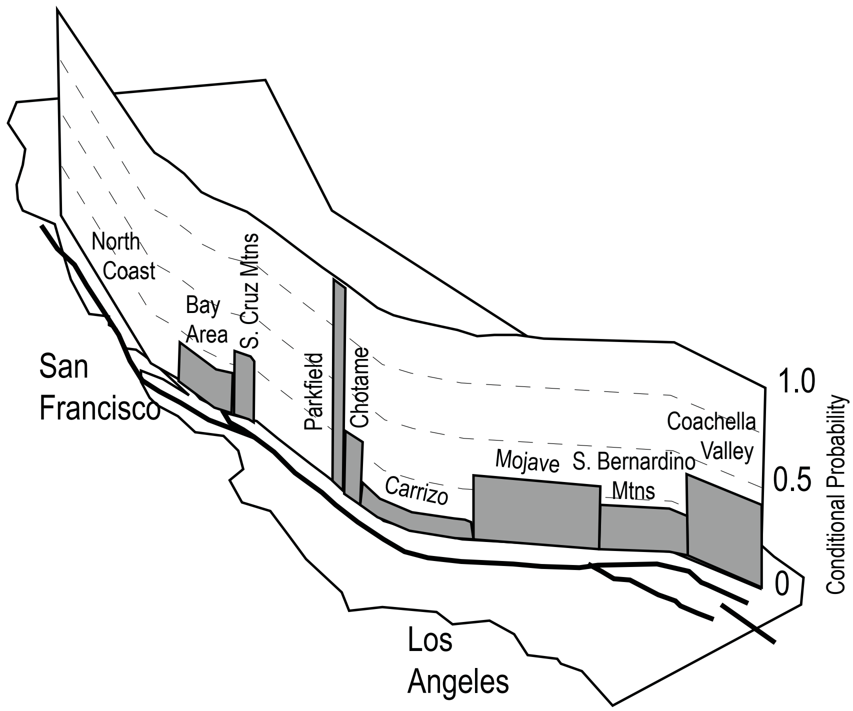

Figure 3.1: Earthquake probabilities on major segments of the San Andreas fault between 1988–2018 (Agnew D.C., et al, 1988).

events (including earthquakes, volcanic eruptions or bolide collisions) is the Poisson distribution, in which the probability of n events occuring during a time interval t is given by

$$p(n, t, \tau) = (t/\tau)^n e^{-t/\tau}/n!, \tag{3.1}$$

given a mean recurrence time of τ for each event. The probability of having one or more events occurring in the same interval t is

$$P(n \geq 1, t, \tau) = 1 - p(0, t, \tau) = 1 - e^{-t/\tau}, \tag{3.2}$$

or approximately t/τ, when $t << \tau$. This latter restriction is after ignored in many probabilistic assessments.

Houston (1980) defined the cumulative probability of exceedance of a given waveheight h_{crit} as

$$P(h \geq h_{crit}) = 1 - \mathrm{e}^{-p(h_{crit})t}, \tag{3.3}$$

over a period of time t (Houston, 1980). Here the event is the occurrence of a tsunami waveheight at a given location, so that $p(h_{crit}) = 1/\tau$, where τ is the return period of a tsunami with waveheight $h \geq h_{crit}$.

The Poisson distribution does not necessarily require a long time series of observations and is useful for mathematically describing short time series which may or may not include all manifestations of the events. However, it is time–independent, having no memory, which means that, at any given time the probability of a new event does not depend on the history of previous occurrences. In lay terms, it applies to a game of dice, where the probability of rolling six is $1/6$ every time one rolls.

By contrast, the seismological record, as well as common intuition, suggest a cyclical behavior for earthquakes, since the strain they release takes time to built up by tectonic processes, an idea first expressed by Reid (1910), following the great 1906 San Francisco earthquake . While earthquake doublets have been documented (Lay and Kanamori, 1980), they clearly involve different elements of a fault plane; in general the recurrence of a megathrust event along a given segment of subduction zone will be less likely the morning following a magnitude 9 earthquake, at that same location along the zone. This is similar to the fact, well known to poker players, that the probability of drawing an ace from an unshuffled deck of cards is reduced (to $1/17 = 3/51$ from $1/13 = 4/52$) right after successfully drawing one. In this example the pool of aces has been reduced by the first successful draw just like the pool of "ripe" subduction zones is inferred to be reduced after a major megathrust earthquake (Stein and Wysession, 2002).

The application of this concept is not without problems, as illustrated, for example, by the rupture of the 2004 Sumatra earthquake, which extended over and beyond the fault areas of the 1881 Car Nicobar and especially the 1941 Andaman Islands earthquakes, which had arguably swept clear of any stress the relevant fault zones. In the 1941 case, this had occurred as recently as 63 years earlier in a region where recurrence times for megathrust events are assumed to be at least $300 years$ (Ortiz and Bilham, 2003).

Notwithstanding this reservation, a time–dependent model is often preferable to represent earthquake statistics. Such models use a probability distribution that depends on a mean recurrence time τ and standard deviation σ of the recurrence time of the specific event, and expresses the probability of a large earthquake at time t after the last event, $p(t, \tau, \sigma)$, as a Gaussian or normal distribution, given by

$$p(t, \tau, \sigma) = \frac{1}{\sigma\sqrt{2\pi}} e^{-\frac{1}{2}\left(\frac{t-\tau}{\sigma}\right)^2}. \tag{3.4}$$

This is the basic premise of time–dependent earthquake models.

In order to find the cumulative probability of occurrence of the specific earthquake by the absolute time T, one simply integrates the distribution function over all times t smaller than T:

$$P(T) = \int_0^T p(t, \tau, \sigma) dt. \tag{3.5}$$

The earthquake occurrence predicted from a Poisson model will have more scattered return periods and the results may be clustered because of the random sampling (Stein and Wysession, 2002). It would be expected to apply better to a worldwide population of earthquakes since the occurrence of a large event on a given fault should not be affected by the activity on another fault in a different tectonic province. On the other hand, the Gaussian model will have a more regular distribution with a smaller standard deviation, and would be more applicable to a single fault zone. Also, for a model that requires a standard deviation close to its mean, a Poisson model may be be more useful, whereas the Gaussian or time–dependent model will apply more readily in the case of a standard deviation significantly less than the mean.

Figure 3.1 shows expected probabilities of major earthquakes on the San Andreas Fault in California. It is worth recalling that a relatively small earthquake with a magnitude of about 6 was predicted in the 1980s to occur near Parkfield by 1993 with a 95% probability. It did not occur until 2004, 11 years later with respect to its date of maximum likelihood in its alleged 22 year cycle (Harris and Arrowsmith, 2006).

3.3 Probabilistic Tsunami Studies

Wiegel (1970) and Ritter and Dupre (1972) appear to be the first published studies in probabilistic tsunami estimates. Wiegel (1970) prepared a frequency of occurrence graph using the observed runup data from five big earthquakes: 1946, 1952, 1957, 1960 and 1964. His work included Crescent City and San Francisco Bay. However, the San Francisco figure did not present any results beyond a runup of about $2m$, and did not have sufficient information for tsunami runup heights for return periods greater than 50 years. Ritter and Dupre (1972) extrapolated Wiegel's San Francisco Bay curve. They did not explain how their extrapolation was estimated. Figure 3.2 shows their results.

Geist and Parsons (2005) reviewed the existing probabilistic studies on tsunami hazards. They described how Soloviev and Go (1969) introduced a probabilistic frequency

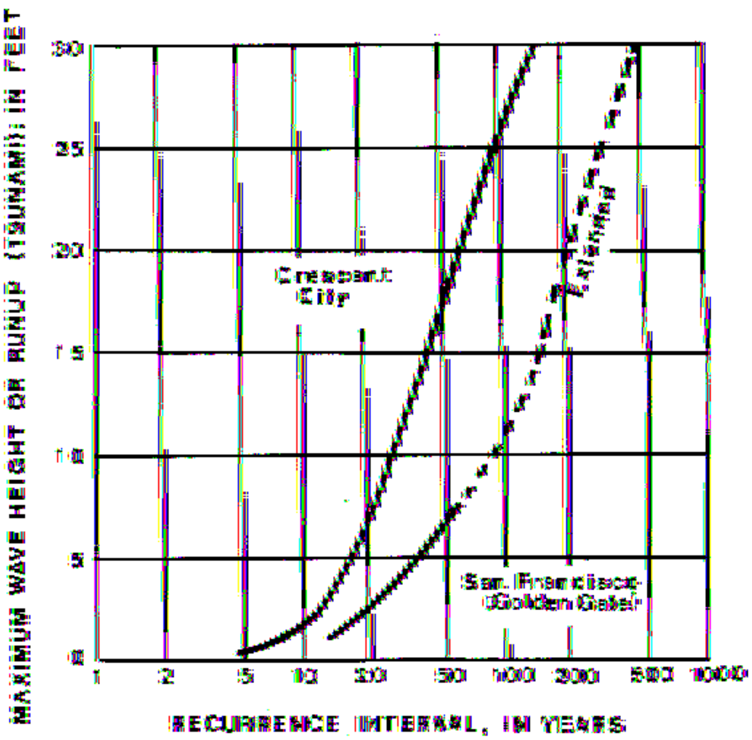

Figure 3.2: Frequency of occurrence of tsunami runup in Crescent City and San Francico Bay according to Wiegel (1970) and as supplemented by Ritter and Dupre (1972).

distribution $p(i)$ expressing the probability of a tsunami of intensity i being generated in any year as

$$p(i) = \alpha \cdot 10^{-\beta i}, \tag{3.6}$$

where α and β are constants, characteristic of each subduction zone, while i is the tsunami intensity, defined by Soloviev and Go (1969) as

$$i = \log_2 \left(\sqrt{2} \cdot h_{avg} \right), \tag{3.7}$$

where h_{avg} is the average runup along a given stretch of coastline, which was left undefined.

This approach is based on the frequency–magnitude relationship introduced by Gutenberg and Richter (1942); who first quantified the observations that there occur more small earthquakes than large ones. Gutenberg and Richter proposed the following expression relating the number N of earthquakes of a magnitude exceeding M as

$$\log_{10} N = a - b \cdot M \tag{3.8}$$

where they noticed that the constant b (universally known among seismologists as just the "b–value") was remarkably and universally close to 1. The constant a on the other hand depends on the population of earthquakes studied and would vary with geographic location and duration of the time window sampled. The value of 1 for b was justified theoretically by Rundle (1989) under the assumption of a scale independent rupture on a fault zone of fractal dimension 2 (which means that each element of the fault zone has an equal probability of seeing its stress released by an earthquake of any size), and using of seismic scaling laws, which govern the growth of fault dimensions with earthquake size. In practice as Okal (2008) has argued, frequency–magnitude studies have been used to palliate the scarcity of large earthquakes by extrapolating to large magnitudes the properties (including recurrence) of smaller events for which an adequate population of samples is available for study (Stein and Wysession, 2002). However, this procedure suffers from the breakdown of scaling laws for large sources (Geller, 1976), even when the physical concept of seismic moment is used to replace the largely empirical magnitude scales (Okal and Romanowicz, 1994).

The assumption underlying the use of an equation such as 3.6, is that in each zone the seismicity triggering tsunamis is homogeneous and that records of tsunami observations are complete. The case of the 15 November 2006 Kuril tsunami which generated local runup of $21m$ on uninhabited islands would have gone unreported in the absence of a field expedition (Bourgeois, 2007), illustrating the limitations of Soloviev and Go's approach.

Soloviev (1970) assumed a constant value of β for all subduction zones, which he calculated as $\beta = 0.31$. Houston and Garcia (1974) and later Houston (1980) converted Equation 3.6 to a natural exponential, rather then a power of 10, form:

$$p(i) = \alpha' \cdot \mathrm{e}^{-\beta' i}, \tag{3.9}$$

in which β' would be expected to be $\beta \times \ln 10$ or $\beta' = 2.30 \cdot \beta$. Geist and Parsons (2005) claim that they then further allowed a variation in the power law with the geographic origin of the tsunami. They found an "excellent" agreement ($\beta' = 0.71$) with Soloviev's value for the Alaska–Aleutians Subduction Zone, but a slightly lower value ($\beta' = 0.63$) for South America–Chile.

On the other hand Burroughs and Tebbens (2005) introduced a receiver–specific power law to estimate a cumulative frequency-size distribution

$$p(h) = Ch^{-\alpha}, \tag{3.10}$$

where h is the maximum tsunami height recorded at a single site, regardless of its geographic origin (note that the α in Equation 3.10 is unrelated to that in Equation 3.6). They applied this approach to records of tsunamis at 12 Japanese sites over several decades, with the resulting exponents α varying from 0.62 to 1.34. The average value, 0.94 was in good agreement with Soloviev's $\beta = 0.31$, given the ratio $\ln 10 / \ln 2 = 3.3$ of the power exponents expected from the combination of Equations 3.6, 3.7 and 3.10.

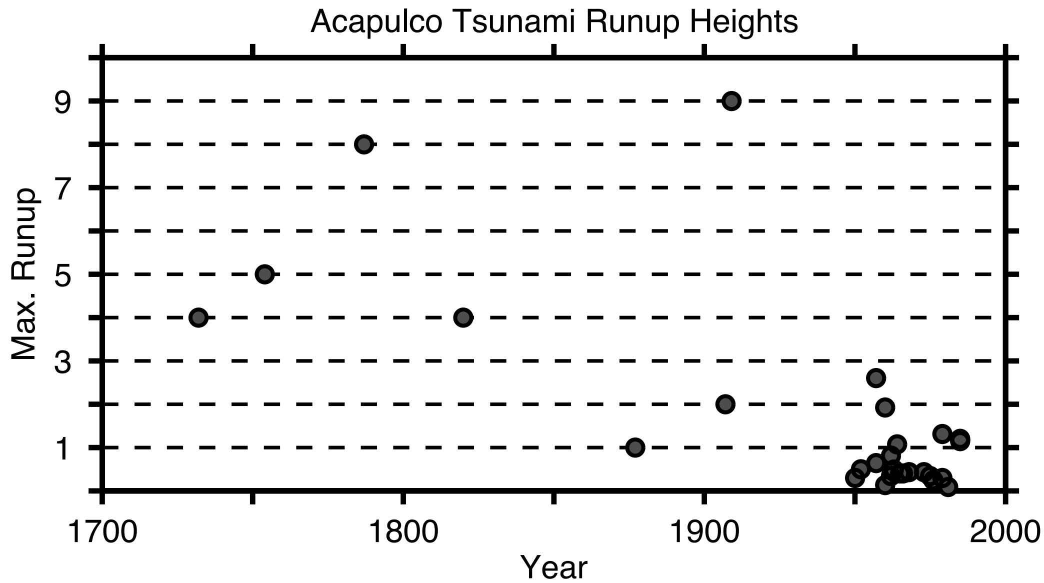

Figure 3.3: Tsunami runup heights at Acapulco, Mexico between 1700 and 2000 from Geist and Parsons (2005).

However, their results are significantly scattered with two stations, Hachinohe and Hanasaki, featuring the lowest values of α and more importantly a significant departure from the power law at high runup amplitudes. The singularity of this observation is compounded by the fact that those two stations are not geographically distinguishable from the other sites with more regular runup distributions.

Geist and Parsons (2005) analyzed data for Acapulco, Mexico as a case study. Their tsunami runup data, shown in Figure 3.3, included visual empirical estimates from historic reports in the period from 1732 until 1950, and tide gauge records thereafter, using a somewhat *ad hoc* conversion of direct instrumental records to runup values. This figure illustrates the difficulties of using statistics from a clearly inhomogeneous dataset. First it is clear that the visual estimates could not resolve runup of less than 1 meter, which explains the clustering of such points after 1950. As a result, such diagrams become highly site–specific, since this plot, for Acapulco ignores the catastrophic 1932 events

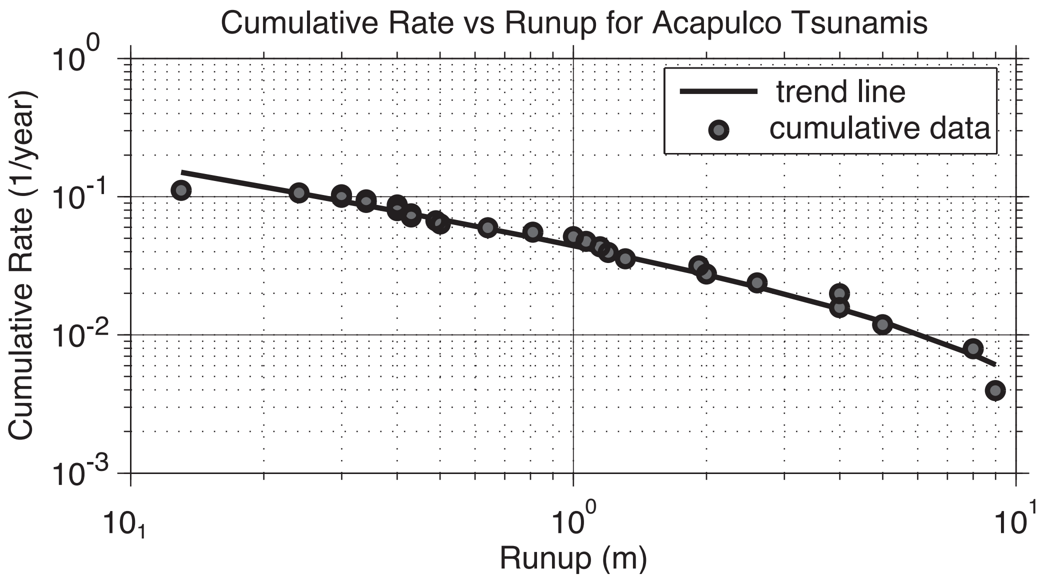

Figure 3.4: Acapulco, Mexico runup data reprocessed from Geist and Parsons (2005) with a trend line for cumulative frequency-size distribution of $p(h) = 0.056(h^{-0.52} - 20^{-0.52})$ – h is runup, $p(h)$ is cumulative frequency-size distribution

in Manzanillo, only $300km$ away (Sanchez and Farreras, 1993; Borrero et al., 1997). Also, the difference in sampling procedures cannot explain the increase after 1950 in runup occurrences between 1 and 3 meters, which could be either real or an artifact of the conversion procedure.

Geist and Parsons (2005) further used a modified version of equation 3.10 known as an upper–truncated power law:

$$p_T(h) = C(h^{-\alpha} - h_U^{-\alpha}). \tag{3.11}$$

Here, h_U is a "maximum" waveheight, which cannot, at least in principle, be exceeded and as such can be interpreted as having infinite repeat period. This kind of relationship has been used widely to describe the populations statistics of a number of tsunami events

Source number	Location	M_w	$L(km)$	$W(km)$	Disp (m)	Return Period (yr)
1	AASZ	9.2	1000	100	17.7	1,313
2	AASZ	9.2	1100	100	18.1	750
3	AASZ	9.2	600	100	–	750
4	AASZ	9.2	1200	100	16.3	1,133
5	AASZ	9.2	1200	100	14.8	750
6	AASZ	8.2	300	100	2.1	875
7	AASZ	8.2	300	100	2.1	661
8	KSZ	8.2	300	100	2.1	661
9	KSZ	8.8	500	100	9.8	100
10	KSZ	8.8	600	100	9.8	100
11	KSZ	8.5	300	100	5.8	500
12	KSZ	8.5	300	100	5.8	500
13	KSZ	8.5	1000	100	5.8	500
14	SASZ	9.5	800	100	40.0	300
15–26	CSZ	9.1	N/A	N/A	N/A	300

Table 3.1: Earthquake scenarios used in the González et al. (2006) study.

(in Japan by Burroughs and Tebbens, 2005, note that the latter study does not differentiate between runup or amplitude estimates and does not provide tables of the data used). In particular, Geist and Parsons (2005) claim that Equation 3.11 works better for locations with limited information about large events. While the concept is appealing in that it describes the maximum tsunami expected from known tectonic events, it carries the intrinsic limitation of having to rely on the existing history of runup available for study to define h_U. For example, this parameter would probably not have been taken as $32m$ for the Aceh province before the Boxing Day tsunami. In Figure 3.4 (reprocessed from Geist and Parsons (2005)), the cumulative rate of tsunamis that exceed the runup value shown on the abscissa is shown for Acapulco. The least–squares curve was obtained as $p(h) = 0.056\,(h^{-0.52} - 20^{-0.52})$ after fixing the maximum height h_U to $20m$.

González et al. (2006) did a pilot study to update the FEMA flood hazard maps for Seaside, Oregon. They studied the 26 worst case scenarios from Table 3.1, eleven of which are from nearfield from the CSZ and fourteen of which are from the farfield sources, eight from the AASZ, five from the KSZ and one from the SASZ. The tsunami and inundation heights from these studies computed to find the probability of exceedance for specified tsunami waveheights and as a result 100–yr and 500–yr flood zones are determined and overlaid on FEMA Flood Insurance Rate Maps for Seaside, Oregon.

Limitations to the time–dependent formalism stem principally from the breakdown of scaling laws at large earthquake sizes. While this breakdown is well documented and well explained by the finite depth of the brittle–ductile transition (Scholz, 1982)–there exists to this day no consensus on the behavior of population statistics for the largest earthquakes (Pacheco et al., 1992; Romanowicz and Rundle, 1993).

This describes to a large extent the populations and the lack of understanding of some of the most fundamental characteristics of earthquake statistics, notably the extent to which large earthquakes can share with smaller events the scale–independent invariant parameters (e.g., stress drops) which ultimately allow the extrapolation of the latter's statistics to populations with few, or even no, records of observations (Okal, 2008). For this reason, a time–independent approach is developed and to compare its results to those of a time–dependent results.

3.4 Probabilistic Tsunami Hazard Assessment for California

In this study, five subduction zones are considered, i.e., the Kuril–Kamchatka and Japan (KSZ), West Aleutians (WASZ), Alaska–East Aleutians (AASZ), Central America (including Mexico) (CASZ) and South America–Chile (SASZ) zones, also shown in Figure 3.5. Note that Cascadia is not included.

For each of these zones, simulations were undertaken for a number of events of variable size and extending over a corresponding number of segments of the NOAA FACTS database. In turn, the return period of each event was computed from the rate of tectonic convergence at the relevant boundary. This tacitly assumes that this convergence is entirely taken up seismically, which has long been known to be incorrect in several subduction zones (Kanamori, 1977a). Indeed, the fraction of tectonic motion expressed seismically (sometimes referred to as the “seismic efficiency” of the boundary) is one of the least well known parameters of seismo–tectonics (Stein et al., 1986), with some subduction zones (e.g., Marianas) totally lacking large earthquakes with a significant contribution to the convergence. The question of understanding to which extent a subduction zone with given physical parameters (age of plate, convergence rate, sediment load, etc.) can support a megathrust event remains unresolved, since the paradigm proposed by (Ruff and Kanomori, 1980) was violated by the 2004 Sumatra earthquake (Stein and Okal, 2007). In this context, the present study targets only subduction zones where very large earthquakes are documented historically and where the seismic efficiency is thought to be high.

Figure 3.5: Source locations of the discretized subduction zones in the Pacific Ocean.

In each subduction zone, a set of 20 generic earthquakes is considered ranging in size from $M_w = 7.65$ to $M_w = 9.30$, and corresponding to a rupture along an increasing number of NOAA FACTS segments. Their characteristics are listed on Table 3.2. The total number of events depends on the particular subduction zone; in the case of AASZ, it was 799 (see Table 3.4). The FACTS database was then used to construct the composite wave fields for each such event through linear combinations of the solutions for the relevant segments, at each of seven targeted offshore sites, which are listed on Table 3.5 and shown in Figure 3.6. For the purpose of this exercise of assembling waveheights to determine probabilities, the computation was stopped at the last point of the coarsest grid from the propagation runs, with coordinates as listed in Table 3.5. The resulting waveheight is used to increment histograms of exceedance for 19 threshold heights ranging from 5 cm to 400 cm. Figure 3.6 shows the locations where the heights were estimated and the grids used in the inundation computations.

The probability of exceedance at a given location and for a given threshold is then computed from an estimate of the return period of each individual event. The latter is derived from the convergence rate at the epicentral plate boundary. The table of Stein and Okal (2007), compiled from recent studies that included GPS measurements, is reproduced in Table 3.3. This table also includes the year of the largest known earthquake in each zone, not necessarily the largest one among our scenarios.

The subduction zones targeted in this analysis for California have been regrouped in the box at the top of Table 3.3. For simplicity, the slip rate has been assumed constant throughout each of the five source regions, and the seismic efficiency is taken universally as 1. The return period of each individual event is then simply assumed to be directly proportional to the slip it releases. Its computation is best illustrated on the following example.

Consider an event in the East Aleutians modeled as a $400km \times 100km$ rupture with a $1m$ seismic slip ($M_w \approx 8.0$). Note that the last time the East Aleutians produced a large earthquake was in 1946 (Okal et al., 2001). Assume that the waveheight from this event at Monterey Bay is $40cm$, and that the return period is sought for a threshold height of $20cm$. This event would then contribute, since its height is higher than $20cm$. Using the slip rate of $64mm/yr$ from Table 3.3, an average return period of $1m/(64mm/yr) \approx 15yr$ for this event is inferred. This annual probability of $(1/15)$ for this tsunami from the East Aleutians will be combined with that of all other events exceeding the threshold at Monterey. The return period for the particular threshold ($20cm$) will simply be the inverse of that cumulative probability. A similar computation is performed for each of the 19 threshold waveheights (5, 10, 15, 20, 30, 40, 50, 60, 70, 80, 100, 120, 150, 180,

case	$L(km)$	$W(km)$	Disp (m)	$mo(Nm)$	M_w
a	100	100	1	3E+20	7.65
b	200	100	1	6E+20	7.85
c	300	100	1	9E+20	7.97
d	400	100	1	1.2E+21	8.05
e	300	100	2	1.8E+21	8.17
f	400	100	2	2.4E+21	8.25
g	500	100	2	3E+21	8.32
h	500	100	3	4.5E+21	8.44
i	600	100	4	7.2E+21	8.57
j	600	100	5	9E+21	8.64
k	700	100	6	1.26E+22	8.73
l	700	100	7	1.47E+22	8.78
m	800	100	8	1.92E+22	8.86
n	800	100	9	2.16E+22	8.89
o	800	100	10	2.4E+22	8.92
p	800	100	12	2.88E+22	8.97
q	800	100	15	3.6E+22	9.04
r	800	100	20	4.8E+22	9.12
s	1000	100	20	6E+22	9.19
t	1000	100	30	9E+22	9.30

Table 3.2: The earthquake scenarios used in time–dependent and independent studies. The smallest earthquake considered is $M_w = 7.65$.

250, 300, 400, $500cm$). Figure 3.7 compiles the resulting return periods as a function of threshold height for each of the five regions, in the case of Crescent City. The final frame (f) shows the global return periods resulting from summing the results from the various epicentral areas.

3.4.1 Time–Independent Estimates for Offshore Tsunami Heights In California

Figure 3.8 regroups the results for six of the seven receiver sites, and return period at six representative threshold heights as listed in Table 3.6. They clearly show that northern California has a higher tsunami risk than southern California. This is expressed in simple

Location	Year	Lat	Lon	Convergence rates (mm/yr)	Plates
South Chile (SASZ)	1960	-39.5	-74.5	70	NZ-SA
Central Chile (SASZ)	1922	-28.5	-70	70	NZ-SA
North Chile (SASZ)	1877	-20	-70.5	68	NZ-AP
South Peru (SASZ)	1868	-18.3	-70.6	67	NZ-AP
North Peru	1940	-10.5	-77	63	NZ-SA
Central America (CASZ)	1992	11.2	-87.8	73	CO-NA
Mexico (CASZ)	1932	19.5	-104.25	30	RI-NA
Alaska (AASZ)	1964	61.04	-147.73	54	PA-NA
East Aleutian (AASZ)	1946	53.31	-162.88	64	PA-NA
West Aleutian (WASZ)	1965	51.1	178.4	73	PA-NA
Kamchatka (KSZ)	1952	52.75	159.5	78	PA-OK
Kuril Islands (KSZ)	1963	44.8	149.5	81	PA-OK
Northeast Japan (KSZ)	1968	40.84	143.22	83	PA-OK
Ecuador-Colombia	1906	1	-81.5	55	NZ-ND
Cascadia	1700	48	-125	42	JF-NA
Nankai	1707	33.2	136.5	57	PS-AM
Ryukyu	1920	30.47	131.29	65	PS-ON
Izu	1947	32.54	141.64	45	PA-PH
Marianas	1929	24.27	142.66	27	PA-MA
Loyalty-Vanuatu	1950	-18.25	167.5	103	AU-NH
Tonga	1865	-20	-173.5	185	NH-CR
Kermadec	1917	-29	-177	63	AU-KE
New Zealand	1931	-39.5	177	43	AU-KE
Java	1994	-10.5	112.8	64	AU-SU
South Sumatra	1833	-3	100	51	AU-SU
North Sumatra	2004	3.3	95.78	33	IN-BU
Makran	1945	24.5	63	28	AR-EU
Lesser Antilles	1974	16.7	-61.4	20	SA-CA

Table 3.3: Plate convergence rate and corresponding earthquake locations and years from Stein and Okal (2007)

Subduction zones	Segments	Number of runs
KSZ	31	519
WASZ	10	99
AASZ	45	559
CASZ	36	619
SASZ	45	799

Table 3.4: Number of runs considered using the scenarios from Table 3.2

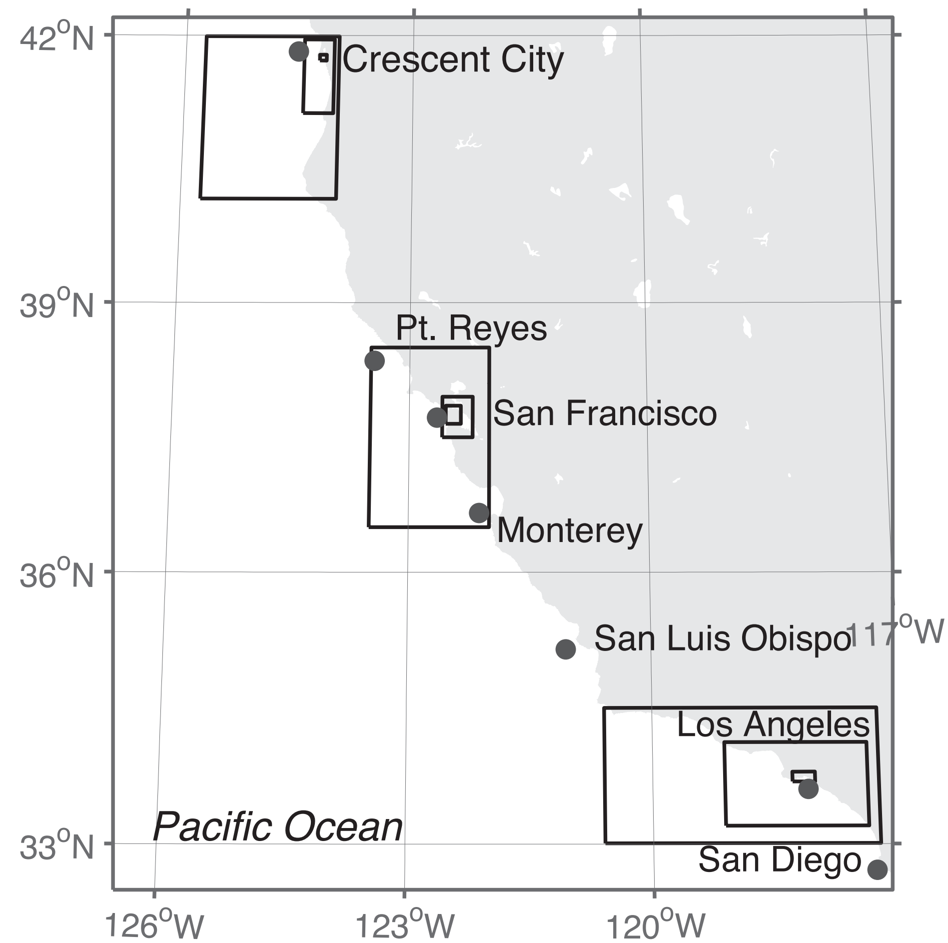

Figure 3.6: The offshore numerical grid locations at Crescent City, Pt. Reyes, San Francisco, Monterey, San Luis Obispo, Los Angeles and San Diego are marked in California map. The coordinates and depth of these locations are listed on Table 3.4. The nested numerical grids for inundation study of Crescent City, San Francisco and Los Angeles Harbor are also shown.

terms by noting that none of the simulations for San Diego or Los Angeles exceeded offshore heights of 2m (and therefore the curves for these sites stop at that height). Indeed, the most extensive damage historically reported in California was in Crescent City.

This is mainly due to the fact that the northern sites (Crescent City, San Francisco) are most vulnerable to AASZ tsunamis, while the southern ones (Los Angeles, San

Location	Longitude	Latitude	Depth (m)
Crescent City	234.95	42.02	422
Pt. Reyes	236.55	38.35	344
San Francisco	237.33	37.72	31
Monterey	237.02	37.72	57
San Luis Obispo	238.95	35.14	448
Los Angeles	241.88	33.61	52
San Diego	242.68	32.713	83

Table 3.5: Coordinates and water depth of the offshore locations used in this study for calculating probabilities of occurance.

	Waveheight (cm)						
	50	100	150	250	300	400	
Crescent City	26	52	105	250	293	469	Return Period (Yr)
Pt. Reyes	42	126	195	313	426	—	
San Francisco	16	60	139	261	426	—	
Monterey	71	174	276	—	—	—	
San Luis Obispo	68	162	249	—	—	—	
Los Angeles	53	293	—	—	—	—	
San Diego	67	218	335	—	—	—	

Table 3.6: Return Period of tsunami waveheights at the California offshore locations listed using earthquake generated waves from the Kuril Islands, the West Aleutians, the Alaska-Aleutians, the Central America and the South America–Chile subduction zones, by assigning return periods from the slip rates from Table 3.3

Diego) are more at risk from the CASZ and SASZ. In turn, directivity effects target California more efficiently from AASZ than from in Central or South America Subduction Zones. The combined effect is a lower tsunami risk in southern California. Specific comparisons, for example between San Francisco and Crescent City, or between Los Angeles and San Diego would require simulations of individual responses of the bays and harbors on a much finer scale than performed here.

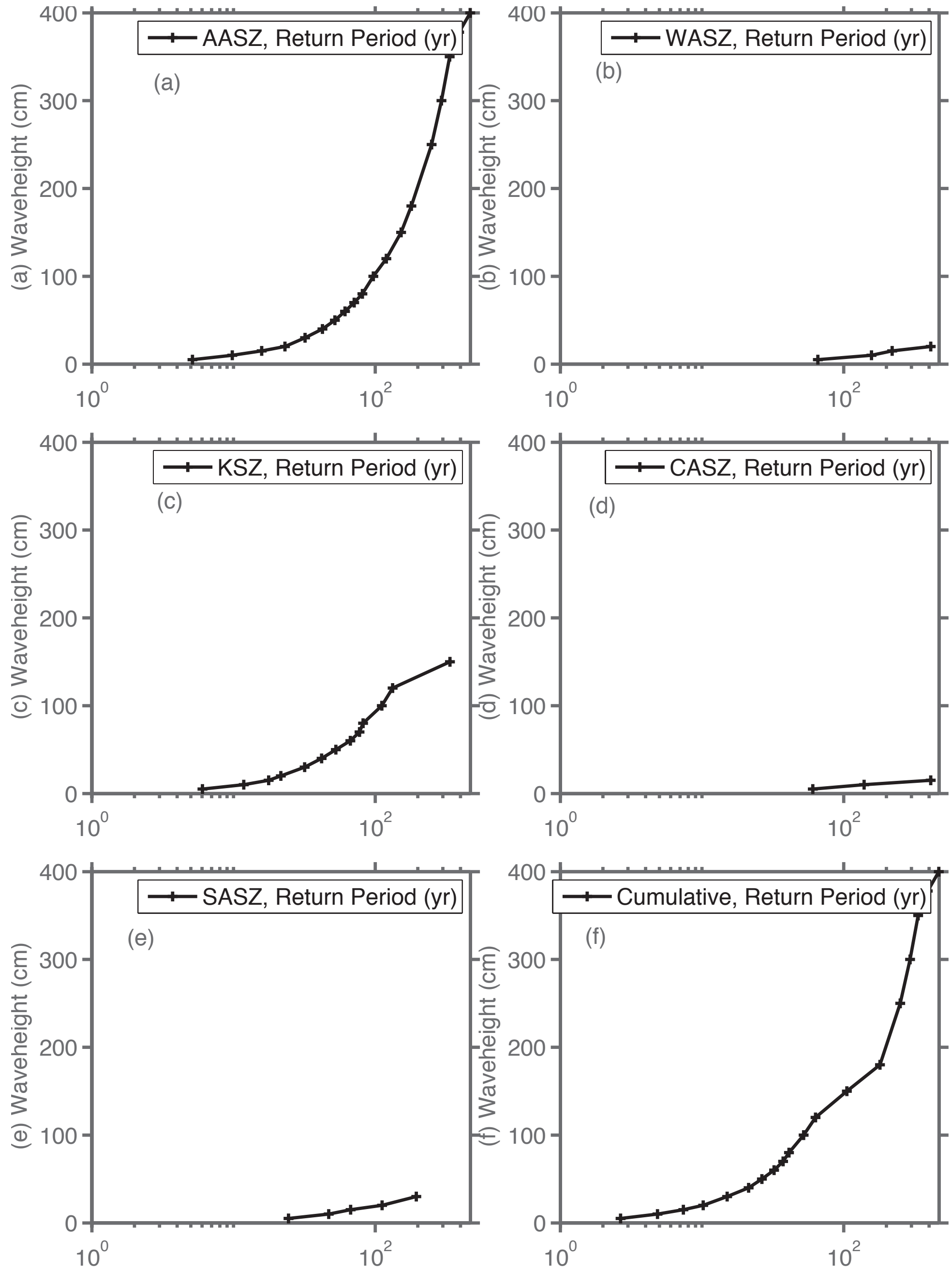

Figure 3.7: Time–independent return period for predicted tsunami heights at Crescent City for different epicentral source regions. Earthquake sources in (a) the Alaska/Aleutians, (b) the West Aleutians, (c) the Kuril Islands, (d) the Central American, and (e) the South America–Chile Subduction Zones. (f) shows the combined results from all farfield sources.

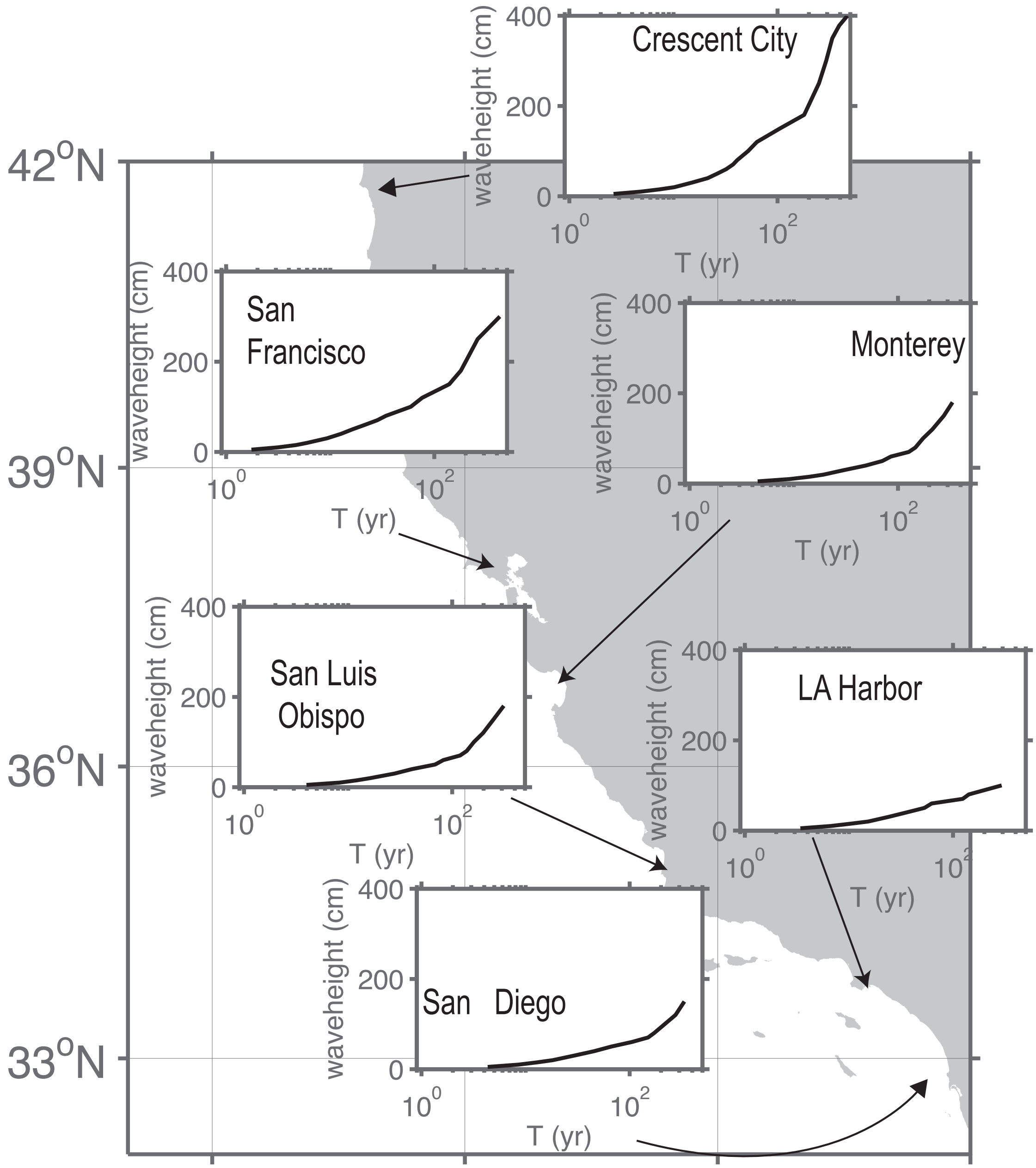

Figure 3.8: Time–independent predicted tsunami heights and their return periods for various locations in California.

3.4.2 Time Dependent Estimates for Offshore Tsunami Heights In California

The time–dependent approach used in this study differs from the time–independent one only in the procedure used to estimate the probabilities (or return periods) of each event, once its waveheights have been computed and, their contribution to exceedance histograms compiled at the various sites. These probabilities are estimated using a frequency-magnitude relation (Gutenberg and Richter, 1942).

For each subduction zone, the Gutenberg-Richter parameters are obtained by applying a least–square fit to the regression of the Centroid Moment Tensor dataset for 1977-2005 (Dziewonski et al., 1983 and subsequent quarterly updates), using the algorithm described by Okal and Romanowicz (1994). Figure 3.9 shows examples of this regression for earthquakes in the Kurils and Alaska regions. Note that the regression is carried out with respect to seismic moment M_0, and hence its slope, β, is 2/3 of the b–value computed from the magnitudes (Molnar, 1979). Note also that these slopes, while generally well matched in worldwide studies (Okal and Romanowicz, 1994; Okal and Sweet, 2007), are lower than their expected value (2/3), and that the breakdown of scaling is not clearly apparent; this is probably an artifact of undersampling. The populations N are then converted to yearly rates by simply dividing them by the duration of the CMT catalog (29 years). It could be argued that the short life span of the CMT catalogue will undersample the population of very large earthquakes and hence overestimate the b–values. The alternative approach, relying on historical or even paleoseismic data would similarly be biased by ignoring small events and hence underestimating the b–value. However, these biases may not happen across the board but rather selectively for specific regions. The occurrence of a single large earthquake (e.g., Mexico 1995, Peru

	Waveheight (cm)						
	50	100	150	250	300	400	
Crescent City	15	37	88	214	315	504	Return Period (Yr)
Pt. Reyes	26	92	169	336	458	—	
San Francisco	11	50	120	280	458	—	
Monterey	50	149	297	—	—	—	
San Luis Obispo	44	138	239	—	—	—	
Los Angeles	45	315	—	—	—	—	
San Diego	52	189	360	—	—	—	

Table 3.7: Time–dependent return period of tsunami waveheights at the California offshore locations listed using earthquake generated waves from the Kuril Islands, the West Aleutians and the Alaska-Aleutians, by assigning return periods using b–value relationship as shown in Figure 3.9

2001, Chile 1995) beyond the critical moment controlling the breakdown of scaling, during the time window sampled for the frequency–size regression, might be sufficient to significantly alter its b–value slope at large sizes.

The results for the time dependent return period are shown in Table 3.7 (this is analogous to Table 3.6 for the time independent return period), Figure 3.10 (analogous to Figure 3.7) and Figure 3.11 (analogous to Figure 3.8). Note that these new results differ in terms of return periods from those of the time–independent study. This property persisted even when using a historical and paleo–seismic population in the frequency–magnitude regression, and it may thus express a systematic bias of the method (Okal, 2007). The latter could be due to the inclusion, in the population used by the time–dependent approach, of events that are not directly related to the subduction, such as outer rise and crustal earthquakes.

3.4.3 Tsunami Return Period of Crescent City, San Francisco And Los Angeles Harbor

Three harbors, from northern, central, and southern California are further investigated for the return period by the time–independent methodology explained earlier in this section, using the inundation model developed in the deterministic studies of Chapter 2. The nested numerical grids used for these harbors, Crescent City, San Francisco and Los Angeles are shown in Figure 3.6. The previously mentioned scenarios from Table 3.2 are individually modeled on each subduction zone segments with a total of 559 cases on the AASZ only, for a total number of 2595 inundation runs (Table 3.4).

Figure 3.12 shows the variation of the tsunami waveheight estimates using inundation models versus the return period, at the Crescent City tide gauge. The maximum modeled waveheight at the tide gauge location is $10.2m$, from extreme scenarios. The total combined return period is also compared to individual return periods from each subduction zone. The results for tsunamis from the AASZ is similar to the cumulative return. The curves for the KSZ and SASZ sources are fairly steep, while the WASZ and the CASZ tsunami hazard is shown lower compared to the others.

In the earlier section, the tsunami return period was computed at an offshore tide gauge location with depth$= 422m$, based on the assumption of linear propagation for superposition and using the Pacific Ocean tsunami propagation database from FACTS. The maximum waveheight at Crescent City was estimated about $401cm$ at $422m$ depth every 469 years. When an inundation model is employed and the waveheight is computed at $5.6m$ depth, this waveheight is amplified by 2.5. In Figure 3.13, the return period from inundation model is compared to time independent and time dependent estimates. Waveheights are normalized by the maximum waveheight from the computation. In summary, the results suggest a $1m$ wave at the Crescent City tide gauge every 7 years, $2m$ every 20 years, $3m$ every 45 years, $5m$ every 92 years, and the biggest wave, $10m$, every 469 years triggered from an earthquake at the AASZ.

Figures 3.14 and 3.15 are similar to Figure 3.13 and compare the return periods of tsunami waveheights computed inundation runs to those computed offshore locations at San Francisco and Los Angeles, respectively. In Figure 3.14, the maximum waveheight at the tide gauge is $7.6m$ compared to $3.3m$ offshore, an amplified 2.3 times (similar to Crescent City). However, in Figure 3.15, the maximum computed offshore waveheight increases from $1.2m$ to $1.7m$ at the tide gauge, with an amplification factor of 1.4.

Probabilistic waveheight predictions for the Crescent City tide gauge can be used to fit exponential or power relations, as in previous studies. A Gutenberg and Richter (exponential) type relationship is obtained by plotting waveheight occurrence in Figure 3.16. The frequency distribution suggested by Houston (1980) is found as $p(h) = .368 \times e^{-.0054h}$, where h is the waveheight. A power frequency distribution is obtained in Figure 3.17 as $p(h) = 27.096 \times h^{-1.293}$, which is a similar type of relationship as in Geist and Parsons (2005).

3.4.4 Conclusion and Discussion

Clearly, the most important result from our probabilistic studies is that the tsunami risk in California decreases from north to south. It is possible to identify three separate regions in terms of tsunami hazard: the northern one extending from the Oregon border to south of Monterey, the central one from Monterey to Point Conception and the southern one from Pt. Conception to the Mexican border. This classification is illustrated by comparing return periods for similar wave amplitudes at the various coastal sites. For example a waveheight of $1m$ is expected every 52 years off Crescent City, 126 years off Pt. Reyes, 60 years off San Francisco and 139 years off Monterey, but only every 162 years off San Luis Obispo, 293 years off Los Angeles and 218 years off San Diego. This trend towards increasing return periods from north to south, obtained with the time–independent algorithm, is similar for other waveheight thresholds, and also when using the time dependent approach.

We emphasize again that this latitudinal gradient along the coast expresses the different geographic origins of the tsunamis threatening the various regions, with northern California exposed to the AASZ and southern California to the Central and South American Subduction Zones. Another feature expressed in the dataset is that only the northern coastlines (Crescent City, Pt. Reyes, San Francisco and Monterey) can expect maximum offshore waves exceeding $3m$, while in central California waveheights will not exceed $2.5m$ and $2m$ in southern California. It is unlikely that the latter two values could be exceeded in the future by an unsuspected earthquake, since events with magnitude 9.3 ("t" type in Table 3.2) have been included even in subduction zones where they are not known in the seismic record, e.g., Mexico and the extreme Western Aleutians. However we have not included the possibilities of submarine landslides. A further remark dramatically illustrated during the 2006 Kuril event, is that northern California can be at risk even from distant earthquakes of a class ($M_w \approx 8.3$) which falls short of the megathrust label.

Figure 3.18 compares Wiegel (1970) and Ritter and Dupre (1972) tsunami return periods for San Francisco and Crescent City with the periods predicted in this study. Wiegel's observations shown in black for Crescent City and blue for San Francisco.

The dashed blue line represents Ritter and Dupre's (1972) extrapolation for San Francisco, which is extrapolated from the Crescent City curve with a similar slope. The red line that shows Crescent City predictions from the probabilistic study differs from the Wiegel's (1970) observations. However, the San Francisco predictions (green line) have a similar slope, even though the years are shifted. The intriguing part is that the Crescent City predictions for AASZ tsunamis matches Ritter and Dupre's (1972) San Francisco extrapolation. This is no coincidence because four of Weigel's observations were from AASZ, with the 1960 Chile tsunami being the only exception. Considering that Ritter and Dupre's predictions took Crescent City tsunami response as their basis in their extrapolation, Crescent City predictions for AASZ should have a similar slope with San Francisco. Thus, the sensitivity study in Chapter 2 showed that San Francisco Bay has a strong response to AASZ tsunamis and the similarity of San Francisco prediction with Ritter and Dupre's extrapolation should be related to this response as it is mainly affected by AASZ tsunamis. The AASZ has not been as seismically active as it was during the Wiegel's (1970) time, which explains the shift in time.

Finally, we recall that this probabilistic study considers neither the case of Cascadia, which is a regional source requiring more detailed modeling, nor underwater landslide sources, whose statistics remain poorly known despite recent interest in this matter (ten Brink et al., 2007).

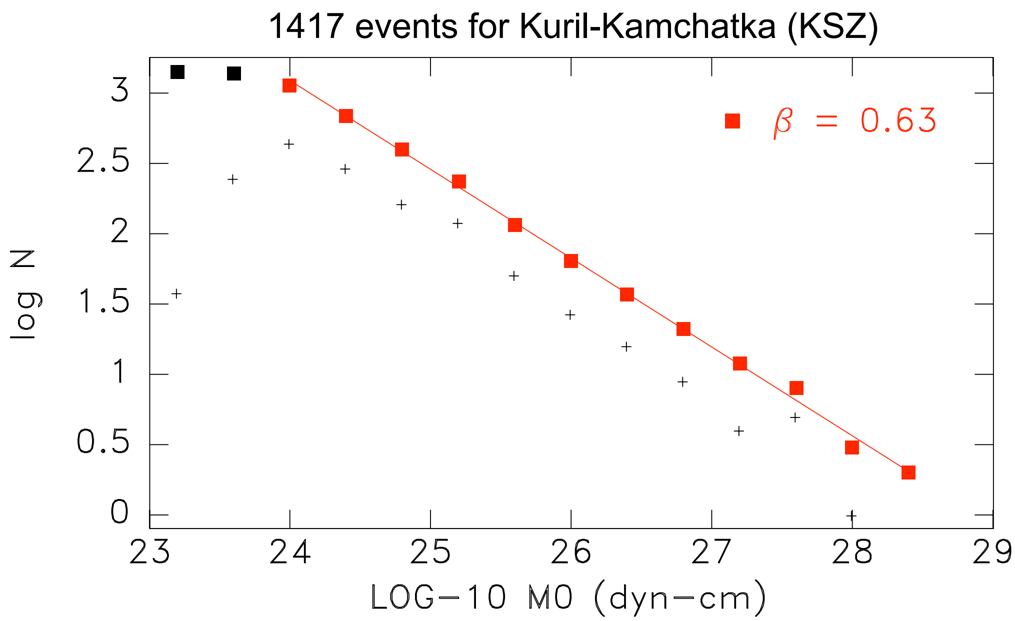

(a)

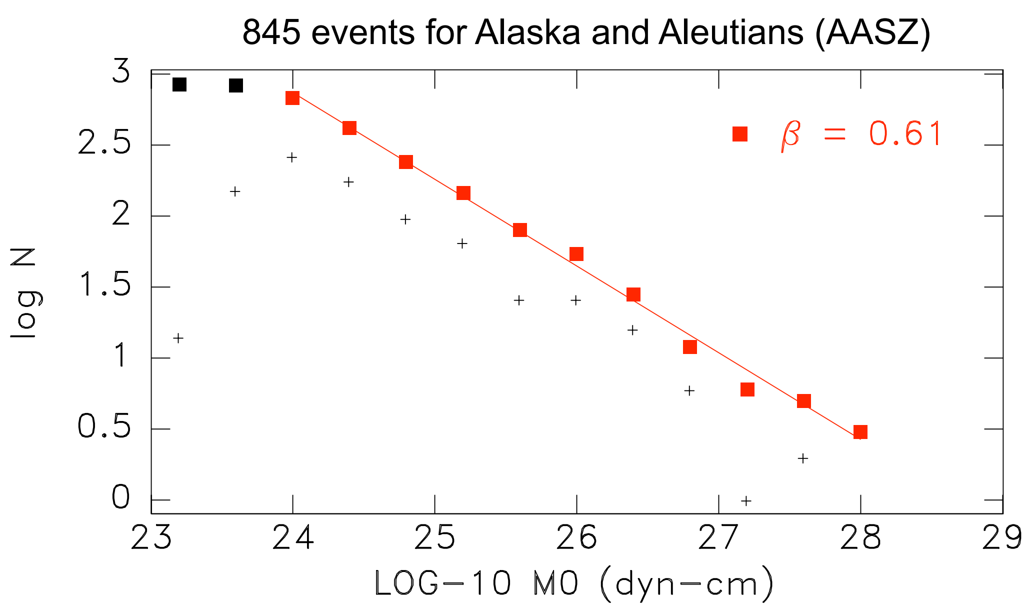

(b)

Figure 3.9: Gutenberg and Richter relationship for (a) Kuril Islands and (b) AASZ.

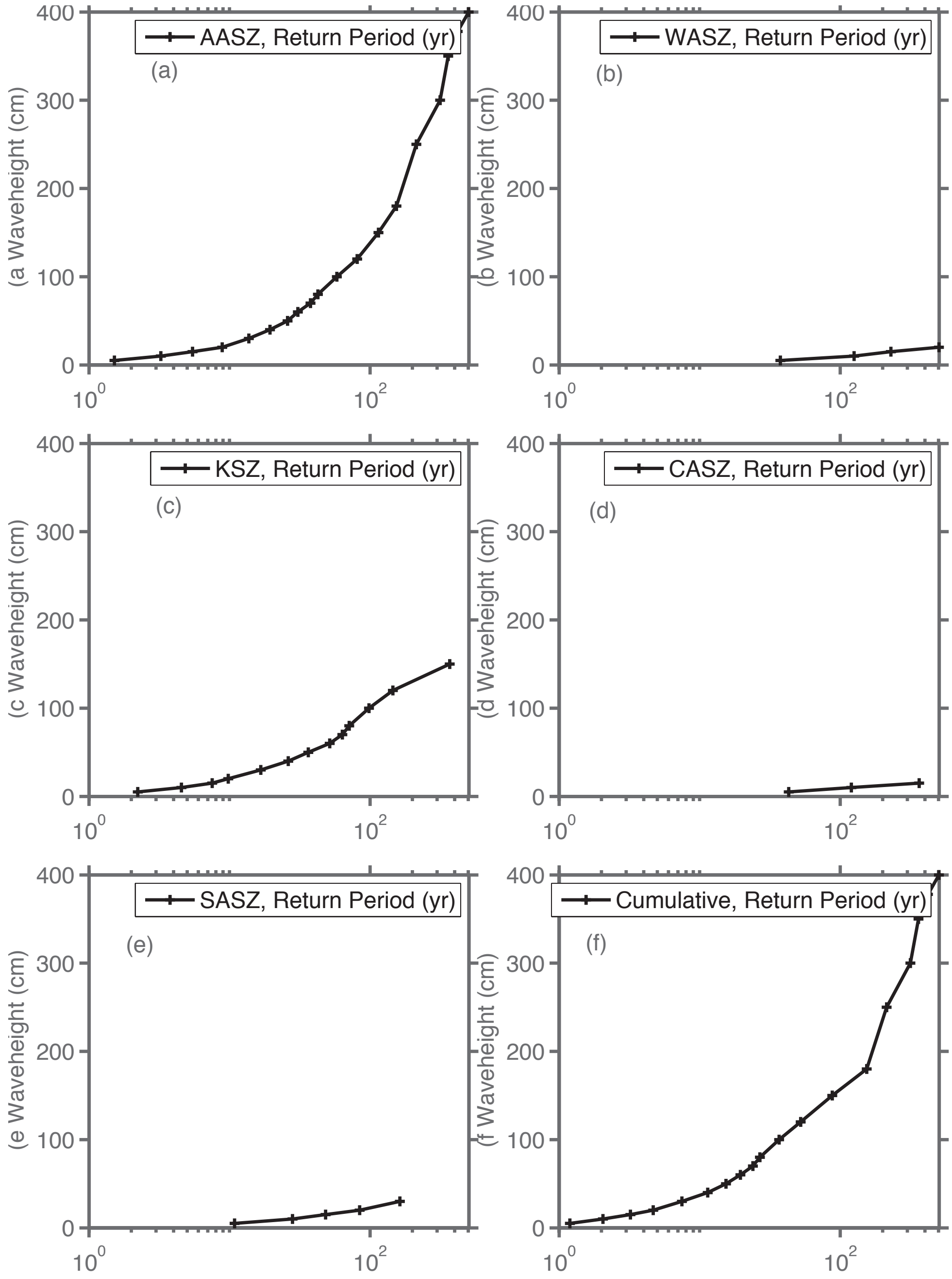

Figure 3.10: Same as Figure 3.7 for time–dependent return period for predicted tsunami heights at Crescent City.

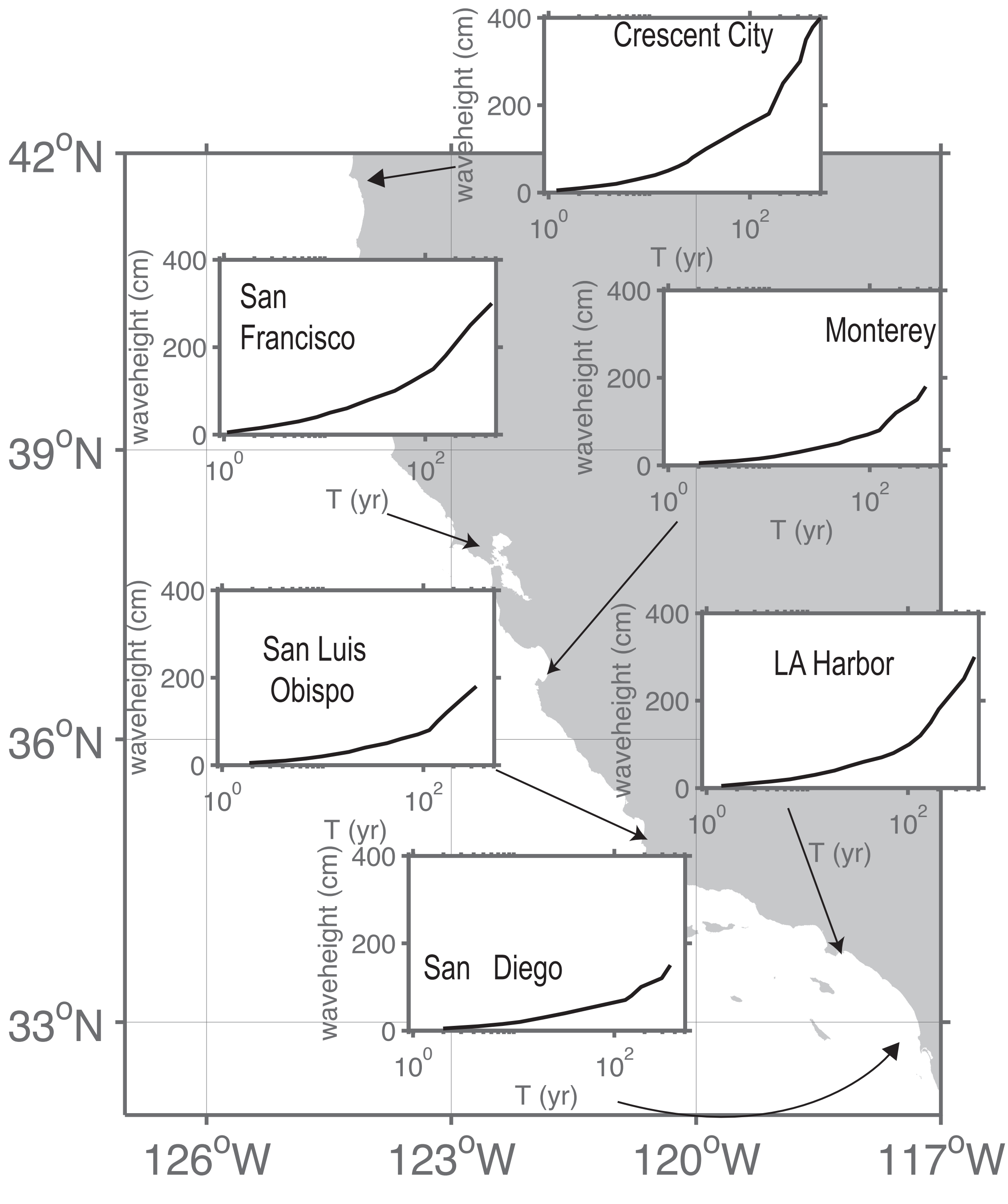

Figure 3.11: Time–dependent predicted tsunami height and their return periods for various locations in California.

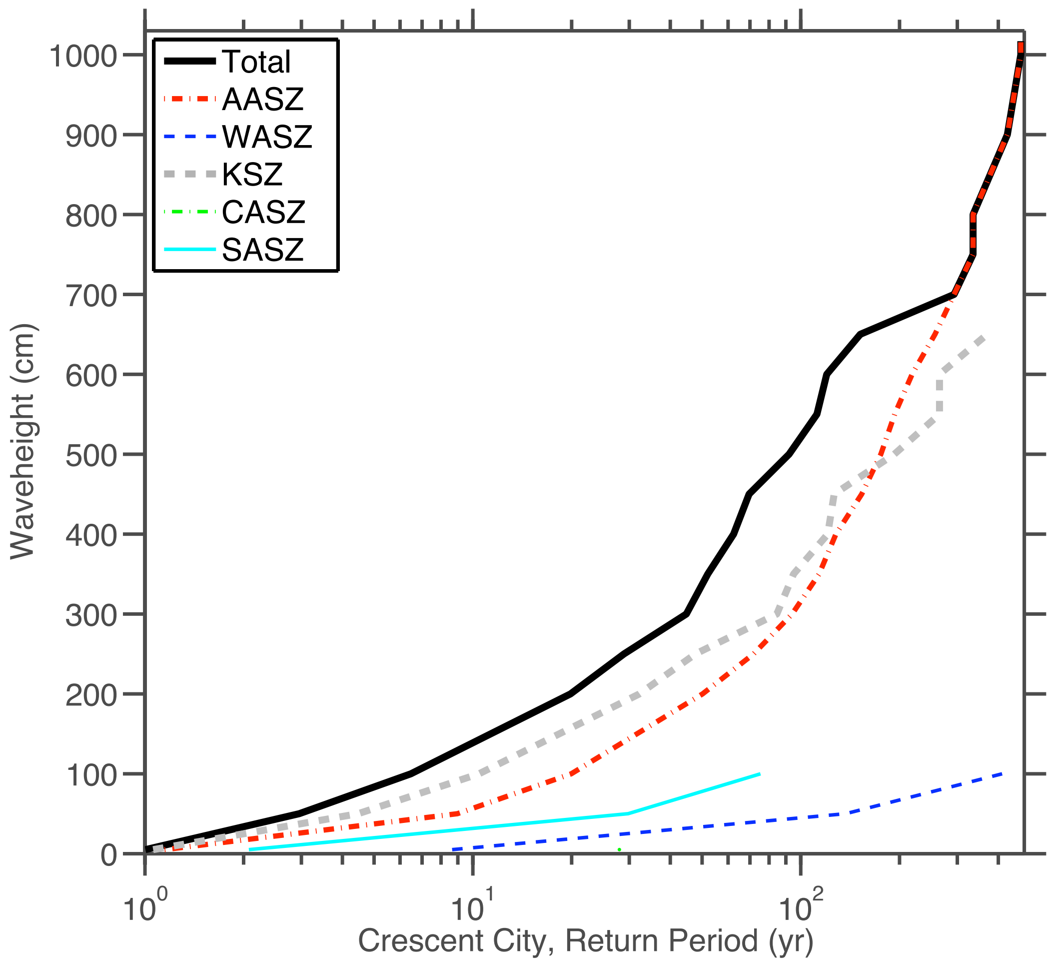

Figure 3.12: Return period of tsunami waveheight at the Crescent City tide gauge at $5.6m$ depth from inundation model runs. In Figures 3.7 and 3.10 the results are from propagation runs at an offshore location at $422m$ depth.

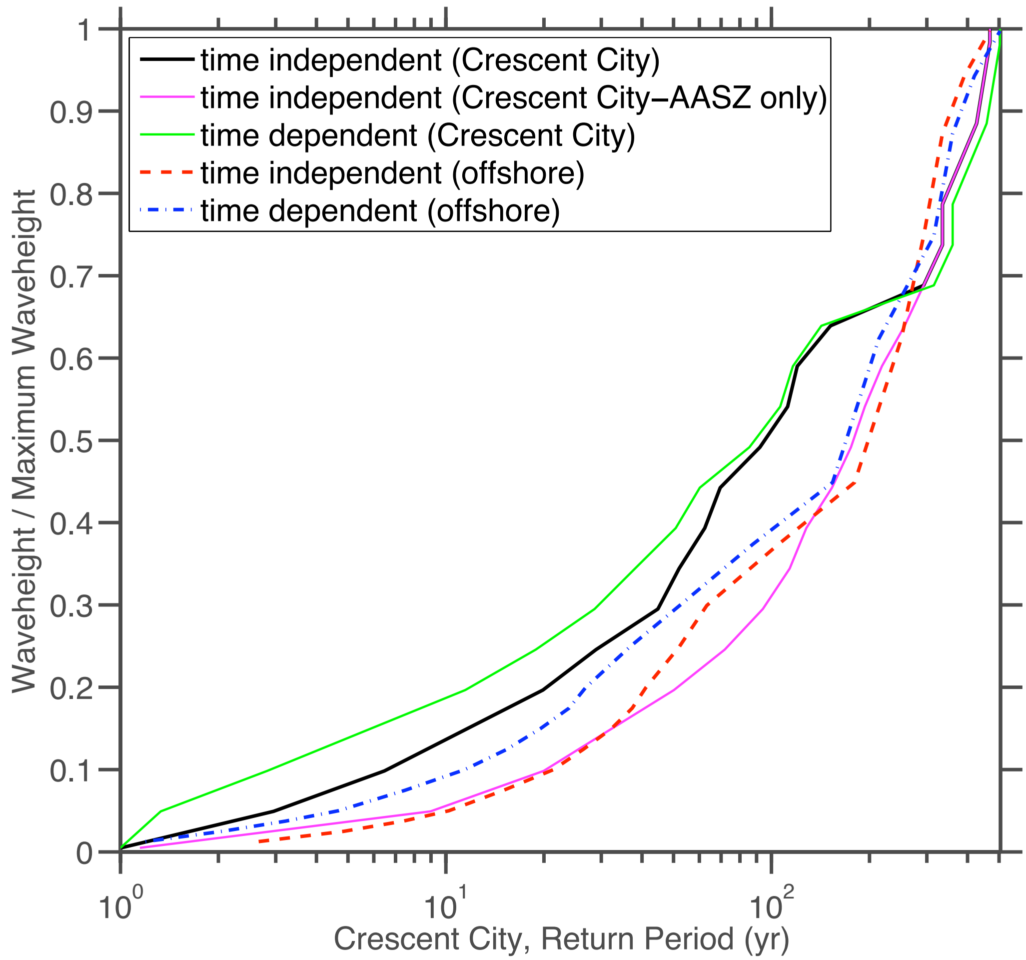

Figure 3.13: Normalized tsunami return period at Crescent City tide gauge at depth= $5.6m$ compared to offshore results at $422m$ depth. Comparison of time dependent and time independent results. The ordinate was normalized with maximum modeled waveheight, $10.2m$ for Crescent City inundation runs and $4m$ for offshore propagation runs.

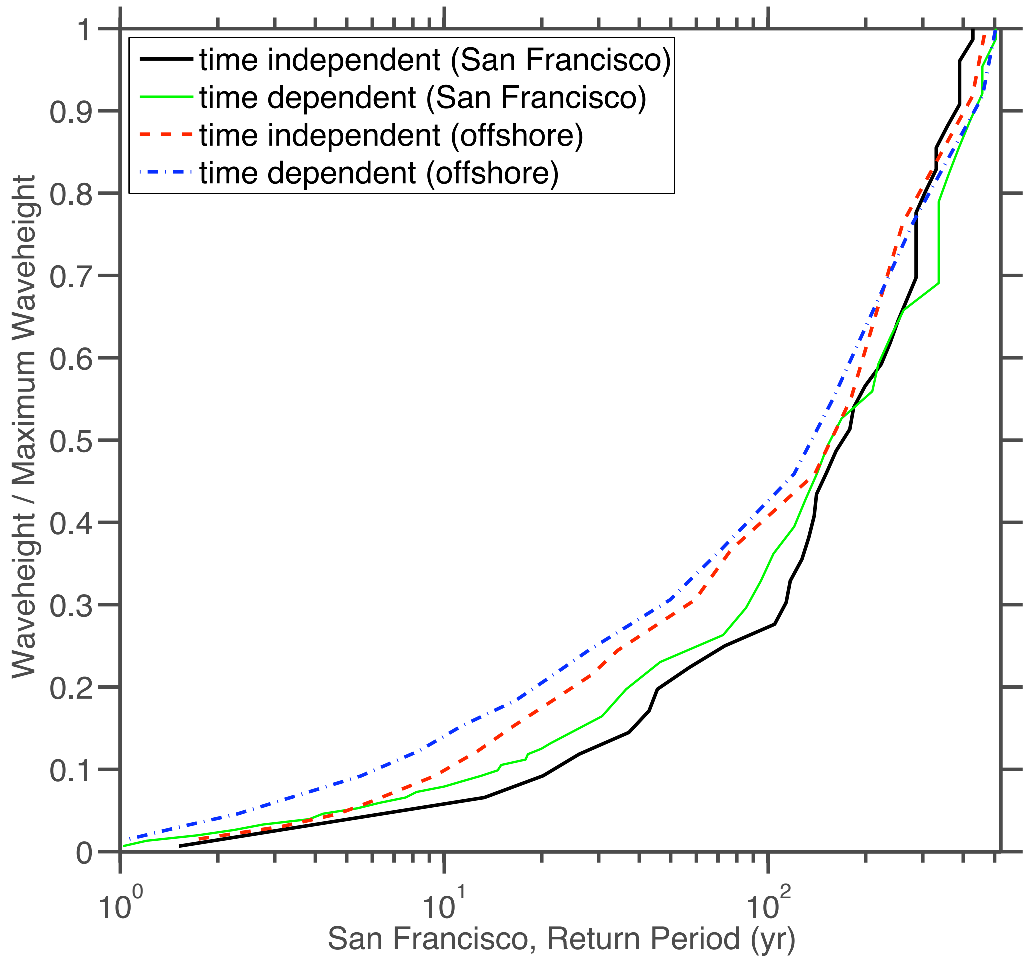

Figure 3.14: Normalized tsunami return period at Presidio, San Francisco tide gauge at depth= $4.7m$ compared to offshore results at $31m$ depth. Comparison of time dependent and time independent results. The ordinate was normalized with maximum modeled waveheight, $7.6m$ for San Francisco inundation runs and $3.3m$ for offshore propagation runs.

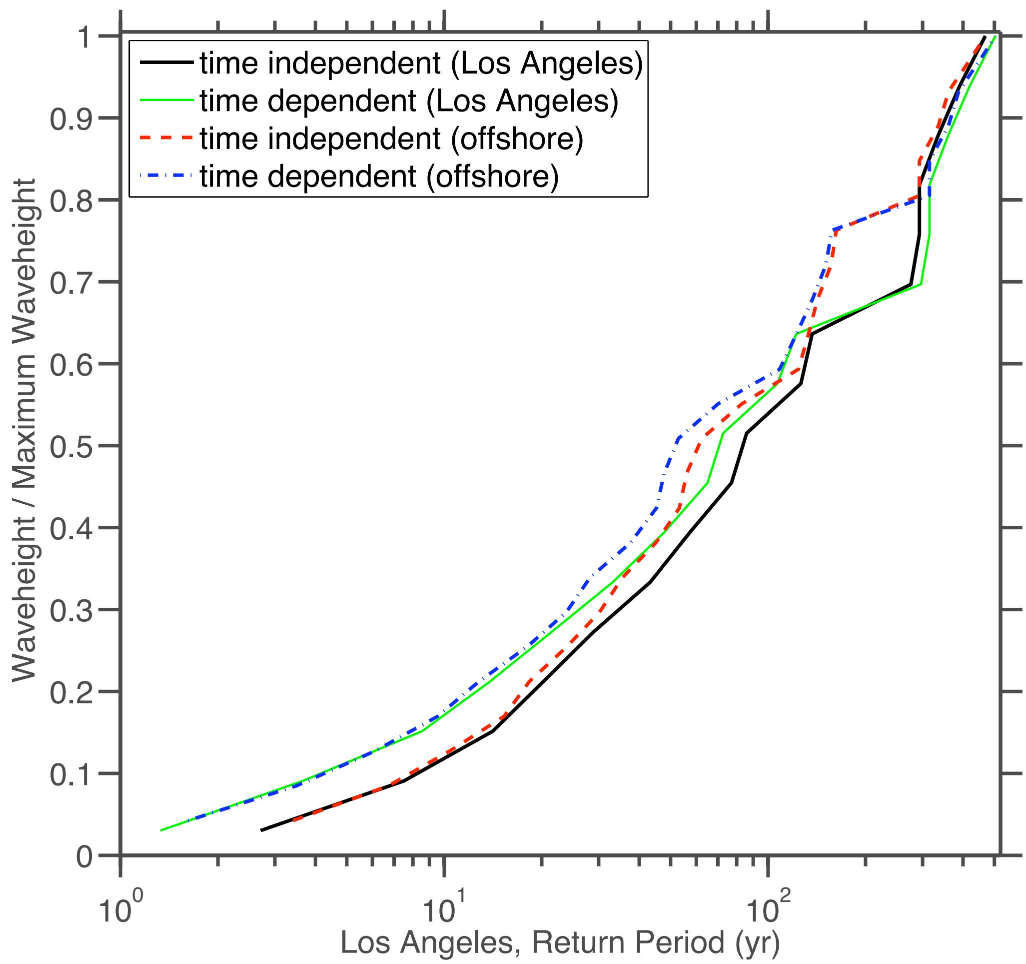

Figure 3.15: Normalized tsunami return period at Los Angeles tide gauge at depth= $15.7m$ compared to offshore results at $52m$ depth. Comparison of time dependent and time independent results. The ordinate was normalized with maximum modeled waveheight, $1.7m$ for Los Angeles inundation runs and $1.2m$ for offshore propagation runs.

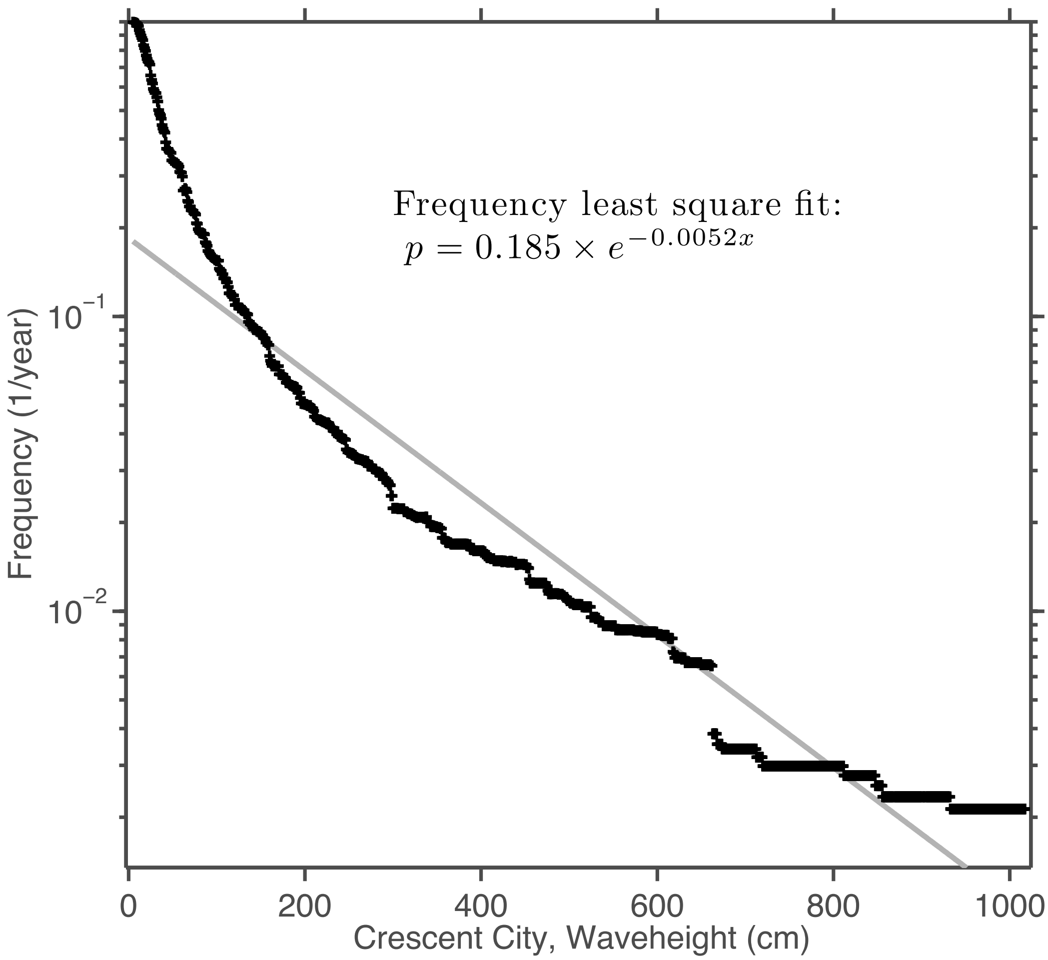

Figure 3.16: Exponential tsunami waveheight recurrence at Crescent City (Gutenberg and Richter, 1942; Houston, 1980).

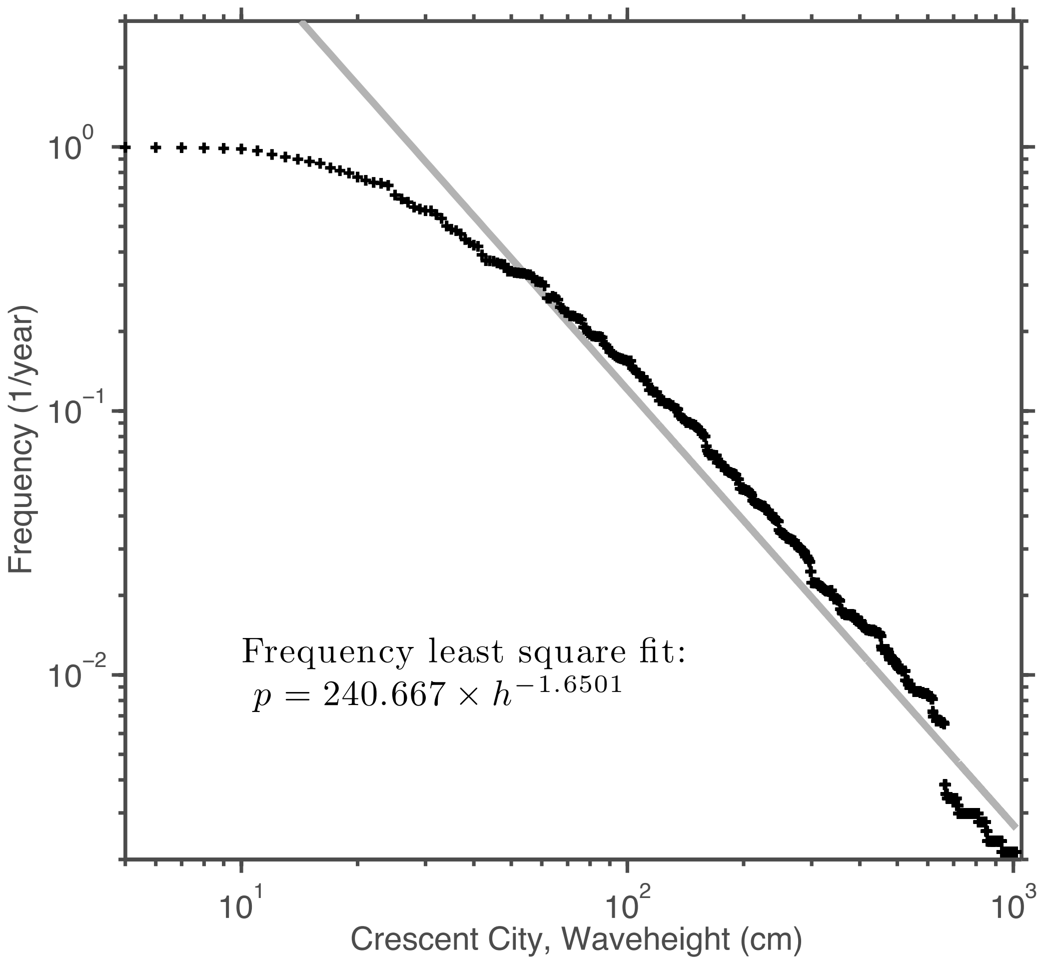

Figure 3.17: Power tsunami waveheight recurrence at Crescent City (Geist and Parsons, 2005; Burroughs and Tebbens, 2005).

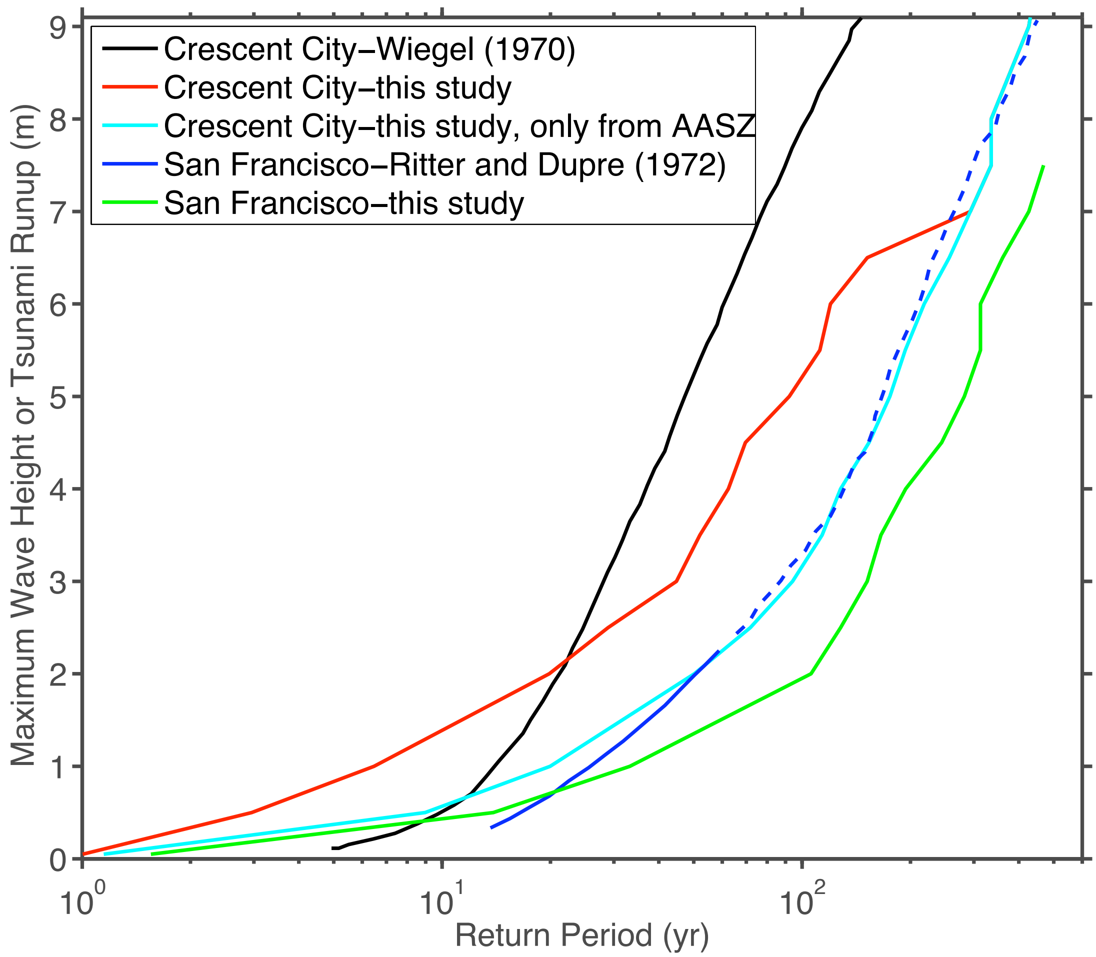

Figure 3.18: Wiegel's (1970) Crescent City predictions for the waveheight based on observations of five earthquakes, and Ritter and Dupre's (1972) San Francisco predictions compared to the computed results for Crescent City and San Francisco. The ordinate indicates waveheight at the tide gauge locations in Crescent City and San Francisco. The legend "maximum waveheight and tsunami runup" is used. This is the same legend as Ritter and Dupre (1972), and it is not possible to differentiate what they meant. Recall that before 1992, runup and waveheight have been used interchangeably.

Chapter 4

Conclusion

Tsunamis are rare events that have caused hazards in US West Coast and California in the recent history. As a scientifically challenging subject, tsunamis have attracted attention on impact estimates that a crucial step in emergency planning and predicting future tsunami hazards.

California is located on the eastern Pacific Ocean and is neighbor to the ocean that experiences the most frequent tsunamis. Two of the three largest tsunamis in the last 100 years, the 1960 Great Chilean and the 1964 Great Alaska earthquakes, occurred in the Pacific Ocean, while Synolakis (2003) lists 97 significant tsunamis between 1891 and 2001 that have occurred in the Pacific Basin.

It's not only the extreme events, as in the 1964 Alaska tsunami that inundated Crescent City 29 city blocks (Dengler and Magoon, 2006; Lander et al., 1993) or the 2004 Boxing Day tsunami inundated up to $4km$ in Banda Aceh (Borrero et al., 2006c), that cause concern. The 15 November, 2006 Kuril Islands tsunami was triggered a $1.76m$ peak to trough tsunami as measured at the tide gauge in Crescent City, California. This moderate tsunami caused \$9.2 million in losses (Dengler et al., 2008; Kelley et al., 2006).

In tsunami hazard assessment, it is crucial to know how often a wave that threatens humans life will arrive and what are the likelihoods of extreme inundation occurring or how frequently our ports and harbors will be in danger. Probabilistic are helpful in emergency management, planning evacuation routes and resource allocation.

Tsunamis can be triggered by earthquakes, volcanic eruptions, meteor impacts or landslides. There are records of historical tsunamis from volcanic eruptions, such as 1883 Krakatau eruption (Francis, 1985; Choi et al., 2003) that has accounts of tsunami wave activity, though meteor impacts are even less common than volcanic eruptions. Recent field survey results and laboratory experiments indicate that the waves generated by landslide or rock fall inherit different wave properties than earthquake generated waves. Landslide generated tsunamis and local earthquakes are studied in Chapter 2 looking at the hazard in Ports and Harbors, while Chapter 3 focussed on probabilistic tsunami hazard only from the farfield earthquakes.

4.1 Tsunami Hazard in California

California extends from $32^o N$ in the south to $42^o N$ in the north and has a long coastline of over $1300 km$. As discussed earlier in Chapter 1, northern and southern California have different geological features that result in different tsunami hazard from different sources of tsunamis. In the north, the Cascadia Subduction Zone (CSZ) is the biggest concern. Starting from the southern end of the subdcution zone, Cape Mendocino, Humboldt Bay, Orick and Crescent City may experience runup distances up to two times of what was experienced in 1964, as discussed in Uslu et al. (2007, 2008) and Chapter 2. Modeling results suggest that the hazard in northern California is very sensitive to the seismic rupture between the Gorda and North American plates. The rupture between Juan de Fuca and North American plate does not pose an equal threat (Chapter 2).

The effect of the Cascadia Subduction Zone decays very rapidly south of Cape Mendocino due to the favorable orientation of central and northern California towards Aleutians and the directivity of tsunamis from Cascadia towards the mid-Pacific. From Cape

Mendocino all the way south to Pt. Conception has greater tsunami hazard from the Eastern Aleutians or Alaska (ASSZ). The sensitivity study in Chapter 2, carried out using NOAA's FACTS database, showed that the central California tsunami responses were higher for tsunamis from AASZ earthquakes than from other sources and may experience a larger hazard than in 1964. Even though an extreme event from the southern end of the CSZ is a cause of concern, locally in the Pacific Northwest Section 2.4 shows that the tsunami waves radiate away from the California coast.

Modeled and historical farfield tsunamis are smaller in amplitude in southern California than the rest of the state. This is partially because of its orientation towards the mid–Pacific, its distance from the AASZ, and the complex offshore geography of the Channel and Santa Catalina islands. However, the sensitivity study in Chapter 2 computed that tsunamis from Peru and Chile Subduction Zones (SASZ) are as dangerous as they are from AASZ. The offshore fault lines in southern California also pose a threat to trigger moderately hazardous tsunamis for ports as well. The biggest danger in southern California is from the submarine landslides from offshore canyons around Redondo, Palos Verdes and Santa Barbara (Borrero et al., 2001; Borrero, 2002; Borrero et al., 2004b).

4.2 Probabilistic Farfield Tsunami Predictions in California

Probabilistic hazard modeling was performed first at seven offshore locations as shown in Figure 3.6, and then later at tide gauge locations at Crescent City, San Francisco and Los Angeles Harbor. The return periods of individual events are calculated with two different methods. First, return periods are calculated from the GPS convergence rate at the plates by assuming that any new event is time independent from the previous earthquakes, and second, by a regression from the Centroid Moment Tensor dataset for 1977-2005 (Dziewonski et al., 1983 and subsequent quarterly updates).

The computations show that the time–dependent or time–independent return periods vary only marginally and tsunamis are more frequent and larger in amplitude in the north from farfield sources and decreases towards the south as in Figures 3.6 and Figures 3.7. Figure 4.1 summarizes the tsunami hazard prediction with a similar figure to McCarthy et al. (1993). The results suggest that California may experience a $1m$ offshore tsunami every 37–52 years at Crescent City, 92–126 years at Pt. Reyes, 50–60 years at San Francisco, 149–174 years at Monterey, 138–162 years at San Luis Obispo, 315–293 years at Los Angeles and 189–218 years at San Diego. The frequency of a $1m$ wave changes at the tide gauge locations from 3–7 years at Crescent City, to 21–33 years at San Francisco and 122–130 years at Los Angeles.

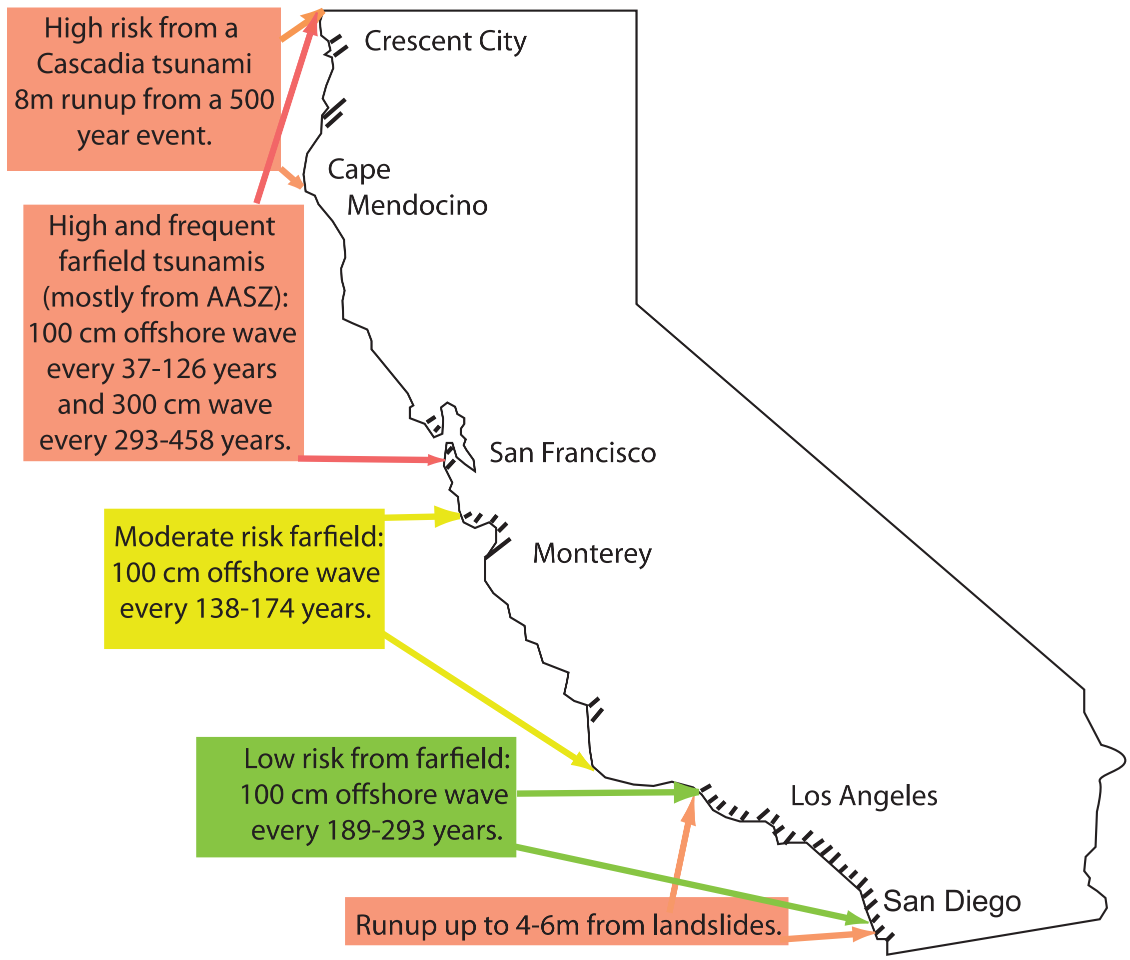

Figure 4.1: Summary of tsunami hazard predictions in California are shown red colors indicating higher risk compared to green with low.

References

Abramson, H. (1998). Evidence for tsunamis and earthquakes during the last 3500 years from Lagoon Creek, a coastal freshwater marsh, Northern California. Master's thesis, Humboldt State University.

Agnew D.C., et al (1988). Probabilities of large earthquakes occuring in california on the san andreas fault. *USGS Open File Report*, 88-398:62 pp.

Ambraseys, N. and Synolakis, C. E. (2009). Tsunami catalogs for the Eastern Mediterranean- revisited. *Manuscript under review*.

Ambraseys, N. N. and Melville, C. P. (1982). *History of Persian earthquakes*. Univ. press, Cambridge.

Ando, M. (1975). Source mechanism and tectonic significance of historical earthquakes along the Nankai through, Japan. *Tectonophysics*, 27:119–140.

Atwater, B. F. (1987). Evidence for great holocene earthquakes along the outer coast of Washington State. *Science*, 236:942–944.

Atwater, B. F. and Hemphill-Haley, E. (1997). Recurrence intervals for the greta earthquakes of the pas 3,500 years at Northeastern Willapa Bay, Washington. Geological Survey Professional Paper 1576, USGS.

Atwater, B. F., Nelson, A. R., Clague, J. J., Carver, G. A., Yamaguchi, D. K., Bobrowsky, P. T., Bourgeois, J., Darienzo, M. E., Grant, W. C., Hemphill-Haley, E., Kelsey, H. M., Jacoby, G. C., Nishenko, S. P., Palmer, S. P., Peterson, C. D., and Reinhart, M. A. (1995). Summary of coastal geologic evidence for past great earthquakes at the Cascadia subduction zone. *Earthquake Spectra*, 11:1–18.

Baptista, A. (2002). Personal communication – (from PG&E, 2002).

Barberopoulou, A., Qamar, A., Pratt, T. L., Creager, K. C., and Steele, W. P. (2004). Local amplification of seismic waves from the Denali Earthquake and damaging seiches in Lake Union, Seattle, Washington. *Geophys. Res. Lett.*, 31:L03607.

Berkman, S. C. and Symons, J. M. (1964). The tsunami of May 22, 1960 as recorded at tide stations. C&GS 25, U.S. Department of Commerce.

Bernard, V., Mader, C., Curtis, G., and Satake, K. (1994). Tsunami inundation model study of Eureka and Crescent City, California. ERL PMEL 103, NOAA.

Borrero, J., Moore II, J. E., Cho, S., and Synolakis, C. (2005). Natural disasters and California: The regional economic cost of a tsunami wave generated by the Palos Verdes slide. In Taylor, C. and VanMarcke, E., editors, *Acceptable risk processes: Natural and man-made hazards.* ASCE.

Borrero, J. C. (2002). *Tsunami Hazards in Southern California.* PhD thesis, University of Southern California, Los Angeles, California.

Borrero, J. C. (2005). Field data and satellite imagery of tsunami effects in Banda Aceh. *Science*, 308(5728):1596.

Borrero, J. C., Dengler, L., Uslu, B., and Synolakis, C. E. (2006a). Numerical modeling of tsunami effects at marine oil terminals in San Francisco Bay. Technical report, The California State Land Commission.

Borrero, J. C., Dolan, J., and Synolakis, C. E. (2001). Tsunami sources within the Eastern Santa Barbara Channel. *Geophys. Res. Lett.*, 28:643–647.

Borrero, J. C., González, F., Titov, V. V., Newman, J., Venturato, A., and Legg, G. (2004a). Application of FACTS as a tool for modeling, archiving and sharing tsunami simulation results. *EOS, Trans. AGU*, 85(47):Fall Meet., Abstract OS23D–1362.

Borrero, J. C., Legg, M. R., and Synolakis, C. E. (2004b). Tsunami sources in the southern California bight. *Geophys. Res. Lett.*, 31:L13211.1–L13211.4.

Borrero, J. C., Ortiz, M., Titov, V., and Synolakis, C. E. (1997). Field survey of Mexican Tsunami produces new data, unusal photos. *EOS, Trans. AGU*, 78(8):85, 87–88.

Borrero, J. C., Sieh, K., Chlieh, M., and Synolakis, C. E. (2006b). Tsunami inundation modeling for western Sumatra. *Proc. Natl. Acad. Sci. U.S.A.*, 103:19673–7.

Borrero, J. C., Synolakis, C. E., and Fritz, H. M. (2006c). Northern Sumatra Field Survey after the December 2004 Great Sumatra Earthquake and Indian Ocean Tsunami. *Earthquake Spectra*, 22:S93–S104.

Bourgeois, J. (2007). Personal Communication.

Bromirski, P. D., Flick, R. E., and Cayan, D. R. (2002). Storminess variability along the California coast: 1858–2000. *Journal of Climate*, 16:982–993.

Bruns, T. R., Cooper, A. K., Carlson, P. R., and McCulloch, D. S. (2002). Structure of the submerged San Andreas and San Gregorio fault zones in the Gulf of the Farallons off San Francisco, California from high resolution seismic–reflection data. Technical report, USGS.

Burroughs, S. M. and Tebbens, S. F. (2005). Power-law scaling and probabilistic forecasting of tsunami runup heights. *Pure and Applied Geophysics*, 162(2):331–342.

Byrne, D. E., Sykes, L. R., and Davis, D. M. (1992). Great thrust earthquakes and aseismic slip along the plate boundary of the Makran subduction zone. *J. Geophys. Res.*, 97:449–478.

Choi, B. H., Pelinovsky, E., Kim, K. O., and Lee, J. S. (2003). Simulation of the trans-oceanic tsunami propagation due to the 1883 krakatau volcanic eruption. *Natural Hazards and Earth System Sciences*, 3:321332.

Cisternas, M., Atwater, B. F., Torrejón, F., Sawai, Y., Machuca, G., Lagos, M., and-Cristián Youlton, A. E., Salgado, I., Kamataki, T., Shishikura, M., Rajendran, C. P., Malik, J. K., Rizal, Y., and Husni, M. (2005). Predecessors of the giant 1960 Chile earthquake. *Nature*, 437:404–407.

Clarke, S. H. and Carver, G. A. (1992). Late holocene tectonics and paleoseismicity, southern Cascadia Subduction Zone. *Science*, 255:188–192.

Cox, D. C. and Mink, J. F. (1963). The tsunami of 23 May 1960 in the Hawaiian Islands. *Bull. Seism. Soc. Am.*, 53:1191–1210.

Cox, D. C. and Morgan, J. (1977). Local tsunamis and possible local tsunamis in Hawaii. Technical Report HIG 77-14, Hawaii Institute of Geophysics.

Dalrymple, R. A. and Kriebel, A. (2005). Lessons in Engineering from the Tsunami in Thailand. *Bridge -Washington- National Academy of Engineering*, 35(2):4–13.

DeMets, C., Gordon, R. G., Argus, D. F., and Stein, S. (1994). Effects of recent revisions to the geomagnetic revearsal time scale on estimates of current plate motion. *Geophys. Res. Lett.*, 21:2191–2194.

Dengler, L. (2007). Personal Communication.

Dengler, L., Uslu, B., Barberopoulou, A., Borrero, J., and Synolakis, C. (2008). The vulnerability of crescent city, california to tsunamis generated by earthquakes in the kuril islands region of the northwestern pacific. *Seis. Res. Let.*, page in publication.

Dengler, L. A. (2006). *Awareness and Preparedness*, pages 51–65. Summary Report on the Great Sumatra Earthquakes and Indian Ocean Tsunamis of 26 December 2004 and 28 March 2005. Earthquake Engineering Research Institute, Oakland, CA.

Dengler, L. A. and Magoon, O. T. (2006). Reassessing Crescent City, California's tsunami risk. In *8th National Conference on Earthquake Engineering*, page R 1451 on cd. Earthquake Engineering Research Institute.

Duke, C. M. (1960). The Chilean Earthquakes of May 1960. *Science*, 132:1797–1802.

Dykstra, D. H. and Jin, W. (2006). Detailed modeling of locally generated tsunami propagation into the ports of Los Angeles and Long Beach. In *30th International Conference on Coastal Engineering*, pages 1603–1616. World Scientific.

Dziewonski, A. M., Friedman, A., Giardini, D., and Woodhouse, J. H. (1983). Global seismicity of 1982: Centroid moment tensor solutions for 308 earthquakes. *Phys. Earth Plan. Int.*, 33:76–90.

Francis, P. W. (1985). The origin of the 1883 krakatau tsunamis. *Journal of Volcanology and Geothermal Research*, 25:349–363.

Fritz, H. M. and Borrero, J. C. (2006). Somalia field survey of the 2004 Indian Ocean tsunami. *Earthquake Spectra*, 22:S219–S233.

Fritz, H. M., Synolakis, C. E., and McAdoo, B. G. (2006). Maldives field survey after the December 2004 Indian Ocean tsunami. *Earthquake Spectra*, 22:S137–S154.

Garcia, A. and Houston, J. (1975). Type 16 flood insurance study: Tsunami predictions for Monterey and San Francisco Bays and Puget Sound. Technical Report WES Report H-75-17, U.S. Army Engineering Station, Vicksburg MD.

Geist, E. L. (2000). Comment on "Origin of the 17 July 1998 Papua New Guinea Tsunami: Earthquake or Landslide?" by E. L. Geist. *Seismol. Res. Lett.* , 71(3):344–351.

Geist, E. L. (2001). Reply to Comments by E. A. Okal and C. E. Synolakis on"Origin of the 17 July 1998 Papua New Guinea Tsunami: Earthquake or Landslide?". *Seismol. Res. Lett.* , 71(3):367–372.

Geist, E. L. and Parsons, T. (2005). Probabilistic analysis of tsunami hazards. *Natural Hazards*, 37(3):277–314.

Geist, E. L., Titov, V. V., and Synolakis, C. E. (2005). Tsunami: Wave of change. *Scientific American*, 294(1):56–63.

Geist, E. L. and Zoback, M. L. (1999). Analysis of the tsunami generated by the $m_w = 7.8$ 1906 San Francisco earthquake. *Geology*, 27:15–18.

Geller, R. J. (1976). Scaling relations for earthquake source parameters and magnitudes. *Bull. Seismol. Soc. Amer.*, 66:1501–1523.

Goldfinger, C., Nelson, C. H., and Johnson, J. E. (2003). Holocene earthquake records from the Cascadia Subduction Zone and Northern San Andreas fault based on precise dating of offshore turbidites. *Annual Review of Earth and Planetary Sciences*, 31:555–577.

González, F., Bernard, E., Dunbar, P., Geist, E., Jaffe, B., glu, U. K., Locat, J., Mofjeld, H., Moore, A., Synolakis, C., Titov, V., and Weiss, R. (2007). Scientific and technical issues in tsunami hazard assessment of nuclear power plant sites. Science Review Working Group NOAA Tech. Memo. OAR PMEL-136, Pacific Marine Environmental Laboratory, Seattle, WA.

González, F., Geist, E., Synolakis, C., Arcas, D., Bellomo, D., Carlton, D., Horning, T., Jaffe, B., Johnson, J., Kanoglu, U., Mofjeld, H., Newmann, J., Parsons, T., Weis, R., Petrson, C., Priest, G., Titov, V., Venturato, A., Weber, J., Wong, F., and Yalciner, A. (2006). Seaside, Oregon tsunami pilot study – Modernization of FEMA flood hazard map. *USGS Open File Report*, 2006–1234:161 pp.

Griffin, W. (1964). *Crescent City's Dark Disaster, March 27-28, 1964*. Crescent City Printing Co.

Gutenberg, B. and Richter, C. F. (1942). Earthquake magnitude, intensity, energy and acceleration. *Bulletin of the Seismological Society of America*, 32:163–191.

Harris, R. A. and Arrowsmith, J. R. (2006). Introduction to the special issue on the 2004 Parkfield earthquake and the Parkfield earthquake prediction experiment. *Bull. Seismol. Soc. Amer.*, 96(4B):S1–S10.

Heaton, T. H. and Kanamori, H. (1984). Seismic potential associated with subduction in the Northwestern United States. *Bulletin of the Seismological Society of America*, 74(3):933–941.

Houston, J. (1980). Type 19 flood insurance study. WES Report HL-80-18, USACE.

Houston, J. and Garcia, A. (1974). Type 16 flood insurance study. WES Report H-74-3, USACE.

Instituto Hidrografico de la Armada (1982). Maremotos en la costa de Chile. Technical report, Valparaiso, Chile.

Jacoby, G. C., E.Bunker, D., and E.Benson, B. (1995). Tree-ring evidence for an A. D. 1700 Cascadia earthquake in Washington and northern Oregon. *Geology*, 25:999–1002.

Jaffe, B. E., Borrero, J. C., Prasetya, G. S., Peters, R., McAdoo, B., Gelfenbaum, G., Morton, R., Ruggiero, P., Higman, B., Dengler, L., Hidayat, R., Kingsley, E., Kongko, W., Lukijanto, Moore, A., Titov, V., and Yulianto, E. (2006). The December 26, 2004 Indian Ocean tsunami in Northwest Sumatra and offshore islands. *Earthquake Spectra*, 22:S105–S136.

Johnson, J. M., Satake, K., Holdahl, S. R., and Sauber, J. (1996). The 1964 Prince William Sound earthquake: Joint inversion of tsunami and geodetic data. *J. Geophys. Res.*, 101(B1):523–532.

Kanamori, H. (1977a). Seismic and aseismic slip along subduction zones and their tectonic implications. *AGU Monograph Maurice Ewing Series*, 1:163–174.

Kanamori, H. (1977b). The energy release of great earthquakes. *J. Geophys. Res.*, 82:2981–2987.

Kawata, Y., Benson, B., Borrero, J. C., Borrero, J. L., Davies, H. L., deLange, W. P., Imamura, F., Letz, H., Nott, J., and Synolakis., C. (1999). Tsunami in Papua New Guinea was as intense as first thought. *EOS, Trans. AGU*, 80(9):101,104–105.

Kelley, A., Dengler, L., Uslu, B., Barberopoulou, A., Yim, S., and Bergen, K. (2006). Recent tsunami highlights need for awareness of tsunami duration. *EOS Transactions AGU*, 87(50):566–567.

Lamberson, R., Grimes, S., and Scarr, D. (1998). A tsunami simulation and shoreline inundation model for Humboldt Bay, pilot study. Technical report, Report to PG&E Geosciences Department.

Lander, J. F., Lockridge, P., and Kozuch, M. (1993). Tsunamis Affecting the West Coast, US 1806-1992. Technical report, U.S. Department of Commerce.

Lay, T. and Kanamori, H. (1980). Earthquake doublets in the Solomon Islands. *Phys. Earth Plan. Int.*, 21:283–304.

Levin, B. W., Kaistrenko, V. M., Rybin, A. V., Nosov, M. A., Pinegina, T. K., Razzhigaeva, N. G., Sasorova, E. V., Ganzei, K. S., Ivel'Skaya, T. N., Kravchunovskaya, E. A., Kolesov, S. V., Evdokimov, Y. V., Bourgeois, J., Macinnes, B., and Fitzhugh, B. (2008). Manifestations of the tsunami on November 15, 2006, on the central Kuril Islands and results of the runup heights modeling. *Doklady Earth Sciences*, 419:335–338.

Liu, P. L.-F., Lynett, P., Fernando, J., Jaffe, B. E., Fritz, H. M., Higman, B., Morton, R., Goff, J., and C. E. Synolakis, C. (2005). Observations by the International Tsunami Survey Team in Sri Lanka. *Science*, 308(5728):1595.

Liu, P. L.-F., Synolakis, C. E., and Yeh, H. H. (1991). Report on the international workshop on long-wave run-up. *Journal of Fluid Mechanics*, 229:675–688.

Liu, P. L.-F., Yeh, H., and Synolakis, C. E., editors (2007). *Advanced Numerical Models for Simulating Tsunami Waves and Runup*, volume 10, Singapore. World Scientific Publishing.

Lopez, A. M. and Okal, E. A. (2006). A seismological reassessment of the source of the 1946 Aleutian 'tsunami' earthquake. *Geophysical Journal International*, 165:835–849.

Magoon, O. T., editor (1962). *The tsunami of May 1960 as it affected Northern California*, Hydraulics Division Conference, Davis, California. ASCE.

Magoon, O. T., editor (1966). *Structural Damage by Tsunamis*, Specialty Conference on Coastal Engineering, Santa Barbara, California. ASCE.

McCarthy, R. J., Bernard, E. N., and Legg, M. R., editors (1993). *The Cape Mendocino Earthquake: A Local Tsunami Wakeup Call?*, In Coastal Zone '93 Volume 3, Proceedings of the Eight Symposium on Coastal and Ocean Management, New Orleans, Louisiana. ASCE.

McCulloch, D. (1985). Evaluating tsunami potential. *U.S. Geol. Survey Prof. Paper*, 1360(374-413).

Minster, J. B. and Jordan, T. H. (1978). Present day plate motions. *J. Geophys. Res.*, 83(B11):5331–5354.

Molnar, P. (1979). Earthquake recurrence intervals and plate tectonics. *Bull. Seismol. Soc. Amer.*, 69:115–133.

Murty, T. S. (1979). Submarine slide-generated water waves in Kitimat Inlet, British Columbia. *J. Geophys. Res.*, pages 7777–7779.

Myers, E. P., Baptista, A. M., and Priest, G. R. (1999). Finite element modeling of potential Cascadia Subduction Zone tsunamis. *Science of Tsunami Hazards*, 17:59–73.

Nanayama, F., Satake, K., Furukawa, R., Shimokawa, K., Atwater, B. F., Shigeno, K., and Yamaki, S. (2005). Unusually large earthquakes inferred from tsunami deposits along the Kuril trench. *Nature*, 434:660–663.

Nelson, A. R., Kelsey, H. M., and Witter, R. C. (2006). Great earthquakes of variable magnitude at the Cascadia subduction zone. *Quaternary Research*, 65(3):354–365.

Nettles, M., Ekström, G., Dziewoński, A. M., and Maternovskaya, N. (2005). Source characteristics of the great Sumatra earthquake and its aftershocks. *EOS, Trans. AGU*, 86(18):Abstract U43A–01.

Okal, E. and Synolakis, C. (2008). Far–field tsunami hazard from mega-thrust earthquakes in the Indian Ocean. *Geophys. J. Intl.*, 172:995–1015.

Okal, E. A. (1988). Seismic parameters controlling far-field tsunami amplitudes: a review. *Natural Hazards*, 1:67–96.

Okal, E. A. (1992). Use of the mantle magnitude M_m for the reassessment of the moment of historical earthquakes. i: shallow events. *Pure and Applied Geophysics*, 139(1):17–57.

Okal, E. A. (2007). Personal Communication.

Okal, E. A. (2008). Personal Communication.

Okal, E. A., Fritz, H. M., Raveloson, R., Joelson, G., Pancosková, P., and Rambolomanana, G. (2006a). Madagascar field survey after the December 2004 indian Ocean tsunami. *Earthquake Spectra*, 22:S263–S283.

Okal, E. A., Fritz, H. M., Synolakis, C., Raad, P., Al-Shijbi, Y., and Al-Saifi, M. (2006b). Field survey of the 2004 Indonesian tsunami in Oman. *Earthquake Spectra*, 22:S203–S218.

Okal, E. A., Plafker, G., Synolakis, C. E., and Borrero, J. C. (2003). Near-Field Survey of the 1946 Aleutian Tsunami on Unimak and Sanak Islands. *Bulletin of the Seismological Society of America*, 93(3):1226–1234.

Okal, E. A. and Romanowicz, B. A. (1994). On the variation of b–values with earthquake size. *Phys. Earth Plan. Int.*, 87:55–78.

Okal, E. A., Sladen, A., and Okal, E. A. S. (2006c). Rodrigues, Maurtius and Réunion Islands field survey after the December 2004 Indian Ocean tsunami. *Earthquake Spectra*, 22:S241–S261.

Okal, E. A. and Sweet, J. R. (2007). Frequency–size distribution of intraplate earthquakes. *Geol. Soc. Amer., Spec. Pub.*, page in press.

Okal, E. A. and Synolakis, C. E. (2001). Origin of the 17 July 1998 Papua New Guinea Tsunami: Earthquake or Landslide? . *Seismol. Res. Lett.* , 71(3):362–366.

Okal, E. A., Synolakis, C. E., Fryer, G. J., Heinrich, P., Borrero, J., Ruscher, C., Arcas, D., Guille, G., and Rousseau, D. (2001). A field survey of the 1946 Aleutian tsunami in the far field . *Seismol. Res. Lett.* , 73:490–503.

Ortiz, M. and Bilham, R. (2003). Source area and rupture parameters of the 31 December 1881 $M_w = 7.9$ Car Nicobar earthquake estimated from tsunamis recorded in the Bay of Bengal. *J. Geophys. Res.*, 108(B10):ESE_11, 16 pp.

Pacheco, J. F., Scholz, C. H., and Sykes, L. R. (1992). Changes in frequency–size relationships from small to large earthquakes. *Nature*, 355:71–73.

Papoulis, A. (1965). *Probability, random variables, and stochastic processes*. McGraw-Hill, New York.

Parsons, T., Sliter, R. W., Geist, E. L., Jachens, R. C., Jaffe, B. E., Foxgrover, A. C., Hart, P. E., and McCarthy, J. (2003). Structure and mechanics of the Hayward-Rodgers Creek Fault step-over, San Francisco Bay, California. *Bull. Seismol. Soc. Amer.*, 93(5):2187–2200.

PG&E (1966). Letter to R. L. Doan, Director of Reactor Licensing, US A.E.C. from R. H. Peterson, that summarizes Dr. Wiegel's conclusions on the tsunami potential at the PG&E's Humboldt Bay Power Plant: 4 pp., plus Wiegel's 1965 report, Tsunamis at the site of the Pacific Gas and Electric Gas and Electric Company Power Plant at Buhne Point, Humboldt Bay, California, plus figures and appendix). Technical report, Pacific Gas and Electric Company.

PG&E (2003). Safety analysis report. Technical Report TR-HBIP-2002-01, Humboldt Bay ISFSI.

Plafker, G. (1965). Tectonic Deformation Associated with the 1964 Alaska Earthquake. *Science*, 148:1675–1687.

Plafker, G. (1969). Tectonics of the March 27, 1964 Alaska Earthquake. *U.S. Geological Survey Professional Paper*, 543-I.

Plafker, G. (1972). Alaskan earthquake of 1964 and Chilean earthquake of 1960: implications for arc tectonics. *J. Geophys. Res.*, 77(5):901–925.

PMSA (2003). Pacific Merchant Shipping Association. http://www.pmsaship.com/trade_files/PMSA_Maritime_Days.pps.

Priest, G. R., Myers, E. P., Baptista, A. M., Fluck, P., K. Wang, K., and Peterson, C. D. (2000). Source simulation for tsunamis: lessons learned from fault rupture modeling of the Cascadia Subduction Zone. *Science of Tsunami Hazards*, 18:77–106.

Raichlen, F. (1966). Harbor resonance. In Ippen, A. T., editor, *Coastline and estuarine hydrodynamics*, pages 281–340, New York, NY. McGraw-Hill.

Rastogi, B. K. and Jaiswal, R. K. (2006). A catalog of tsunamis in the Indian Ocean. *Proc. Natl. Acad. Sci. U. S. A.*, 25:128–143.

Reid, H. F. (1910). The mechanics of the earthquake, the California earthquake of April 18, 1906. Report of the State Earthquake Investigation Commission, 87(2), Carnegie Institute of Washington, Washignton,D. C.

Ritter, J. and Dupre, W. (1972). Maps showing areas of potential inundation by tsunamis in the San Francisco Bay Region, California. *U.S. Geological Survey, Miscellaneous Field Studies*, Map MF-480.

Romanowicz, B. A. and Rundle, J. B. (1993). Scaling relations for large earthquakes. *Bull. Seismol. Soc. Amer.*, 83:1294–1297.

Rueda, F. J. and Schladow, S. G. (2002). Surface seiches in lakes of complex geometry. *Limnol. Oceanogr.*, 47:906–910.

Ruff, L. J. and Kanomori, H. (1980). Seismicity and the subduction process. *Phys. Earth Plan. Int.*, 23:240–252.

Rundle, J. B. (1989). Derivation of the complete Gutenberg–Richter magnitude–frequency relation using the principle of scale invariance. *J. Geophys. Res.*, 94:12337–12342.

Ruscher, C. R. (1999). *The sloshing of trapezoidal reservoirs*. PhD thesis, University of Southern California, Los Angeles, California.

Sahu, V. K., Gahalaut, V. K., Rajput, S., Chadha, R. K., Laishram, S. S., and Kumar, A. (2006). Crustal deformation in the Indo-Burmese arc region: implications Indo-Burmese arc region: implications from the Myanmar and Southeast Asia GPS measurements. *Current Science*, 90:1688–1693.

Sanchez, A. J. and Farreras, S. F. (1993). Catalog of Tsunamis on the Western Coast of Mexico. Technical report, NOAA.

Satake, K., Shimazaki, K., Tsuji, Y., and Ueda, K. (1996). Time and size of a giant earthquake in Cascadia inferred from Japanese tsunami records of January 1700. *Nature*, 379:246–249.

Satake, K., Wang, K., and Atwater, B. F. (2003). Fault slip and seismic moment of the 1700 Cascadia earthquake inferred from Japanese tsunami descriptions. *J. Geophys. Res.*, 108(B11):E–7,1–17.

Savage, J. C., Lisowski, M., and Prescott, W. H. (1981). Geodetic strain measurements in Washington. *J. Geophys. Res.*, 86:4929–4940.

Scholz, C. H. (1982). Scaling laws for large earthquakes: Consequences for physical models. *Bull. Seismol. Soc. Amer.*, 72:1–14.

Soloviev, S. L. (1970). Recurrence of tsunamis in the Pacific. In: *Tsunamis in the Pacific Ocean*. Technical report, East-West Cent., Honolulu, Hawaii.

Soloviev, S. L. and Go, C. N. (1969). Catalog of tsunamis in the Pacific (main data). Technical report, Russian Academy of Sciences, Moscow.

Soloviev, S. L. and Go, C. N. (1974). Catalog of tsunamis on the western shore of the Pacific Ocean. Technical report, Nauka Publishing House, Moscow.

Stein, S., Engeln, J. F., DeMets, C., Gorgon, R. G., Woods, D. F., Lundgren, P. R., Argus, D., Stein, C. A., and Wiens, D. A. (1986). The Nazca–South America convergence rate and the recurrence of the great 1960 Chilean earthquake. *Geophys. Res. Letts.*, 13:713–716.

Stein, S. and Okal, E. A. (2005). Speed and size of the Sumatra earthquake. *Nature*, 434:581–582.

Stein, S. and Okal, E. A. (2007). Ultralong period seismic study of the December 2004 Indian Ocean earthquake and implications for regional tectonics and the subduction process. *Bulletin of the Seismological Society of America*, 97:S279–S295.

Stein, S. and Wysession, M. (2002). *An introduction to seismology, earthquakes, and earth structure*. Malden, MA.

Synolakis, C., Bernard, E., Titov, V., glu, U. K., and González, F. (2007). Standards, criteria, and procedures for NOAA evaluation of tsunami numerical models. NOAA Tech. Memo. OAR PMEL-135, NOAA/Pacific Marine Environmental Laboratory, Seattle, WA.

Synolakis, C. E. (1987). The runup of solitary waves. *Journal of Fluid Mechanics*, 185:523–545.

Synolakis, C. E. (2003). *Tsunami and Seiche*, chapter 9, pages 9.1–9.90. Earthquake Engineering. CRC Press LLC, Boca Raton.

Synolakis, C. E. (2008). Personal Communication.

Synolakis, C. E., Bardet, J.-P., Borrero, J., H. L. Davies E. A. Okal, E. A., Silver, E. A., Sweet, S., and Tappin, D. R. (2002). The slump origin of the 1998 Papua New Guinea tsunami. *Proc. Roy. Soc. London, Ser. A*, 458:763–790.

Synolakis, C. E. and Bernard, E. N. (2006). Tsunami science before and beyond boxing day 2004. *Phil. Trans. R. Soc. A*, pages 2231–2265.

Synolakis, C. E. and Kong, L. (2006). Runup Measurements of the December 2004 Indian Ocean Tsunami. *Earthquake Engineering Research Institute*, 22(S3):S67–S91.

Synolakis, C. E., McCarthy, D., Titov, V. V., and Borrero, J. C., editors (1997). *Evaluating the Tsunami Risk in California*, California and the World Ocean '97 Proceeding of the Conference, San Diego, California. ASCE.

Synolakis, C. E. and Okal, E. A. (2005). 1992-2002: Perspective on a decade of post-tsunami surveys. In Satake, K., editor, *Tsunamis: Case studies and recent developments, Adv. Natur. Tech. Haz.*, volume 23, pages 1–30. Springer.

Tadepalli, S. and Synolakis, C. E. (1994). The run up of N-waves on sloping beaches. *Proceedings of the Royal Society, London*, 445(Series A):99–112.

Tadepalli, S. and Synolakis, C. E. (1996). Model for the leading waves of tsunamis. *Phys. Rev. Lett.*, 77(10):2141–2144.

Tanioka, Y., Ruff, L. J., and Satake, K. (1995). The Great Kuril earthquake of Oct. 4, 1994 tore the slab. *Geophys. Res. Lett.*, 22(13):1661–1664.

ten Brink, U. S., Geist, E. L., and Andrews, B. D. (2007). Size distribution of submarine landslides and its implication to tsunami hazard in Puerto Rico. *Geophys. Res. Let.*, 33(11):L11307, 4 pp.

The Bay Institute (2006). About the Bay. http://www.bay.org/about_the_bay.htm.

Titov, V. V. and González, F. (1997). Implementation and testing of the method of splitting tsunami (MOST) model. Technical Memorandum ERL PMEL 112, NOAA.

Titov, V. V., González, F. I., Bernard, E. N., Eble, M. C., Mofjeld, H. O., Newman, J. C., and Venturato, A. J. (2005a). Real-time tsunami forecasting: Challenges and solutions. *Natural Hazards*, 35(1):35–41.

Titov, V. V., Rabinovich, A. B., Mofjeld, H. O., Thomson, R. E., and González, F. I. (2005b). The global reach of the 26 December 2004 Sumatra Tsunami. *Science*, 309:2045–2048.

Titov, V. V. and Synolakis, C. E. (1997). Extreme inundation flows during the Hokkaido-Nansei-Oki tsunami. *Geophys. Res. Lett.*, 24(11):1315–1318.

Titov, V. V. and Synolakis, C. E. (1998). Numerical modelling of tidal wave runup. *J. Waterw. Port Coast. Ocean Eng.*, 124:157–171.

TOPEX (2007). http://topex.ucsd.edu/WWW_html/srtm30_plus.html.

Toppozada, T., Bennett, J. H., Halstrom, C. L., and Young, L. G. (1992). 1898 “Mare Island” earthquake at the southern end of the Rodgers Creek fault. In *Proc. of the Second Conf. on Earthquake Hazards in the Eastern S. F. Bay Area*, number 113 in Special Edition, pages 385–392. CA Dept. of Conservation, Division of Mines and Geology.

Toppozada, T., Borchardt, G., Haydon, W., and Peterson, M. (1995). Planning scenario in Humboldt and Del Norte Counties for a great earthquake on the Cascadia Subduction Zone. Special Publication 115, California Department of Conservation, Division of Mines and Geology.

Toppozada, T. R. (2006). Personal Communication.

USGS Earthquake Database (2007). (USGS) Historic Earthquake Data Base. http://earthquake.usgs.gov/regional/world/historical.php.

Uslu, B., Borrero, J. C., Dengler, L., and Synolakis, C. E. (2007). Tsunami inundation at Crescent City generated by earthquakes along the Cascadia Subduction Zone. *Geophys. Res. Lett.*, 34:L20601.

Uslu, B., Borrero, J. C., Dengler, L., Synolakis, C. E., and Barberopoulou, A. (2008). Tsunami inundation from great earthquakes on the Cascadia Subduction Zone along the northern California coast. In *Solutions to Coastal Disasters*. ASCE.

Wang, K., He, J., Dragert, H., and James, T. S. (2001). Three-dimensional viscoelastic interseismic deformation model for the Cascadia subduction zone. *Earth, Planets, and Space*, 53:295–306.

Wang, K., Wells, R., Mazzotti, S., Hyndman, R. D., and Sagiya, T. (2003). A revised dislocation model of interseismic deformation of the Cascadia Subduction Zone. *J. Geophys. Res*, 108(B1):ETG_9, 13 pp.

Wei, Y., Bernard, E. N., Tang, L., Weiss, R., Titov, V. V., Moore, C., Spillane, M., Hopkins, M., and glu, U. K. (2007). Real-time experimental forecast of the Peruvian tsunami of August 2007 for U.S. coastlines. *Geophys. Res. Let.*, 35:L04609.

Wentworth, C. M., Graham, S. E., Pike, R. J., Beukelman, G. S., Ramsey, D. W., and Barron, A. D. (1997). Summary distribution of slides and earth flows in the San Francisco Bay Region, California. *U.S. Geol. Survey, Open File Report*, 97-745C.

Whitmore, P. M. (1993). Expected tsunami amplitudes and currents along the North American coast for Cascadia subduction zone earthquakes. *Natural Hazards*, 22:59–73.

Wiegel, R. L. (1970). *Earthquake engineering*, chapter Tsunamis, pages 253–306. Prentice Hall, Englewood Cliffs, N. J.

Wilson, B. W. and Torum, A. (1967). Engineering damage from the Tsunami of the Alaskan Earthquake of March 27, 1964. Final Report Conract no. DA-49-055-CIVENG-66-6, U.S. Army Corps of Engineers, Coastal Engineering Research Center, Technical Memorandum No. 25.

Working Group on California Earthquake Probabilities (2003). Earthquake probabilities in the San Francisco Bay region 2002-2031. *U. S. Geol. Survey Open-File Report*, 03-214.

Yamaguchi, D. K., Atwater, B. F., E.Bunker, D., E.Benson, B., and Reid, M. S. (1997). Tree-ring dating the 1700 Cascadia earthquake. *Nature*, 389:922–923.

Yanenko, N. N. (1971). *The Method of fractional steps*. Springer, New York. translated by M. Holt.

Yeats, R. S. (1997). *The Geology of Earthquakes*. Oxford, New York.

Yeh, H., Titov, V. V., Gusiakov, V., Pelinovsky, E., Khramushin, V., and Kaistrenkov, V. M. (1995). The 1994 Shikotan earthquake tsunamis. *Pure and Applied Geophysics*, 144:855–874.

Yeh, H. H., Liu, P. L. F., and Synolakis, C. (1996). *Long-wave runup models*. World Scientific.

Young, R. (2006). Personal Communication.

Zachariasen, J., Sieh, K., Taylor, F. W., Edwards, R. L., and Hantoro, W. S. (1999). Submergence and uplift associated with the giant 1833 Sumatran subduction earthquake: Evidence from coral microatolls. *J. Geophys. Res.*, 104:895–919.

Appendix A

A Case Study, Modeling Tsunamis at the Persian Gulf

A.1 Introduction

In this section, tsunamis triggered in the Makran Subduction Zone (MSZ) in south Pakistan are studied. Three hypothetical cases are used to evaluate the tsunami hazard in the Gulf of Oman and the Persian Gulf, in particular at vulnerable harbors from tsunamis originating at the MSZ, especially at various locations in Kuwait, Saudi Arabia, Bahrain, Qatar, the United Arab Emirates and Oman.

The major motivations is the major earthquake of 27 November 1945 in the central part of the coast of Pakistan ($M_0 = 1.8 \times 10^{28}$ dyne·cm). Its source region probably triggered similar events in 1851 (and possibly 1864) to the west, and 1765 to the east, as shown on Figure A.1 (Byrne et al., 1992; Ambraseys and Melville, 1982). In addition, it is probable that a major earthquake occurred in 1483 to the west, along the present-day Iranian coastline (Ambraseys and Melville, 1982).

Under Ando's (1975) model, the possibility that all three segments (A, B, C on Figure A.1) could rupture at once is considered. This constitutes the first source. The 1483 earthquake along the Gulf of Oman is our second source, and the third one is a supersposition of the first two, featuring a rupture extending all the way from Karachi to the Straits of Hormuz (Okal and Synolakis, 2008).

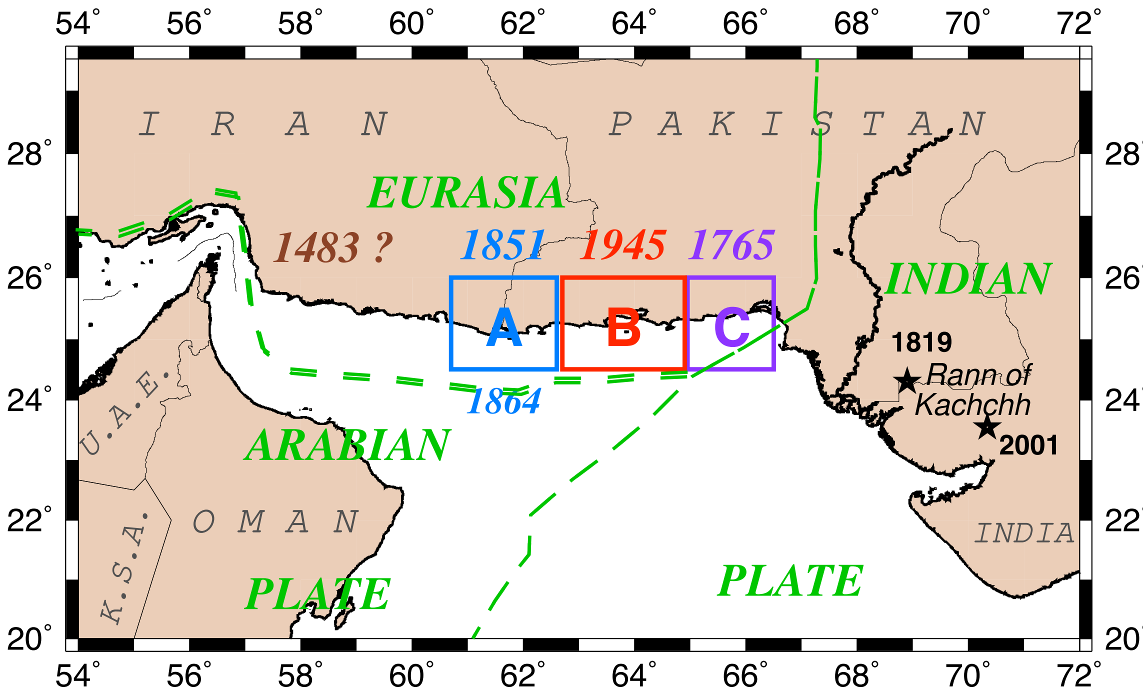

Figure A.1: Map of the Makran coast of Pakistan and Iran, after Byrne et al. (1992). The three blocks "A","B","C" sketch the probable rupture areas of the earthquakes of 1851 (1854), 1945 and 1765. Model I envisions the simultaneous rupture of the three blocks, while Model II corresponds to the probable 1483 rupture to the West. Model III is a superposition of Models I and II. To the East, the stars show the epicenters of the intraplate events of 2001 and 1819, which did not generate tsunamis in the ocean from Okal and Synolakis (2008).

A.2 Sources

The first source models a rupture of $550km \times 100km$ with a seismic slip of $7m$. For the second source, a rupture of $450km \times 150km$ with a $6m$ seismic slip was used. The third source is just a superposition of the first two. Details are summarized in Table A.2 and Figure A.2.

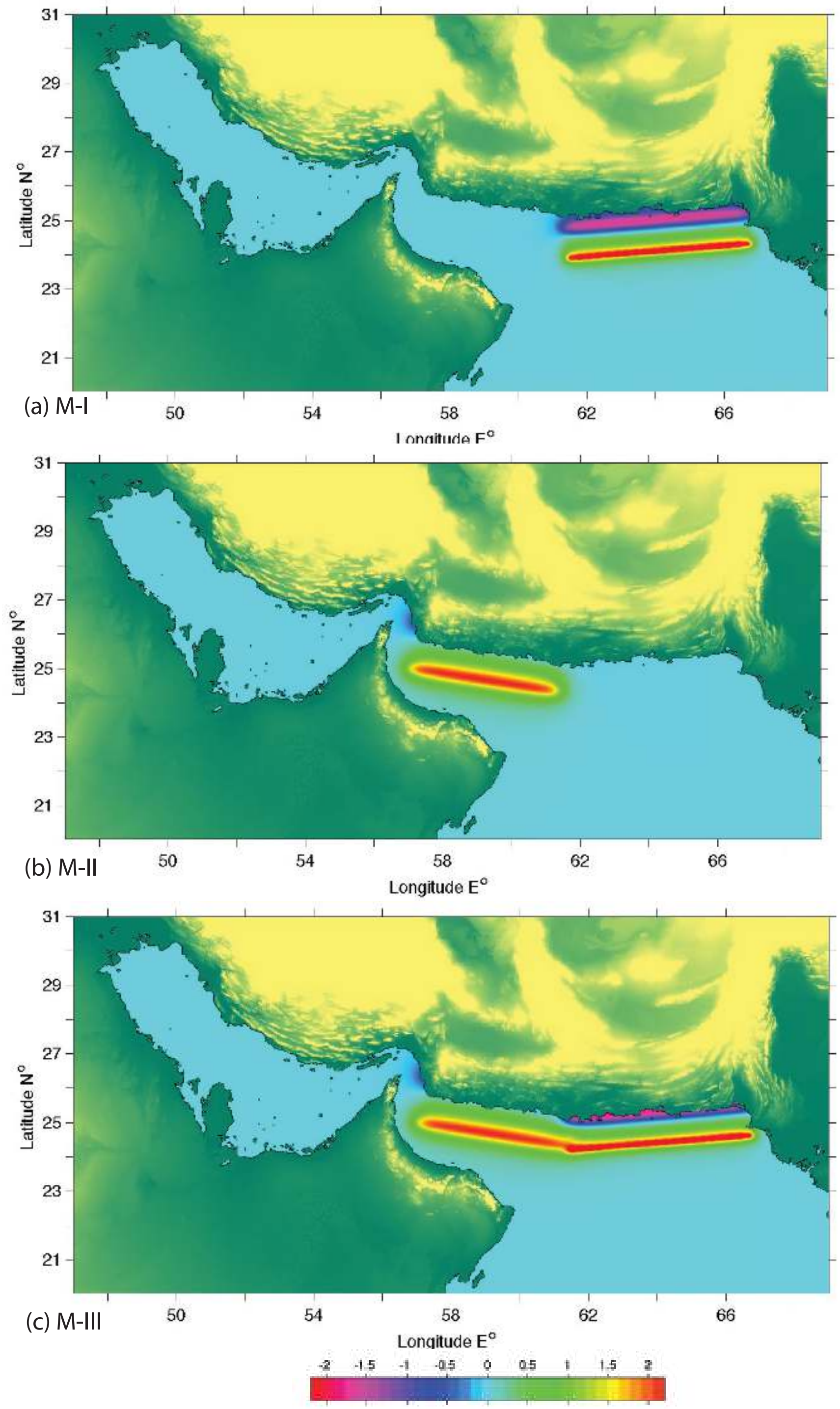

Figure A.2: Initial conditions for MSZ earhtquakes.

EQ	L (km)	W (km)	Disp (m)	M_w
M-I	550	100	7	8.6
M-II	450	150	6	8.6
M-III	1000	125	6.5	8.9

Table A.1: Source parameters of MSZ earthquakes in Persian Gulf and Oman Gulf.

A.3 The Computational Model

The Method Of Splitting Tsunamis (MOST) was used in the numerical modeling, as described in Chapter 1.

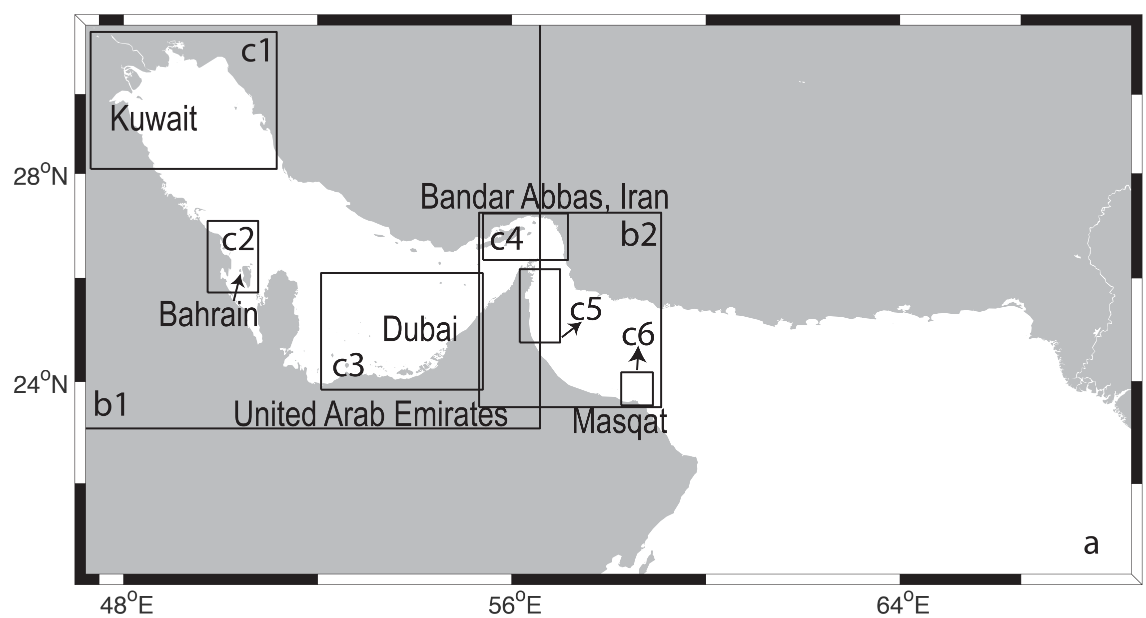

Figure A.3: Numerical grids used in Makran study.

Numerical grids in this study were obtained from a 30-arcsec database derived from TOPEX (2007). Three nested grids for numerical stability and computation speed were used. In Figure A.3, the whole image shows the a grid with 1.5 arc-sec resolution, two different B grids with 30 arc-sec resolution and six high resolution inundation (C) grids with different resolutions between 6 and 15 arc-sec.

A.4 Results

The model results show that the worst case for the Persian Gulf and the Gulf of Oman is scenario M–II, i.e., a partial rupture on west MSZ. Resulting maximum wave heights from the three cases are presented in Figures A.5, A.6, A.7 and A.8, and in this figure we do not see a large difference between M–II and M–III. We looked in more detail at the time histories of virtual tide gauges off Ad Damman, Bahrain, Dubai, Bandar Abbas, East of Bandar Abbas, Diba, Al Fujayra and Masqat, as shown on Figures A.5, A.6, A.7 and A.8. We note that M–II results in a large wave, M–I results in a small wave and M–III results in the superposition of these two cases with an opposite phase. Because of the phase difference, M–II is larger than M–III.

The Gulf is extremely shallow with an average depth of $50m$, not exceeding $100m$ anywhere through its expanse. This makes the waves go slower and causes dissipation. Bahrain is $575km$ from the mouth of the Gulf and Kuwait is more than $900km$ away, which helps reduce the tsunami height. In Figure A.5, the maximum wave height is shown $17cm$ at Ad Damman and $8cm$ at Bahrain. On the other hand, it reaches $40cm$ at Dubai, closer from the straits of Hormuz; waves of this size are known to have caused damage in harbors, as seen in Crescent City following the Kurils earthquake of 15 November 2006 (Kelley et al., 2006).

Outside the Persian Gulf, four gauges were located in the Gulf of Oman, two of them in Iran around Bandar Abbas, one in the United Arab Emirates at Al Fujayrah and the last one in Oman at Masqat to monitor offshore waveheights in the computation.

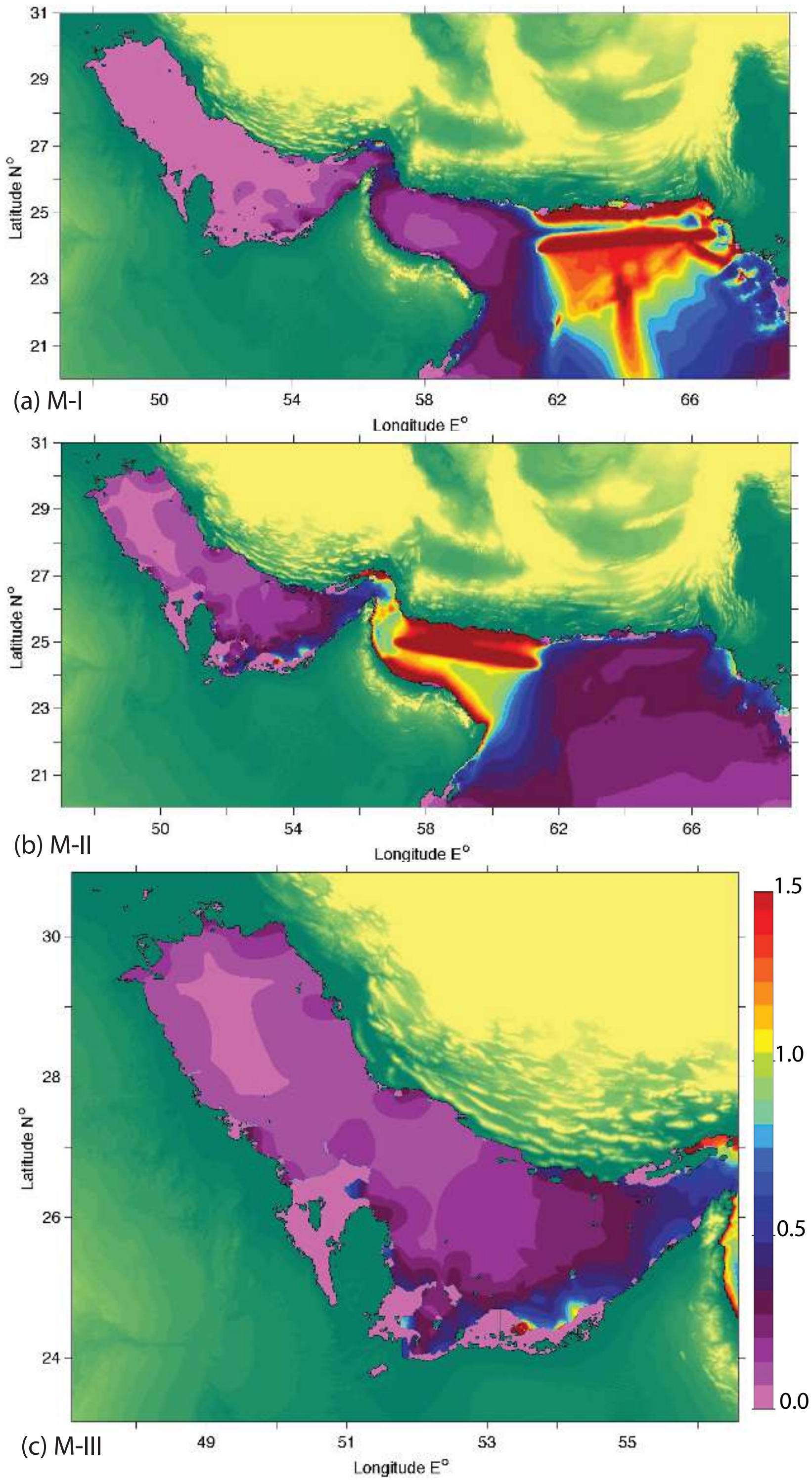

Figure A.4: Maximum waveheight plot from all three cases.

As seen in Figures A.7 and A.8, all four show regular wave periods and wave heights between 1 to $2m$, which suggests significant tsunami hazard. As the tsunami sources are located nearby, the definition and implementation of tsunami evacuation zones is strongly recommended, as well as a vigorous education program.

It should be emphasized that these results are very preliminary and can only be used to infer that the tsunami hazard in the Gulf is substantial. More specific predictions will be require both higher resolution and a dispersive hydrodynamic model.

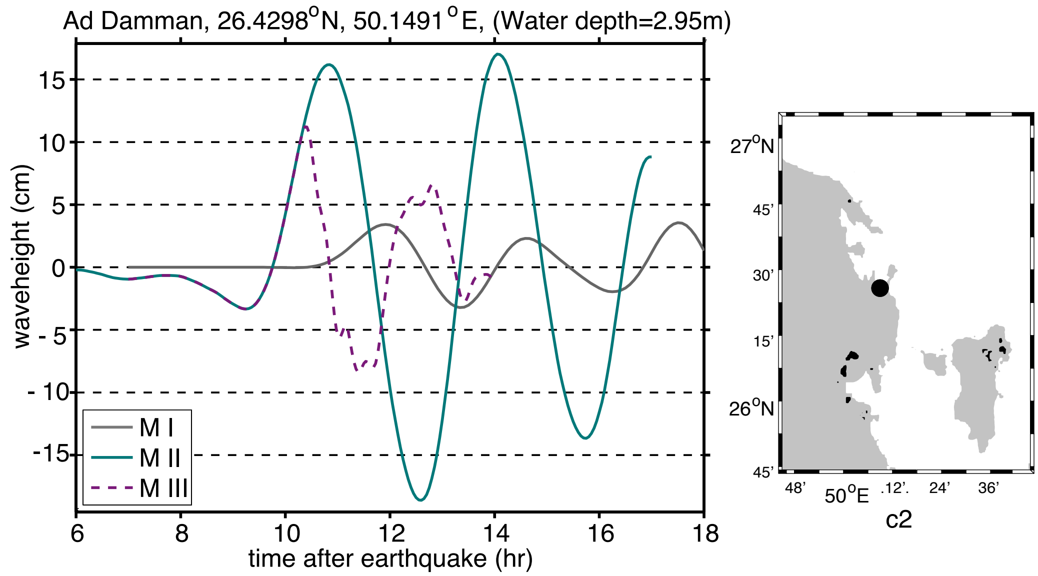

(a) Ad Damman

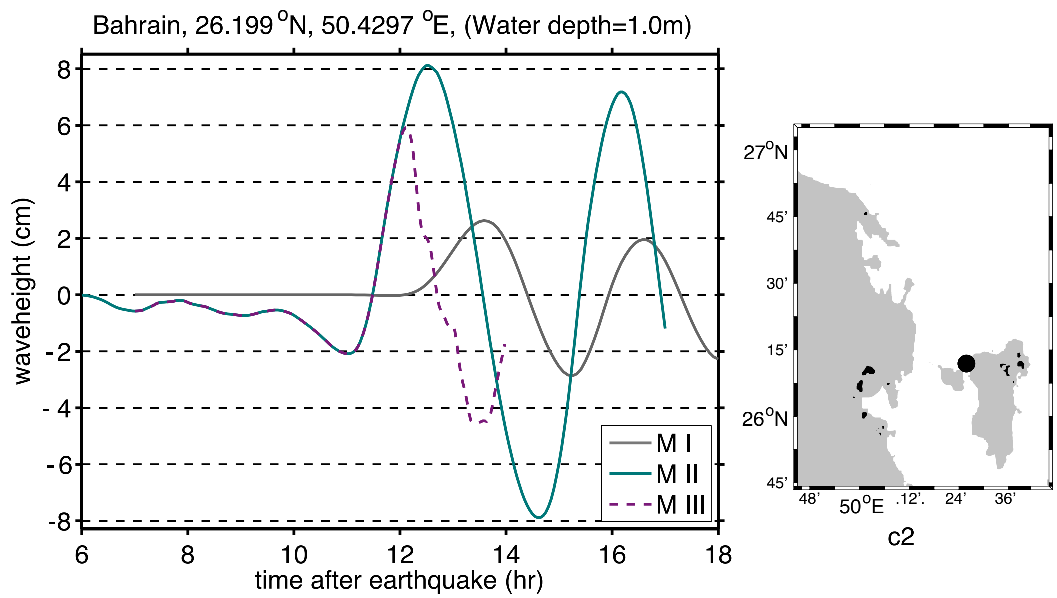

(b) Bahrain

Figure A.5: Comparison of water surface profiles of all three scenarios at (a) Ad Damman and (b) Bahrain.

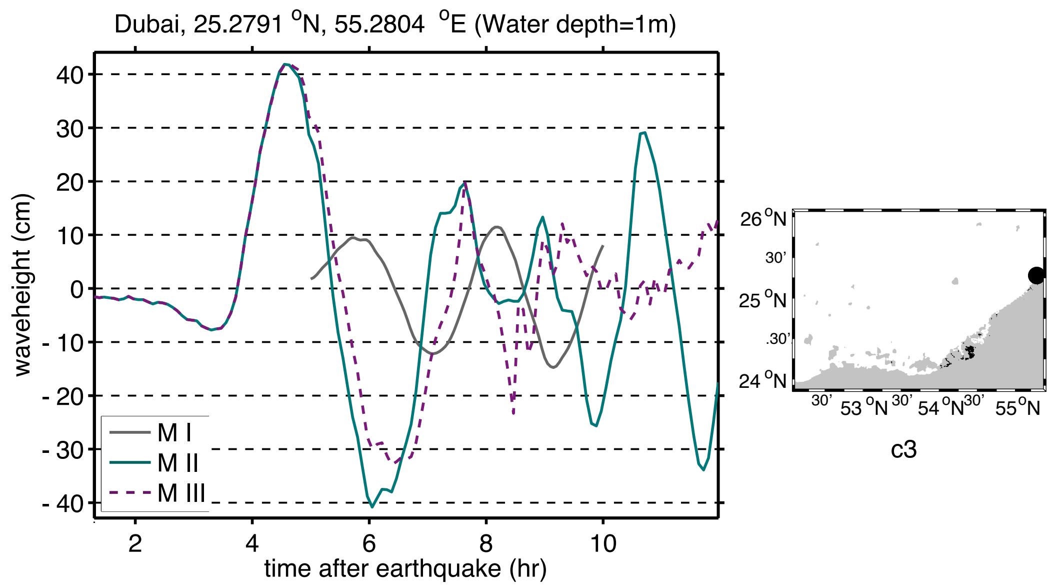

(a) Dubai

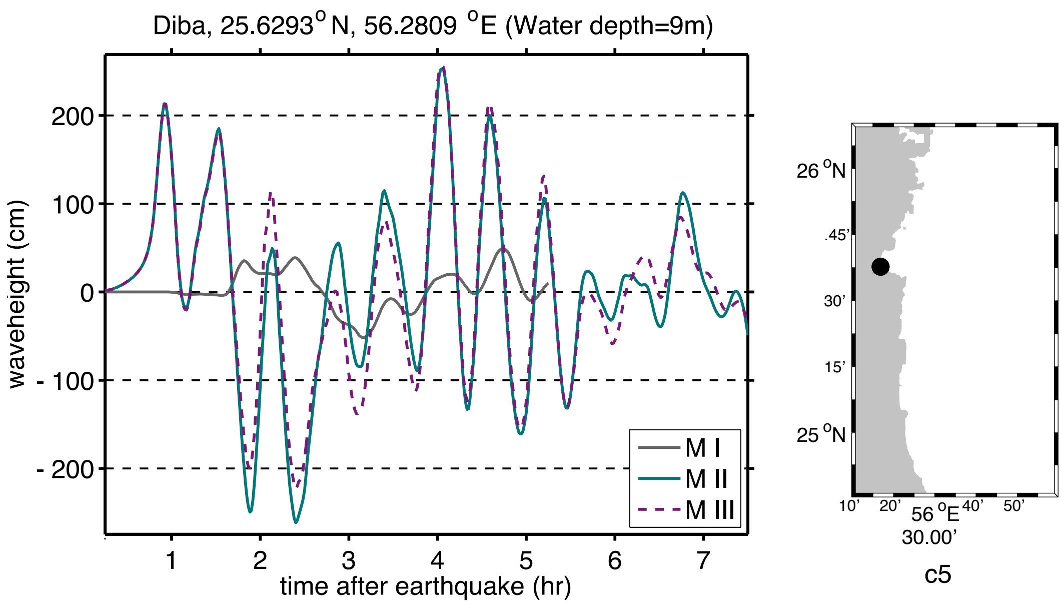

(b) Diba

Figure A.6: Comparison of water surface profiles of all three scenarios at (a) Dubai and (b) Diba.

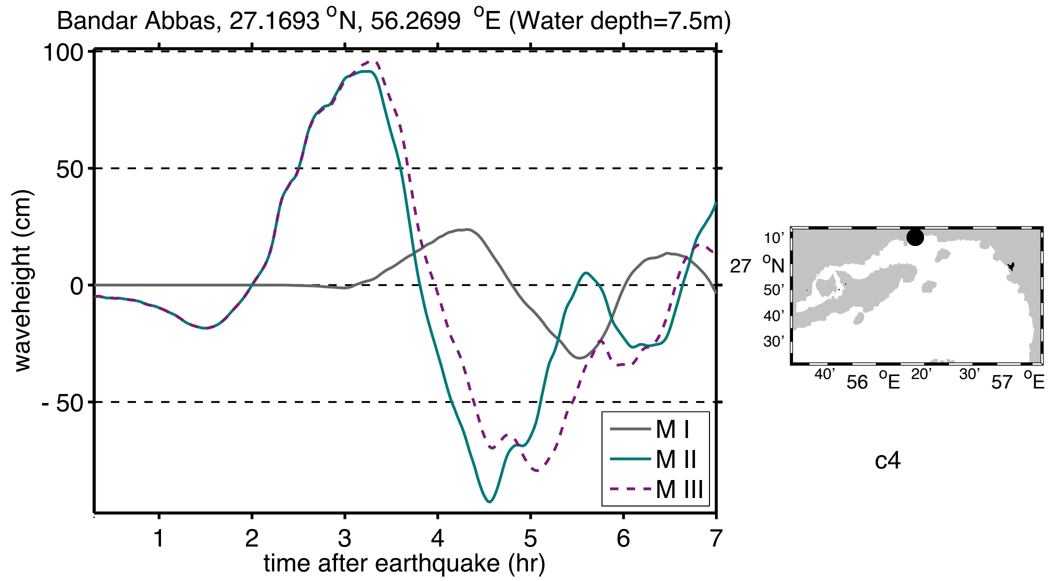

(a) Bandar Abbas

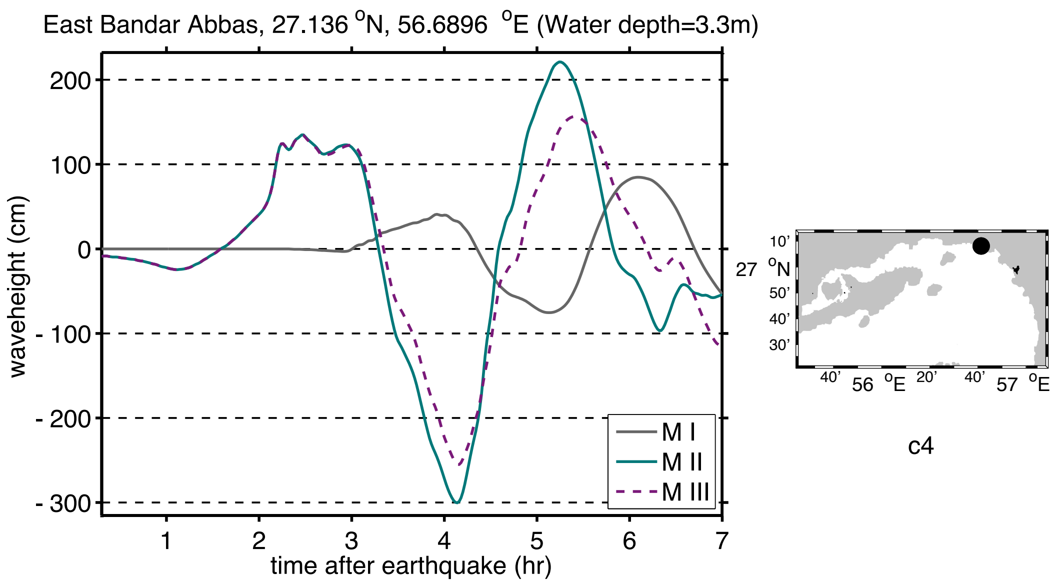

(b) E. Bandar Abbas

Figure A.7: Comparison of water surface profiles of all three scenarios at (a) Bandar Abbas and (b) E. Bandar Abbas.

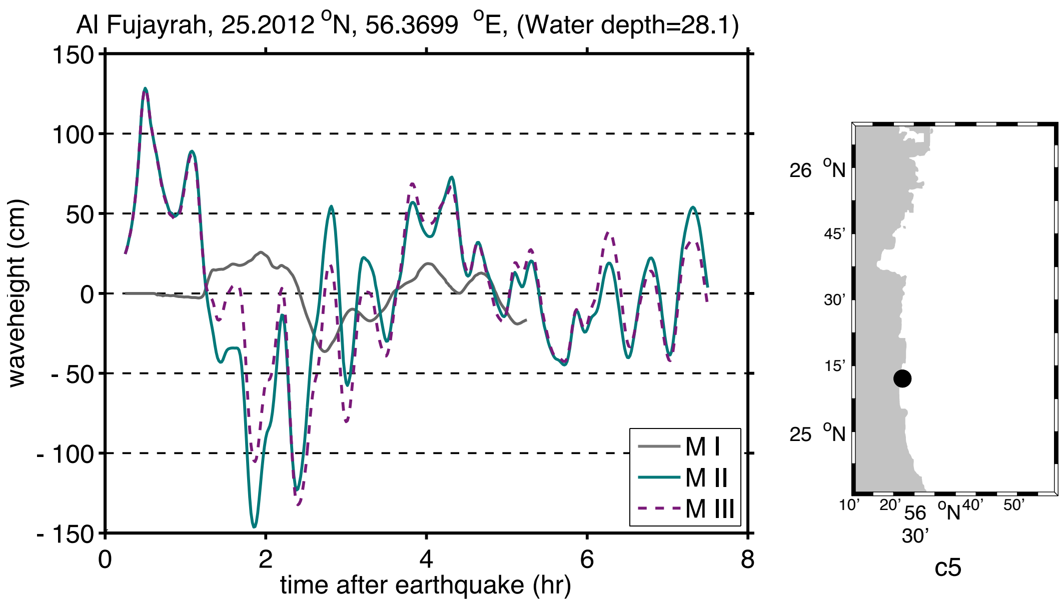

(a) Al Fujayrah

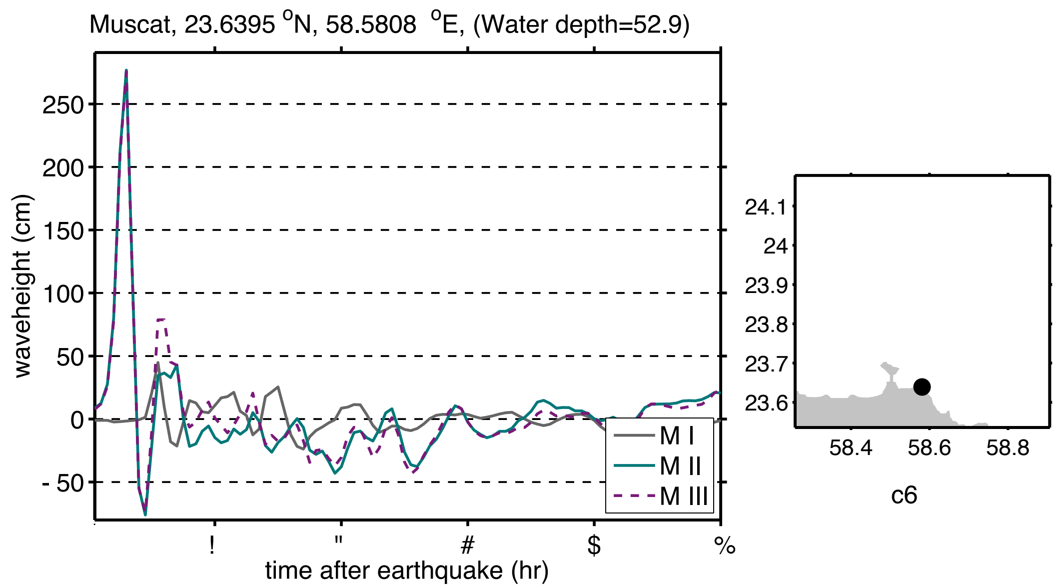

(b) Masqat

Figure A.8: Comparison of tide gauge records from all three cases for (a) Al Fujayrah and (b) Masqat.

Appendix B

A Case Study, Numerical Modeling of Thailand

B.1 Introduction

One of the biggest tsunami of recorded human history was triggered by the great 26 December 2004 earthquake. The earthquake epicenter was close to Banda Aceh, where the biggest inundation distances were experienced (Borrero, 2005) .

This event had all the special effects of a tsunamigenic event. The earthquake rupture was slow and as long as $1200km$ long with variable slips reaching up to $30m$ in the northern part of the rupture zone. This special tsunami traveled around the Indian Ocean causing devastation in India, Maldives (Fritz et al., 2006), Sri Lanka (Liu et al., 2005) and even as far as Somali, Africa (Fritz and Borrero, 2006).

Thailand, famous with its touristic beaches that attract people from all over the world, is located on the eastern part of the Andaman Sea that has a narrow opening to the Indian Ocean. It was also devastated by the Boxing Day tsunami. Many tourists that were having vacationing at Phi Phi Islands, Phuket and Phang Nga lost their lives (Dalrymple and Kriebel, 2005).

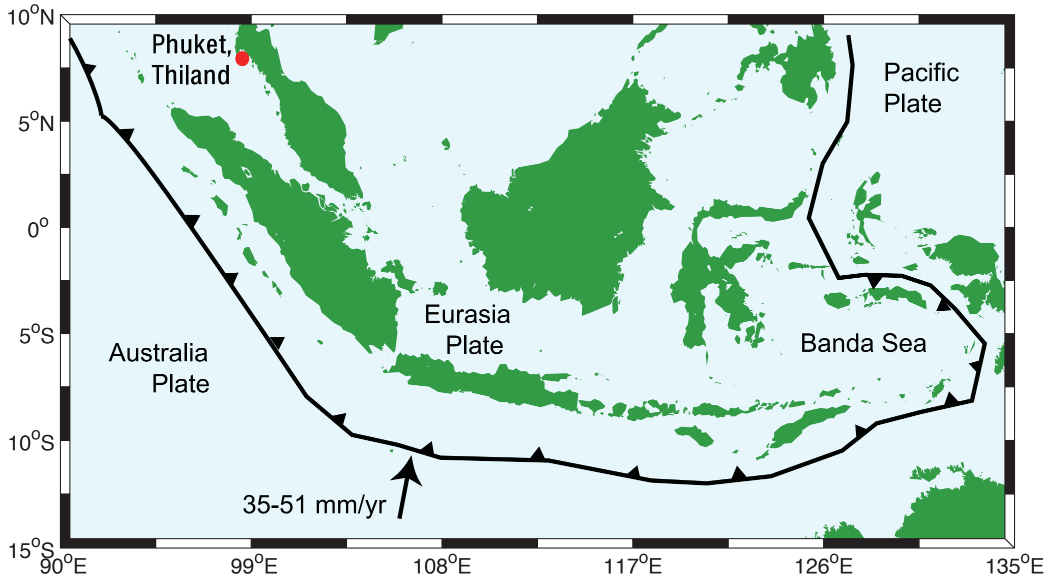

Figure B.1: Tectonics of Indonesia (convergence rate from Stein and Okal, 2007).

B.2 Earthquake Sources and Tsunami Model in Indian Ocean

The geological information available before 2004 had not been suggestive of a mega–thrust tsunamigenic fault line of the scales of the 2004 Sumatra earthquake. Latest studies showed that the 2004 was not the first time the Indian Ocean experienced a trans-oceanic tsunami. Here, some historical events in the Indian Ocean and their effects on Thailand are studied.

Paleoseimic studies of the Sumatra Subduction Zone suggest that similar earthquake as in 2004 occurred along the southern Sumatra every 200 to 240 years (Borrero et al., 2006b). The Sunda Arc tectonics setting is shown in Figure B.1. As explained in Borrero et al. (2006b), the subduction zone ruptured in 1797 and 1833 prior to the mega-tsunami in 2004.

Rastogi and Jaiswal (2006) have listed ninety tsunamis in the Indian Ocean between 326 B.C. and 2005 A.D; seventy of these are from the Sumatra Subdcution Zone and the remaining from the Bangladesh-Myanmar Coast on the north, which has well-documented tsunamis, and the Makran Coast in the northwest, which has one recorded tsunami. Tsunamis may not be as frequent as they in Pacific Ocean; however, some have claimed that the Indian Ocean experiences on average one tsunami every year.

The 1833 earthquake size has been determined by studying the coral bands around the Mentawai Islandsi, which are similar to tree rings, suggesting that the 1833 earthquake was a $M_w 8.8-9.2$, as a result of a rupture of $13m$ a $550km \times 175km$ (Zachariasen et al., 1999).

The Indian and Sundaland plate interaction has a $36mm/yr$ convergence rate derived from the GPS measurements (Sahu et al., 2006). This triggers great earthquakes in the Myanmar region, for instance, the 1897 $M_w 8.7$ earthquake.

There is paleoseismic evidence of tsunamis around the Persian Gulf. The most recent tsunamigenic earthquake took place at the Makran region in 1945, see Appendix A. We model it with a $M_w 8.7$ earthquake, which was a rupture of $7m$ slip over a $550km \times km$, following the study of Byrne et al. (1992).

We study tsunamis in the Indian Ocean with in a single propagation model and propagated them until the Andaman Sea, where they are passed through at the boundaries to the three nested grids, as shown in Figure B.2. The model used is MOST (Titov and Synolakis, 1997, 1998), and discussed in Chapter 1 and Appendix A.

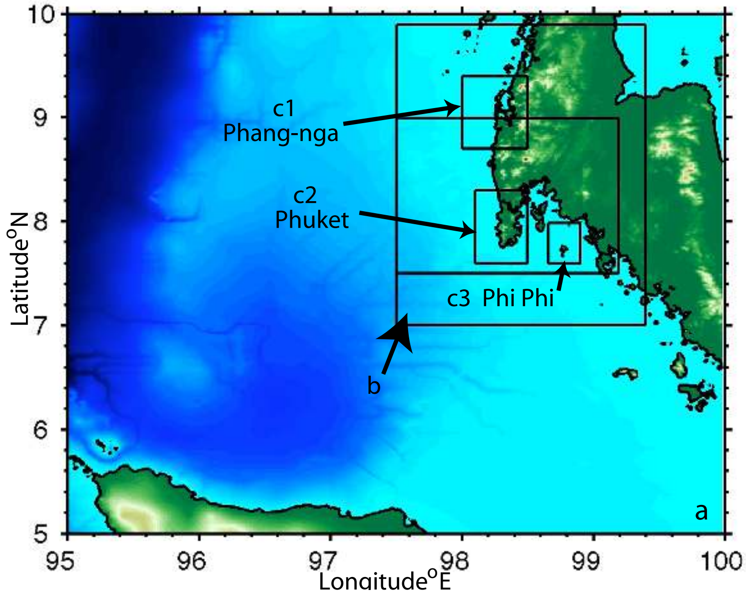

Figure B.2: Numerical grids used for Thailand.

B.3 Results

The model results suggest that the runup heights at Thailand from the 2004 event are much higher than from other sources from the rest of the Indian Ocean. The 2004 Sumatra event had the best orientation to penetrate the Andaman Sea, among all others in Indian Ocean. The waves from Myanmar sources are blocked by the Andaman-Nicobar Islands and the tsunamis from Makran are not strong enough to reach to the Thailand.

Figures B.3, B.4 and B.5 shows the maximum wave and runup heights from 2004 event at the Phang Nga, Phuket and Phi Ph. Our model suggests a maximum waveheight around $7m$ resulting in runup around $15 - 20m$ at all of the three beaches.

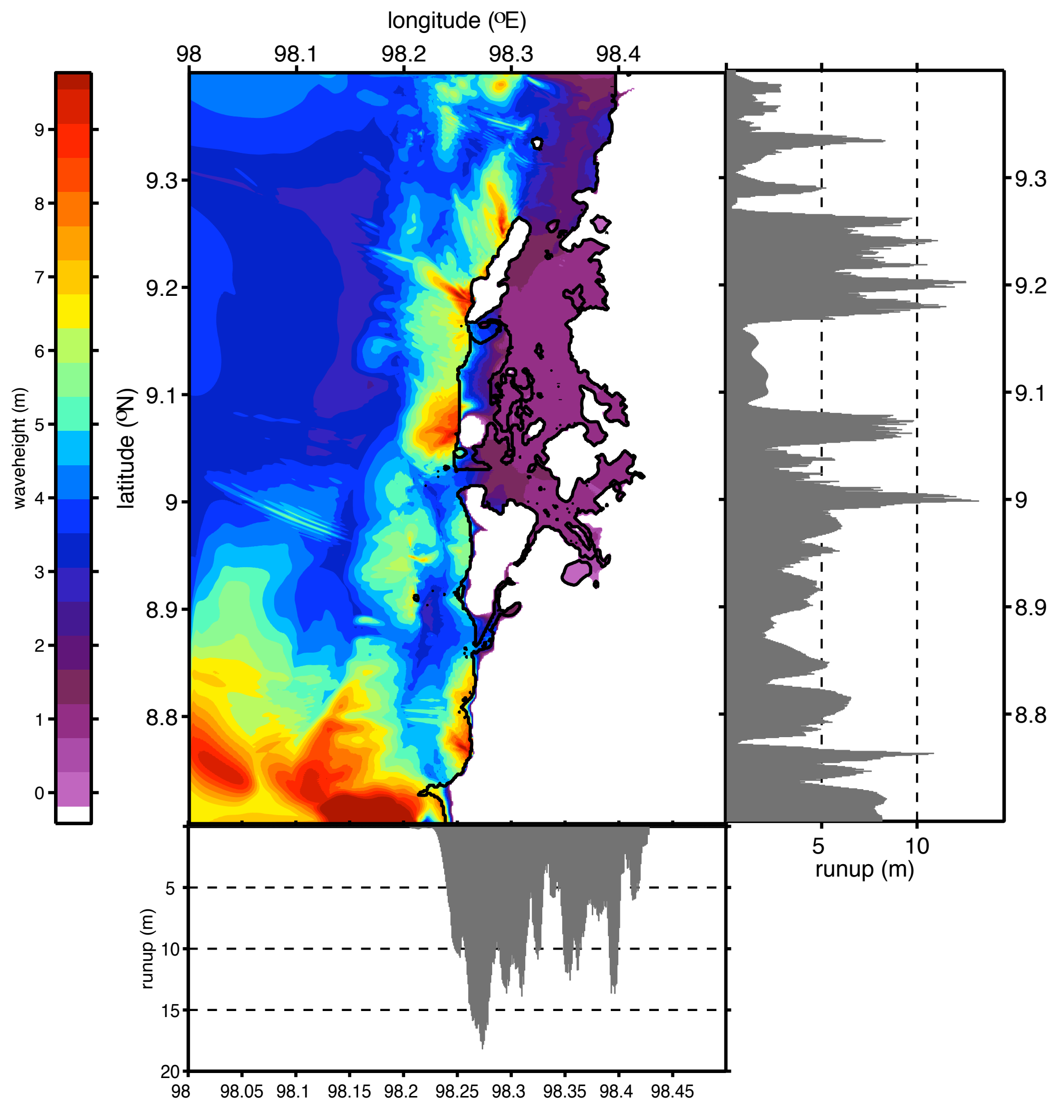

Figure B.3: Maximum waveheight distribution, overland flowdepth and runup heights in Phang-nga, Thailand.

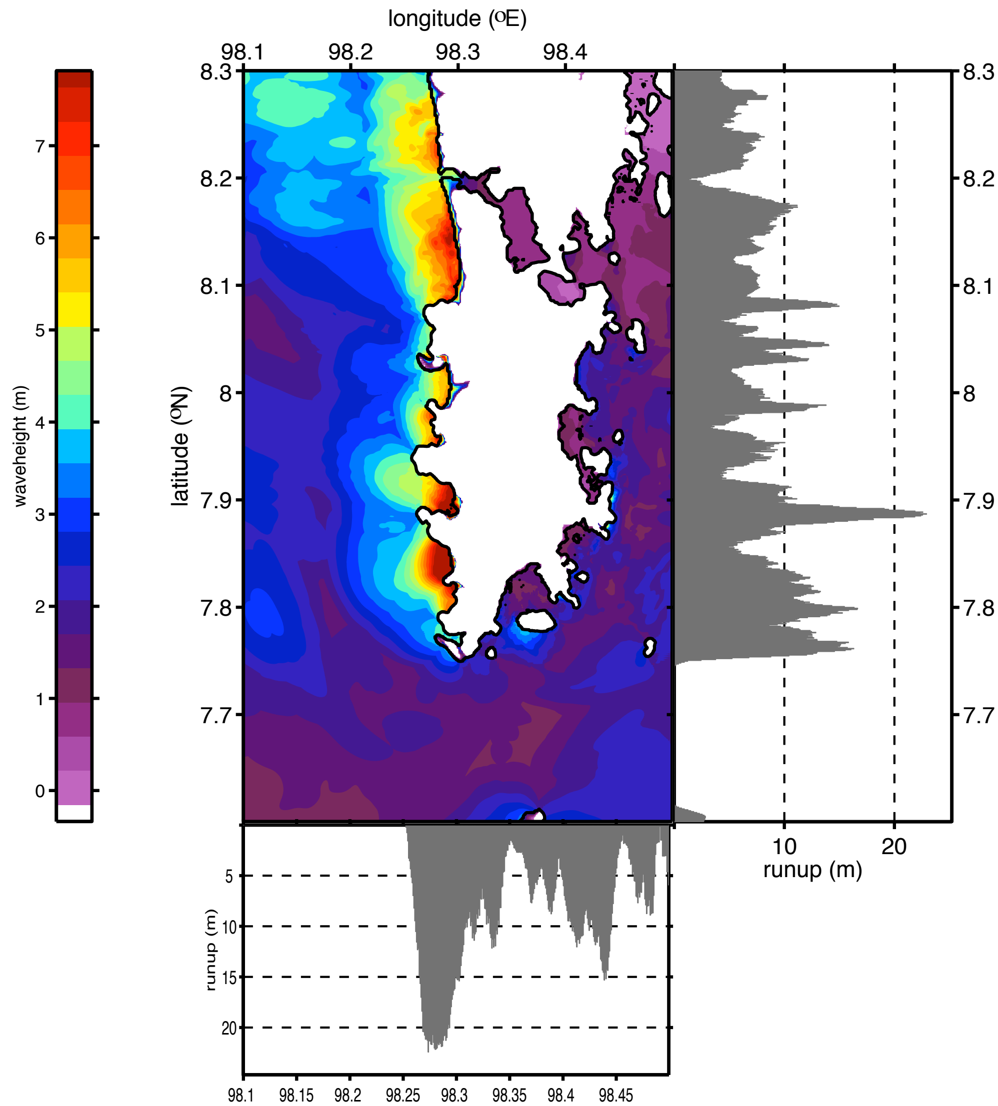

Figure B.4: Maximum waveheight distribution, overland flowdepth and runup heights in Phuket, Thailand.

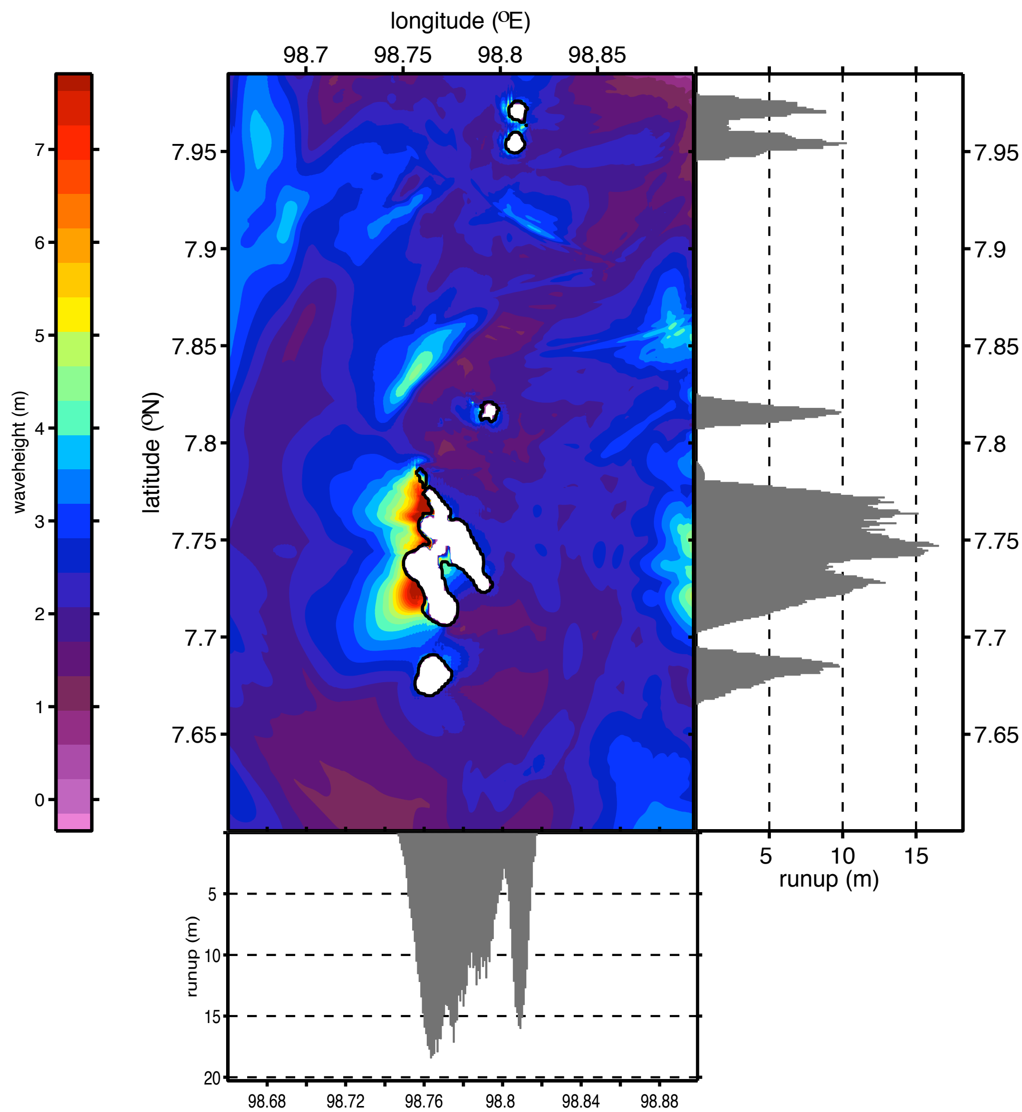

Figure B.5: Maximum waveheight distribution, overland flowdepth and runup heights in Phi Phi, Thailand.

Appendix C

Tide Gauge Records from 1952, 1960 and 1964

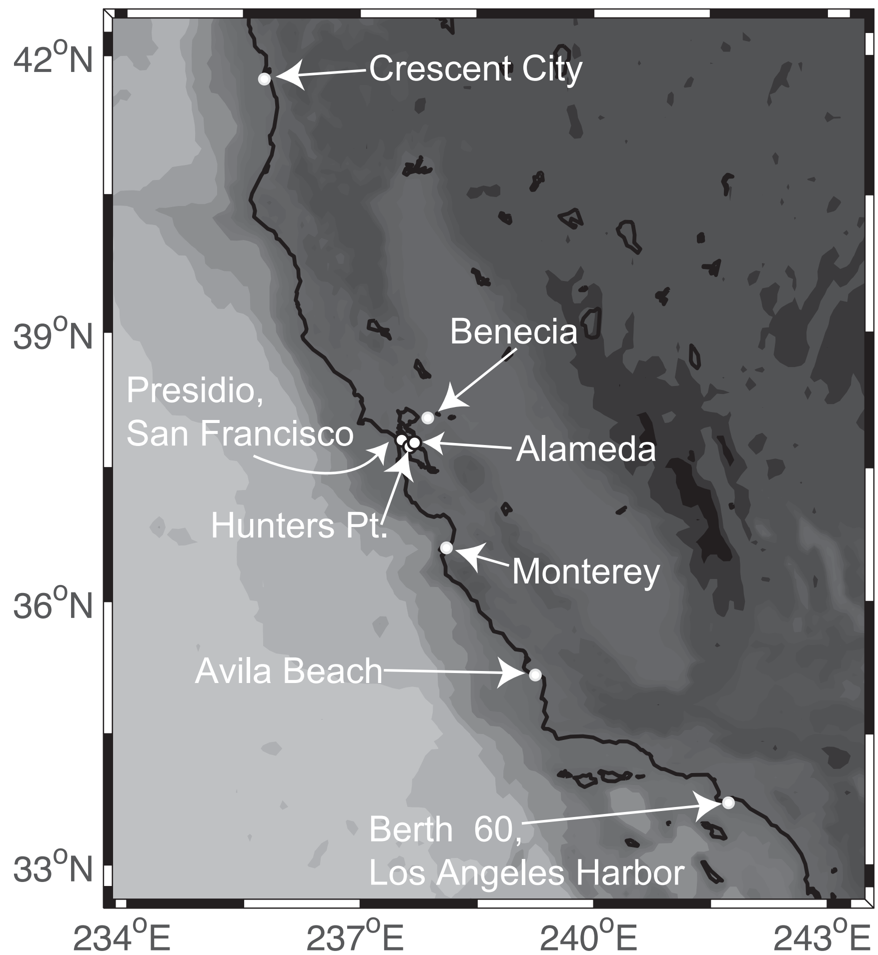

Figure C.1: Locations of the tide gauges used in this report is shown in figure.

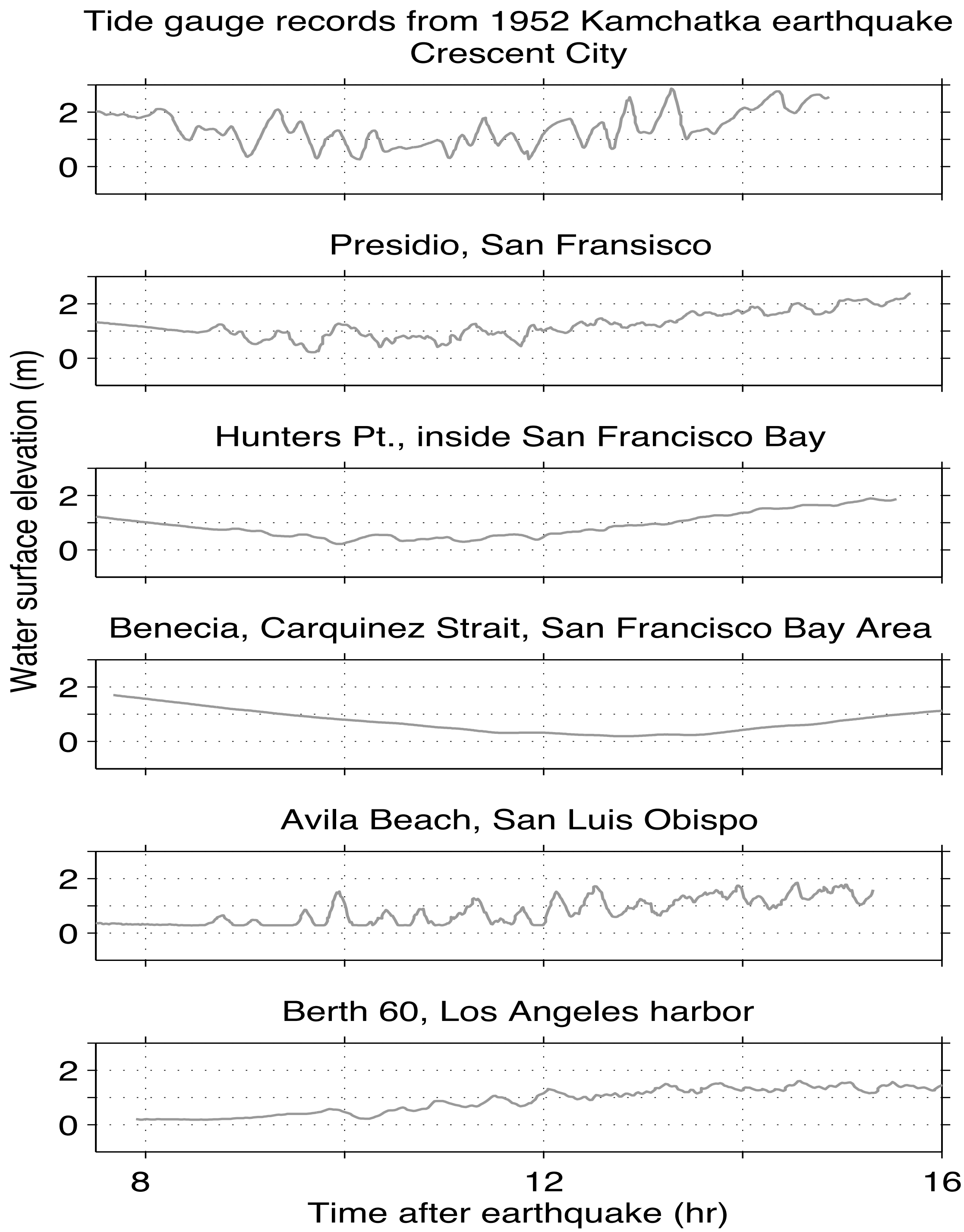

Figure C.2: Tide gauge records from 1952 events are shown above. Tide is not filtered in this plot. Gauge readings are from Crescent City, Presidio in San Francisco, Hunters Pt. inside the San Francisco Bay, Benecia at Carquinez Strait in San Francisco Bay area, Avila Beach at San Luis Obispo and Berth 60 at Los Angeles.

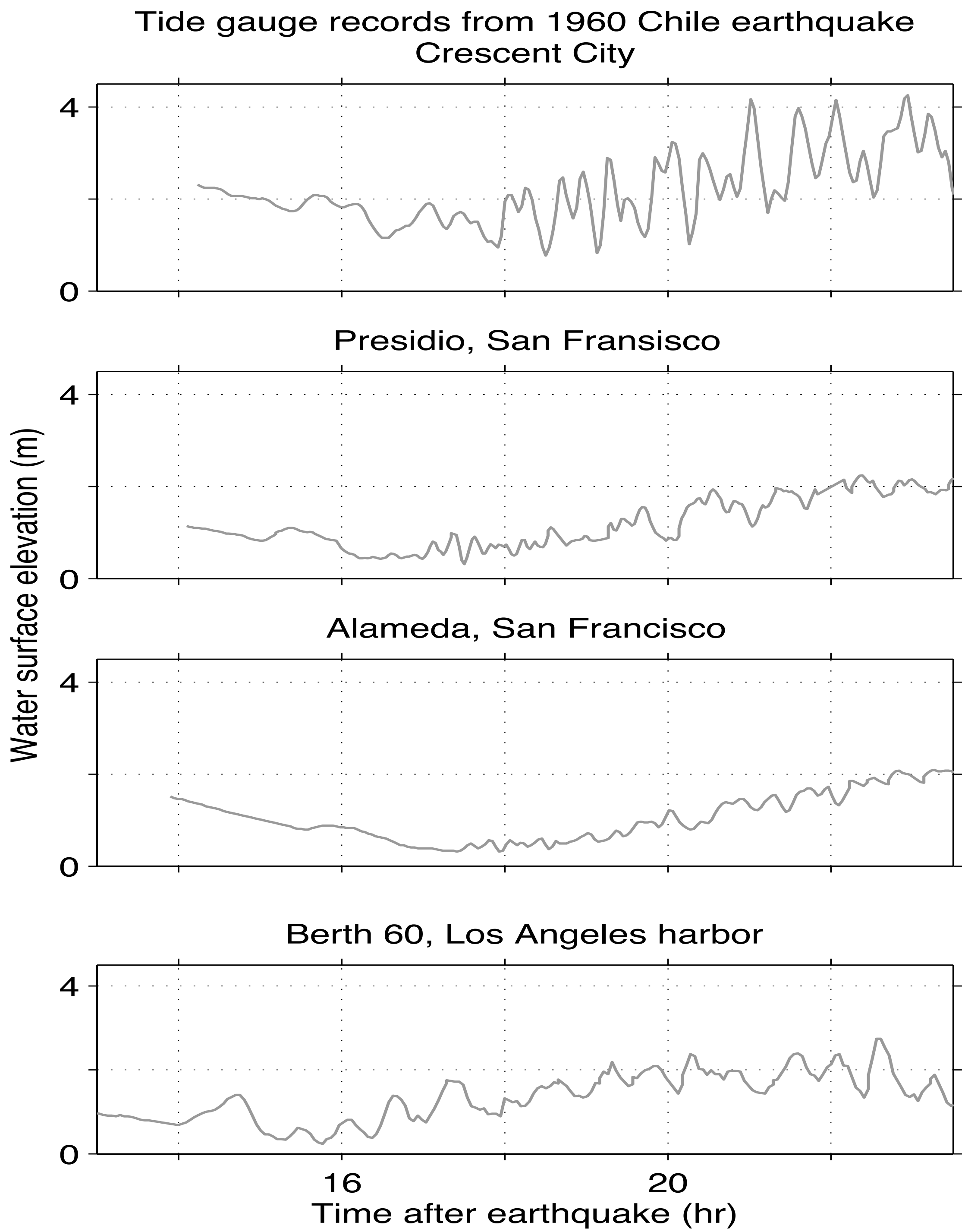

Figure C.3: Tide gauge records from 1960 events are shown above. Records are plotted without any filtration. Gauge readings are from Crescent City, Presidio in San Francisco, Alameda in San Francisco Bay and Berth 60 at Los Angeles.

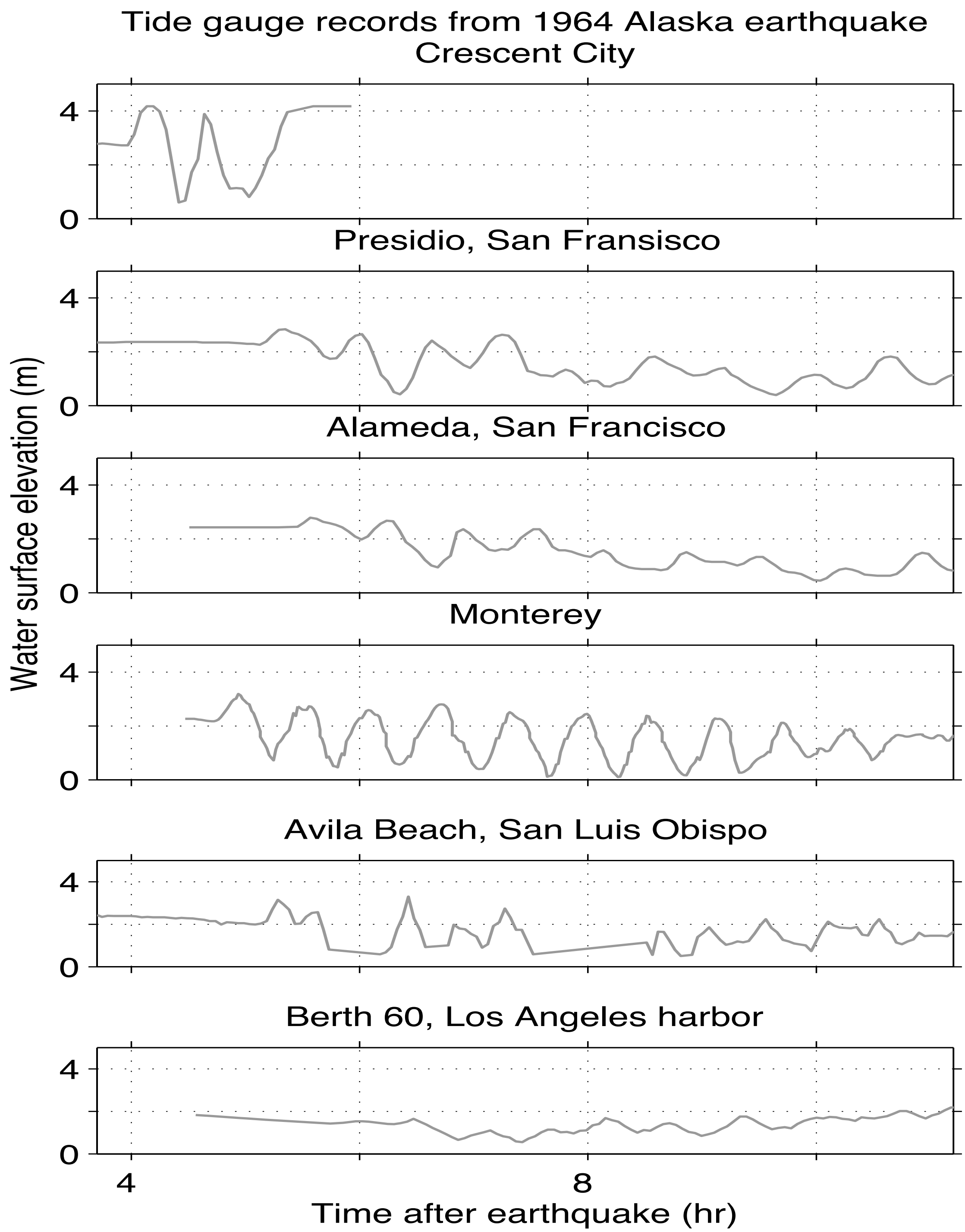

Figure C.4: Tide gauge records from 1964 events are shown above. Records are plotted without any filtration. Gauge readings are from Crescent City, Presidio in San Francisco, Alameda in San Francisco Bay, Moneterey, Avila Beach in San Luis Obispo and Berth 60 at Los Angeles.

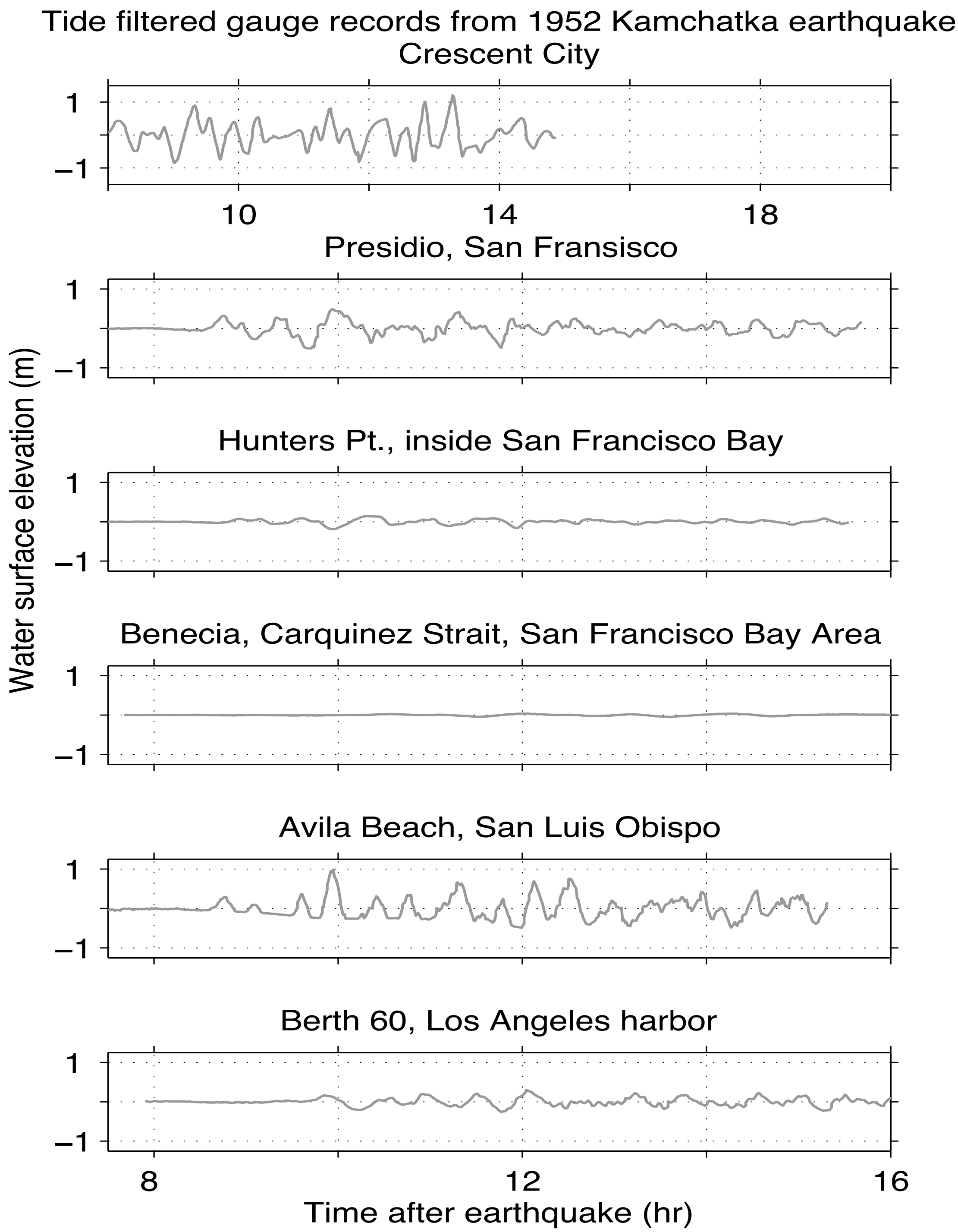

Figure C.5: Tide gauge records from 1952 events are shown above. Records are filtered for tide. Gauge readings are from Crescent City, Presidio in San Francisco, Hunters Pt. inside the San Francisco Bay, Benecia at Carquinez Strait in San Francisco Bay area, Avila Beach at San Luis Obispo and Berth 60 at Los Angeles.

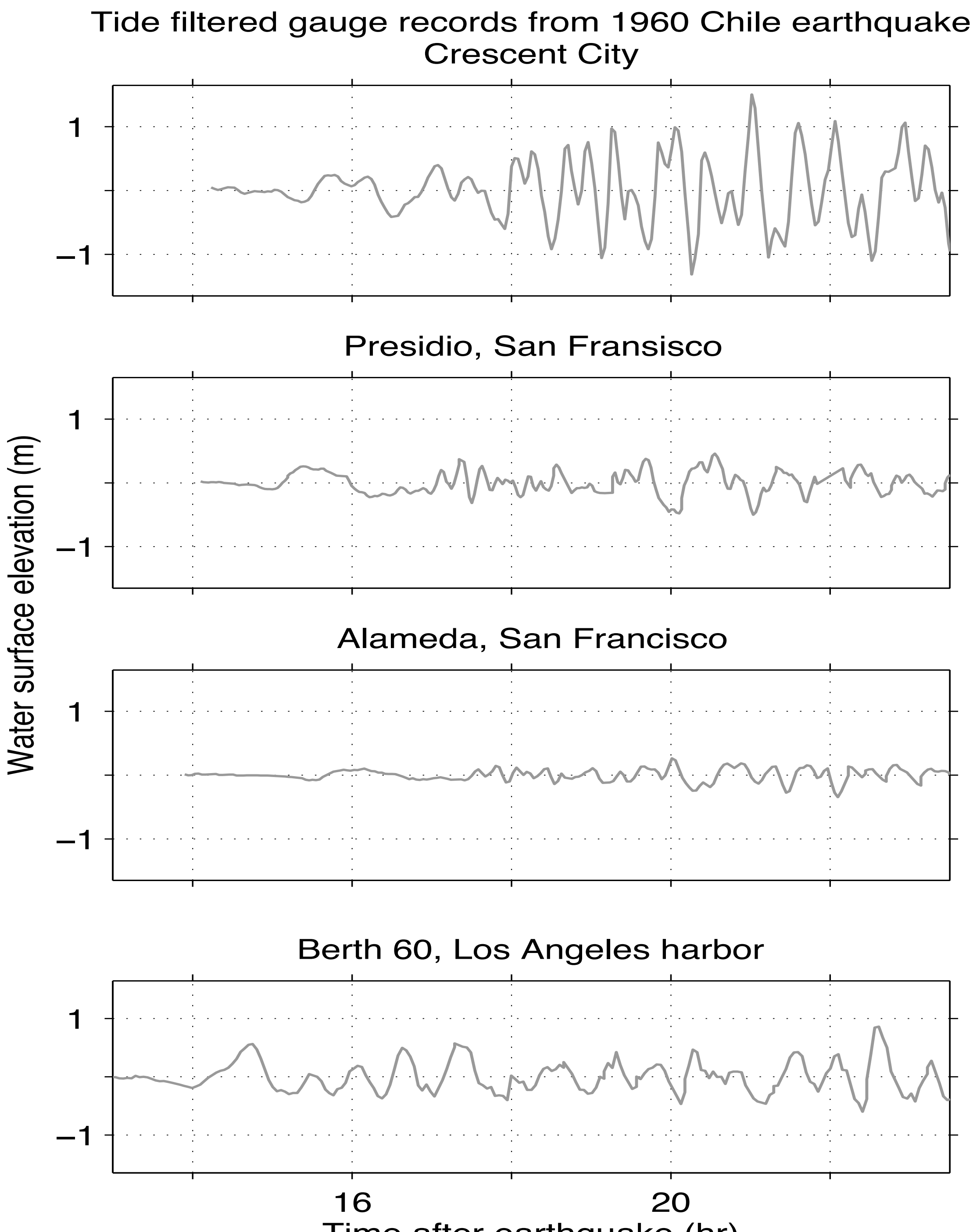

Figure C.6: Tide gauge records from 1960 events are shown above. Records are filtered for tide. Gauge readings are from Crescent City, Presidio in San Francisco, Alameda in San Francisco Bay and Berth 60 at Los Angeles.

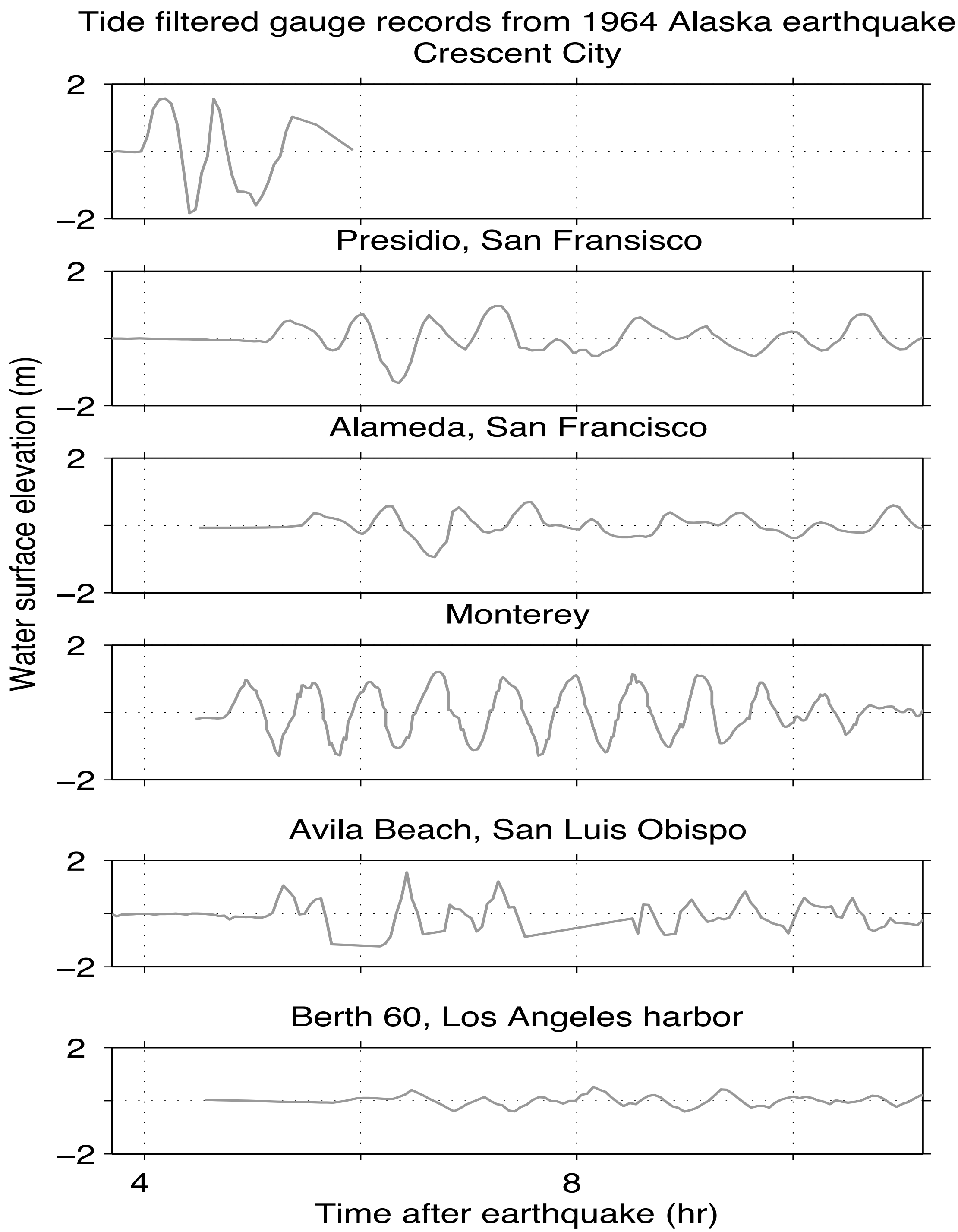

Figure C.7: Tide gauge records from 1964 events are shown above. Records are filtered for tide. Gauge readings are from Crescent City, Presidio in San Francisco, Alameda in San Francisco Bay, Moneterey, Avila Beach in San Luis Obispo and Berth 60 at Los Angeles.